

The Pennsylvania State University

The Graduate School

Department of Mechanical and Nuclear Engineering

**DEVELOPMENT OF MASTER DESIGN CURVES
FOR PARTICLE IMPACT DAMPERS**

A Thesis in

Mechanical Engineering

by

Michael Yichung Yang

© 2003 Michael Yichung Yang

Submitted in Partial Fulfillment
of the Requirements
for the Degree of

Doctor of Philosophy

December, 2003

The thesis of Michael Yichung Yang was reviewed and approved* by the following:

Gary H. Koopmann
Distinguished Professor of Mechanical Engineering
Thesis Co-Advisor
Chair of Committee

George A. Lesieutre
Professor of Aerospace Engineering
Thesis Co-Advisor

Stephen A. Hambric
Associate Professor of Acoustics
Thesis Co-Advisor

Richard C. Benson
Professor of Mechanical Engineering
Head of the Department of Mechanical and Nuclear Engineering

*Signatures are on file in the Graduate School

ABSTRACT

Particle impact dampers (PIDs) are enclosures partially filled with particles of various sizes, shapes, and materials. When attached to a vibrating structure, they dissipate energy through inelastic collisions between the particle bed and the enclosure wall. In this thesis, the development of master design curves to predict the damping and mass characteristics of particle impact dampers are presented. A power measurement technique enabled the time-efficient measurement of the damping and mass properties of the PID. The power measurement technique enjoys several advantages over traditional loss factor measurements, including the flexibility to analyze the behavior of the PID at any frequency or excitation amplitude, and the ability to predict the damping and mass contribution for any structure operating under the same conditions. Using this power measurement technique, a large number of experiments were conducted to determine the effects of vibration amplitude, excitation frequency, gap size, particle size, and particle mass on the dissipated power and effective mass of the PID. A high speed digital video camera was used to directly observe particles in motion under different conditions, which greatly aided the interpretation of the data trends and the development of the master design curves. Based on the data trends from the power measurements and the insight gained from the videos, the power data was systematically collapsed into a pair of two-dimensional master design curves with unitless axes which are comprised of combinations of design parameters. The damping and mass efficiencies of the PID may be predicted from the design curves for specific applications. An interpretation of the

design curves is given, and the performance of a PID on a structure is used to verify their predictive capabilities.

TABLE OF CONTENTS

LIST OF FIGURES	viii
LIST OF TABLES	xvi
ACKNOWLEDGEMENTS	xvii
Chapter 1 Introduction	1
1.1 Description of Particle Impact Damping	1
1.2 Literature Review	3
1.2.1 Early Work on Impact and Particle Impact Dampers.....	3
1.2.2 Review of Experimental Work.....	4
1.2.3 Review of Modeling Techniques.....	7
1.2.4 Review of Previous Applications	11
1.2.5 Comparison of Impact and Particle Impact Dampers.....	13
1.2.6 Summary of Previous Work	14
1.3 Approach and Procedure.....	15
Chapter 2 Early Experimental Work.....	17
2.1 Comparison of Behavior with Lumped Mass.....	17
2.2 Effect of Particle Impact Damper Location.....	20
2.3 Effect of Friction and Gap Size	24
2.4 Summary of Early Experiments.....	33
2.5 Design of Ensuing Experiments	34
Chapter 3 Measurement of Particle Impact Damper Properties	36
3.1 Theoretical Background.....	37
3.2 Power Measurement Technique: Proof of Concept.....	38
3.2.1 Description of Experimental Setup to Measure Power	39
3.2.2 Verification of Trapped Power Measurement with Lumped Mass	42
3.2.3 Verification of Power Measurement Technique Using Particle Impact Dampers	46
3.2.4 Summary of Proof of Concept of Power Measurement Technique	59
3.3 Power Measurements.....	60
3.3.1 Effect of Amplitude on Optimum Gap and Effective Mass	60
3.3.2 Effect of Particle Size on Optimum Gap Size	63
3.3.3 Effect of Particle Size on Effective Mass.....	69
3.3.4 Effect of Vibration Amplitude on Dissipated Power and Effective Mass	70
3.3.5 Effect of Frequency on Dissipated Power and Effective Mass	77
3.4 Summary of Power Measurements	79

Chapter 4 Slow-Motion Videos of Particle Motion	81
4.1 General Motion of Particles.....	82
4.2 Motion of Particles Relating to Dissipated Power.....	84
4.3 Motion of Particles Relating to Effective Mass.....	88
4.4 Summary of Observations	89
Chapter 5 Master Design Curves	91
5.1 Collapse of Data Curve for Dissipated Power.....	91
5.1.1 Collapse of Dissipated Power Efficiency With Respect to Frequency	94
5.1.2 Collapse of Power Dissipation Efficiency With Respect to Gap Size	98
5.1.3 Collapse of Dissipated Power Efficiency With Respect to Particle Size	104
5.1.4 Collapse of Dissipated Power Efficiency With Respect to Particle Mass	109
5.1.5 Curve Fit of Dissipated Power Efficiency Master Curve	113
5.2 Collapse of Data Curve for Mass.....	116
5.2.1 Collapse of Mass Efficiency With Respect to Frequency	117
5.2.2 Collapse of Mass Efficiency With Respect to Gap Size	121
5.2.3 Collapse of Mass Efficiency With Respect to Particle Size.....	127
5.2.4 Collapse of Mass Efficiency With Respect to Particle Mass	130
5.2.5 Curve Fit of Mass Efficiency Master Curve.....	133
5.3 Comparison and Interpretation of Master Design Curves	135
5.4 Implementation of Video Correction.....	140
5.5 Relating the Master Design Curves to a Structure.....	146
5.5.1 Prediction of Loss Factor from DPE Master Design Curve	150
5.5.2 Prediction of Effective Mass from MEPB Master Design Curve	155
5.6 PID Design Recommendations.....	161
5.6.1 Building the Master Design Curves	162
5.6.2 Limitations of the Master Design Curves.....	163
5.6.3 Recommended Number of Layers	163
5.6.4 Other Recommendations and Considerations	164
5.6.5 Recommended Design Procedure.....	165
5.7 Summary and Conclusions	166
Chapter 6 Conclusions and Future Work	168
6.1 Early Experimental Work	168
6.2 Development and Verification of Power Measurement Technique	169
6.3 Measurement of Particle Impact Damper Properties Using Power	169
6.4 Slow Motion Videos	171
6.5 Master Design Curves.....	172
6.6 Design Recommendations	173

6.7 Summary of Major Contributions.....	174
6.8 Future Work.....	175
Bibliography	177
Appendix A Description of Enclosures	183
A.1 Acrylic-Aluminum Enclosure.....	183
A.2 Aluminum Enclosure.....	191
Appendix B Supplementary Power Measurement Verifications	197
B.1 Analysis of Transducer Phase Error.....	197
The sensitivity of the trapped power to transducer phase error is shown in Figures B.3 and Figure B.4. It is apparent that trapped power, although affected by transducer phase error, is significantly less sensitive than active power. Phase errors as high as 10% only cause a 1.5% error.....	201
B.1.1 Correction of Transducer Phase Error	202
B.2 Verification of Power at Discrete Frequency.....	205
B.3 Measurement of Loss Factor Using Pole-Zero Curve Fitting Method	212
B.4 Verification of Power Measurement Using Airpot Pneumatic Viscous Damper	214
Appendix C Interpolation with Neural Networks.....	226
C.1 Fundamentals of Neural Networks	226
C.2 Backpropagation Networks.....	228
C.2.1 Training Algorithm for Backpropagation Networks	228
C.2.2 Summary of Training Algorithm for Backpropagation Networks.....	236
C.2.3 The Levenberg-Marquardt Algorithm	236
C.2.4 Summary of Levenberg-Marquardt Training Algorithm for Backpropagation Networks	241

LIST OF FIGURES

Figure 1.1: Impact damper and particle impact damper	2
Figure 1.2: Type I, II, III periodic impact motions [27]	9
Figure 2.1: Experimental Setup	18
Figure 2.2: Particle Impact Damper.....	18
Figure 2.3: Comparison of PID and Lumped Mass	19
Figure 2.4: Honeycomb sandwich beam.....	21
Figure 2.5: Honeycomb beam, mode 1 (38 Hz).....	21
Figure 2.6: Honeycomb beam, mode 3 (486 Hz).....	21
Figure 2.7: Frequency response for mode 1 – particles at end of beam	23
Figure 2.8: Frequency response for mode 3 – particles near middle of beam	24
Figure 2.9: Schematic of experimental setup.....	25
Figure 2.10: Particle enclosure with adjustable gap	27
Figure 2.11: Sample experimental curves for different gap sizes. Acceleration = 31 g, 200 1/16 inch spherical brass ball bearings.	28
Figure 2.12: Effects of coating buildup on maximum accelerance. Circles indicate measurements taken immediately after enclosure cleanings. Gap size = 1.0 mm, acceleration = 43 g	30
Figure 2.13: Measured loss factors for different gap sizes and acceleration levels....	31
Figure 2.14: Resonance frequencies for different gap sizes	33
Figure 3.1: Enclosures with adjustable screw top.....	39
Figure 3.2: Schematic of power measurement setup	40
Figure 3.3: Picture of power measurement setup (laser vibrometer not shown)	41
Figure 3.4: Power and equivalent mass data for 136 gram mass.....	43
Figure 3.5: Power and equivalent mass data for 200 gram mass.....	44

Figure 3.6: Power and equivalent mass data for 369 gram mass.....	45
Figure 3.7: Aluminum ground structure with clamped beam.....	47
Figure 3.8: Attachment of shaker, force sensor, and PID to beam center	48
Figure 3.9: Particle enclosure with clear acrylic walls	49
Figure 3.10: Completed beam setup for set 1	50
Figure 3.11: Picture of power measurement setup with aluminum-acrylic enclosure.....	51
Figure 3.12: Velocity profile of beam with PID at fundamental resonance	53
Figure 3.13: Measured and predicted loss factors for PID on beam at first beam resonance with varying amplitude (11 x 2 x $\frac{1}{4}$ inch beam).....	53
Figure 3.14: Measured and predicted loss factors for PID on beam at first beam resonance with varying amplitude (12 x 2 x $\frac{1}{4}$ inch beam).....	54
Figure 3.15: Completed beam setup for set 2	55
Figure 3.16: Velocity profile of 30 inch beam at 127 Hz	57
Figure 3.17: Measured and predicted loss factors for PID on 30 inch beam with varying gap size	58
Figure 3.18: Dissipated power with changing gap and amplitude.....	61
Figure 3.19: Effective mass of PID with changing gap and amplitude	63
Figure 3.20: Aluminum enclosure	64
Figure 3.21: FCC atom-site (a) and hard-sphere (b) cell models. Source: G.T. Murray, <i>Introduction to Engineering Materials: Behavior, Properties, and Selection</i> . Marcel Dekker, Inc. 1993. p. 123.	65
Figure 3.22: Stacking sequence for FCC structure. Source: G.T. Murray, <i>Introduction to Engineering Materials: Behavior, Properties, and Selection</i> . Marcel Dekker, Inc. 1993. p. 125.	66
Figure 3.23: Dissipated power vs. volume fraction for different particle sizes	67
Figure 3.24: Dissipated power vs. gap size for different particle sizes	68
Figure 3.25: Incomplete layer of particles	69

Figure 3.26: Effective mass vs. gap size for different particle sizes.....	70
Figure 3.27: Relationship between dissipated power and displacement. 1/16 inch particles. 0.79 mm gap size.....	71
Figure 3.28: Relationship between dissipated power and displacement. 1/16 inch particles. 1.35 mm gap size.....	72
Figure 3.29: Relationship between dissipated power and displacement. 1/8 inch particles. 3.97 mm gap size.....	73
Figure 3.30: Relationship between dissipated power and displacement. 3/16 inch particles. 5.93 mm gap size.....	74
Figure 3.31: Relationship between effective mass and displacement. 1/16 inch particles. 0.79 mm gap size.....	75
Figure 3.32: Change in transition displacement with gap and particle size.....	77
Figure 3.33: Effect of frequency on dissipated power. 1/16 inch particles.	78
Figure 3.34: Effect of frequency on dissipated power. 1/8 inch particles.	78
Figure 4.1: Vertical (left) and horizontal (right) motion of PID.....	82
Figure 4.2: Single particle in enclosure	84
Figure 4.3: Optimal particle bed impact	85
Figure 4.4: Non-optimal particle bed impact. Gap below optimum.	86
Figure 4.5: Non-optimal particle bed impact. Gap above optimum.	87
Figure 4.6: Friend and Kinra model – extended contact time for high amplitudes. Source: R.D. Friend and V.K. Kinra, <i>Journal of Sound and Vibration</i> , 233(1), pp. 93-118. Particle impact damping. 2000.	88
Figure 5.1: Uncollapsed dissipated power vs. displacement	93
Figure 5.2: Uncollapsed power data. 600 1/16 inch particles. Gap = 0.79 mm.....	95
Figure 5.3: DPE collapse on frequency. 600 1/16 inch particles. Gap = 0.79 mm....	96
Figure 5.4: DPE collapse on frequency. 174 3/32 inch particles. Gap = 2.73 mm...97	97
Figure 5.5: DPE collapse on frequency. 22 3/16 inch particles. Gap = 2.37 mm....98	98
Figure 5.6: Uncollapsed dissipated power data. 1/8 inch particles.....	99

Figure 5.7: DPE collapse on gap size. 600 1/16 inch particles.....	100
Figure 5.8: DPE collapse on gap size. 174 3/32 inch particles.....	101
Figure 5.9: DPE collapse on gap size. 75 1/8 inch particles.....	102
Figure 5.10: DPE collapse on gap size. 37 5/32 inch particles.....	103
Figure 5.11: DPE collapse on gap size. 22 3/16 inch particles.....	104
Figure 5.12: Uncollapsed dissipated power data for different particle sizes	105
Figure 5.13: DPE collapse on particle size. 10.5 grams total particle mass	106
Figure 5.14: DPE collapse on particle size with smallest gap sizes removed. 10.5 grams total particle mass	107
Figure 5.15: DPE collapse on particle size with smallest gap sizes removed and number of layers included. 10.5 grams total particle mass.....	109
Figure 5.16: DPE collapse on total particle mass. 1/16 inch particles.....	111
Figure 5.17: DPE collapse on total particle mass. 3/32 inch particles.....	112
Figure 5.18: DPE collapse on total particle mass. 1/8 inch particles.....	113
Figure 5.19: Curve fits for dissipated power master curve.....	115
Figure 5.20: Effective mass vs. displacement, 600 1/16 inch particles, gap = 0.79 mm	118
Figure 5.21: MEPB collapse on frequency, 600 1/16 inch particles, gap = 0.79 mm	119
Figure 5.22: MEPB collapse on frequency, 174 3/32 inch particles, gap = 2.73 mm	120
Figure 5.23: MEPB collapse on frequency 22 3/16 inch particles, gap = 2.37 mm ..	121
Figure 5.24: Effective mass vs. displacement for 174 3/32 inch particles	122
Figure 5.25: MEPB collapse on gap size, 600 1/16 inch particles	123
Figure 5.26: MEPB collapse on gap size, 174 3/32 inch particles	124
Figure 5.27: MEPB collapse on gap size, 75 1/8 inch particles	125
Figure 5.28: MEPB collapse on gap size, 37 5/32 inch particles	126

Figure 5.29: MEPB collapse on gap size, 22 3/16 inch particles	127
Figure 5.30: Effective mass vs. displacement for all particle sizes	128
Figure 5.31: MEPB collapse on particle size, 10.5 grams total particle mass	129
Figure 5.32: MEPB collapse on particle size with number of layers included, 10.5 gram total particle mass	130
Figure 5.33: MEPB collapse on total particle mass, 1/16 inch particles	131
Figure 5.34: MEPB collapse on total particle mass, 3/32 inch particles	132
Figure 5.35: MEPB collapse on total particle mass, 1/8 inch particles	133
Figure 5.36: Curve fits for mass efficiency master curve	134
Figure 5.37: Superposition of master design curves, 3/32 inch particles, 10.5 gram particle bed.....	136
Figure 5.38: Superposition of master design curves, 1/8 inch particles, 10.5 gram particle bed.....	137
Figure 5.39: Osculation condition. Source: R.D. Friend and V.K. Kinra, <i>Journal of Sound and Vibration</i> , 233(1), pp. 93-118. Particle impact damping. 2000....	138
Figure 5.40: Impact between particle bed and enclosure for $\Delta = \Gamma$	138
Figure 5.41: Impact between particle bed and enclosure for $\Delta < \Gamma$	139
Figure 5.42: Impact between particle bed and enclosure for $\Delta > \Gamma$	140
Figure 5.43: Sample measurement of video gap, 1/16 inch particles	141
Figure 5.44: Comparison of video gap and measured gap.....	142
Figure 5.45: PDE collapse on gap size with video correction. 600 1/16 inch particles.....	144
Figure 5.46: MEPD collapse on gap size with video correction. 600 1/16 inch particles.....	145
Figure 5.47: Aluminum ground structure with clamped beam	147
Figure 5.48: Attachment of shaker, force sensor, and PID to beam center	148
Figure 5.49: Aluminum enclosure with adjustable screw top.....	149

Figure 5.50: Completed beam setup	150
Figure 5.51: DPE master design curve and loss factor	151
Figure 5.52: DPE master design curve and loss factor, y-axes scaled to 4.05	154
Figure 5.53: DPE master design curve and loss factor, y-axes scaled to 3.57	155
Figure 5.54: Pinned beam with rotary springs and center mass	156
Figure 5.55: Half of symmetric beam	156
Figure 5.56: Effective mass of PID calculated from beam's first natural frequency ..	160
Figure 5.57: Mass efficiency of the particle bed based on natural frequency and master design curve	161
Figure A.1: Acrylic-aluminum enclosure	184
Figure A.2: Exploded view of acrylic-aluminum enclosure	185
Figure A.3: Acrylic-aluminum enclosure – bottom machine drawing	186
Figure A.4: Acrylic-aluminum enclosure – enclosure wall machine drawing	187
Figure A.5: Acrylic-aluminum enclosure – cap machine drawing	188
Figure A.6: Acrylic-aluminum enclosure – screw top machine drawing	189
Figure A.7: Acrylic-aluminum enclosure – securing ring machine drawing	190
Figure A.8: Aluminum enclosure	191
Figure A.9: Exploded view of aluminum enclosure	192
Figure A.10: Aluminum enclosure – bottom machine drawing	193
Figure A.11: Aluminum enclosure – enclosure wall machine drawing	194
Figure A.12: Aluminum enclosure – screw top machine drawing	195
Figure A.13: Aluminum enclosure – securing ring machine drawing	196
Figure B.1: Transducer phase error for dissipated power. Percent error vs. (ϕ_F - ϕ_V).	199
Figure B.2: Transducer phase error for dissipated power. Percent error vs. phase error.....	200

Figure B.3: Transducer phase error for trapped power. Percent error vs. $(\phi_F - \phi_V)$..	201
Figure B.4: Transducer phase error for trapped power. Percent error vs. phase error.....	202
Figure B.5: Schematic of transducer phase error calibration setup.	203
Figure B.6: Picture of transducer phase error calibration setup.....	204
Figure B.7: Schematic of power measurement setup.....	205
Figure B.8: Picture of power measurement setup (laser vibrometer not shown).....	207
Figure B.9: Verification of discrete power dissipation – 1/16” particles, 0.238 m/s pk	208
Figure B.10: Verification of discrete power dissipation – 1/16” particles, 0.368 m/s pk.....	209
Figure B.11: Verification of discrete power dissipation – 1/8” particles, 0.235 m/s pk	209
Figure B.12: Verification of discrete power dissipation – 1/8” particles, 0.352 m/s pk	210
Figure B.13: Verification of discrete power dissipation – 3/32” particles, 0.225 m/s pk.....	211
Figure B.14: Verification of discrete power dissipation – 3/32” particles, 0.361 m/s pk.....	211
Figure B.15: <i>s</i> -plane plot for a pair of complex poles	214
Figure B.16: Airpot model 2KS160A2.0F dashpot. Source: http://www.airpot.com . Specifications for Stock Dashpot Model 2KS160.....	216
Figure B.17: Aluminum ground structure with clamped beam	217
Figure B.18: Attachment of shaker, force sensor, and impedance head to beam center.....	219
Figure B.19: Beam with Airpot dashpot attached.....	220
Figure B.20: Entire beam with Airpot attached.....	221
Figure B.21: Velocity profile of beam with Airpot damper	223

Figure B.22 : Measured and predicted loss factors for Airpot damper.....	225
Figure C.1 : Simple neuron with bias	226
Figure C.2 : Hard-limit activation function	227
Figure C.3 : Three-layer network	229
Figure C.4 : Three-layer network, abbreviated notation.....	229
Figure C.5 : Hyperbolic tangent	235
Figure C.6 : First derivative of hyperbolic tangent.....	235

LIST OF TABLES

Table 2.1: Comparison of PID and Lumped Mass – Summary of Results.....	20
Table 2.2: Description of individual components	26
Table 3.1: Description of individual components for power measurement.....	40
Table 3.2: Summary of power and equivalent mass data	45
Table 3.3: Mass of components for set 1	49
Table 3.4: List of experimental equipment for beam setup set 1	50
Table 3.5: List of experimental equipment for beam setup set 2.....	56
Table 3.6: Mass of components for set 2	56
Table 3.7: Particle sizes and quantity	64
Table 5.1: Particle sizes, quantity, and mass. 10.5 gram particle bed.	92
Table 5.2: Number of layers for 10.5 gram particle bed.....	108
Table 5.3: Particle sizes, quantity, and mass. 14 gram particle bed.	110
Table 5.4: Number of layers for 14 gram particle bed.....	110
Table 5.5: List of experimental equipment	149
Table B.1: Description of individual components for transducer phase error calibration	203
Table B.2: Description of individual components for power measurement	206
Table B.3: Summary of experimental parameters	208
Table B.4: List of experimental equipment for Airpot verification experiment.....	222

ACKNOWLEDGEMENTS

The author is indebted to many people who have helped him throughout this work. Many thanks go to Professors Gary Koopmann, Stephen Hambric, and George Lesieutre. In their role as research advisors, they have been a constant source of insight, inspiration, and encouragement. Thanks also go to Professor Richard Benson, for his role as committee member, and for taking the time to read and improve this thesis.

The author wishes to extend his gratitude to those who performed administrative functions vital to the completion of this work. These people include Karen Thal, Frank Archibald, Jenny Houser, Elisabeth Tucker, and Chris Gephart.

Many thanks to Dr. Weicheng Chen for his advice and support, and to many others in the Pennsylvania State University community, especially Mike Grissom, Patty Driesch, Brad Biehl, Jeremy Frank, Michael Philen, J.D. Miller, and Arnie Fontaine. Their technical contributions were essential to the completion of this work.

The author would like to acknowledge the support and friendship of many in the State College community, including Vanessa van den Heuvel, Jim Tallman, Carl Pray, the residents of the “House of Five”, and the members of the Penn State Ultimate community.

Special thanks go to the author’s parents, Ted and Eveline Yang, and to his brother, David Yang. This work would not have been possible without their incredible love, support and encouragement.

Financial support for this work was provided by Pat Purtell at the Office of Naval Research, under Grant Number N00014-01-1-1041.

Chapter 1

Introduction

The use of damping to control structural vibrations is well documented [1].

Damping treatments are particularly useful for cases of 1) harmonic excitation resulting in resonant or near-resonant response 2) broadband excitation resulting in a response dominated by resonant modes and 3) shock- or impact-excited free vibration resulting in undesirable and detrimental transient response. Damping treatments are used for noise reduction, fatigue reduction, vibration isolation, and absorption of impact energies.

Traditional damping treatments use viscoelastic materials to convert strain energy into heat energy through the internal movements of long, intertwined molecules. Their primary disadvantage is that their properties depend on temperature, frequency, and strain and thus they are difficult to use in environments with extreme temperatures or temperature gradients [2].

1.1 Description of Particle Impact Damping

Particle impact dampers (PID's) are enclosures or structural voids partially filled with particles (e.g. sand, ball bearings, etc.) When the structure moves, the particles collide with each other and with the enclosure causing damping through inelastic or nearly inelastic collisions. The dynamic response of the primary system is modified by such additional damping and mass.

There are two types of these dampers: impact dampers and particle impact dampers. Impact dampers consist of a single large auxiliary mass placed inside of an enclosure; whereas particle dampers consist of a large number of smaller masses (see Figure 1.1).

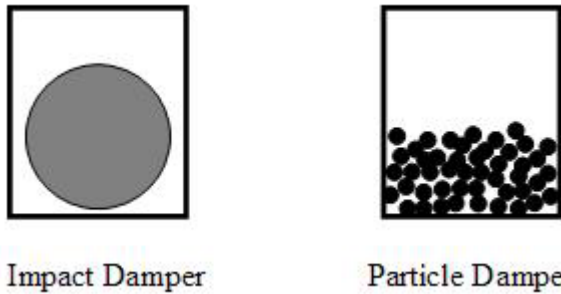


Figure 1.1: Impact damper and particle impact damper

Particle damping can be added to a structure in two ways – by attaching an enclosure to an exterior surface or by partially filling manufactured or pre-existing voids inside the structure with particles. Using pre-existing or manufactured voids in the structure has the additional benefit of being extremely low-profile, provided that structural integrity is not compromised.

There are a significant number of design parameters that can affect the performance of the particle damper. These include particle size, shape, number, and density; the size and shape of the enclosure, and the properties that affect the particle-particle and particle-enclosure interactions. These include the coefficients of friction and restitution. The amount of free space (gap size or volume fraction) given the particles is of primary importance. Further complexity can be added by introducing conglomerates of particles of different sizes, shapes, and materials. In addition, both the damping and

mass effects are highly nonlinear with respect to both the excitation amplitude and spectral properties. Harmonic and random excitation will each cause the damper to behave in a different manner.

1.2 Literature Review

Previous work concerning particle and impact dampers can be generally divided into three categories: experiments to characterize parameter effects, modeling of the phenomenon, and application to structures. The literature review is organized in the same manner and is preceded by a short historic excerpt highlighting some of the earliest papers on particle damping.

1.2.1 Early Work on Impact and Particle Impact Dampers

The earliest known work deals exclusively with impact dampers. In 1945, Lieber and Jensen [3] studied an impact damper for the purpose of controlling aircraft flutter, fatigue, and vibration. They assumed two impacts occur per cycle and found that maximum damping occurs if the phase angle between the motion of the auxiliary and primary mass is 180 degrees.

In 1956, Grubin [4] derived two solutions to the motion of an impact damper. The first describes the motions of the auxiliary and primary mass completely and must be solved numerically after the first impact. The second solution assumes steady-state motion and is not complete. However, the two solutions agree with each other for a

sufficiently large number of collisions. Grubin also found that the impact damper is most effective at resonance and that increasing the coefficient of restitution at resonance makes the damper more efficient. No experiments were performed to verify the solutions.

In 1957, Warburton [5] followed on Grubin's work by giving an alternative method of obtaining a steady-state solution for the impact damper. This was done by modifying the disturbing force to have a phase component, which allows an impact at the right end of the container to occur at $t=0$. Both Warburton and Grubin assumed two impacts occur per cycle, an assumption that was later found true only under special circumstances.

1.2.2 Review of Experimental Work

Veluswami and Crossley [6] used three different materials to coat the impacting plates in their impact dampers. The three materials were aluminum, nylon, and rubber-coated aluminum. The enclosure was excited with a sine wave and it was found that the softer materials had a lower coefficient of restitution and provided a smaller amount of damping at resonance.

Sadek *et al.* [7, 8] examined the effects of gravity on impact dampers and found that the dampers performed best under “zero gravity” conditions, i.e. when the damper is excited in a direction perpendicular to gravity. The dampers are most effective when two symmetric and equal impacts occur per cycle and the effect of gravity is to cause the impulses at the ends of the container to be unequal in magnitude. The effect of gravity can be overcome if the acceleration of the enclosure is high enough. This can be

accomplished either by increasing the magnitude of the excitation force or by increasing the frequency of excitation.

Bapat and Sankar [9] attached an impact damper to the end of a cantilever beam and studied both the transient free decay and steady-state forced vibration response. The transient free decay showed a linear decay of vibrations initially, followed by an exponential decay after a considerable decrease in vibration. The linear decay corresponds to damping by the impact damper and the exponential decay to damping inherent in the beam. This also shows that the impact damper ceases to work once acceleration amplitudes fall below a certain level. Forced vibration tests revealed an optimum gap size, which was a function of displacement amplitude and frequency. The gap size is simply the distance between the top of the particle bed and the ceiling of the enclosure. These same results were later independently confirmed by Ema and Marui [10], who attached an impact damper to a leaf spring with a mass.

Cempel and Lotz [11] experimented with eight different types of enclosures, including plastic bags, metal boxes, plastic boxes, and bags with an internal framework. They found that the most effective enclosure to be a hard plastic bag which provided a coefficient of restitution near zero, quiet operation, and the second-highest loss factor. The highest loss factor was provided by the metal box, but it was accompanied by a high noise level and great sensitivity to the amount of clearance given to the particles. The response of the hard plastic bag was largely insensitive to gap size.

Sensitivity to clearance was also investigated by Papalou and Masri [12] while studying different combinations of particle sizes. They found that using a greater number

of smaller particles resulted in less sensitivity to clearance. Unfortunately, the smaller particles were also less effective. An optimum clearance was still found for all cases.

Hollkamp and Gordon [13] performed a series of experiments that were designed to identify which design parameters were most important for maximum damping. They tested seven different particle types of differing materials, sizes, and shapes. It was discovered that particle damping has a strong dependence on excitation amplitude, clearance, particle size, attachment location, and mass. There was a weak dependence on particle shape.

The majority of experimental work involving particle impact dampers used harmonic structural excitation. However, Papalou and Masri [14] and Panossian and Bice [15] both performed tests using random structural excitation. Papalou and Masri mounted a particle damper on an equivalent single-degree-of-freedom (SDOF) system. The damper dimensions could be changed with four adjustable brackets. The authors report that the effect of the container dimensions only seemed to be noticeable when the ratio of the particle mass to primary system mass is high. They also report that a low mass ratio is beneficial when the damper movement is low. This stands in stark contrast to many other authors who all report that a high mass ratio is beneficial, regardless of the damper movement.

Panossian and Bice tested free-free and cantilevered aluminum beams with drilled holes filled partially full of particles. The term “non-obstructive particle damping (NOPD)” is used to describe the partial filling of existing or manufactured holes with particles. Its benefits include the ability to add damping to a structure with a minimum of mass and an extremely low profile. The authors found that the highest damping can be

achieved by placing the particles in locations of highest kinetic energy. There is no mention of an optimum clearance and how it relates to excitation amplitude.

1.2.3 Review of Modeling Techniques

There are several different ways in which researchers have attempted to model the behavior of impact and particle dampers. Since particle dampers exhibit such complex behavior, the majority of the work in the literature deals with impact dampers. Many authors model a bed of particles as a single particle, i.e. modeling a particle damper as an impact damper. The different methods that have been documented thus far are described below.

The simplest way to model a single particle within an enclosure is to assume that the damper is subjected to two symmetric, equi-spaced impacts. This is the approach used by Masri [16] who derives two coupled, non-linear, algebraic equations one for the motion of the primary structure without impacts and one for the structure with impacts. These equations are solved numerically through iteration. Popplewell and Liao [17] simplify the modeling process even further by deriving an equation for the optimum gap size under optimum conditions. Unfortunately, they did not verify their model with experiments. The work was extended by Mansour and Filho [18], who include the effects of Coulomb friction. They find that friction decreases impact damper performance at resonance and increases it off resonance. Again, no experiments were performed to verify the model. All of the above examples are models for harmonic excitation. Masri and Ibrahim [19] present a model for random excitation based on the assumption of two

symmetric, equi-spaced impacts. This is done by superposing the discrete harmonic responses over a wide frequency band. Their solution becomes more accurate with respect to experimental measurements as the collisions become more inelastic.

Unfortunately, other researchers have shown that two symmetric, equi-spaced impacts per cycle only occur under special circumstances. Veluswami and Crossley [6] were among the first to observe the particle impacting one side of the enclosure multiple times before impacting the other side. Their work was extended by Bapat *et al.*[20] and Popplewell *et al.* [21], who demonstrated that symmetric, equi-spaced impacts will only occur when there is no gravity, the coefficient of restitution is identical on both sides of the enclosure, the gap size is optimal, and the system is excited near resonance.

An alternative method of modeling impact dampers is to track the individual motions of the enclosure and particle through time. These methods are usually implemented with a computer program. Blazejczyk-Okolewska and Peterka [22] use this method to solve for the motion of a harmonically excited SDOF system. The authors point out that more complicated types of motion can be analyzed with the same method. Friend and Kinra [23] analyzed a beam with a given initial displacement and release. They use empirical data to find the “effective coefficient of restitution” of a *particle* damper and then successfully predict the behavior of the beam with differing initial displacements. This is a good example of idealizing a bed of particles as a single particle with special impact properties. The equivalent damping coefficient is found by summing the total energy dissipated in the impacts and dividing by the maximum kinetic energy in the system. Masri and Ibrahim [24] extended Friend and Kinra’s work by using the Runge-Kutta method to analyze the response over time of a SDOF system subjected to a

random excitation. The previous papers all made the assumption that the impacts are governed by a coefficient of restitution and occur instantaneously. Valuswami *et al.* [25] use Hertz's law of impact to represent the relative motion of the particle during impact as a brief half wave.

Chatterjee, Mallik, and Ghosh [26] used both an analytical solution assuming two symmetric, equi-spaced impacts per cycle and a numerical time-tracking model. They found the time-tracking approach showed motion that was different and more complex than the analytical solution.

Araki *et al.* [27, 28, 29], Yokomichi *et al.* [30], and Maley [31] all assume that the particles originate on the bottom of the enclosure, move together, and impact the enclosure plastically. Furthermore, the particle bed moves in one of three ways. Type I motion occurs when each particle collision is followed by a period of rest before eventual separation; Type II corresponds to the particle bed leaving the enclosure top just after impact; and Type III involves motion where the particle never impacts the top of the enclosure (See Figure 1.2).

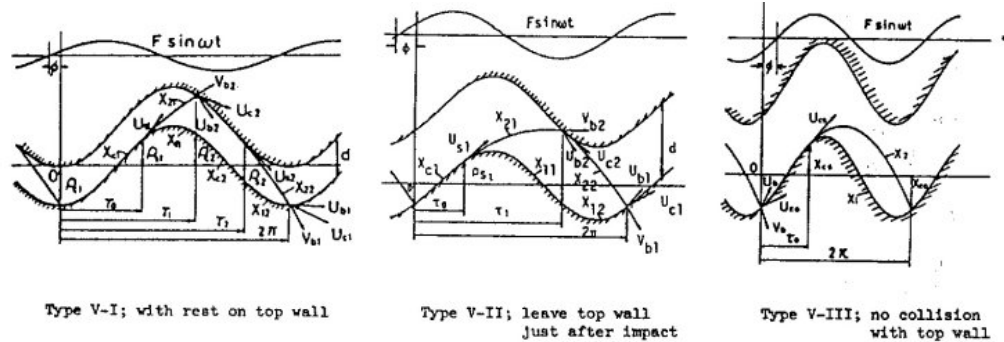


Figure 1.2: Type I, II, III periodic impact motions [27]

All of the previous methods involve the motion of a single particle, moving unidirectionally in an enclosure. The particle dynamics method attempts to model the movements and interactions of every single particle in the enclosure. Mathematical models governing particle-particle and particle-enclosure interactions are critical. Inaccurate models can lead to very unrealistic results. Furthermore, these methods are very computationally expensive, and often require parallel computing techniques.

Fowler, Flint, and Olson [32, 33] point out that while other modeling techniques are good for modeling external interactions (particle-wall), they are poor at modeling internal interactions (particle-particle). The authors also propose a design method using a particle dynamics simulation code called X3D.

Saluena *et al.* [34, 35, 36], used particle dynamics to model the three “phases”, or regimes of damping (solid, liquid, and gas) that appear when a large number of small particles is excited in an enclosure. The solid regime occurs when the particles move together with no relative motion between particles. The fluid regime is characterized by the formation of convection patterns and the gas regime is characterized by the independent, unpredictable motion of individual particles. Damping is large around the fluidization point (which occurs around 1 g of acceleration), diminishes in the liquid regime, and rises again in the gas regime.

Tianning *et al.* [37] use particle dynamics to find the relative importance of friction. They report that for very small particles, the majority if the energy is dissipated through friction, but as the particle size increases, energy dissipation through impacts becomes more important.

1.2.4 Review of Previous Applications

The literature contains a multitude of papers that describe the application of impact or particle dampers to real structures. These include honeycomb structures, high- and low-temperature applications, rotating structures, and others.

Honeycomb structures are ideal for particle damping because they have a large number of voids throughout the entire structure that are available for particle placement. Wang and Yang [38] put solder balls into the cells of a honeycomb cantilevered beam, and reported that placing the balls in areas of high vibration is desirable. Maley and Sun [31, 39] placed sand in the cells of single- and double-core honeycomb panels. The damping was increased by over 2200% for the best case. Panossian [40] sandwiched metallic particles between two copper sheets and reported acoustic attenuation of 5 dB at low frequencies and up to 27 dB at high frequencies.

Two of the primary advantages of particle dampers are their insensitivity to temperature fluctuation and their ability to operate at extremely high and low temperatures. Panossian [40, 41] performed experiments with the LOX Inlet Tee on the Space Shuttle Main Engine, where high amplitude vibrations caused cracks to form. Four 1-mm diameter holes were drilled and partially filled with metallic balls of differing size and material. The performance or mass characteristics of the Inlet Tee were not changed, and a 25% increase in damping was recorded.

Traditional damping treatments are often difficult to apply to rotating structures because these structures cannot accept high-profile add-ons and still perform as required. For example, attaching a tuned vibration absorber onto the blade of an airplane propeller

would most likely have undesirable consequences. The tuned vibration absorber could interfere with air flow and reduce the efficiency of the propeller. Particle damping, on the other hand, can be placed in the interior of a structure where it will not interfere with normal operation.

Duffy *et al.* [42] used an impact damper to reduce the vibration in rotor blades for the purpose of extending their service lives. Centrifugal acceleration of up to 3,100 g's were achieved during experimentation. Ema and Marui [43] applied an impact damper to long, thin cutting tools to suppress chatter vibration and improve cutting stability. Skipor and Bain [44] applied an impact damper to a web-fed printing press to reduce "streaking" which is caused by vibratory bending of the image carrying cylinders. The authors point out two advantages of the impact damper: the amount of added structural mass and rigidity is kept to a minimum and since the damper is integral to the cylinder, no additional maintenance is required. A 79% reduction in peak response is reported.

A small amount of work has been done using particle damping for isolation. Sato *et al.* [45] use particle damping to dampen a rigid vibration-isolation system constructed mainly of pipes and granular materials. A cylinder was excited by an electromagnetic force, and the level of noise generated from the cylinder was analyzed. A significant reduction in noise level was reported.

Particle damping can also be used to augment other vibration control methods. Tuned vibration absorbers are prime candidates for particle damping because the absorbers themselves have a large amount of kinetic energy at their tuned frequency. Ying and Semercigil [46], and Semercigil *et al.* [47] used impact dampers to reduce the amplitude of the secondary split peaks and make the absorbers more useful for broadband

applications. Collette *et al.* [48] and Ma *et al.* [49] applied impact damping to a tuned vibration absorber and attached the combined system to a two-degree-of-freedom system. Ma specifically attempted to reduce the large amount of space a tuned vibration absorber needs to operate.

Impact and particle dampers have been used in a wide variety of other applications. This includes antennae [50], traffic signal structures [51], hang-gliders [52], and boring tools [53, 54]. A particularly interesting application [55] is the addition of particles to a polyester honeycomb core in airplanes to help extinguish flame fronts and reduce blast effects from a bomb or an explosion in a center fuselage tank. Tests show that the product, known as “BlastGard,” attenuated both blast and thermal energy and helped prevent flames from propagating.

1.2.5 Comparison of Impact and Particle Impact Dampers

Impact dampers have the potential to be more effective than particle dampers but they must be tuned to operate at a specific frequency for a specific amplitude of excitation. Several authors [3, 5] have reported the extreme sensitivity of impact dampers to changes in operating conditions or parameters and therefore it is difficult to use an impact damper for broadband applications or for applications involving changing operating conditions. Other reported problems [56, 57, 61] include high noise levels and wear of contact surfaces. Wear of contact surfaces can cause changes in operating parameters which can dramatically reduce the efficiency of the impact damper as stated previously.

Particle dampers, on the other hand, exhibit a much lower sensitivity to parameter or operating changes and cause less noise and contact surface wear [62]. They are more easily applied to broadband problems, or applications involving changing operating conditions. The drawback is that particle dampers exhibit significantly more complex behavior and are more difficult to model.

1.2.6 Summary of Previous Work

There have been a few facts established about particle dampers. Higher mass ratios lead to more effective dampers. Also, the extreme sensitivity of impact dampers to operating conditions and parameters has been well documented, as well as the corresponding relative insensitivity of particle dampers.

Unfortunately, there is much that is still not known. The relation of the optimum gap size to other parameters such as excitation frequency and amplitude, particle size and shape, mass, etc. is still not understood. A lack of insight also exists about the behavior of the particles under different conditions. This has greatly hampered attempts to model the damping and mass a PID would add to a system. Furthermore, much of the modeling in the literature was never verified experimentally.

In spite of this lack of knowledge, however, impact and particle dampers have been successfully implemented for a wide variety of applications. Many of these applications are probably not “optimal” but the results have been successful nonetheless, showing that particle dampers can be effective even when applied imperfectly. This

indicates that once a more complete understanding of the phenomena is gained, particle damping will be even more effective for a wide range of applications.

1.3 Approach and Procedure

The fundamental goals of this dissertation are to develop greater insight into the behavior of the particle impact damper, identify and characterize key design variables that influence the effectiveness of the damper, develop a model that will allow prediction of damper effectiveness and implement techniques that will allow for the successful prediction of a structure's response when a particle impact damper is attached.

Due to the complex nature of the damper, the majority of the work conducted is experimental. Early experiments are designed to give a "feel" for how particle impact dampers behave and are used to help identify key design variables. Based on this information, later experiments are designed to characterize the effects of these key variables on the damper properties. A new method is developed that allows for the measurement of both the mass and damping properties of particle impact dampers without the supplementary use of a primary structure. This allows the characterization of design variables to be done quickly.

Other experiments are designed to give insight into the behavior of the particles. This was accomplished using high-speed digital cameras and by analyzing the time-signature of the impact force. These experiments supplement the others by providing a physical explanation of the results. They also aid in the design of a model based upon

first principles. The model is verified through by comparing its predictions with the results of experiments with a particle impact damper on a vibrating structure.

Chapter 2

Early Experimental Work

The experiments described in this chapter were designed to provide some preliminary insight into particle impact damping. They were also designed to identify key design variables and to guide the design of future experiments.

The experiments include a comparison with a lumped mass on a dynamic system, an exploration of the effect of particle impact damper location, and a preliminary study of the effects of friction and gap size.

2.1 Comparison of Behavior with Lumped Mass

The first experiment compared the two responses of a cantilevered beam when a lumped mass or particle impact damper (PID) was placed on the free end. The goal of the test was to compare the change in resonance frequency and beam response for the lumped mass and particle impact damper. The beam was connected to an electromagnetic shaker with a stinger and the accelerance was measured with an accelerometer and force gage (Figure 2.1). The particle damper (Figure 2.2) measured two inches on each side and was constructed of a $\frac{1}{4}$ inch thick Nomex honeycomb core sandwiched between 1/16 inch thick transparent acrylic sheets which enabled observation of particle motion. The honeycomb cells were filled approximately three-quarters full

with sand. Total mass of the particle damper was 18.7 grams, while the lumped mass was 19.2 grams.

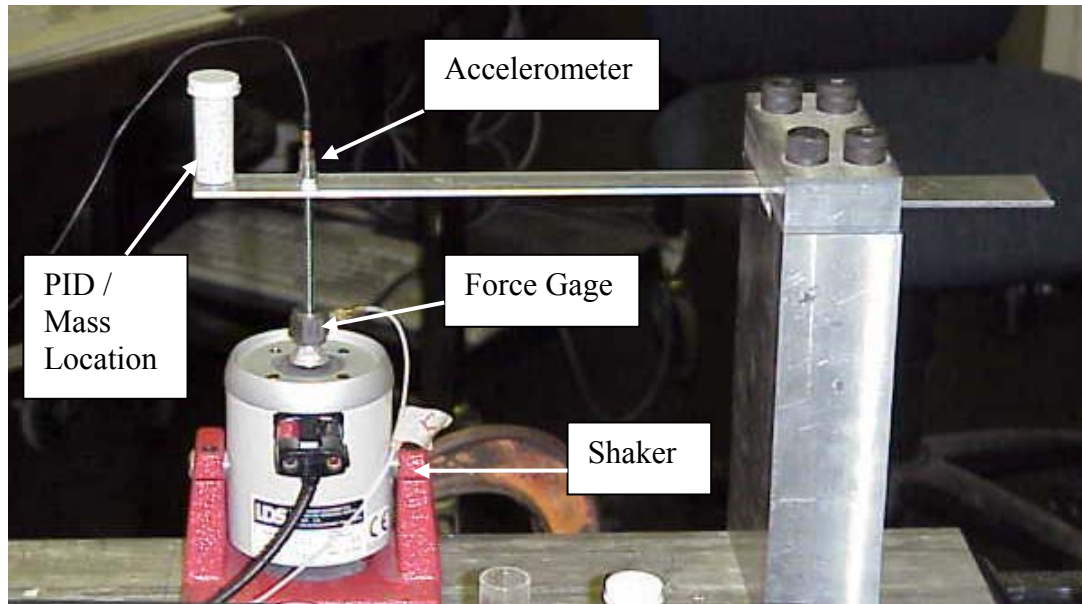


Figure 2.1: Experimental Setup

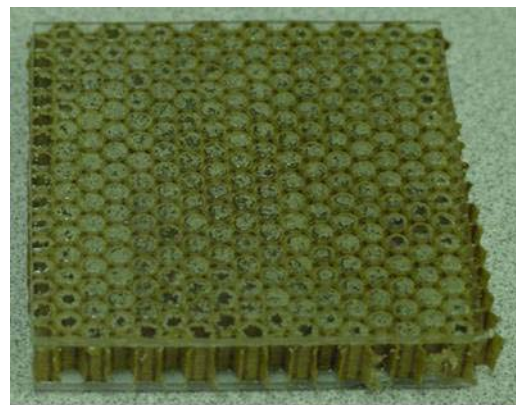


Figure 2.2: Particle Impact Damper

White noise was used to excite the structure at amplitude sufficient to cause both top and bottom impacts within the particle damper enclosure. The first mode of the

beam's response was analyzed, and the results are illustrated in Figure 2.3 and summarized in Table 2.1. The effects of adding the PID and lumped mass to the beam lowers its natural frequency, but the PID has a lower effective mass because the particles are in motion and do not stay in contact with the beam. The PID was significantly more effective in lowering the peak accelerance, reducing the peak by 77% (12.6 dB), compared to the lumped mass, which reduced the peak by only 45% (5.21 dB). The shape of the resonance peak with the PID is significantly less sharp, indicating increased damping.

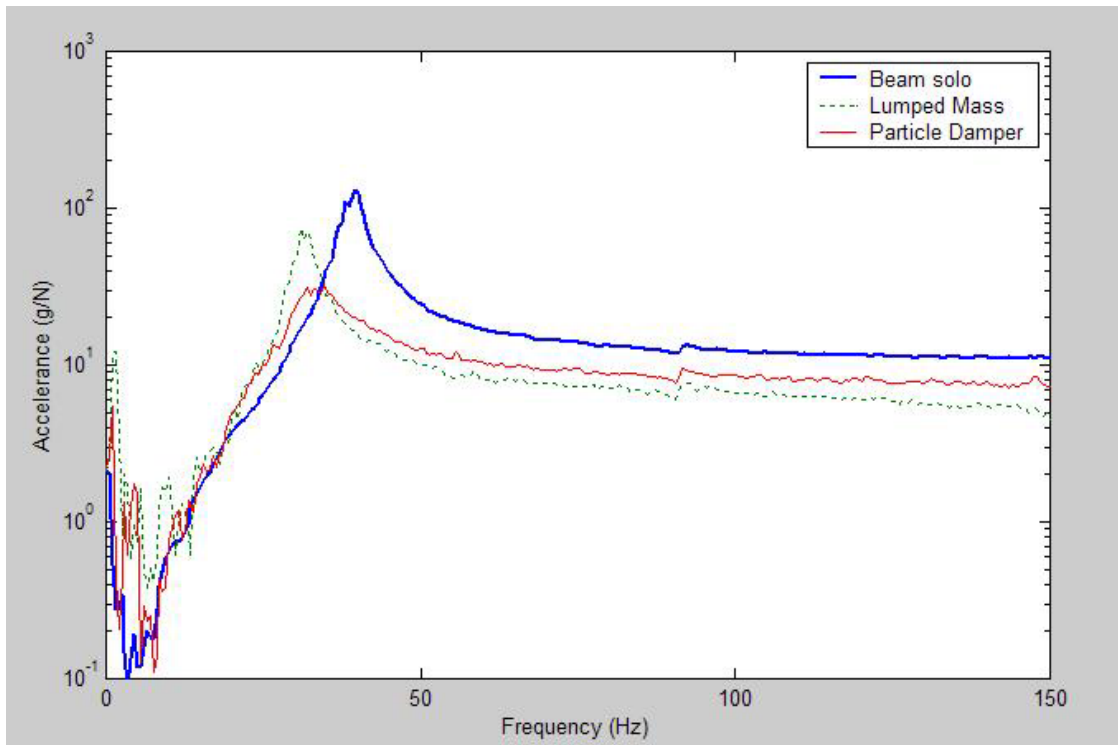


Figure 2.3: Comparison of PID and Lumped Mass

Table 2.1: Comparison of PID and Lumped Mass – Summary of Results

	Resonance Frequency (Hz)	Maximum Accelerance (g/N)
Beam by itself	40	133
Beam with Lumped Mass	31	73
Beam with PID	34	31

2.2 Effect of Particle Impact Damper Location

This experiment explores the effects of PID location in relation to the antinode of a composite beam's modal response. Two sandwich beams were constructed, consisting of $\frac{1}{4}$ inch thick Nomex honeycomb core sandwiched between $\frac{1}{16}$ inch thick transparent acrylic sheets, which allowed direct observation of particle motion. The beams measured 12 inches long x 2 inches wide. Three beams were made – one without any particles and two with sand particles in different locations. With one inch of one end of the beam clamped, an electromagnetic shaker was attached 9 inches from the free end via a nut and stinger and velocity measurements were taken with a laser vibrometer in one-inch increments along the beam. The mass of the beam is approximately 67 grams filled with 7 grams of sand. A picture of the beam is shown in Figure 2.4. Sand was placed in two separate antinodal locations to target the 1st (Figure 2.5) and 3rd (Figure 2.6) beam mode, respectively. The shaker was driven with white noise at varying amplitudes to excite the beam.

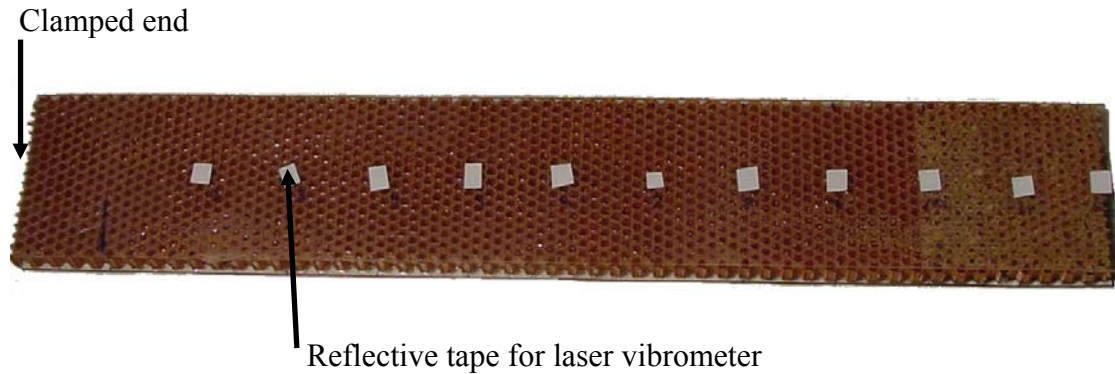


Figure 2.4: Honeycomb sandwich beam

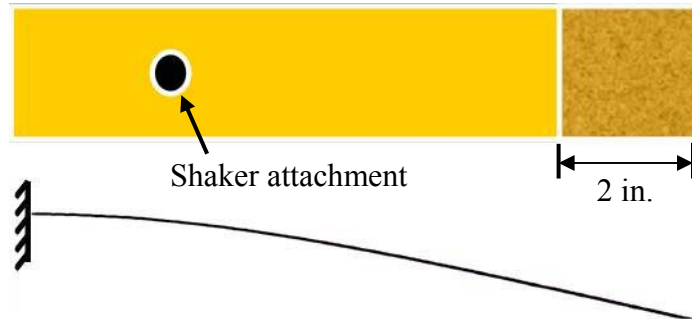


Figure 2.5: Honeycomb beam, mode 1 (38 Hz)

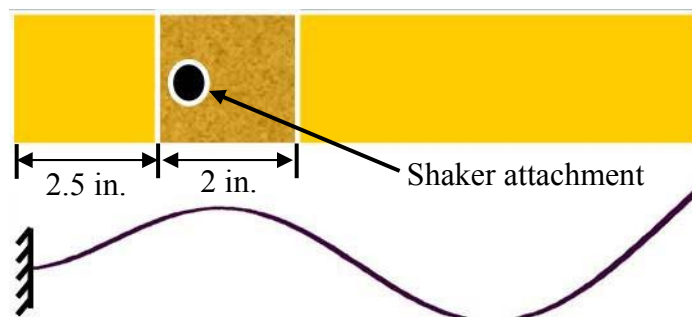


Figure 2.6: Honeycomb beam, mode 3 (486 Hz)

The magnitude of mobility (velocity/force) at each of the 11 measurement points was summed and the effect of the sand on the targeted modes was examined. Figure 2.7 shows the change in the first mode as sand was placed at the free end of the beam and excited at various excitation levels. The sand widens the peak and reduces its amplitude. The amount of damping achieved increases as the source strength increases. The damping was most effective when the excitation was at its highest, resulting in a peak reduction of approximately two-thirds (9.5 dB). This maximum damping also corresponded to sand impacts with both the top and bottom of the beam. A mass effect was also observed as the resonance peak shifted from 38 to 30 Hz. This frequency shift did not appear to be sensitive to the excitation level.

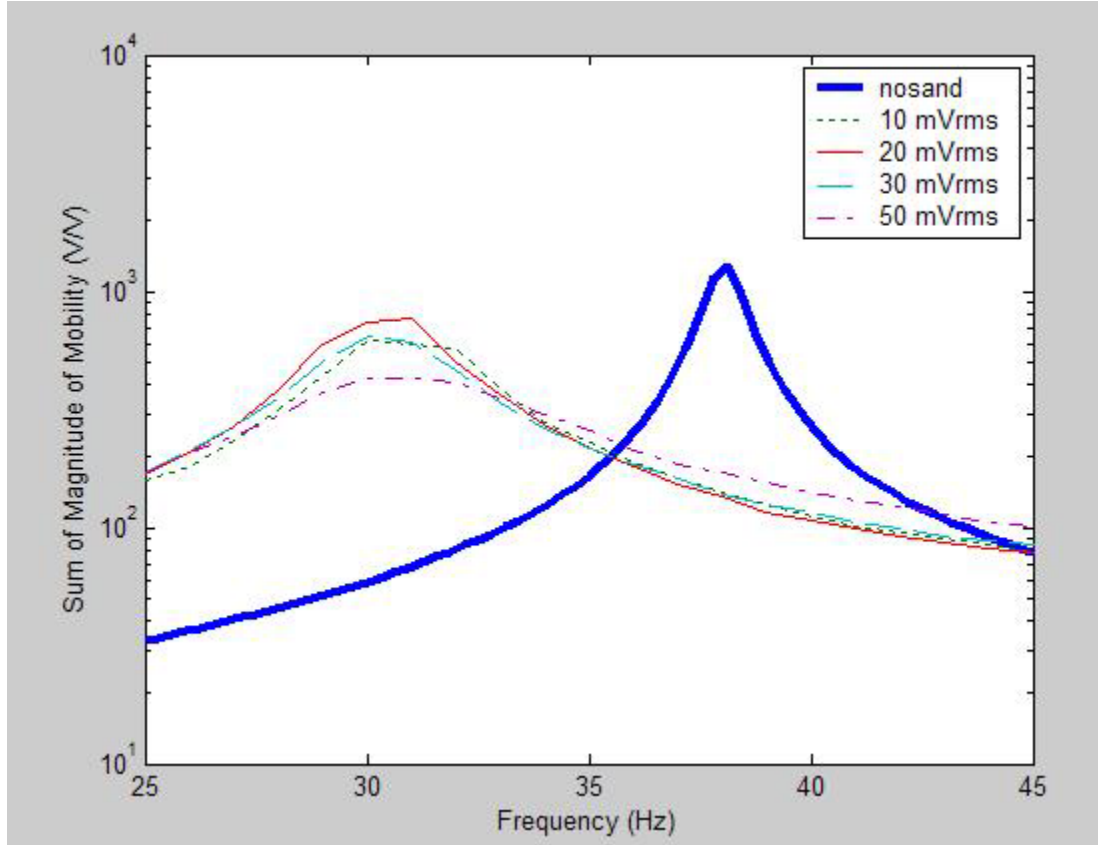


Figure 2.7: Frequency response for mode 1 – particles at end of beam

Placing the sand near the middle of the beam resulted in significantly less dramatic changes (Figure 2.8) for the targeted third mode. No significant reduction was observed and the peak frequency did not seem to shift appreciably. This is due to the location of sand placement. The sand has been placed too close to the clamped end of the beam and therefore there is very little movement, even at the highest excitation levels. This lack of motion results in both an insignificant damping and mass effect. Visually, it was observed that the sand did not move. Higher excitation levels should produce some sand motion (because it is distributed) and therefore damping, but these higher levels could not be obtained without risking structural damage to the beam.

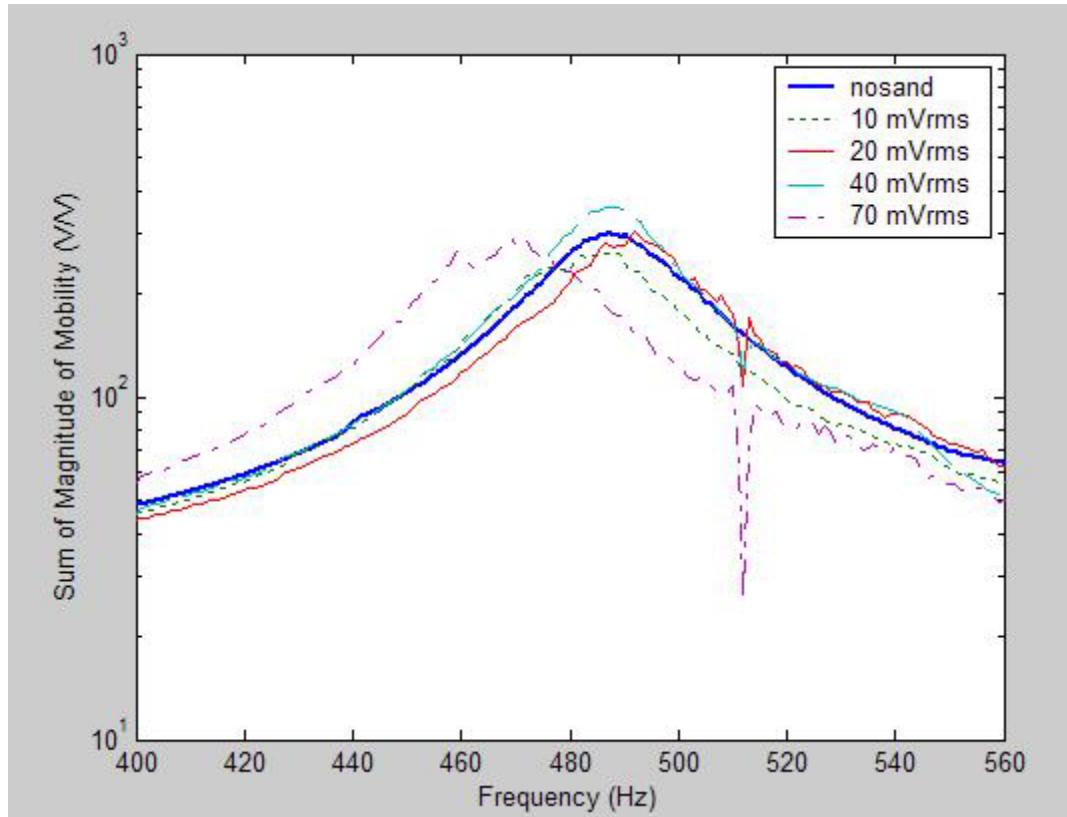


Figure 2.8: Frequency response for mode 3 – particles near middle of beam

2.3 Effect of Friction and Gap Size

An experiment was conceived to measure the effect of a particle damper on a single-degree-of-freedom (SDOF) system. An enclosure filled with 200 1/16 inch spherical ball bearings was attached to the center of an aluminum beam clamped at both ends. The beam was vertically excited at the center with a sine-sweep signal via an electromagnetic shaker. Force and acceleration measurements were taken with a force gage and accelerometer, respectively. The fundamental mode of the beam was treated as

an equivalent SDOF system and analyzed. A schematic of the experimental setup is shown in Figure 2.9, and a description of the individual components is given in Table 2.2.

The modal mass of a mode is the mass in an equivalent single-degree-of-freedom system. For a uniform beam, it is defined as [58]

$$M_n = m_b \int_0^L \phi_n^2 \bar{x} dx \quad (2.1)$$

where M_n = modal mass of the n th mode
 m_b = total mass of the uniform beam
 ϕ_n = the n th eigenvector scaled from 0 to 1
 \bar{x} = x/L = relative position on beam
 L = length of beam.

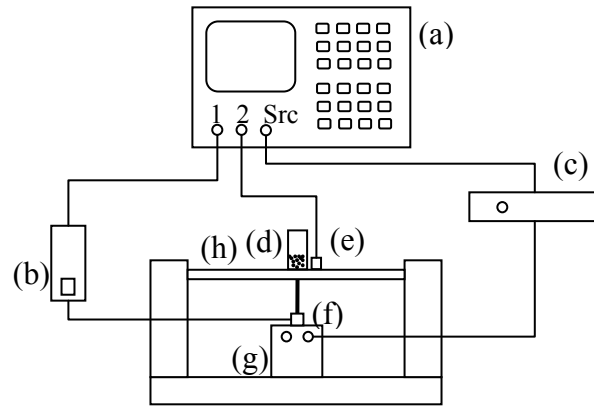


Figure 2.9: Schematic of experimental setup

Table 2.2: Description of individual components

(a)	Agilent 35670A signal analyzer
(b)	PCB model 486A16 charge amplifier
(c)	SPA 400 stereo amplifier
(d)	Particle damping enclosure (38.1 grams) - 200 1/16 inch brass particles (2.90 grams)
(e)	PCB 303A02 accelerometer
(f)	PCB 208A02 force gage
(g)	Electromagnetic shaker
(h)	Clamped aluminum beam. 10”L x 2”W x ¼” D. Modal mass of beam (mode 1) = 141 grams

A picture of the particle enclosure is shown in Figure 2.10. It is constructed primarily of aluminum with transparent acrylic sidewalls that allows the motion of the particles to be seen. The enclosure has a threaded top that allows adjustment of the gap size. A threaded securing ring prevents the gap size from changing during testing. Schematics for the construction of the enclosure can be found in Appendix A.

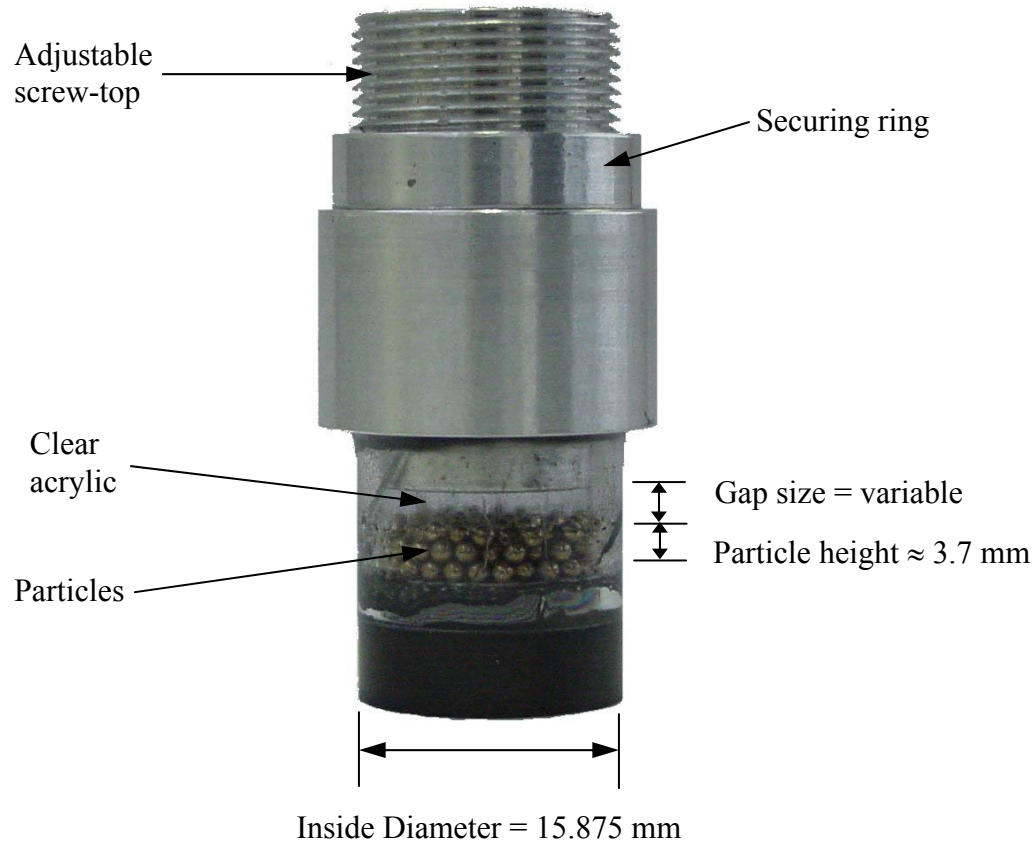


Figure 2.10: Particle enclosure with adjustable gap

A sine signal was slowly swept through the beam's first response frequency while the accelerance was measured. A sample set of measurement data curves is shown in Figure 2.11. This data shows that the gap size has a strong effect on both the maximum accelerance and resonance frequency. Larger gap sizes correspond to higher values of resonance frequency, which would correspond to a reduced effective mass. The existence of an optimum gap size is also apparent. For this case, the optimum gap size would appear to be between 0 and 0.5 mm. More discussion on the effects of the gap size appears later in this chapter.

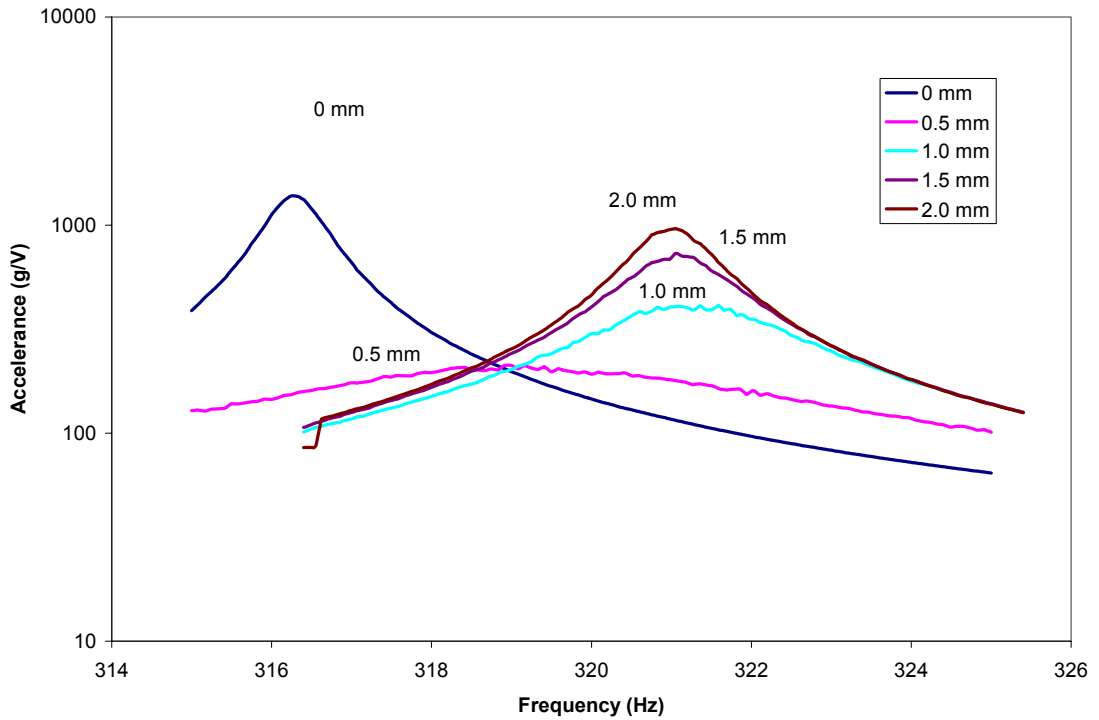


Figure 2.11: Sample experimental curves for different gap sizes. Acceleration = 31 g, 200 1/16 inch spherical brass ball bearings.

During experimentation, a dark coating formed on the particles and enclosure walls. The rate of formation was observed to be proportional to acceleration and inversely proportional to gap size. For sinusoidal motion, several thousand vibration cycles were needed to form a coating. This can occur quickly in systems that vibrate at mid to high frequencies. Observation under a microscope revealed that this coating seems to consist of the residual machine oil that coats the ball bearings as well as the metallic powder that forms when repeated impacts chip the coating on some types of ball bearings.

This dark coating significantly decreased the effectiveness of the particle damper. The extent of the decreased effectiveness depends on the material of the ball bearings. Chrome-coated steel, aluminum, and copper all caused thick coatings to form which significantly reduced the damping, while brass produced a significantly smaller amount of coating. Figure 2.12 shows the change from initial accelerance as consecutive measurements were taken for aluminum, brass and copper. The enclosure was occasionally cleaned with denatured alcohol, and these cleanings are marked with circles. The figure shows that as the coating forms, a significant increase in maximum accelerance is seen. As consecutive measurements were taken, the coating thickened which resulted in a steadily increasing accelerance. Periodic cleanings of the enclosure reduce accelerance back to initial levels.

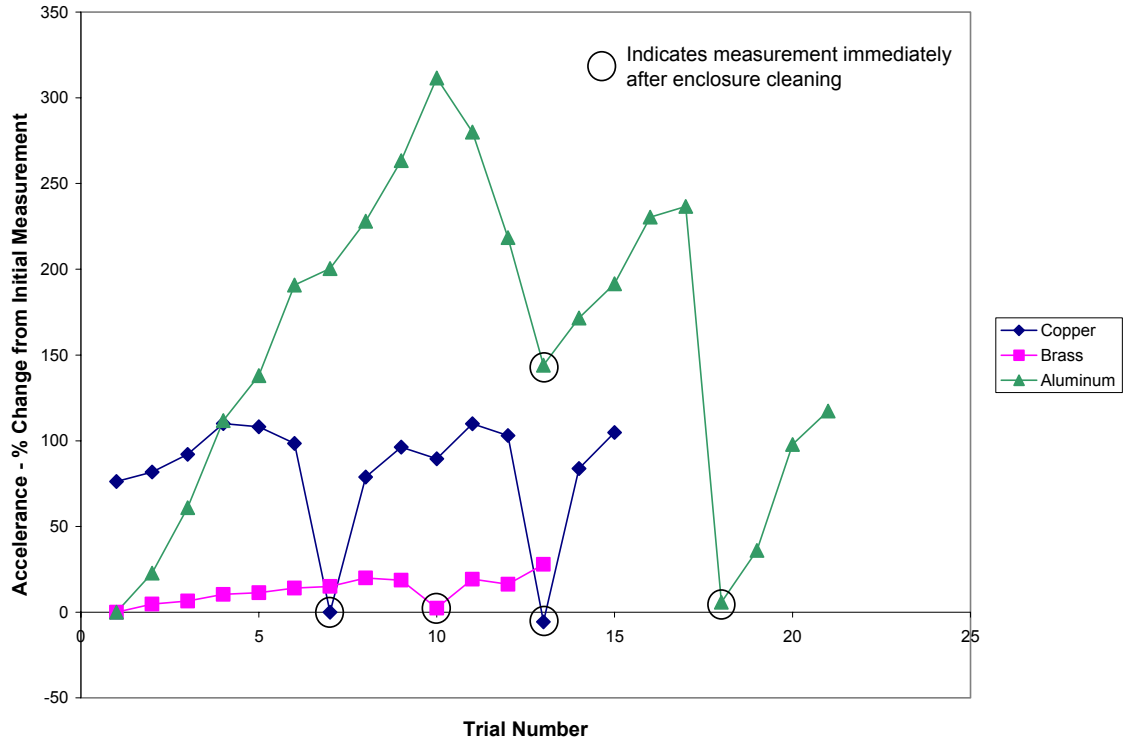


Figure 2.12: Effects of coating buildup on maximum accelerance. Circles indicate measurements taken immediately after enclosure cleanings. Gap size = 1.0 mm, acceleration = 43 g.

The coating increases the friction within the enclosure. This reduces the velocity of the particle bed as it travels through the enclosure and results in a lower velocity at impact. The coating also causes the particles to stick together, resulting in a fewer number of particle-particle collisions within the particle bed and lowering the overall energy dissipation. These effects reduce damping by lowering the kinetic energy lost at impacts. This experimental evidence agrees with Mansour and Filho's [18] analytic model which predicted reduced damping with increased friction.

Loss factor measurements were taken at gap sizes of 0 (lid firmly on top of ball bearings), 0.25, 0.5, 0.75, 1.0, 1.5, and 2.0 millimeters; and at accelerations of 18, 26, 31,

34, 36, and 43 g's. The half-power method [59] was used to calculate loss factor. These results are presented in Figure 2.13.

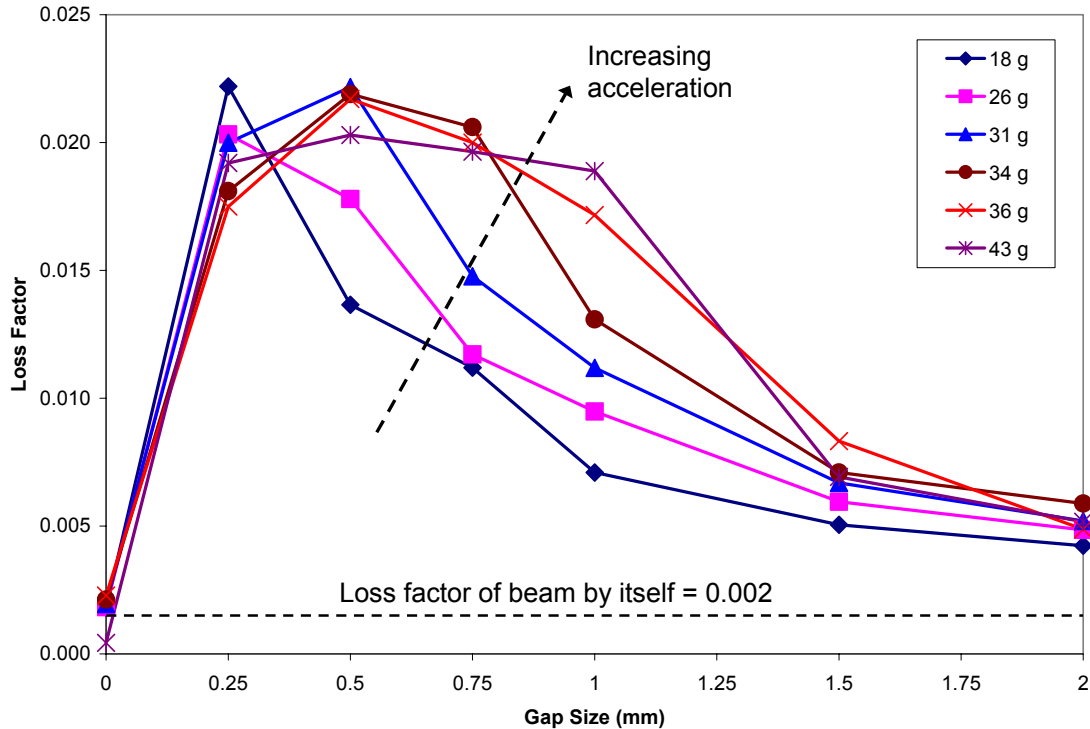


Figure 2.13: Measured loss factors for different gap sizes and acceleration levels.

For a gap size of 0 mm, the ball bearings do not have any room to move. Therefore, there is no mechanism for energy dissipation and the measured loss factors do not differ from that of the beam by itself. As the gap size increases, the particles are given more room to move and the damping quickly increases to a maximum value which occurs at an optimum gap size. If the gap size is increased beyond the optimum, the damping decreases.

The optimum gap size increases with increasing acceleration. It has an optimum value of 0.25 mm at 18 and 26 g's of acceleration. As the acceleration increases, the

optimum gap size increases to 0.50 mm. Once the acceleration reaches 31 g, the range of effective gap sizes is steadily increased. This is seen as a broadening of the loss factors' "peak" with increasing acceleration.

Overall, the loss factor of the beam was increased by over 10 times, demonstrating the effectiveness of the particle impact damper particularly at high amplitudes of excitation. Furthermore, the mass ratio (particle mass divided by modal mass of beam) was only 0.016, showing that large increases in damping can be achieved without adding a large amount of mass.

Experiments also revealed a shift in the resonance frequency of the combined beam-particle damper system. This frequency shift is sensitive to both acceleration and gap size. Figure 2.14 shows that the resonance frequency increases with gap size until the frequency of the beam with an empty enclosure is reached. This shows that as the particles are given more room to move, they spend less time in contact with the enclosure. This results in a lower mass effect and higher resonance frequency. Higher acceleration levels resulted in a higher mass effect, which implies that the particles spend more time in contact with the enclosure.

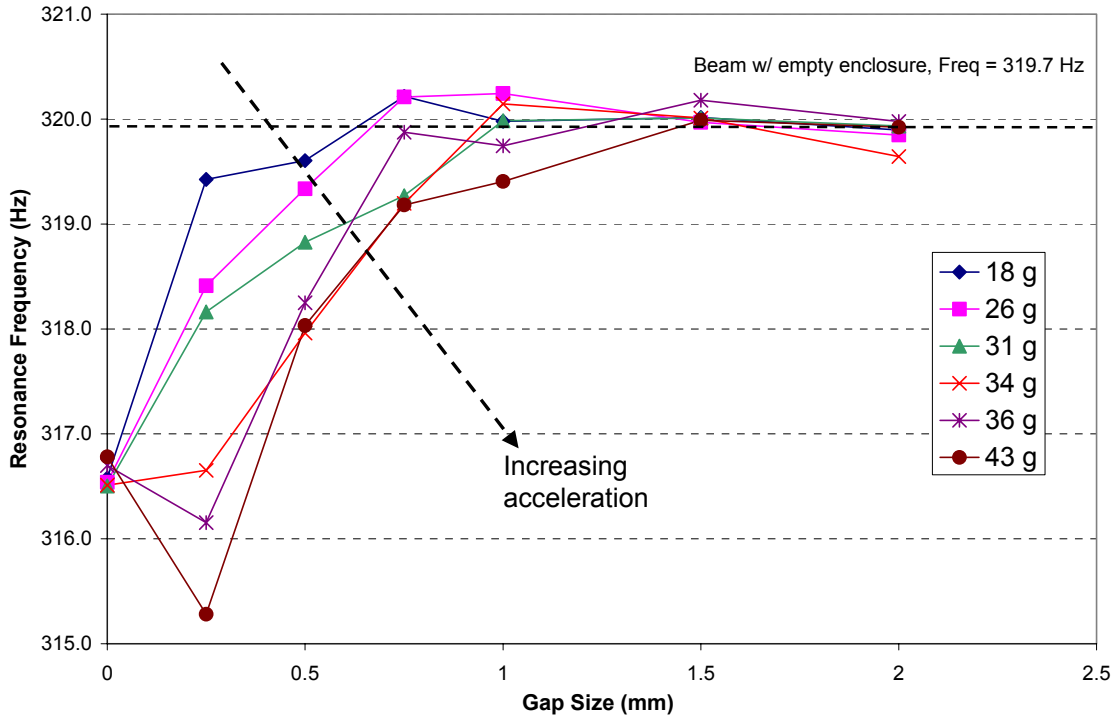


Figure 2.14: Resonance frequencies for different gap sizes

2.4 Summary of Early Experiments

Several experiments have been carried out that confirmed many of the hypotheses and observations summarized in Chapter 1. For example, experimental results showed that particle dampers add both mass and damping to the existing structure and that they are more effective than lumped masses for reducing maximum accelerance. Furthermore, particle dampers must be placed in locations of high movement. This is because higher damping takes place when impacts occur with both sides of the enclosure. Application of

a particle damper to an equivalent SDOF system revealed that increased particle-enclosure friction reduced the effectiveness and that an optimum gap size exists. Higher accelerations resulted in a higher optimum gap size, and a broader gap range over which the damper was still highly effective. A small gap size resulted in a reduction in resonance frequency, but increasing the gap size quickly reduced the mass effect.

2.5 Design of Ensuing Experiments

Several important particle impact damper design variables have been identified with the aid of these early experiments. Changing the location of the PID on a structure revealed the sensitivity of the PID to the excitation characteristics. Therefore, the effect that changes in frequency and amplitude have on the properties of the PID are studied. The gap size had a significant effect on both the added mass and damping and is a design variable that can be easily altered during the design stage of the damping treatment. Finally, even though no preliminary studies were done on particle size, future experiments study their effect.

Friction had the effect of reducing the effective damping over time. This also has the effect of making it very difficult to obtain repeatable results. Therefore, future experiments use brass particles which were found to be the most insensitive to friction.

The use of a slow-sine sweep to measure the loss factor of a structure with a PID was judged to be too time-consuming. Another disadvantage is that results on one structure cannot easily be used to predict the response of a different structure with the same PID. Furthermore, experiments are limited to the resonance frequencies of the

structure. Future experiments use a different technique that will allow the measurement of the damping and mass properties at any frequency or velocity. These results of these measurements are generalized and thus applicable to any structure.

Chapter 3

Measurement of Particle Impact Damper Properties

The loss factor due to the addition of a particle impact damper (PID) to a vibrating system is commonly measured by analyzing the frequency response of the structure around its resonance frequencies. This technique suffers from several drawbacks. First, damping measurements are limited to the natural frequencies of the structure. Second, the amount of maximum energy is different for different structures, being dependent on the unique properties (mass, stiffness) of the structure. Since loss factor is a function of the maximum energy, loss factor measurements cannot be applied to other structures. Third, loss factor measurements are often calculated using the half-power method, which is limited to cases of light damping.

In this dissertation, the damping and mass properties of a PID are measured in terms of power, both dissipated and reactive. These measurements can be made at any frequency and amplitude and can be applied to any structure. Power measurements can also be taken much more quickly than loss factor measurements. Excitation with a sinusoid at a single frequency is sufficient for a power measurement, compared to the half-power method, which requires a slow sine-sweep for a non-linear system such as the particle impact damper. The use of a random signal will yield different results since the particle impact damper is a non-linear system dependent on the spectral properties of the excitation.

3.1 Theoretical Background

The equation for average power flow is

$$P = \frac{1}{2} F_{pk} V_{pk}^* . \quad (3.1)$$

For harmonic excitation, the root-mean-square (rms) response is $1/\sqrt{2}$ the peak (pk) response. Therefore, average power flow can alternatively be written as

$$P = F_{rms} V_{rms}^* \quad (3.2)$$

where F is the complex force and V^* is the complex conjugate of the complex velocity. $Real\{P\}$ is as the active, or “dissipated power,” and $Imag\{P\}$ is the reactive, or “trapped power.” Dissipated power is the rate of energy dissipation and trapped power is a measure of the kinetic energy in the system that is not dissipated.

The loss factor contribution of a PID on a system can be predicted if the dissipated power of the PID is known at the system operating conditions. One definition of loss factor is

$$\eta = \frac{E_{dissipated}}{E_{maximum}}, \quad (3.3)$$

where η is the added loss factor, $E_{dissipated}$ is the amount of dissipated energy, and $E_{maximum}$ is the maximum strain or kinetic energy. Note that the strain and kinetic energy are equal at resonance.

Since power is the time derivative of energy, Eq. 3.3 can be rewritten as

$$\eta = \frac{Real\{P\}/\omega}{E_{maximum}}, \quad (3.4)$$

where ω is the radian frequency.

The effective mass of a PID, m , can theoretically be found from the trapped power. The maximum kinetic energy of a moving mass is

$$E_{kinetic} = \frac{1}{2} m V_{pk} V_{pk}^* = m V_{rms} V_{rms}^*. \quad (3.5)$$

Applying the time derivative relationship between power and energy, and solving for m gives

$$m \approx \frac{Imag\{P\}}{\omega V_{rms} V_{rms}^*}. \quad (3.6)$$

Note that this relationship is approximate, since it is not known how the reactive power is affected by the collisions between the enclosure and particle bed.

3.2 Power Measurement Technique: Proof of Concept

Several experiments were performed to validate the power measurement technique. The following sections describe the experimental setup to measure power, verify the measurement of mass with trapped power, and verify the prediction of loss factor on a structure using dissipated power. Supplemental experiments conducted to supplement the validation of the power measurement technique are located in Appendix B.

3.2.1 Description of Experimental Setup to Measure Power

All power measurements were conducted by placing particles inside an enclosure with an adjustable screw top. The two different enclosures used are shown in Figure 3.1. Full descriptions of the enclosures along with machine drawings can be found in Appendix A. The enclosure was then attached to a force sensor which was in turn attached to an electromagnetic shaker. A laser vibrometer was used to measure the velocity of the enclosure and an Agilent dynamic signal analyzer was used to collect and process the data. A schematic is illustrated in Figure 3.2 and a photograph is shown in Figure 3.3. Table 3.1 provides a detailed listing of the equipment used.



Figure 3.1: Enclosures with adjustable screw top

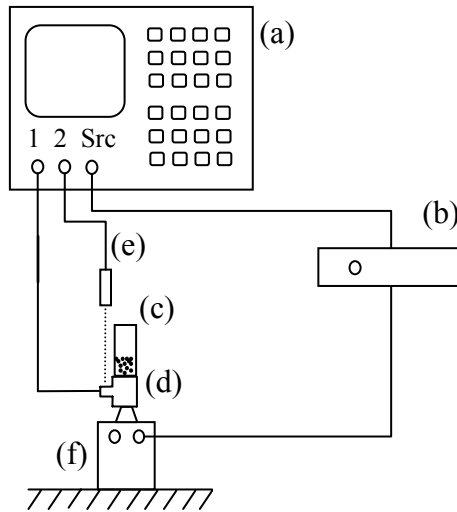


Figure 3.2: Schematic of power measurement setup

Table 3.1: Description of individual components for power measurement

(a)	Agilent 35670A dynamic signal analyzer
(b)	SPA 400 stereo amplifier
(c)	Particle Impact Damper
(d)	PCB 208M51 force sensor SN 10996
(e)	Polytec OFV 502 fiber interferometer with Polytec OFV 2600 vibrometer controller
(f)	Electromagnetic shaker – Clamped to massive granite table

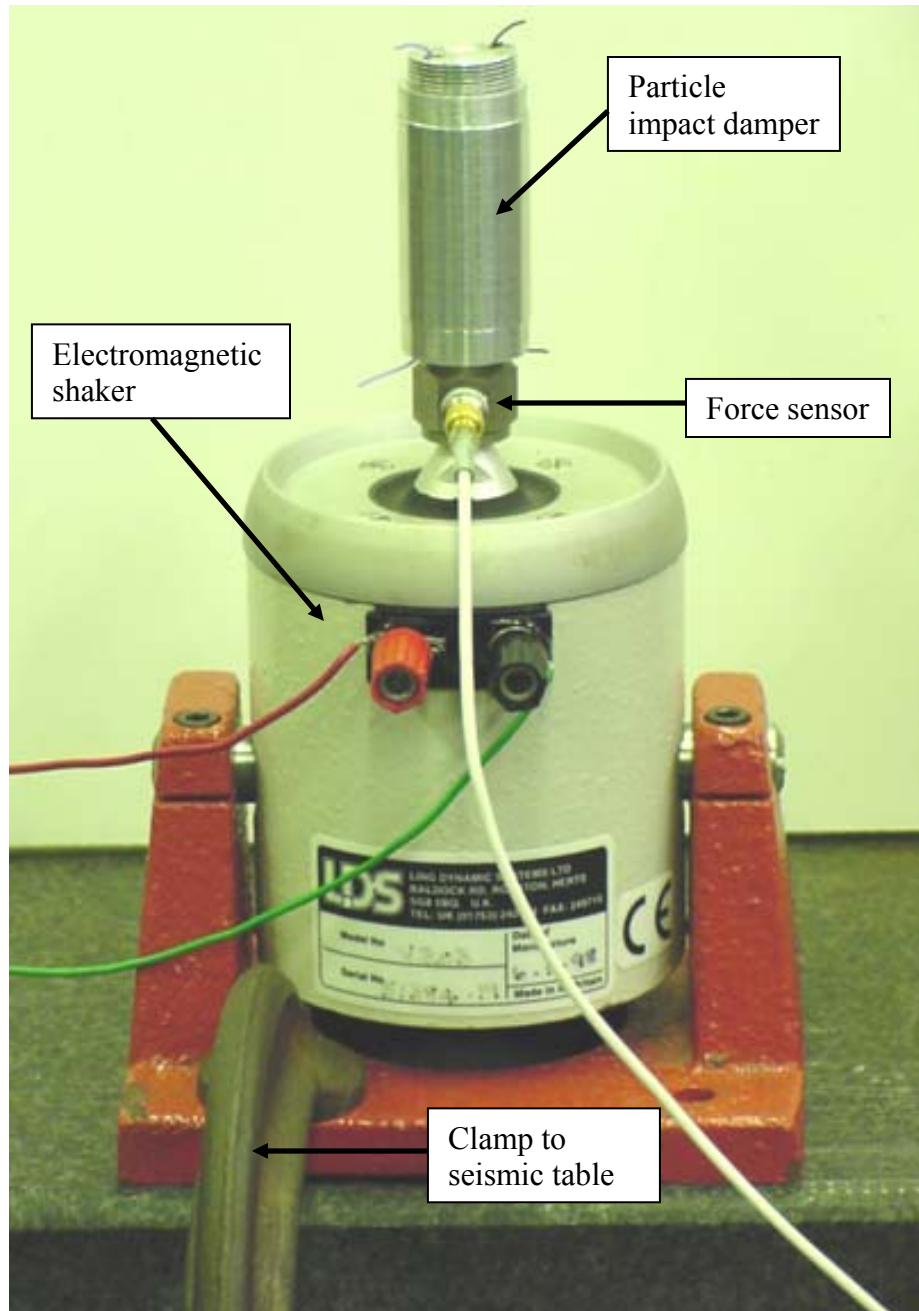


Figure 3.3: Picture of power measurement setup (laser vibrometer not shown)

3.2.2 Verification of Trapped Power Measurement with Lumped Mass

The setup shown in Figures 3.2 and 3.3 was used to measure the dissipated and trapped power of different lumped masses. The signal analyzer was used to excite the masses between 0 and 400 Hz with a swept-sine signal. A triple-beam balance was used to measure the masses and Eq. 3.6 was used to calculate the equivalent mass.

The results for masses of 136, 200, and 369 grams are shown in Figures 3.4 - 3.6. The dissipated power is negligible for all cases and the mass computed from reactive power is very close to the statically measured mass. A summary of the results are given in Table 3.2.

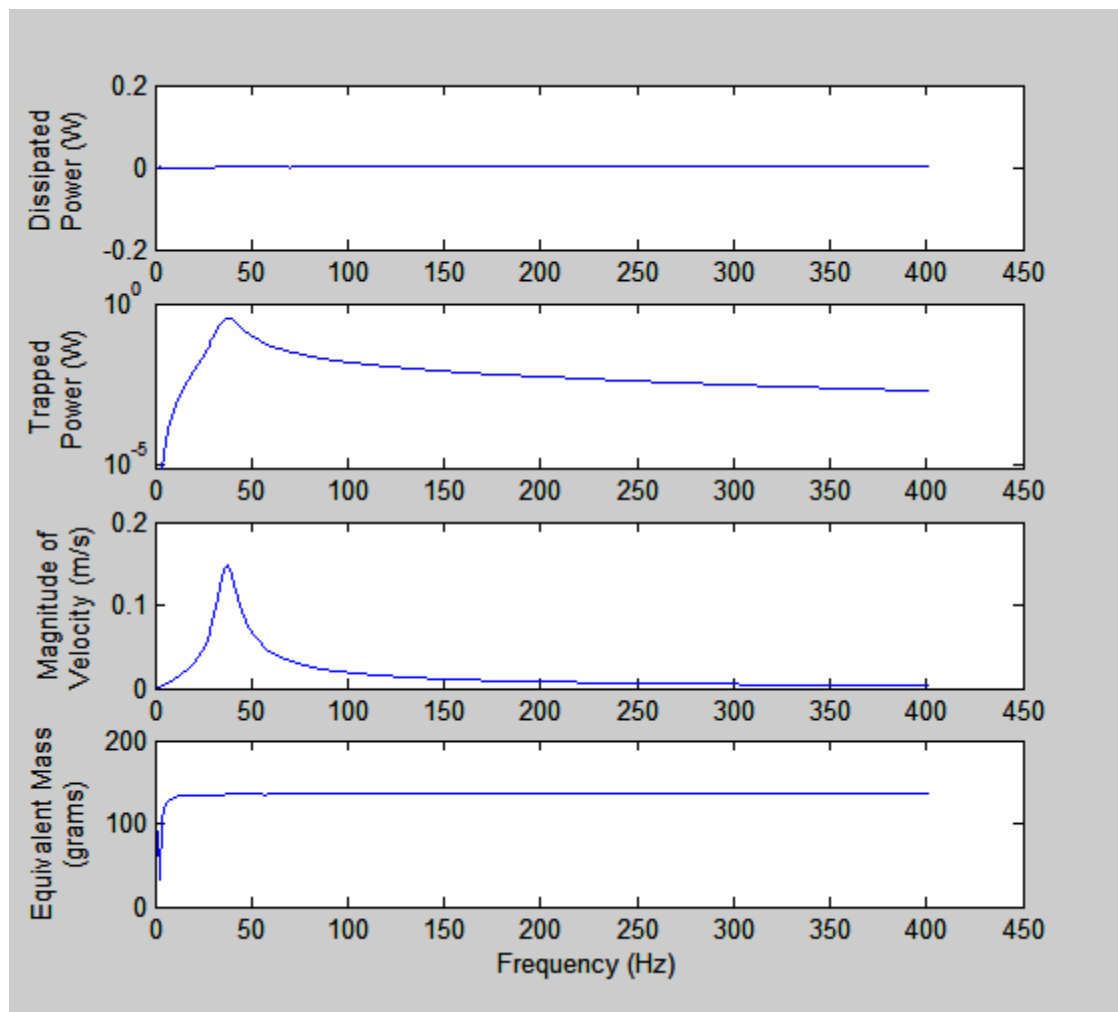


Figure 3.4: Power and equivalent mass data for 136 gram mass

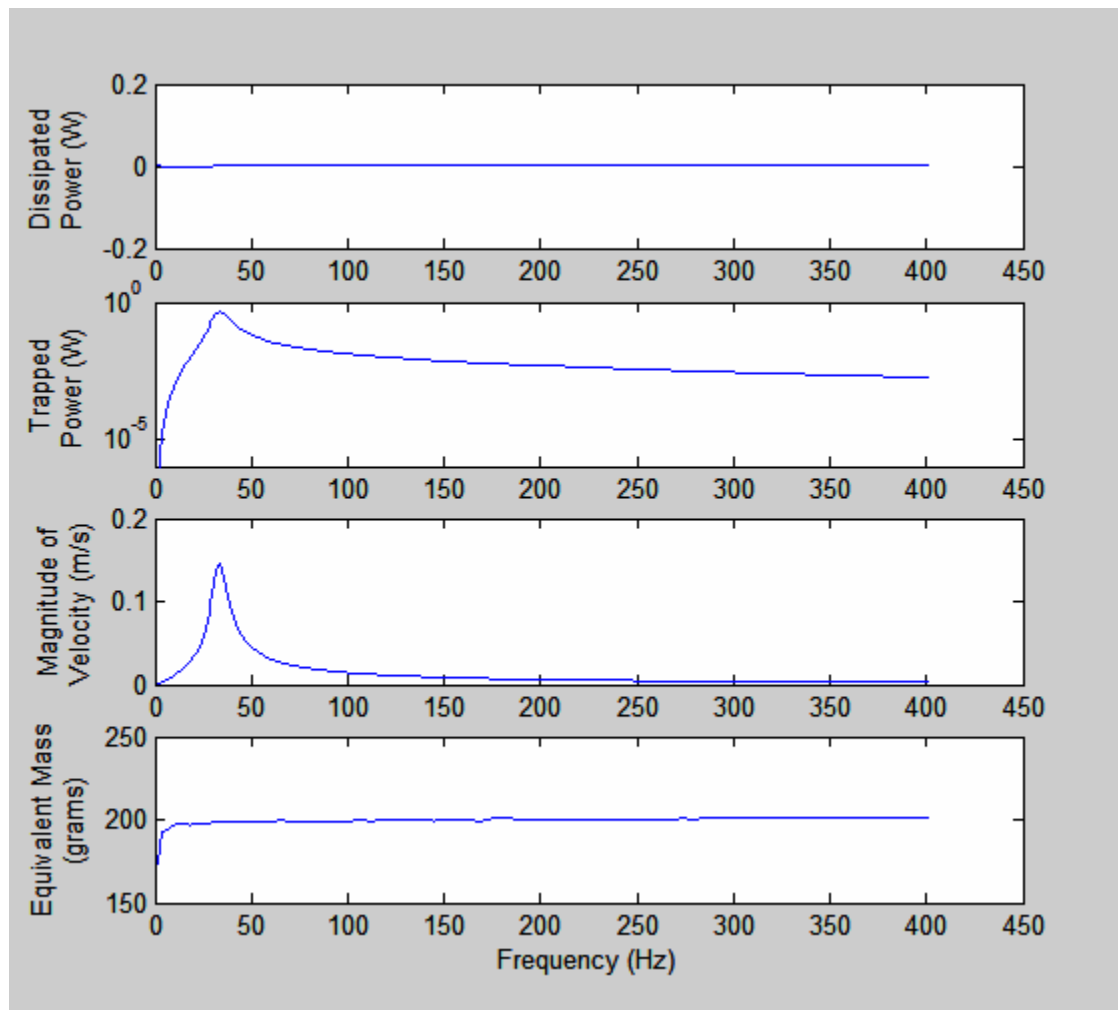


Figure 3.5: Power and equivalent mass data for 200 gram mass

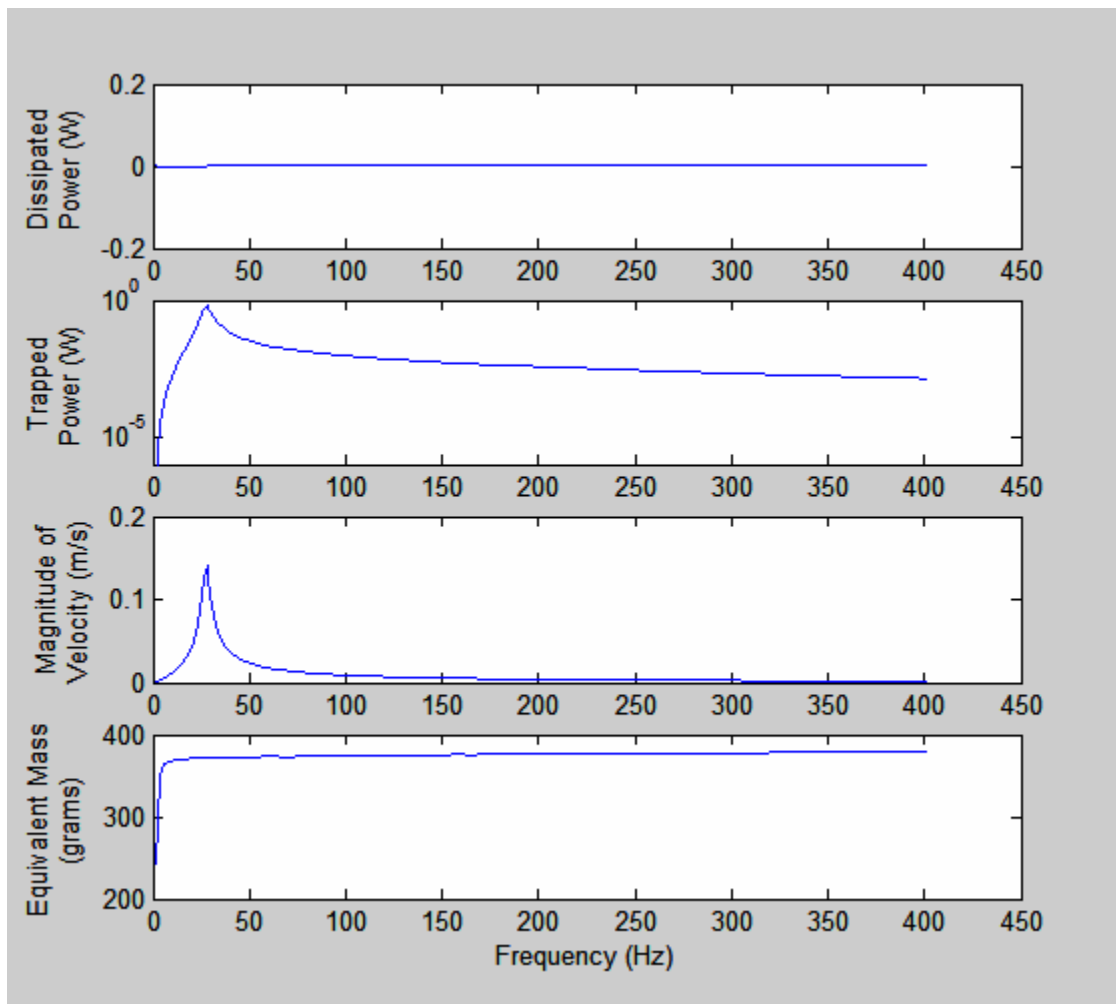


Figure 3.6: Power and equivalent mass data for 369 gram mass

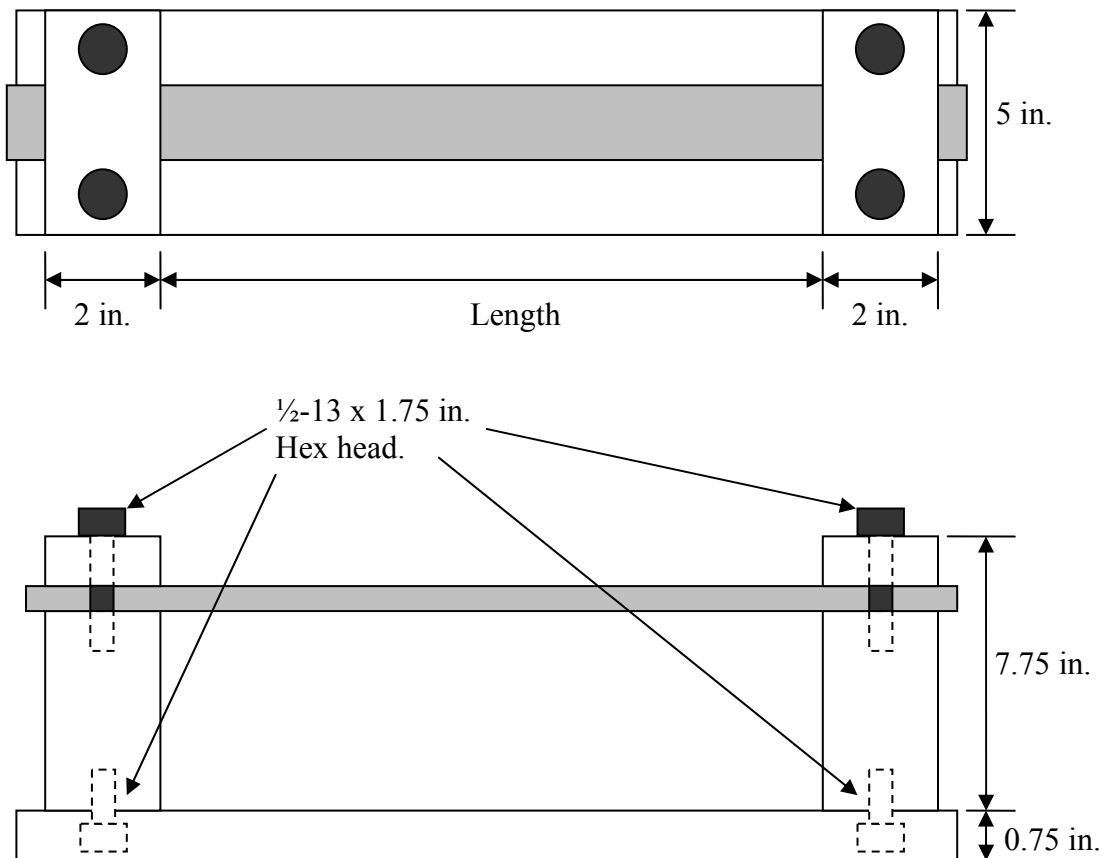
Table 3.2: Summary of power and equivalent mass data

Statically measured mass (grams)	Mass from reactive power (grams)
136	137
200	201
369	376

3.2.3 Verification of Power Measurement Technique Using Particle Impact Dampers

Two sets of experiments were performed to verify the computation of loss factor using dissipated power. Their purpose was to show that the loss factor of a system with a PID can be predicted using a power measurement. In the first set of experiments, the input excitation level was varied while keeping the properties of the PID unchanged. In the second set of experiments, the input excitation level was held constant while changing the gap size of the PID.

An aluminum 6160 T6 beam was clamped to a ground structure which was in turn clamped to a seismic table (Figure 3.7). A small hole was drilled in the center of the beam and an electromagnetic shaker was connected to the center of the beam by placing a threaded stinger through the hole. One hex nut was used on either side of the beam to “sandwich” the beam and connect it to the stinger. A force sensor was placed below the beam to measure the input force and laser vibrometer was used to measure the PID’s velocity. This setup is shown in Figure 3.8.



(Drawing not to scale)

Figure 3.7: Aluminum ground structure with clamped beam

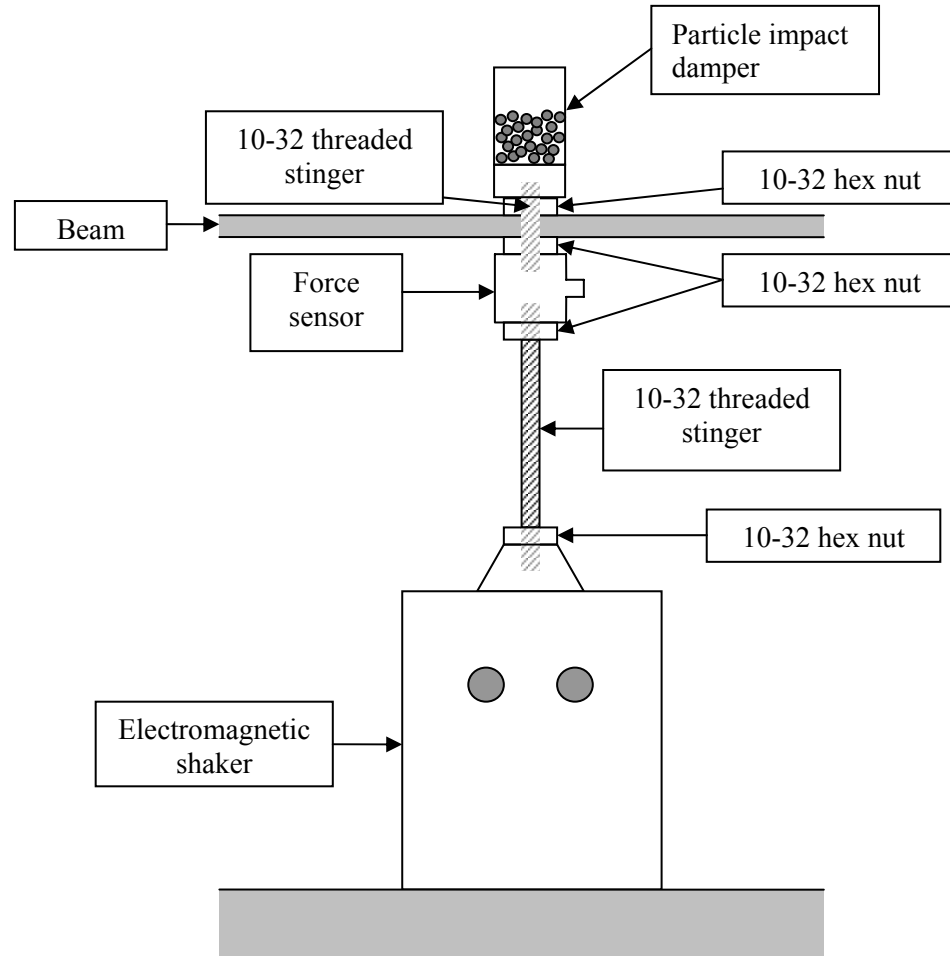


Figure 3.8: Attachment of shaker, force sensor, and PID to beam center

Set 1 – Variable Input Excitation Amplitude, Fixed PID Properties

These experiments were performed on two clamped beams of different lengths. The first beam measured 11 x 2 x 1/8 inches, and the second measured 12 x 2 x 1/8 inches. Both are made of 6061 T6 aluminum. The particle enclosure is constructed primarily out of aluminum with clear acrylic enclosure walls (see Figure 3.9). These clear walls allow the motion of the particles to be seen. The top has threads that allow

the gap size to be adjusted and a locking ring to ensure that gap does not change during measurements. This experiment used 200 1/16 inch diameter brass ball bearings for the particles, with a gap size of 0.54 mm. The masses of the particles, enclosure, and beams are listed in Table 3.3. A laser vibrometer was used to measure the velocity profile of the beam and the velocity of the enclosure. A picture of the completed beam setup is shown in Figure 3.10, and Table 3.4 lists each component.

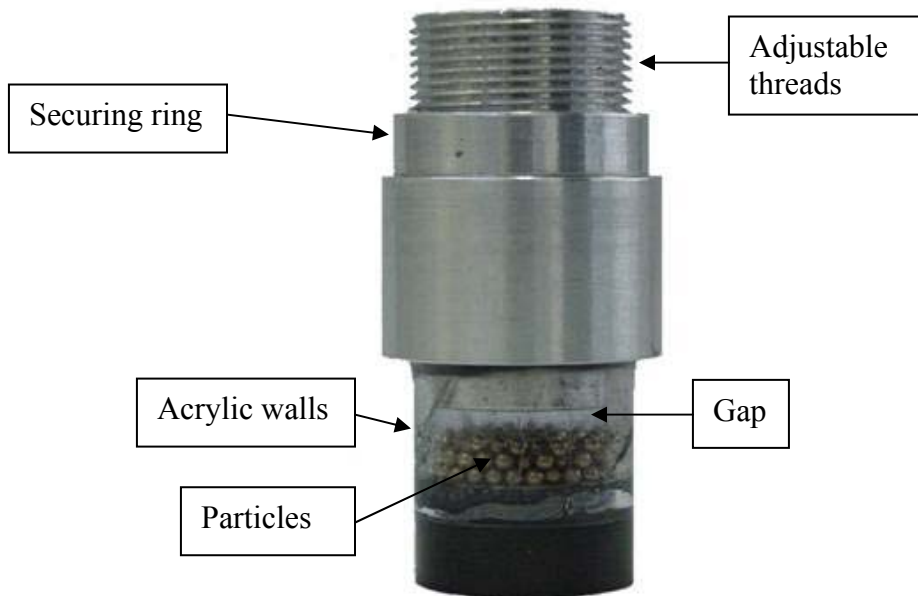


Figure 3.9: Particle enclosure with clear acrylic walls

Table 3.3: Mass of components for set 1

Component	Mass (grams)
12 x 2 x 1/8 inch aluminum beam	133.2
11 x 2 x 1/8 inch aluminum beam	122.1
200 1/16 inch diameter brass ball bearings	3.5
Particle enclosure (without particles)	36.0

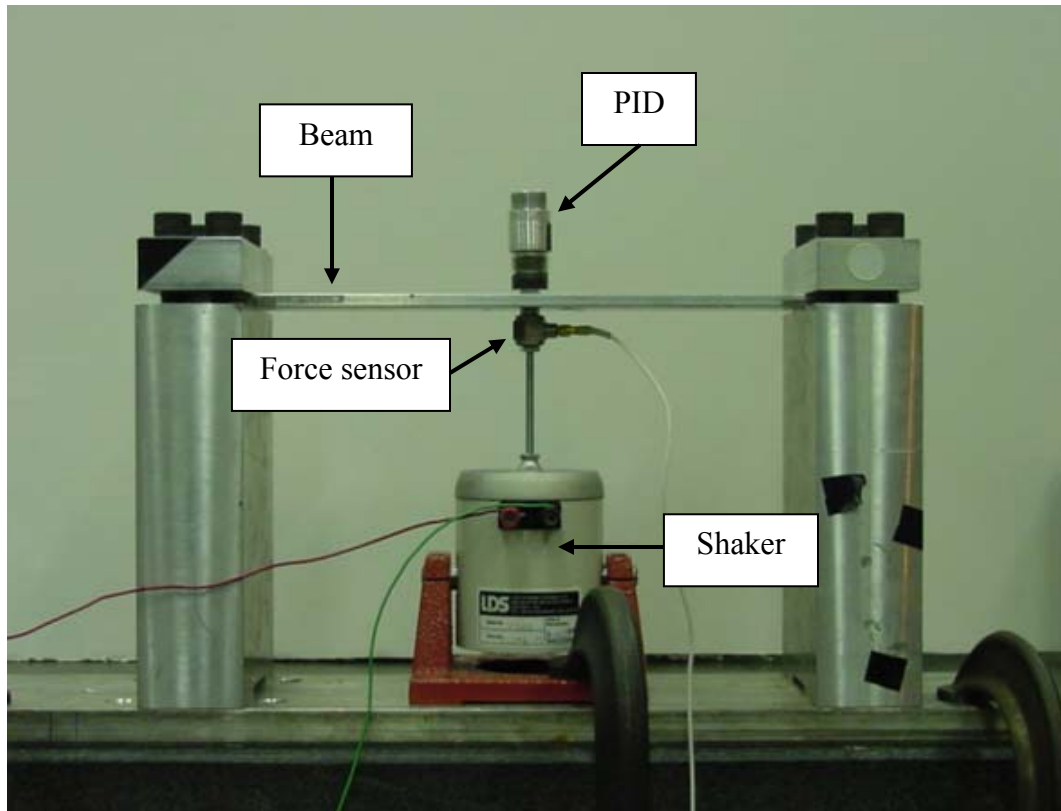


Figure 3.10: Completed beam setup for set 1

Table 3.4: List of experimental equipment for beam setup set 1

Quantity	Description
1	11 x 2 x 1/8 or 12 x 2 x 1/8 inch aluminum 6160 T6 beam
1	Particle enclosure
200	1/16 inch brass ball bearings
1	Beam clamping and grounding assembly
1	LDS V203 electromagnetic shaker SN 51884-19
1	PCB 208A02 force sensor SN 9801
1	Agilent 35670A dynamic signal analyzer
1	Polytec OFV 502 fiber interferometer with Polytec OFV 2600 vibrometer controller
2	10-32 threaded stinger
4	10-32 hex nut
4	Clamps
1	Roll of reflective tape

Power measurements were subsequently taken using the same experimental setup described earlier by Figure 3.2 and Table 3.1. These measurements do not require a structure, so the beam has been removed. A picture of this setup is shown in Figure 3.11.

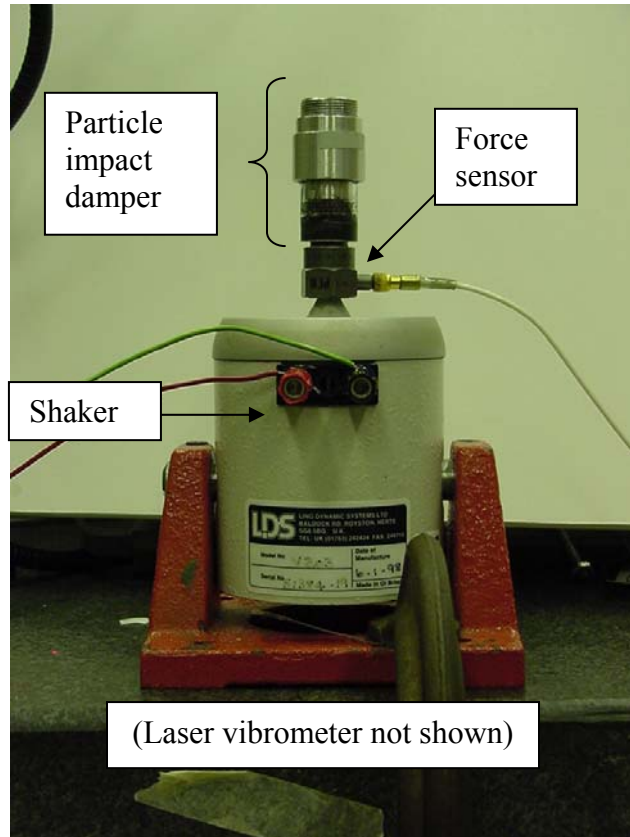


Figure 3.11: Picture of power measurement setup with aluminum-acrylic enclosure

Slow sine sweep measurements measured the frequency response of the beam with the attached PID near the system's fundamental natural frequency (118 Hz) at varying input levels. The pole-zero curve-fitting method (described in Appendix B, section 4) was used to compute the loss factors of the bare beam and the beam with the PID attached. The loss factor contribution of the PID was then found by subtracting the loss factor of the bare beam from the loss factor of the beam with PID attached. The

laser vibrometer was used to measure the velocity profile of the beam in one-inch increments; it closely matched the theoretical first eigenvector at all input levels and for both the 11 inch and 12 inch beams (see Figure 3.12). The kinetic energy in the beam is estimated by discretizing the beam into N segments and summing the energy in each segment. The equation for this is

$$E_{maximum} = \frac{1}{2} \sum_{i=1}^N m_i v_i^2 + \frac{1}{2} \sum_{j=1}^M m_j v_j^2 \quad (3.7)$$

where m_i is the mass of the i th segment, v_i is the transverse velocity of the center of the i th segment, m_j is the mass of any discrete attachments, and v_j is the velocity of those discrete attachments. Discrete attachments include stingers, hex nuts, and other moving elements that add to the kinetic energy of the entire system. Rotational components have been ignored, and were assumed to be negligible because the PID was placed in a location where the translational motion was much greater than the rotational motion.

The PID was then placed on the shaker and excited at the same frequencies and amplitudes to measure the power. The loss factor from these power measurements was calculated using Eq. 3.4, and compared to the measured loss factors. These results are shown in Figures 3.13 and 3.14.

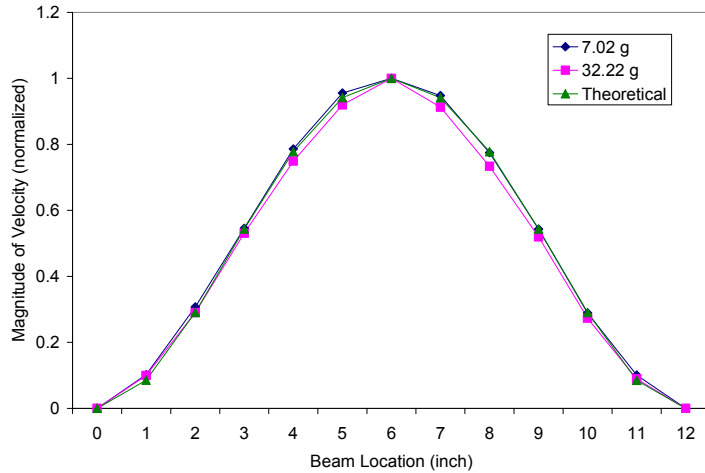


Figure 3.12: Velocity profile of beam with PID at fundamental resonance

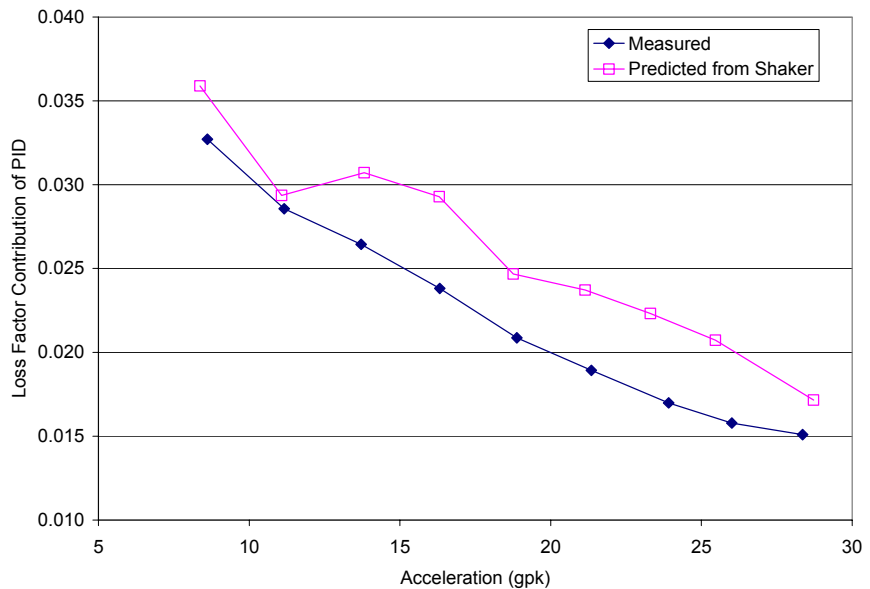


Figure 3.13: Measured and predicted loss factors for PID on beam at first beam resonance with varying amplitude (11 x 2 x 1/4 inch beam)

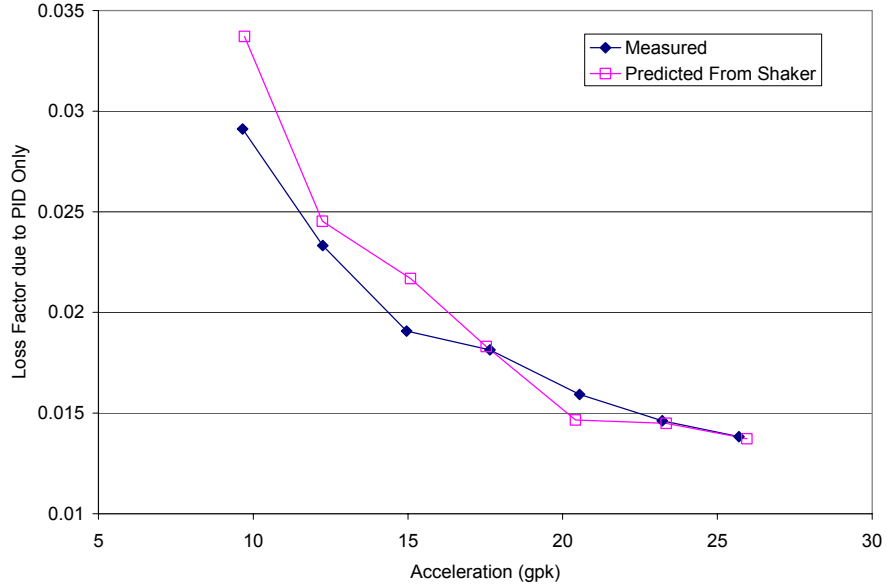


Figure 3.14: Measured and predicted loss factors for PID on beam at first beam resonance with varying amplitude (12 x 2 x ¼ inch beam)

The loss factor predicted using the power measurement technique on the shaker matches the measured loss factor reasonably well. For the majority of cases, the predicted loss factor is too high indicating that either the measured dissipated power is too high, or the kinetic energy in the beam is too low. It is quite feasible that the kinetic energy measurement of the primary structure is not complete, since includes small movements in the support structure as well as rotational components were not measured.

Set 2 – Fixed Input Excitation Amplitude, Variable Gap Size

This experiment was conducted on a single 6061 T6 aluminum beam measuring 30 x 2 x 1/8 inches and clamped at both ends. It is designed to show that the loss factor of a structure can be predicted using power measurements when the properties of the PID are changed. The same grounding structure and enclosure described earlier were used

(see Figures 3.8 and 3.9). However, the number of 1/16 inch brass particles was doubled to 400. The same setup was also used to measure the power of the PID on the shaker (see Figure 3.11). A picture of the completed beam setup is shown in Figure 3.15, and Table 3.5 lists each component. The masses of the beam, enclosure, and particles are given in Table 3.6.

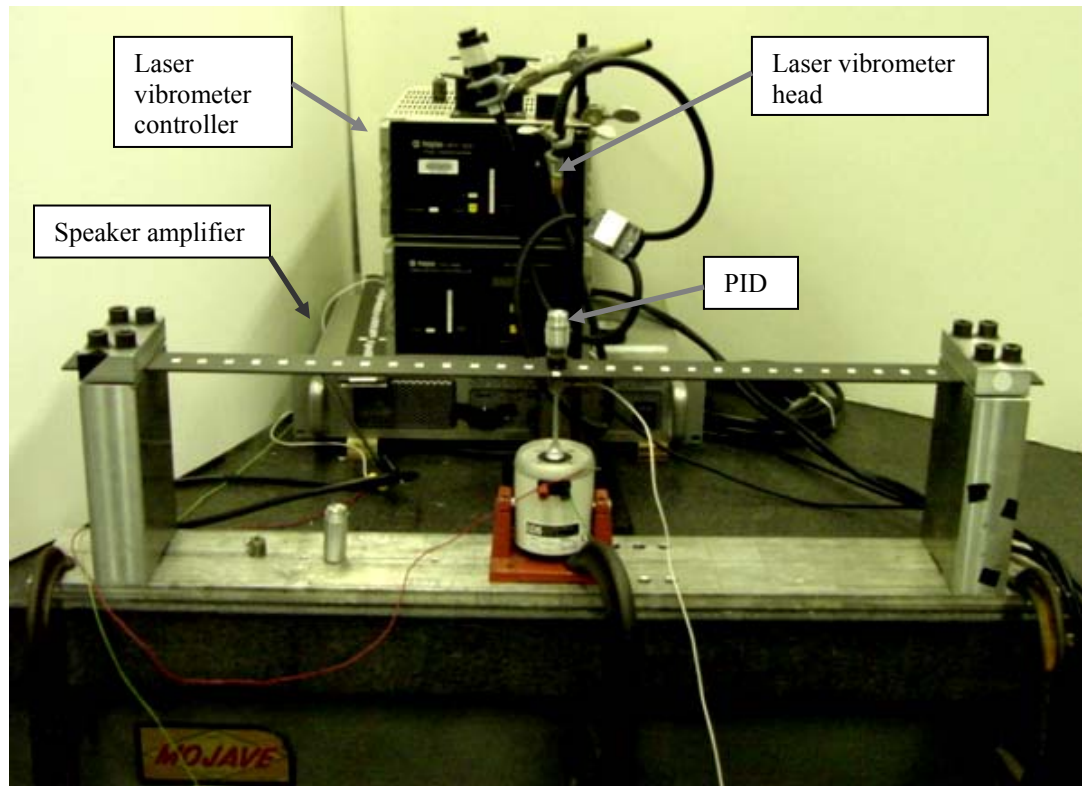


Figure 3.15: Completed beam setup for set 2

Table 3.5: List of experimental equipment for beam setup set 2

Quantity	Description
1	30 x 2 x 1/8 inch aluminum 6160 T6 beam
1	Particle enclosure
400	1/16 inch brass ball bearings
1	Beam clamping and grounding assembly
1	LDS V203 electromagnetic shaker SN 51884-19
1	PCB 208A02 force sensor SN 9801
1	Agilent 35670A dynamic signal analyzer
1	Polytec OFV 502 Fiber Interferometer with Polytec OFV 2600 Vibrometer Controller
2	10-32 threaded stinger
4	10-32 hex nut
4	Clamps
1	Roll of reflective tape

Table 3.6: Mass of components for set 2

Component	Mass (grams)
30 x 2 x 1/8 inch aluminum 6061 T6 beam	333.1
400 1/16 inch diameter brass ball bearings	7.0
Particle enclosure (without particles)	36.0

A slow sine sweep was used to measure the frequency response of the beam with the attached PID at the system's third natural frequency (127 Hz). The input level was kept constant and chosen so that an easily measurable amount of damping existed. The gap size was adjusted from 0 to 1.19 mm in a series of measurements. The velocity profile of the beam at its third bending resonance is shown in Figure 3.16. The addition of the PID to the center of the beam changes the third mode shape by lowering the relative response of the beam center. It also shifts the location of the two antinodes towards the center. The velocity profile at the third natural frequency was insensitive to

changes in the gap size, which indicates that the same normalized velocity profile can be used for the kinetic energy calculations at all gap sizes. Since the addition of the PID caused significant changes to the theoretical mode shape, the measured mode shape was used to calculate kinetic energy.

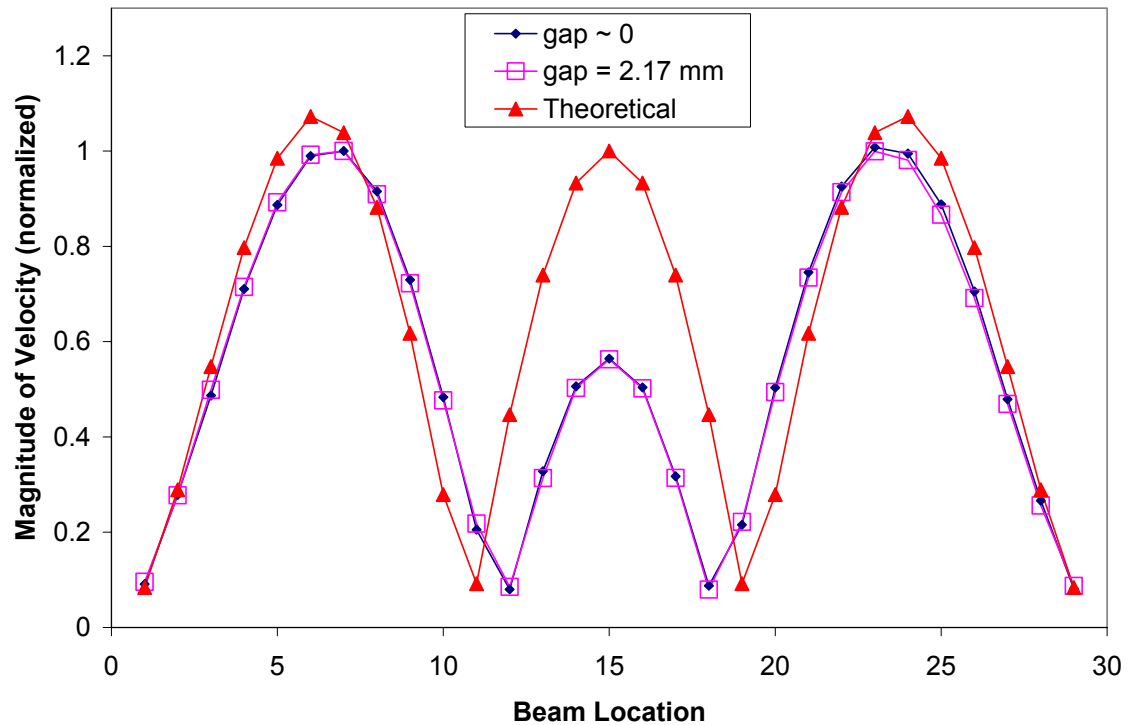


Figure 3.16: Velocity profile of 30 inch beam at 127 Hz

The PID was placed on the shaker and excited at the same frequencies and amplitudes to measure power. The loss factor was calculated, and compared to the measured loss factors. This result is shown in Figure 3.17.

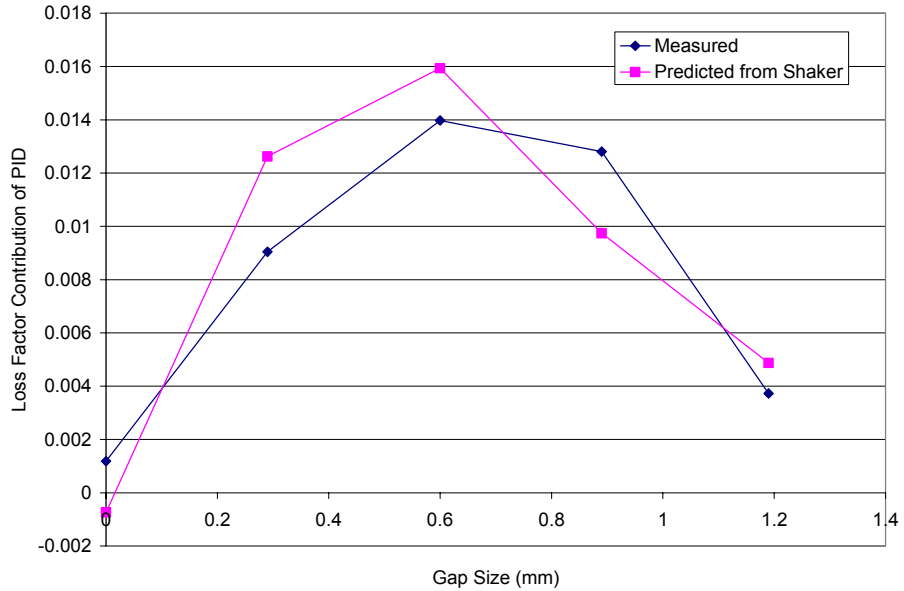


Figure 3.17: Measured and predicted loss factors for PID on 30 inch beam with varying gap size

Once again, the loss factor was successfully predicted within acceptable error.

Overall, the power measurement technique both over- and under-predict the loss factor contribution of the PID with the largest error equal to 0.0036 and occurring at a gap size of 0.29 mm.

The negative loss factor predicted at zero gap size was the result of a fictitious dissipated power measurement due to transducer phase error. Even though this error was corrected, power measurements of PID's that dissipate very little power are still sensitive to even minute errors in phase.

3.2.4 Summary of Proof of Concept of Power Measurement Technique

Several methods were used to validate the concept of using measured power to predict the effect of a PID on a structure. The first group of measurements validates the measurement of trapped power using lumped masses. The successful conversion of trapped power into mass verifies the theory that will allow the mass effect of the particle impact dampers to be approximately determined.

The second group of experiments attempted to verify that dissipated power measurements could be combined with the kinetic energy calculation of a structure at resonance to predict a loss factor. This was done using two PID's with differing amounts of particles. The primary systems were clamped-clamped aluminum beams of different lengths and thicknesses.

The results from these experiments show an acceptable level of agreement between the measured and predicted loss factors. The errors that exist are due to a combination of these factors:

1. Incorrect measurement and calculation of the kinetic energy in the primary system.
2. Residual transducer phase error (see Appendix B).
3. Loss factor measurement error.

The measurement of kinetic energy in the primary system is challenging because it is difficult to account for the energy of rotational degrees of freedom as well as energy that flows beyond the boundary conditions. Transducer phase errors can lead to negative values of dissipated power, and have a greater effect for cases where the PID dissipates a

very low amount of energy (see Appendix B). Errors in loss factor measurement can be due to noise in the frequency response function or to residual contributions from neighboring resonances. In the experiments conducted, the frequency response functions were largely noise-free, and the systems were deliberately chosen so that the natural frequencies were widely spaced. However, the measured loss factors were small (< 0.035 for PID's), which makes accurate measurements more difficult.

In conclusion, the use of measured power to predict the damping and mass effects of particle impact dampers on a structure has been confirmed. The remainder of this chapter deals with how the power changes as the input parameters (gap size, particle size, amplitude, frequency) are changed.

3.3 Power Measurements

Previous sections have shown that a measurement of the mass and damping contribution of a PID can be made by measuring power independent of a primary structure. This section describes experiments that were used to determine how different input variables (gap size, amplitude, frequency) affect the properties of a particle impact damper. For all tests, the setup shown in Figure 3.2 was used.

3.3.1 Effect of Amplitude on Optimum Gap and Effective Mass

In this section, the effects of enclosure amplitude on dissipated power and effective mass are shown. The first experiment used the enclosure shown in Figure 3.9.

400 brass ball bearings measuring 1/16 inches in diameter filled the enclosure to a height of approximately 49.77 mm. The enclosure was excited at varying amplitudes at 127 Hz.

Figure 3.18 illustrates how dissipated power changes with amplitude and gap size. For each amplitude, there is a gap size that results in the highest dissipated power. This is called the *optimum gap size* and was previously discussed in Chapter 2. The optimum gap size increases with increasing amplitude. The increase in dissipated power with increasing amplitude can be attributed to a greater amount of energy transferred to, and dissipated in, the particle bed.

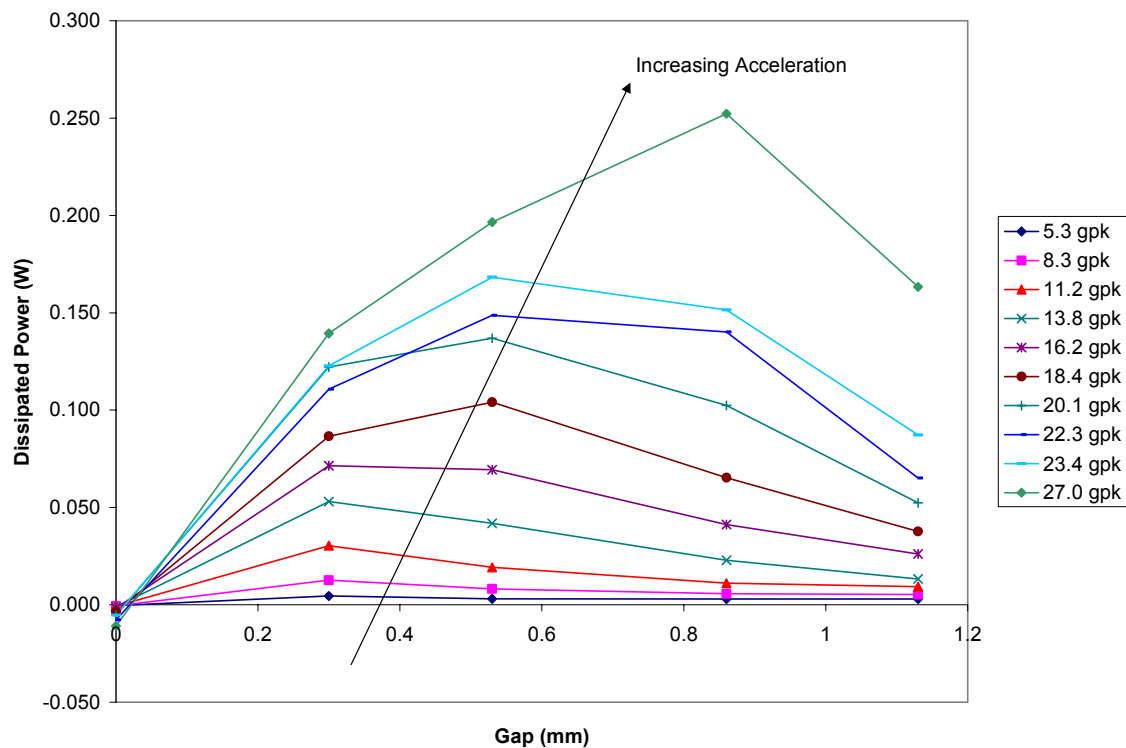


Figure 3.18: Dissipated power with changing gap and amplitude

Figure 3.19 shows how the effective mass of the PID changes under the same operating conditions. The effective mass generally increases with increasing acceleration and decreases with increasing gap size. At zero gap size, the effective mass is near the static mass of the PID (42 grams) because the particles have very little room to move and behave essentially like a lumped mass. As the gap size increases, the particles have more room to move, and spend less time in contact with the enclosure walls, reducing the mass effect. Higher vibration amplitudes result in a higher effective mass and a reduced sensitivity to gap size. This could occur because at higher amplitudes, the particle bed moves through the void more quickly, spending less time in the air, and more time in contact with the enclosure walls.

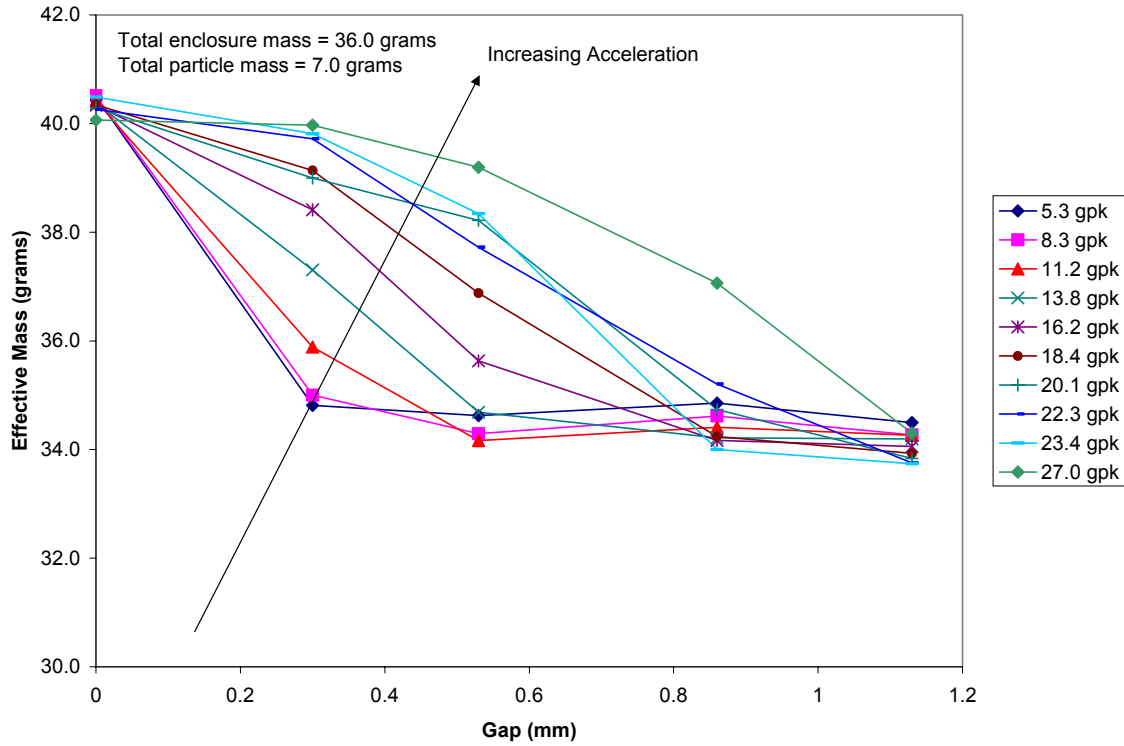


Figure 3.19: Effective mass of PID with changing gap and amplitude

3.3.2 Effect of Particle Size on Optimum Gap Size

This experiment used the aluminum enclosure shown in Figure 3.20 (see Appendix A). Brass ball bearings of different size and number were used with the total mass being nearly equivalent (see Table 3.7). The enclosure was excited with a sinusoid at 80 Hz at constant velocity.



Figure 3.20: Aluminum enclosure

Table 3.7: Particle sizes and quantity

Diameter (in.)	Quantity	Mass per BB (grams)	Total Mass (grams)
1/16	600	0.0175	10.50
3/32	174	0.0605	10.53
1/8	75	0.1408	10.56
5/32	37	0.2808	10.39
3/16	22	0.4802	10.56

Mass of empty enclosure = 46.35 grams

Gap size is related to volume fraction, which is the total volume of the particles divided by the total volume in the enclosure. This is written as

$\text{Volume Fraction} = \frac{N_p \times V_p}{V_{encl}},$	(3.8)
---	-------

where N_p is the number of particles, V_p is the volume per particle, and V_{encl} is the volume of the enclosure. For a cylindrical enclosure with spherical particles, this equation becomes

$$\text{Volume Fraction} = \frac{N_p \times \frac{1}{3}\pi D_p^3}{\frac{1}{4}\pi D_{encl}^2 \times (H_o + gap)} = \frac{4N_p D_p^3}{3D_{encl}^2} \times \frac{1}{H_o + gap}, \quad (3.9)$$

where D_p is the particle diameter, D_{encl} is the inside diameter of the enclosure, and H_o is the inside height of the enclosure when the gap size is zero. Note that for spherical particles of finite diameter, it is not possible to achieve a volume fraction of unity due to the voids that exist between particles. The theoretical maximum volume fraction is 0.74, which is equivalent to the atomic packing factor for the face-centered-cubic (FCC) crystalline structure [60]. The FCC structure (Figure 3.21) is the packing structure spheres form when they are stacked on top of each other (Figure 3.22).

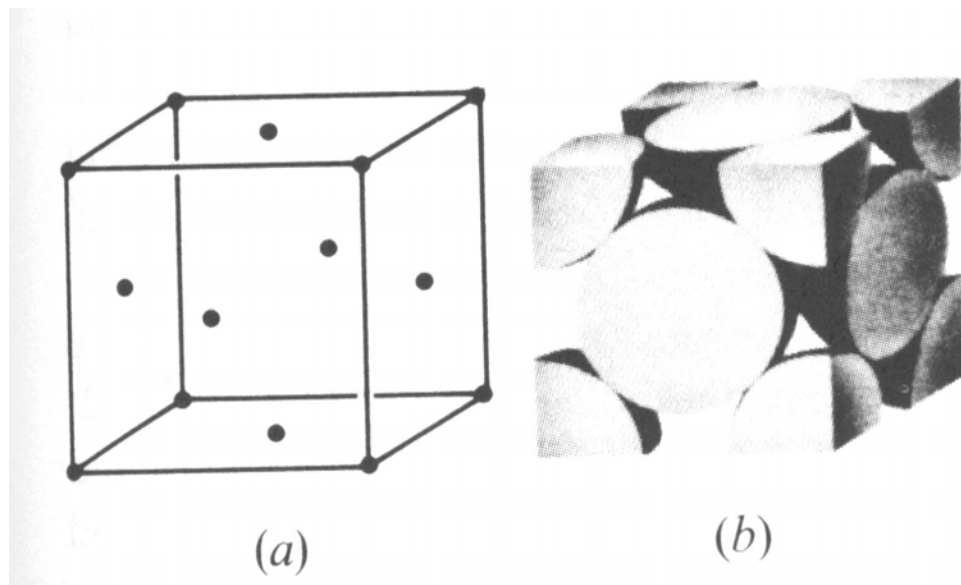


Figure 3.21: FCC atom-site (a) and hard-sphere (b) cell models. Source: G.T. Murray, *Introduction to Engineering Materials: Behavior, Properties, and Selection*. Marcel Dekker, Inc. 1993. p. 123.

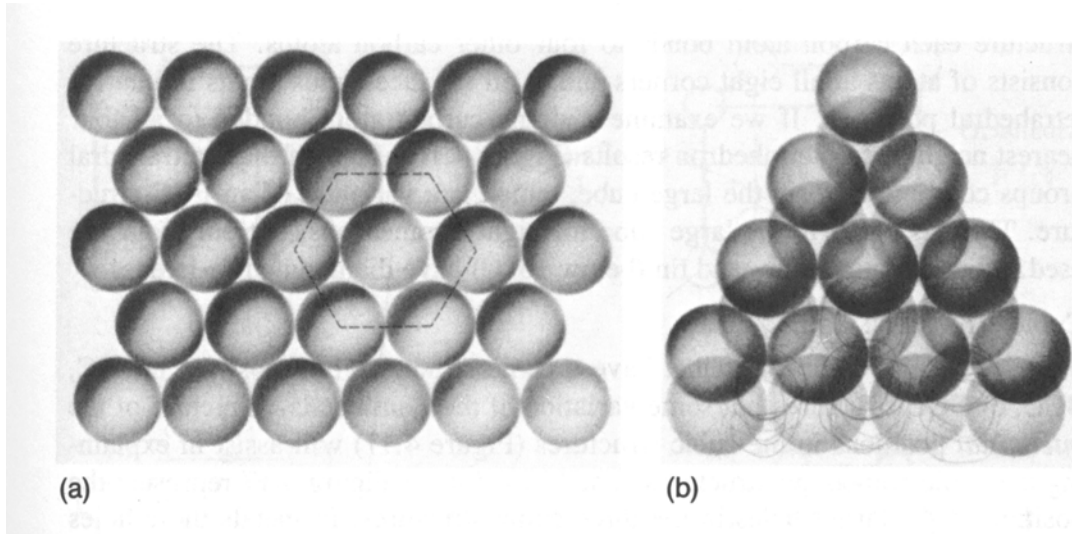


Figure 3.22: Stacking sequence for FCC structure. Source: G.T. Murray, *Introduction to Engineering Materials: Behavior, Properties, and Selection*. Marcel Dekker, Inc. 1993. p. 125.

The expression for gap size in terms of volume fraction can be written

$$\text{gap} = \frac{4N_p D_p^3}{3D_{encl}^2} \times \frac{1}{\text{Volume Fraction}} - H_o. \quad (3.10)$$

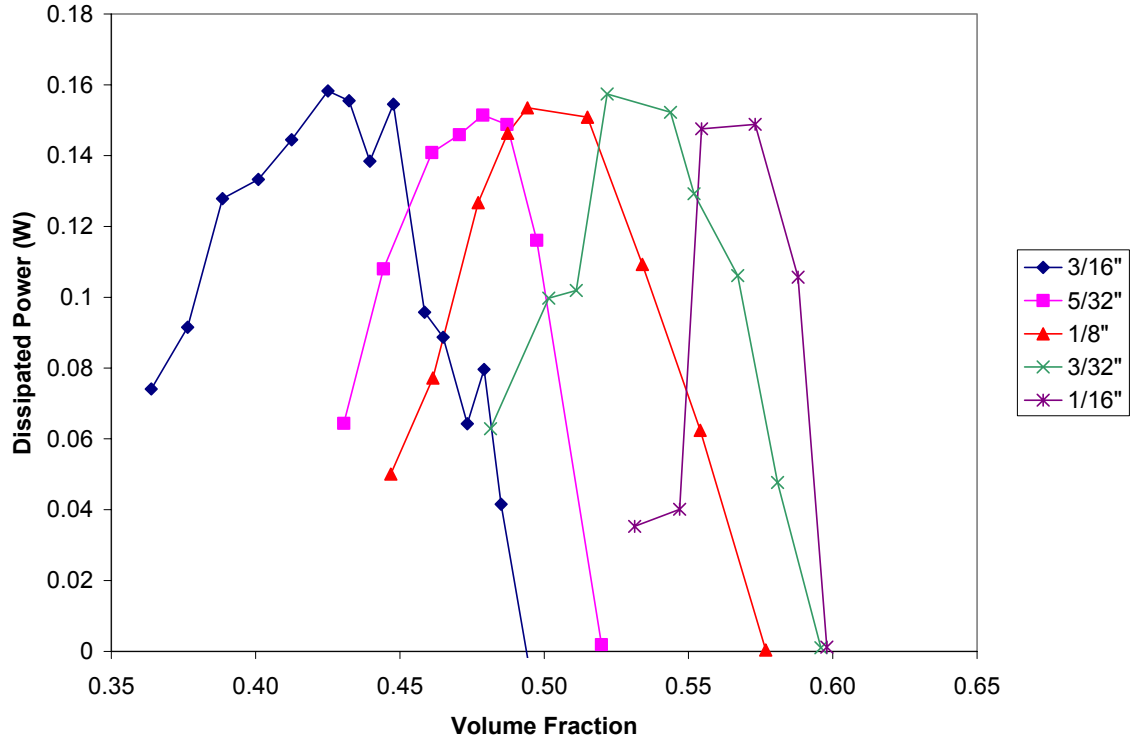


Figure 3.23: Dissipated power vs. volume fraction for different particle sizes

Figure 3.23 shows how dissipated power changes with varying volume fraction and particle size. The maximum dissipated power is the same, regardless of particle size. Since the particle beds all have the same mass, the highest attainable power dissipation is evidently independent of particle size. The optimum volume fraction decreases with increasing particle size.

Figure 3.24 shows that the range of gap sizes that gives optimum or near-optimum power dissipation increases with particle size. The importance is from a design standpoint, because it indicates that larger particle sizes result in a PID that is less sensitive to small deviations in gap size. Therefore, using larger particles can result in a more robust damper. It is also evident that optimum gap size increases with particle size.

The exception is the 5/32 inch case, which has an optimum gap that is smaller than the optimum gap for 3/32 inch particles. This could be a result of an incomplete layer of particles (illustrated in Figure 3.25).

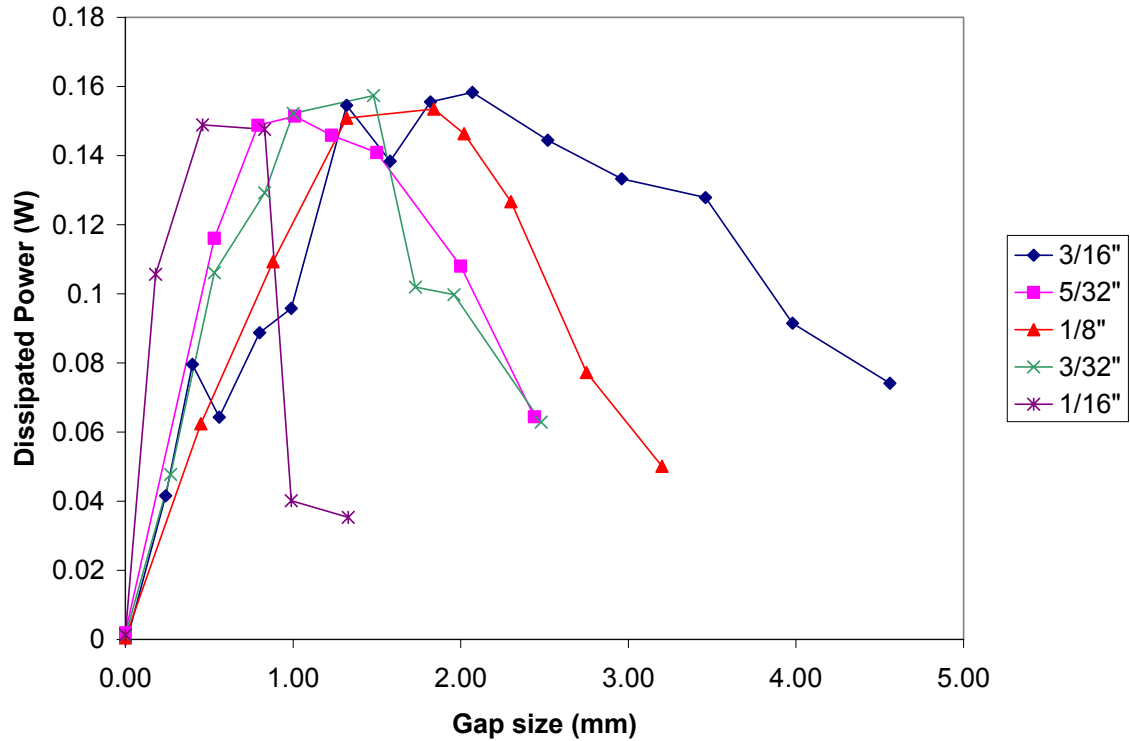


Figure 3.24: Dissipated power vs. gap size for different particle sizes

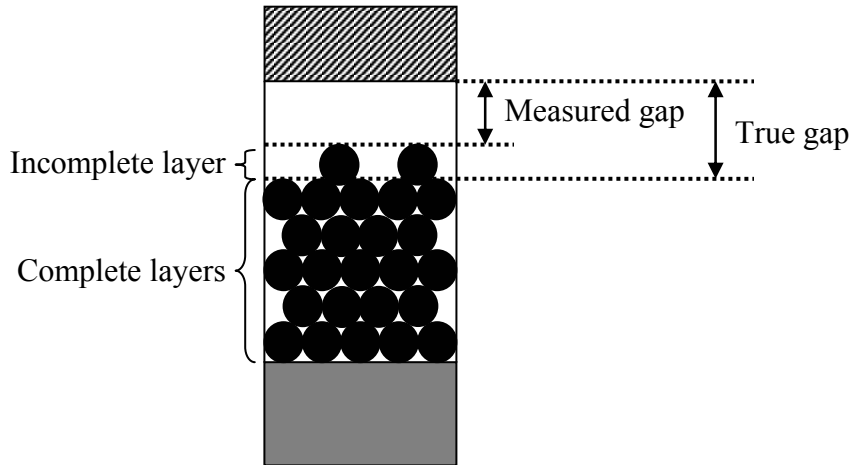


Figure 3.25: Incomplete layer of particles

3.3.3 Effect of Particle Size on Effective Mass

Figure 3.26 shows that the effective mass of the PID is smaller for large gap sizes. This is intuitively correct because larger volume fractions allow more space for the particles to move in, thereby reducing the amount of time the particles are in contact with the enclosure. The figure also shows that larger particles have higher effective masses.

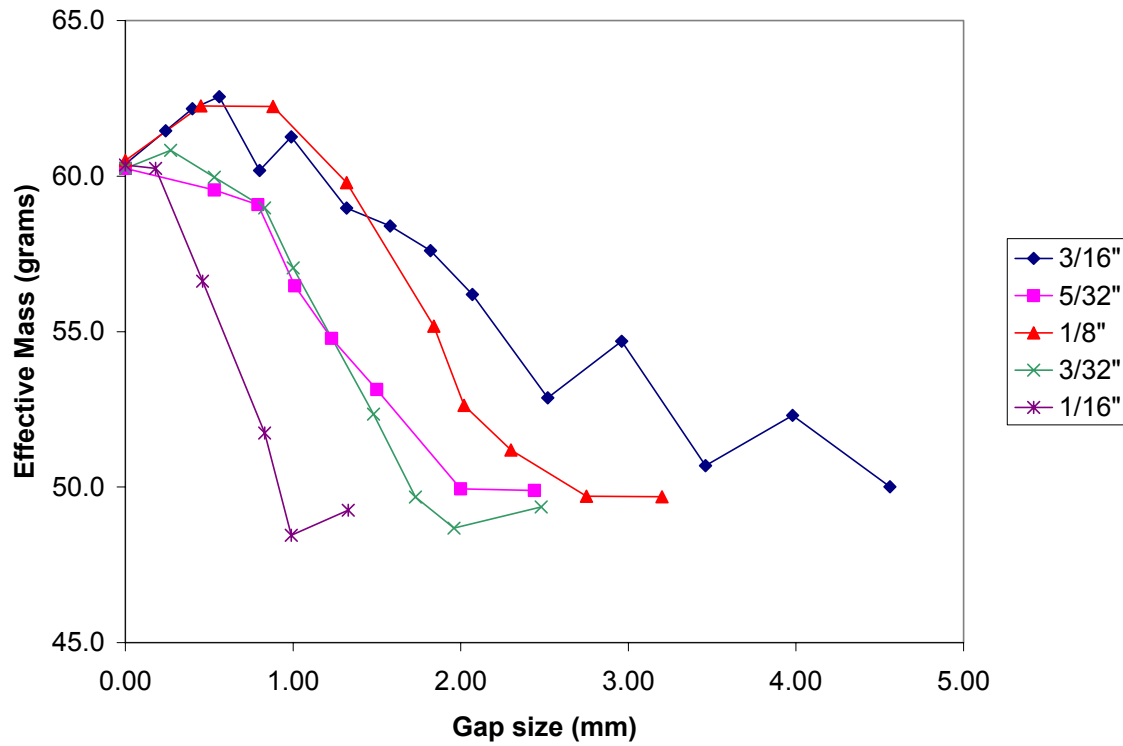


Figure 3.26: Effective mass vs. gap size for different particle sizes

3.3.4 Effect of Vibration Amplitude on Dissipated Power and Effective Mass

The same data in Section 3.3.3 was used to analyze the effect of vibration amplitude on dissipated power and effective mass. Figures 3.27 and shows how the dissipated power increases with increasing displacement. The slope increases once the displacement exceeds a certain value. Higher excitation frequencies result in a greater increase in slope. The displacement where the slope changes increases with gap size. This is illustrated in Figure 3.28, which shows results for 1/16 inch particles when the gap size is increased to 1.35 mm. This transition to a higher slope exists for any particle

size, as shown by Figures 3.29 and 3.30, which depict the data for 1/8 and 3/16 inch particles, respectively. The transition to the higher slope appears to become more gradual as the particle size increases.

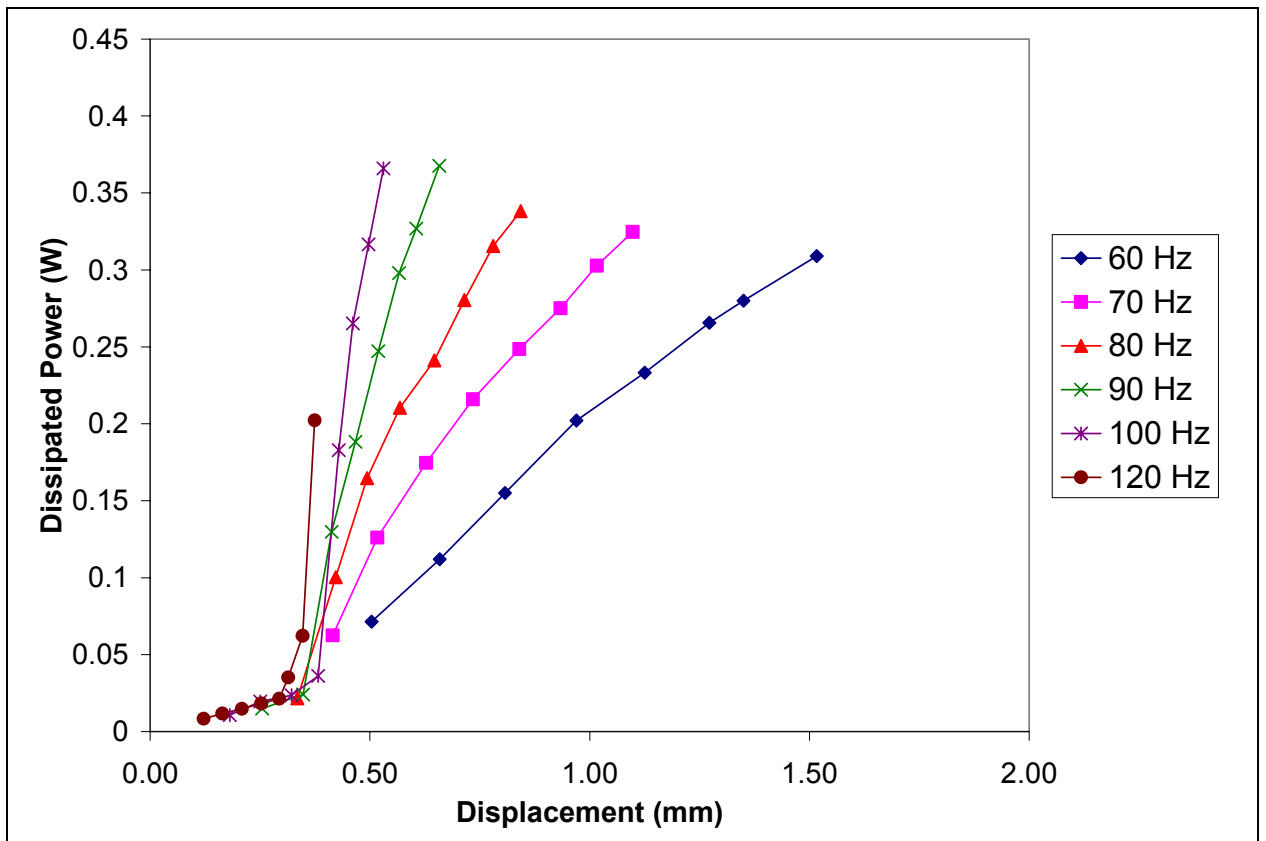


Figure 3.27: Relationship between dissipated power and displacement. 1/16 inch particles. 0.79 mm gap size.

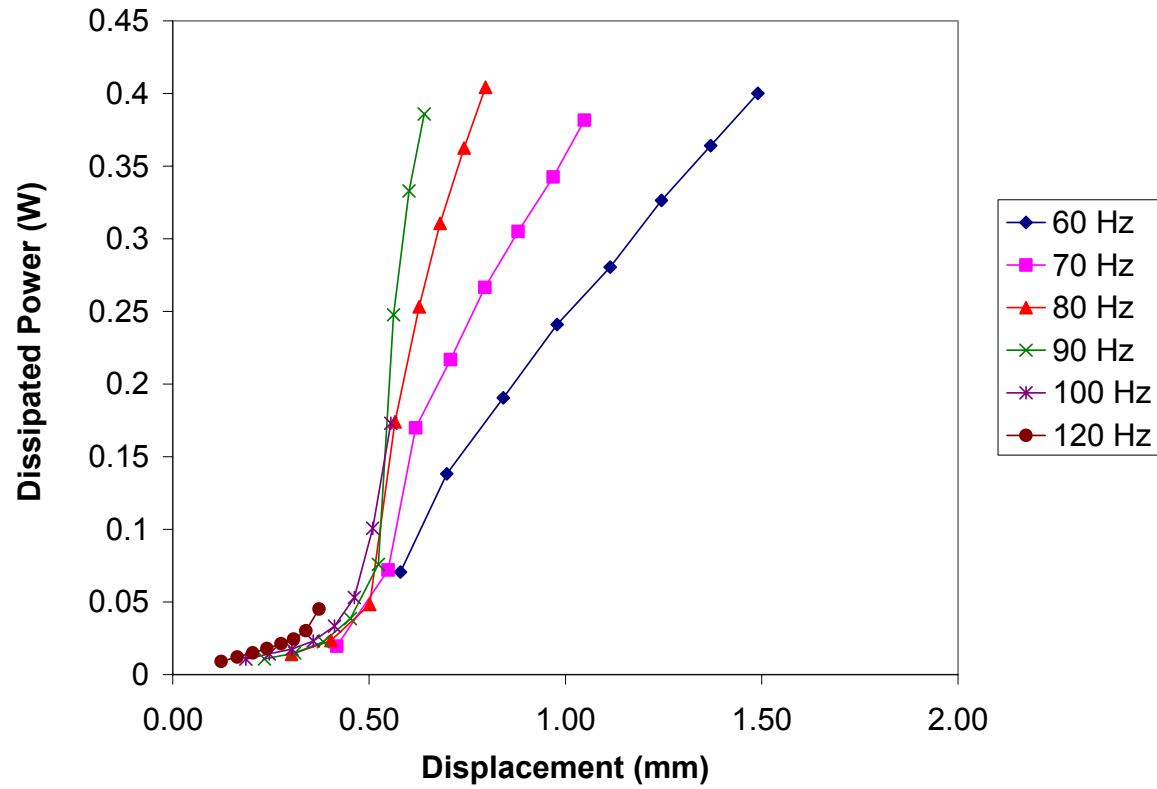


Figure 3.28: Relationship between dissipated power and displacement. 1/16 inch particles. 1.35 mm gap size.

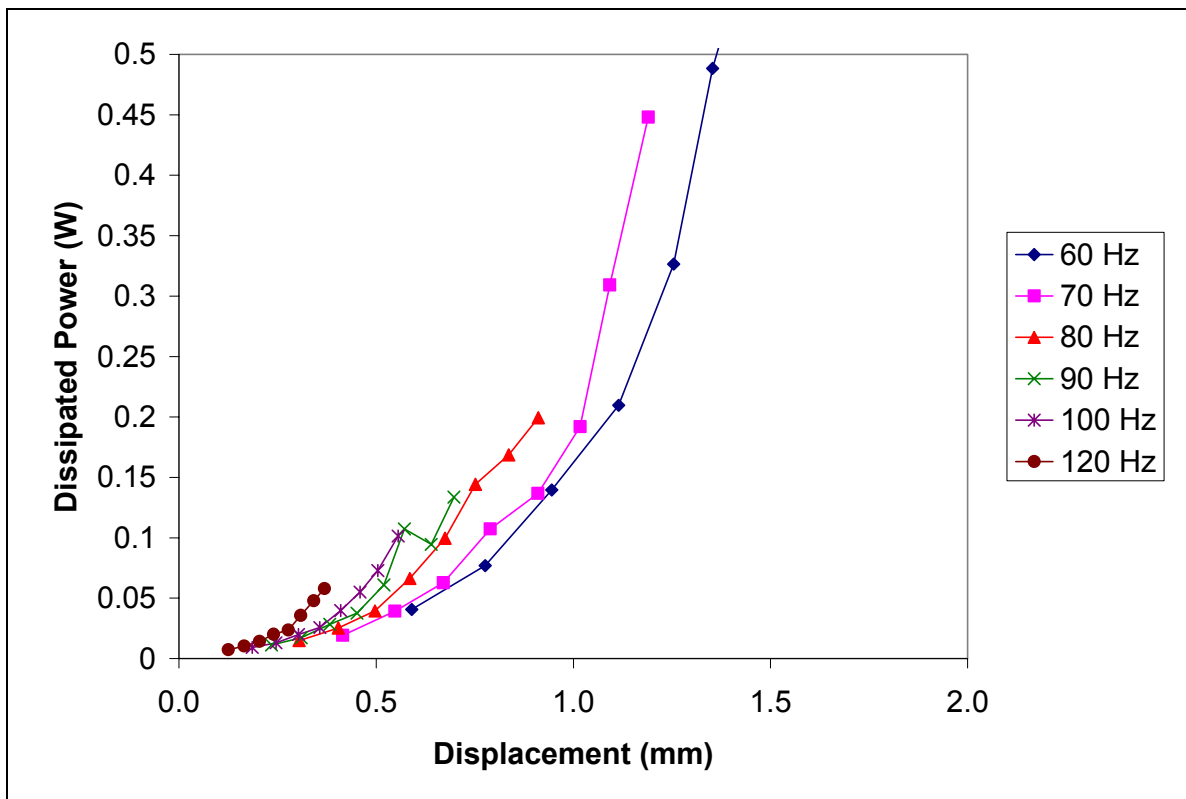


Figure 3.29: Relationship between dissipated power and displacement. 1/8 inch particles. 3.97 mm gap size

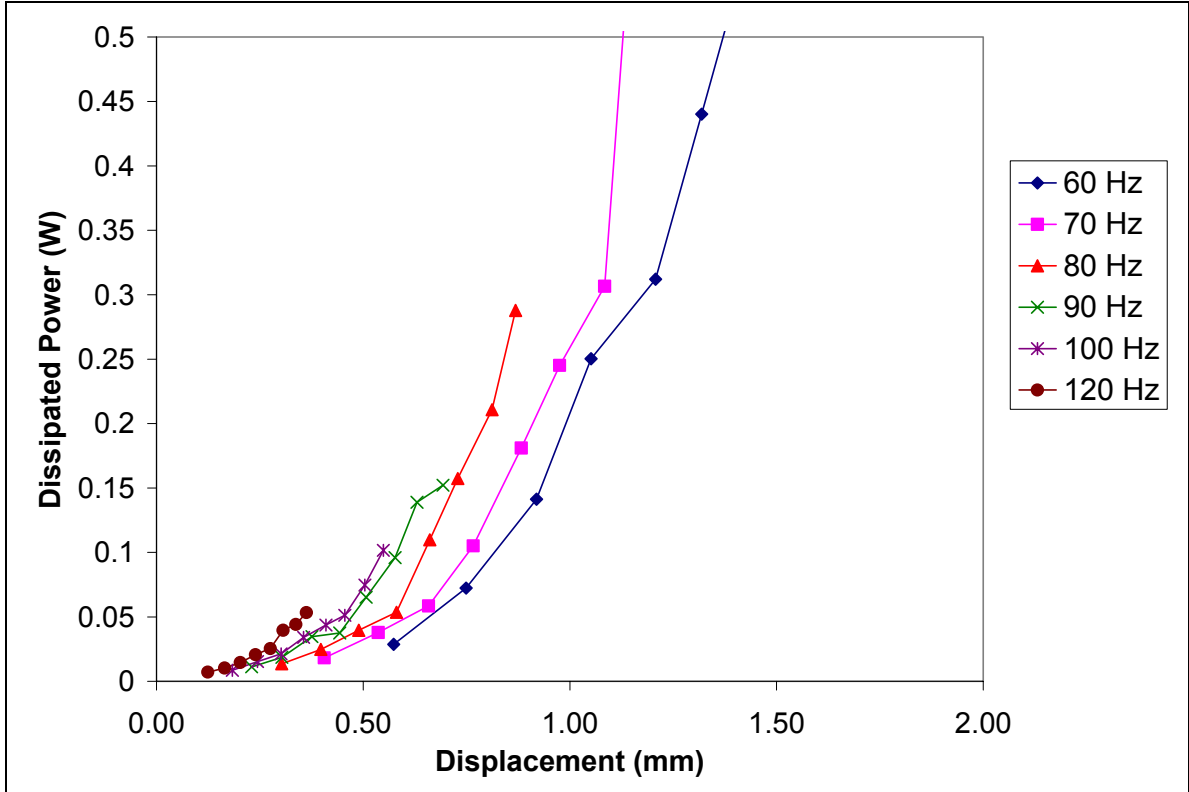


Figure 3.30: Relationship between dissipated power and displacement. 3/16 inch particles. 5.93 mm gap size.

Figure 3.31 shows plots for effective mass with the same parameters as Figure 3.27. The relationship between effective mass and displacement also changes at a certain displacement. Effective mass steadily drops until the transition displacement is reached. After the transition displacement, it increases and eventually approaches a constant value. The effective mass appears to be completely insensitive to changes in frequency. The change in the relationship between effective mass and displacement occurs at the same displacement as the change for dissipated power.

Theoretically, the effective mass would be minimally bound by the static mass of the enclosure without any particles (46.35 grams), and maximally bound by the static

mass of the enclosure with particles (56.85 grams). Figure 3.31 shows that the effective mass at the transition displacement approaching but not quite reaching the lower bound. This corresponds to the case where the particles are spending a large fraction of time out of contact with the enclosure, and therefore contributing very little to the effective mass of the PID. On the other hand, the effective mass of the PID exceeds the upper bound once the displacement exceeds approximately 0.6 millimeters. A possible explanation is that it is possible for the effective mass of the PID to exceed its statically measured mass. This would be a result of an auxiliary mass (the particles) moving out-of-phase with and impacting the primary mass (the enclosure).

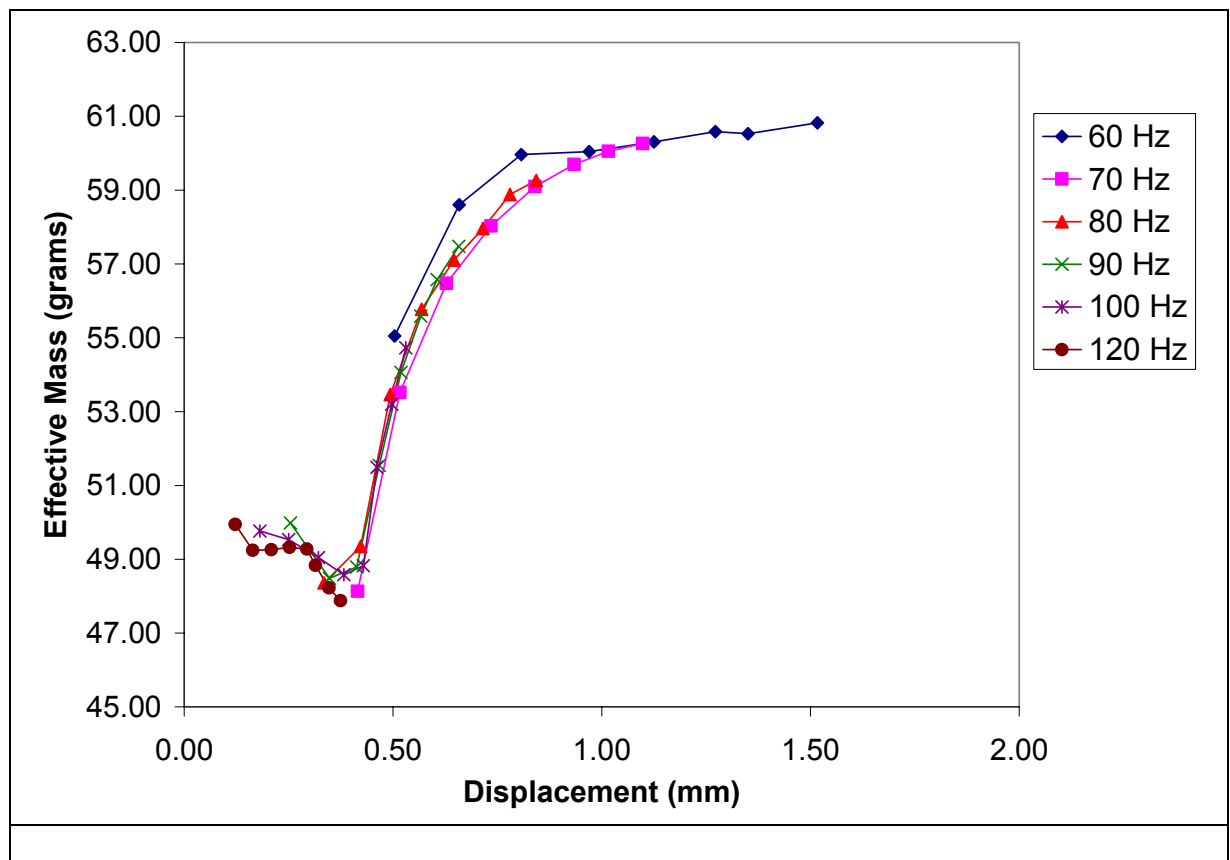


Figure 3.31: Relationship between effective mass and displacement. 1/16 inch particles. 0.79 mm gap size.

The *transition displacement* occurs at the transition from one data relationship to the other. Figure 3.32 illustrates how the transition displacement changes with gap and particle size. The transition displacement generally increases with gap size and decreases with particle size. The lone exception is the plot for the 5/32 inch particle size. This can be explained by the existence of a partial layer (see Figure 3.25). Compensating for the partial layer increases the gap size and moves the data curve to the right, where it follows the general trend.

These trends reveal that the transition displacement likely corresponds to the condition that results in the inception of ceiling impacts by the particle bed. Intuitively it makes sense that a higher displacement would be needed for ceiling impacts if the gap size was increased.

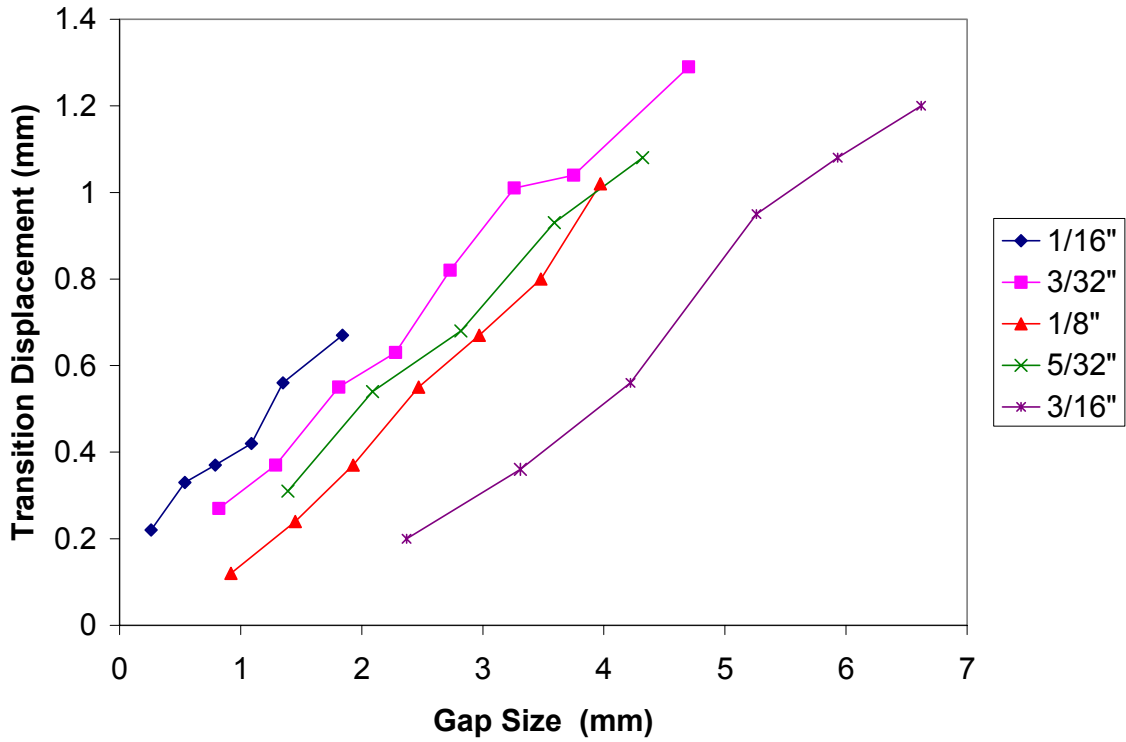


Figure 3.32: Change in transition displacement with gap and particle size.

3.3.5 Effect of Frequency on Dissipated Power and Effective Mass

To study the effect of frequency on dissipated power and effective mass, a neural network was used to perform an interpolation amongst the available data points. Neural networks are named for and inspired by biological nervous systems, and consist of simple elements called *neurons* operating in parallel. A more detailed discussion of neural networks and their use in this dissertation can be found in Appendix C.

The effect of frequency on dissipated power is illustrated for 1/16 inch and 1/8 inch particles in Figure 3.33 and Figure 3.34, respectively. An increase in frequency results in a corresponding increase in dissipated power. The exception to this trend occurs for high gap sizes at low displacements (see Figure 3.33, plot on right side).

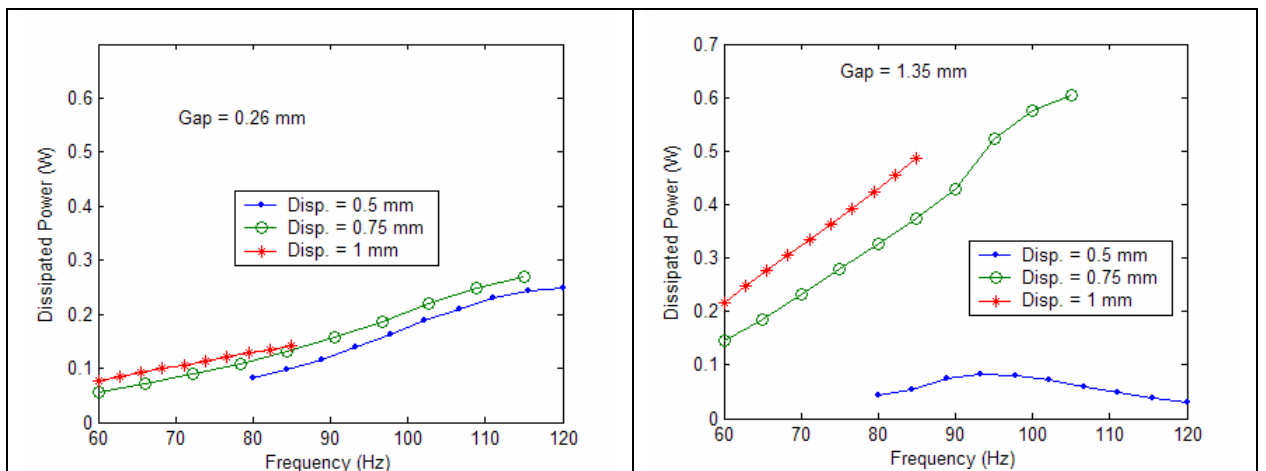


Figure 3.33: Effect of frequency on dissipated power. 1/16 inch particles.

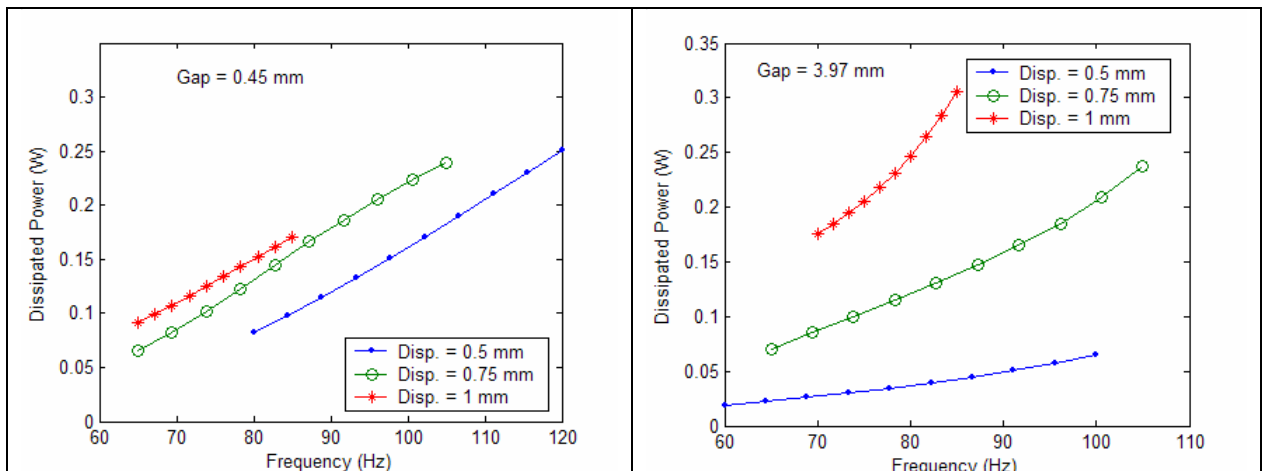


Figure 3.34: Effect of frequency on dissipated power. 1/8 inch particles.

3.4 Summary of Power Measurements

In this chapter, power measurements were introduced as an efficient and accurate method of measuring both the damping and mass contributions of a particle impact damper (PID). The theory was presented for the conversion of dissipated and trapped power to loss factor and effective mass, respectively, and several experiments were conducted to verify the accuracy of these conversions.

Power measurements were taken for PIDs at different frequencies, amplitudes, gap sizes, and particle sizes. These measurements were taken to determine how the properties of the PID change as the excitation conditions and design variables change.

For each PID, an optimum gap size, characterized by a maximum power dissipation, existed. This optimum gap size increased with increasing excitation amplitude and particle size. Overall, the amount of power dissipated increased with amplitude and frequency and was insensitive to particle size. The relationship between dissipated power and displacement changed at a transition displacement, which decreased with increasing particle size and increased with increasing gap size.

The effective mass was found to increase with increasing amplitude and increase with decreasing gap size. Unlike dissipated power, effective mass is sensitive to particle size with larger particles increasing effective mass. A transition displacement, which occurs at the same particle size and gap size as that for dissipated power, changes the relationship between effective mass and displacement. The data trend for displacements less than the transition is characterized by a negative slope. The trend for gap sizes above

the transition is characterized by a positive but steadily decreasing slope, with the effective mass steadily approaching a constant value.

The effective mass was also found to exceed the static mass of the PID at high displacements. A possibility is that having an auxiliary mass that moves out of phase and impacts the primary mass results in an effective mass that can exceed the static mass. This phenomenon will be discussed further in Chapter 5.

The response of particle impact dampers to several design variables has now been established. The purpose of the next chapter will be to use high speed photography to gain insight to explain the data trends that were discovered.

Chapter 4

Slow-Motion Videos of Particle Motion

Two different high speed digital cameras were used to observe particle motion in a cylindrical enclosure for different particle sizes, frequencies, amplitudes, and orientations (horizontal or vertical). The goal of this work was to gain insight into the behavior of the particle impact damper (PID), explain some of the data trends reported in previous chapters, and provide a foundation for modeling efforts.

Two high speed digital cameras were used, a Kodak EktaPro 1000 HRC and a Kodak SR-Ultra Motion Corder Analyzer. Both are capable of frame rates as high as 1000 frames per second. During filming, care was taken to avoid aliasing by sampling above the Nyquist frequency which is double the excitation frequency.

Since this work is in video format, it is difficult to properly display the results here. Still pictures from the video are presented, but readers should refer to the attached compact disk which contains a short Microsoft® PowerPoint presentation highlighting the findings. For convenience, slide numbers are cross-referenced throughout the chapter. The compact disk and PowerPoint presentation have been formatted for PC computers. Alternative formats are available upon request.

4.1 General Motion of Particles

Initially, 200 1/16" spherical brass ball bearings were placed into a cylindrical enclosure with transparent acrylic side walls (see Appendix A). The particle depth was approximately 3.7 mm and the gap size was varied between 0.75 and 1.5 mm.

Slide 5 reveals that the type of motion the particles exhibit depends on the orientation of the enclosure's motion with respect to gravity. Figure 4.1 depicts an enclosure being excited in both the vertical and horizontal directions. Vertical motion is characterized by bulk motion of the particles with little relative motion of individual particles. Horizontal motion, by comparison, shows motion similar to the side-to-side "sloshing" of a liquid wherein particles at the top of the enclosure move more than particles near the bottom. The consequence of this observation is that measurements for PIDs taken in one orientation cannot be extrapolated to another orientation. All previous measurements were done in the vertical orientation, and therefore the data trends observed thus far are limited to the case of vertical motion. Furthermore, all subsequent modeling efforts and observations will be limited to vertical motion.

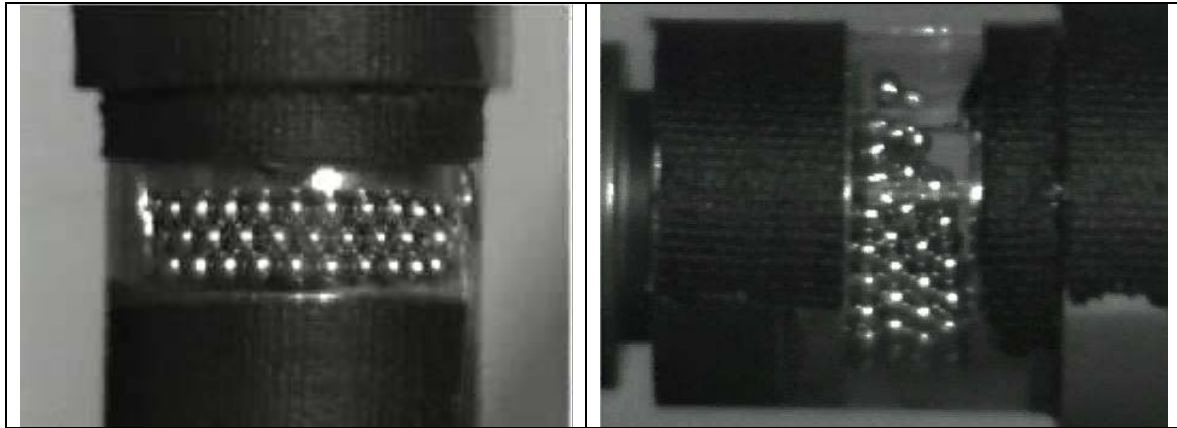


Figure 4.1: Vertical (left) and horizontal (right) motion of PID

Figure 4.1 also shows how the particles exhibit bulk motion and move together when the enclosure is vertically oriented. There is little to no exchange of position between particles. This was true for both sinusoidal and random excitement (see Slide 6). Slide 6 also shows that the impact between the particle bed and the enclosure occurs nearly instantaneously and is very inelastic with a coefficient of restitution near zero.

Close examination of Slide 7 reveals the expansion and contraction of the particle bed when it is in motion. There is an immediate contraction of the particle bed upon impact, followed by an expansion of the bed shortly after impact. This expansion and contraction can be attributed to the passage of wave-like motion through the granular medium. Unpredictable motion of the individual particles can also be seen. This motion causes the particles to impact each other, causing energy dissipation with each impact. These impacts are the dominant dissipation mechanism for the PID.

The behavior of a single ball was compared to the motion of the particle bed (Figure 4.2 and Slide 8). The purpose was to make observations of the impact behavior of a single particle. This would lead to greater understanding of the particle-particle collisions that occurred in a particle bed. The particle shown is a single 3/16" diameter steel ball. The videos show that the motion of a single ball is extremely unpredictable. This can be caused both by any spinning of the ball and by the sensitivity of the impact to very small deviations in the surface of the ball and enclosure. Based on these observations, it is apparent that the motion of a single ball is very different than the motion of a bed of particles. Any single ball model would require the inclusion of surface irregularities and rotary motion, and would therefore be inappropriate for a bed of particles.



Figure 4.2: Single particle in enclosure

4.2 Motion of Particles Relating to Dissipated Power

Slow motion videos were also used to examine the optimum gap. Numerous other researchers [13, 30, 28, 62, 74], as well as work presented earlier in this dissertation, refer to its importance as a major parameter, but there has been no visual evidence linking it to particle motion.

Slide 10 shows 75 1/8" diameter brass ball bearings in an enclosure with different gap sizes. The movies show that the optimum gap occurs when the enclosure and particle bed are moving towards each other just prior to impact, resulting in maximum *relative impact velocity*. This is shown in Figure 4.3, where the dark line indicates the particle bed location. The other lines indicate the top and bottom of the enclosure for sinusoidal

excitation in the vertical orientation. Note how the enclosure and particle bed are moving towards each other at impact.

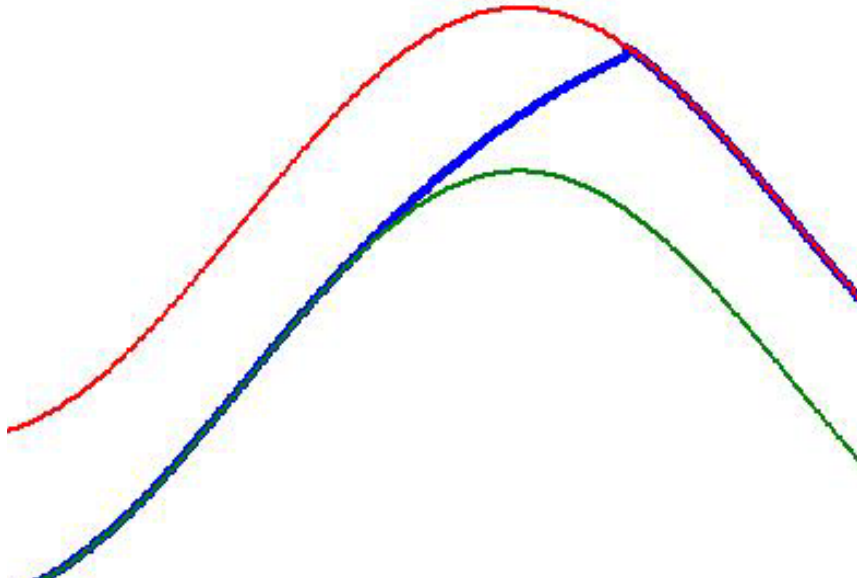


Figure 4.3: Optimal particle bed impact

When the gap is below optimum, the ceiling is impacted not long after floor separation. Therefore, ceiling impact occurs while the enclosure has very little motion. If the gap size becomes extremely small, impact can occur when the enclosure is moving *away* from the particle bed, resulting in very low power dissipation. This is illustrated in Figure 4.4.

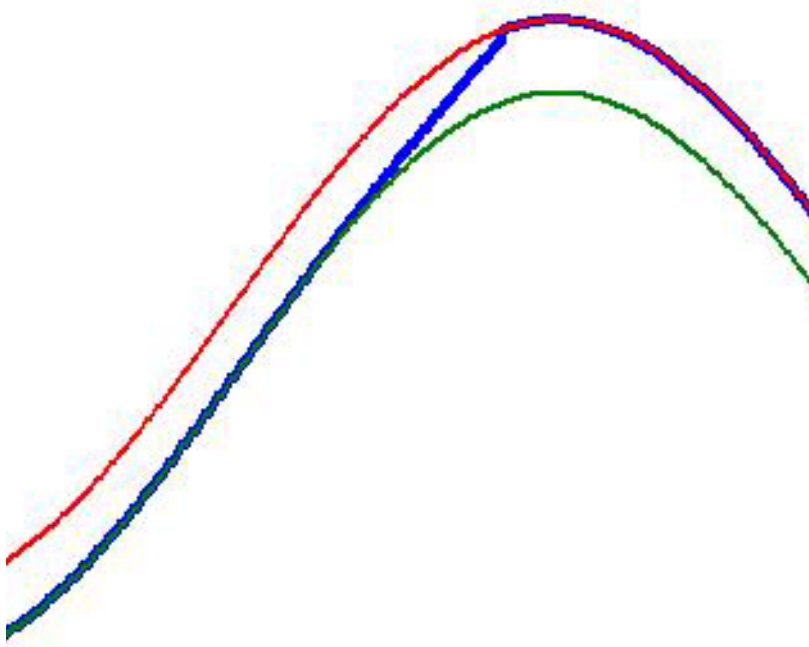


Figure 4.4: Non-optimal particle bed impact. Gap below optimum.

When the gap is above optimum, ceiling impact occurs at a relatively long time after floor separation. By this time, the force of gravity has significantly slowed the upwards velocity of the particle bed. This results in a low relative impact velocity, and can, in cases of gap sizes significantly greater than optimum, result in a ceiling impact that does not involve the entire particle bed, or no ceiling impact at all. This is illustrated in Figure 4.5.

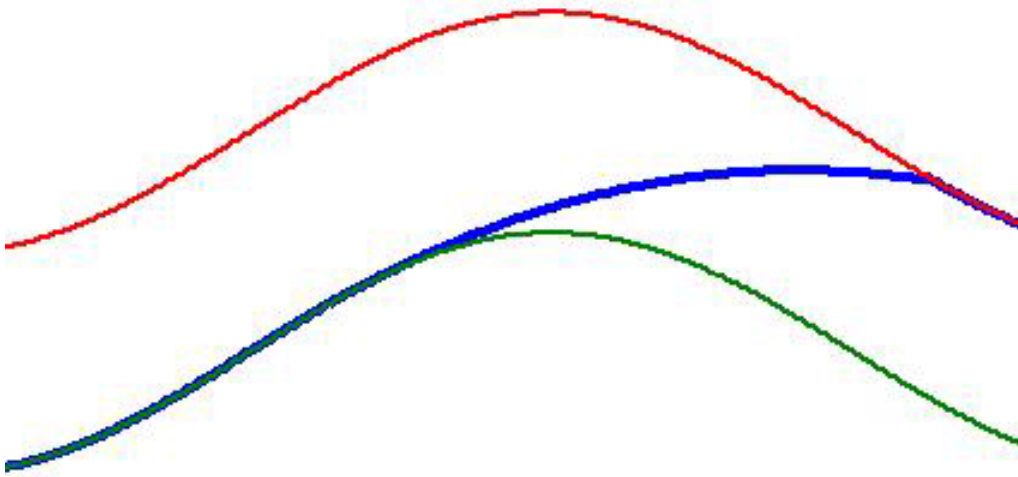


Figure 4.5: Non-optimal particle bed impact. Gap above optimum.

Slide 11 shows 22 3/16" diameter brass ball bearings in an enclosure with different gap sizes. The animations show how larger particles exhibit greater expansion of the particle bed after impact. This effectively decreases the amount of space between the particle bed and enclosure, resulting in ceiling impacts that occur soon after separation, and results in lower power dissipation (see Figure 4.4). The gap size must be increased to achieve maximum dissipation, which is why optimum gap sizes are larger for larger particles.

Slide 11 also shows that increased expansion of the particle bed also increases the range of gap sizes that will still result in a ceiling impact. This is why using larger particles results in a PID that is less sensitive to gap size.

4.3 Motion of Particles Relating to Effective Mass

In Chapter 3, higher amplitudes resulted in a higher effective mass. Slide 13 shows that when the amplitude is increased the particles stay in contact with each side of the enclosure for a longer period of time. This correlates to a higher mass effect. Previous researchers have also made this observation, including Friend and Kinra [23]. Friend and Kinra's model simplifies the particle impact damper by assuming that the particle bed can be treated as a single mass. Since the particle bed exhibits bulk motion, Friend and Kinra's model can be used to examine the effect of amplitude on effective mass. In Figure 4.6 the dark line indicates particle location, while the other lines indicate the top and bottom of the enclosure for sinusoidal excitation in the vertical orientation. It is clear that high amplitudes cause the particle bed to stay in contact with the enclosure for the majority of the period of excitation, which increases the effective mass.

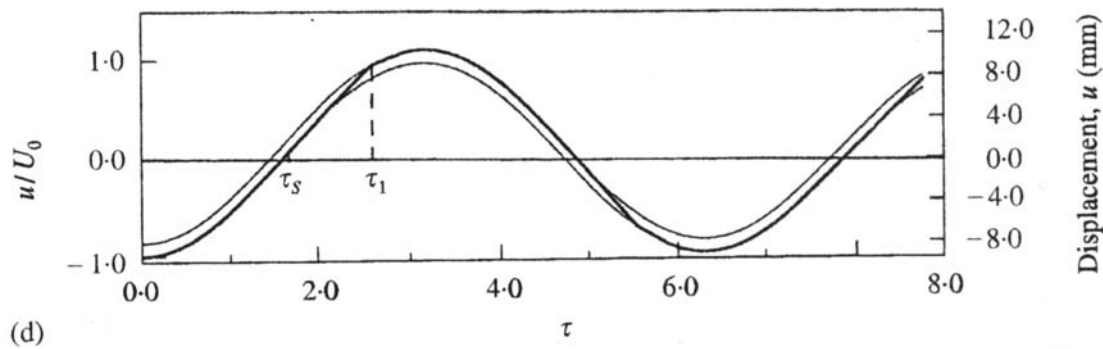


Figure 4.6: Friend and Kinra model – extended contact time for high amplitudes. Source: R.D. Friend and V.K. Kinra, *Journal of Sound and Vibration*, 233(1), pp. 93-118. Particle impact damping. 2000.

4.4 Summary of Observations

High speed digital video cameras were used to gain insight into the behavior of particle impact dampers and explain some data trends that were reported in previous chapters. These insights will also be used to provide a foundation for modeling efforts.

The behavior of the particles was found to heavily depend on the direction of the enclosure motion with respect to gravity. Vertical motion is characterized by bulk motion of the particles with the impact between the particle bed and enclosure being almost completely inelastic. Horizontal motion is characterized by particle motion similar to a liquid “sloshing” back and forth. Since the types of motion are so different, it is not possible to extrapolate the data taken in the vertical orientation to the horizontal.

Closer examination revealed the expansion and contraction of the particle bed due to wave-like motion through the granular medium. This effect causes the particles to move randomly causing impacts between particles and dissipating energy.

The behavior of a single ball was studied in order to gain insight into the individual particle-particle collisions that occur in the particle bed. Unlike the granular bed behavior, it was observed that the motion of the single ball in an enclosure is extremely unpredictable.

An optimum gap size was identified under conditions where the relative velocity of the enclosure and particle bed is maximized. This occurs when the difference in phase between the velocity of the enclosure and particle bed approaches 180 degrees. Higher

amplitudes result in an increased optimum gap size because the particle bed impacts the enclosure ceiling at an earlier time, resulting in a lower relative velocity. Larger particles increase the optimum gap size because of an increase in bed expansion after impact. This also results in an earlier ceiling impact.

The videos show that the effective mass is greater for higher amplitudes because the particle bed stays in contact with the enclosure for a longer period of time. In general, the effective mass is directly proportional to the amount of time the particle bed contacts the enclosure.

Chapter 5

Master Design Curves

Optimal particle impact damping (PID) treatments are difficult to design because of their non-linear behavior and sensitivity to several design variables, not all of which may be independently changed. Therefore, there is a need for master design curve that collapses the existing dissipated power and effective mass data. These design curves explain the fundamental physics of PID behavior and can be easily used by designers to design optimal PID treatments for vibrating structures.

The data is collapsed around unitless parameters that are comprised of the design variables examined. These variables are frequency, gap size, displacement, particle size, and total mass of the particle bed.

An experiment was done to demonstrate that the master design curves can be used to predict the damping and mass effects of a PID on a structure. Lastly, a series of design recommendations are made.

5.1 Collapse of Data Curve for Dissipated Power

The same data in Section 3.3.3 was used to generate the master design curve. This data consists of power measurements taken on an electromagnetic shaker as the frequency, particle size, gap size, and amplitude were changed. A list of the particle

sizes, number of particles, and total mass of each particle bed is shown in Table **5.1**. A second set of data was later taken with a more massive particle bed.

Table 5.1: Particle sizes, quantity, and mass. 10.5 gram particle bed.

Diameter (in.)	Quantity	Mass per BB (grams)	Total Mass (grams)
1/16	600	0.0175	10.50
3/32	174	0.0605	10.53
1/8	75	0.1408	10.56
5/32	37	0.2808	10.39
3/16	22	0.4802	10.56

For purposes of comparison, Figure **5.1** provides an example of what the uncollapsed data looks like. Dissipated power data from different particle sizes, gap sizes, and frequencies is shown. It is clear that it would be difficult for a designer to use those curves to design a particle impact damping treatment or to gain insight into the behavior of the particles. Other plots of the uncollapsed data are presented throughout the text to further establish this point.

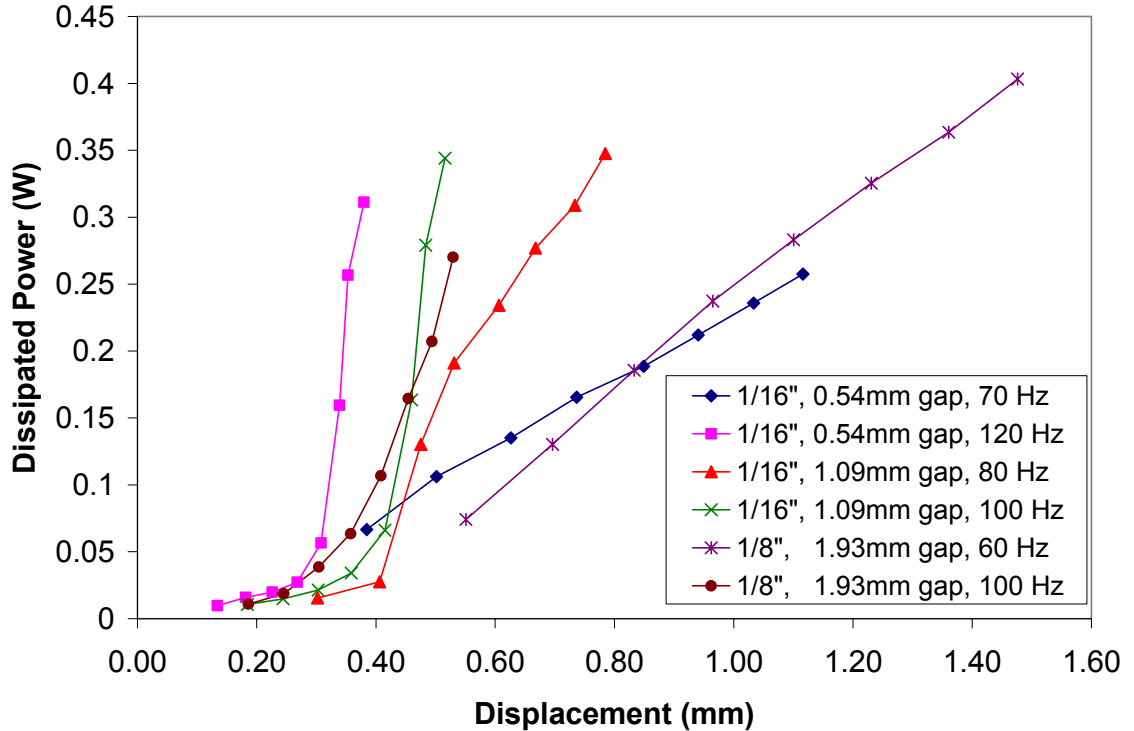


Figure 5.1: Uncollapsed dissipated power vs. displacement

There was a desire to collapse the entire data set onto a single two-dimensional plot that would allow a designer to predict the power that would be dissipated in a PID given the input variables. To this end, the term *dissipated power efficiency (DPE)* [23] was introduced and used as the y-axis term. It is defined as the ratio of the dissipated power divided by the total available power and therefore has the convenient properties of being unitless and having a value between zero and one. Mathematically, it is defined as

$$DPE = \frac{P_{dissipated}}{P_{total}} = \frac{\text{Re}(P)}{\omega m_{bed} |V|^2}, \quad (5.1)$$

where $Re(P)$ is the real component of the power, V is the velocity, ω is the frequency in rad/sec, and m_{bed} is the total mass of the particle bed.

For the x-axis, it was desired to choose a non-dimensional term that could describe the motion of the particles inside the enclosure. It is known that the power dissipation changes dramatically once the particles begin to impact the ceiling. This condition is controlled by the amplitude of the enclosure motion and the gap size. Therefore, *displacement/gap* was chosen as the x-axis.

5.1.1 Collapse of Dissipated Power Efficiency With Respect to Frequency

The collapse of the data curves was tested one design variable at a time. The collapse with respect to frequency was tested first. Figure 5.2 shows what the dissipated power data looks like before it is collapsed for 1/16 inch particles. Figures 5.3, 5.4, and 5.5 show how the data collapses with respect to frequency for various particle and gap sizes. The plots show good collapse for all cases. The data for large particles (3/16 inch) is noisier than the data for small particles (1/16, 3/32 inch), which is expected due to the significantly higher impact forces involved with a fewer number of more massive particles.

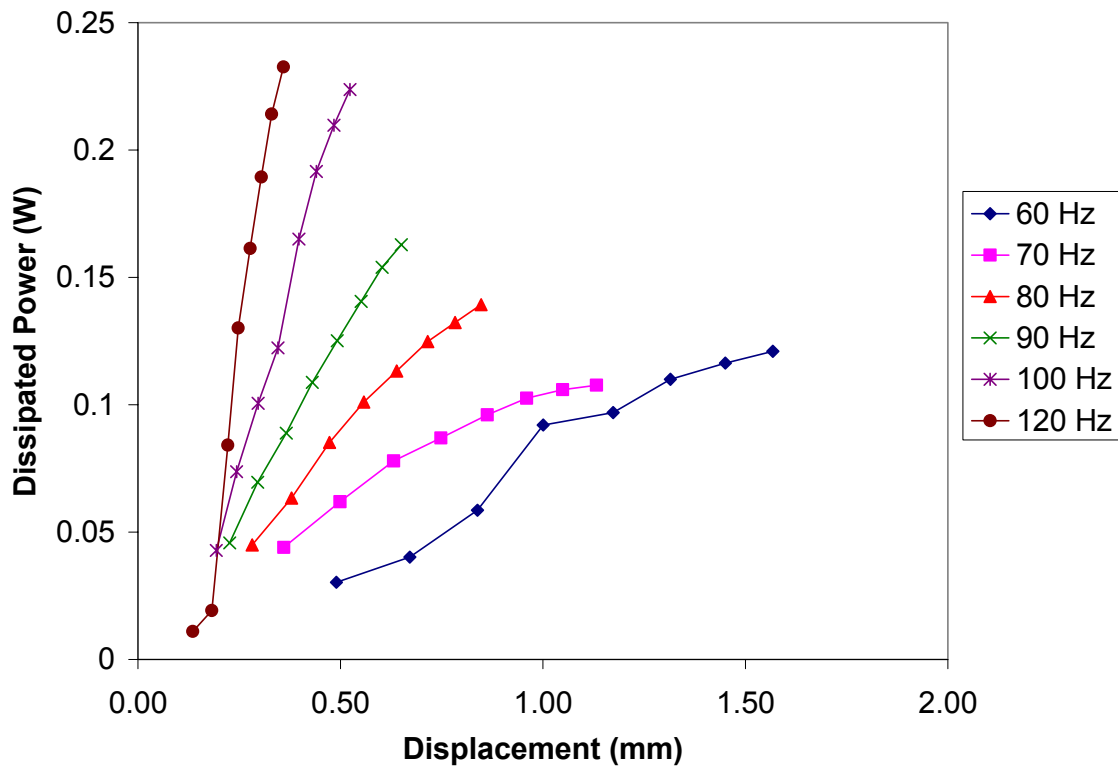


Figure 5.2: Uncollapsed power data. 600 1/16 inch particles. Gap = 0.79 mm

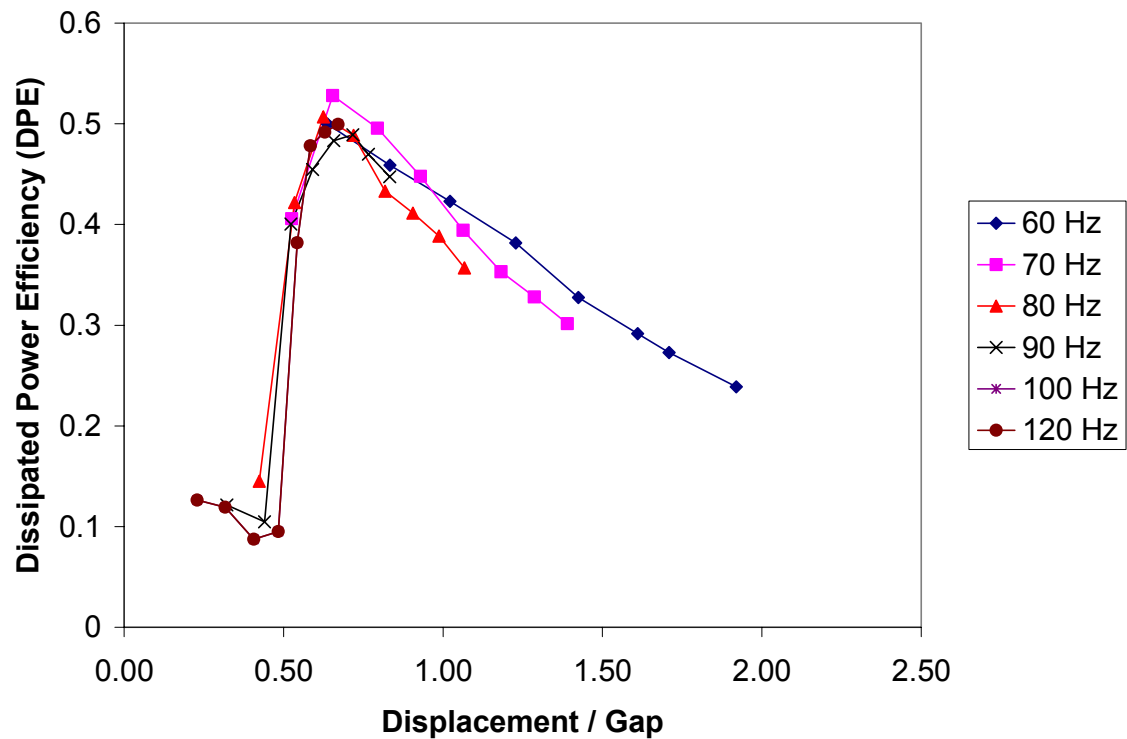


Figure 5.3: DPE collapse on frequency. 600 1/16 inch particles. Gap = 0.79 mm

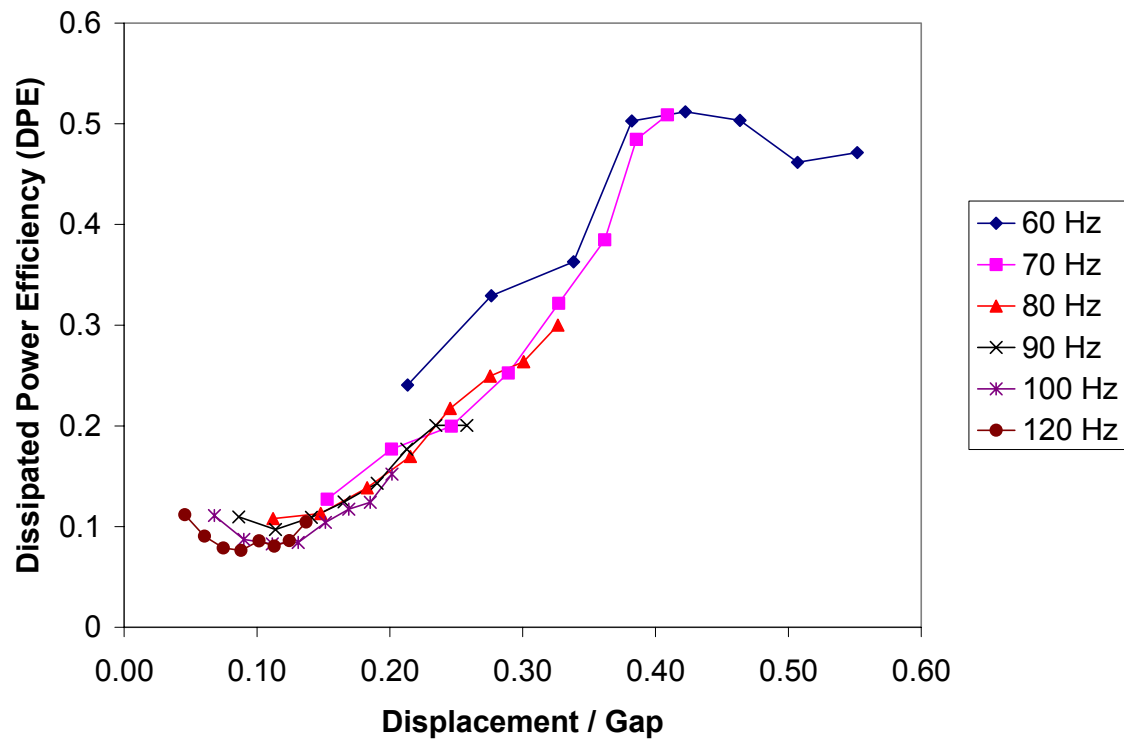


Figure 5.4: DPE collapse on frequency. 174 3/32 inch particles. Gap = 2.73 mm

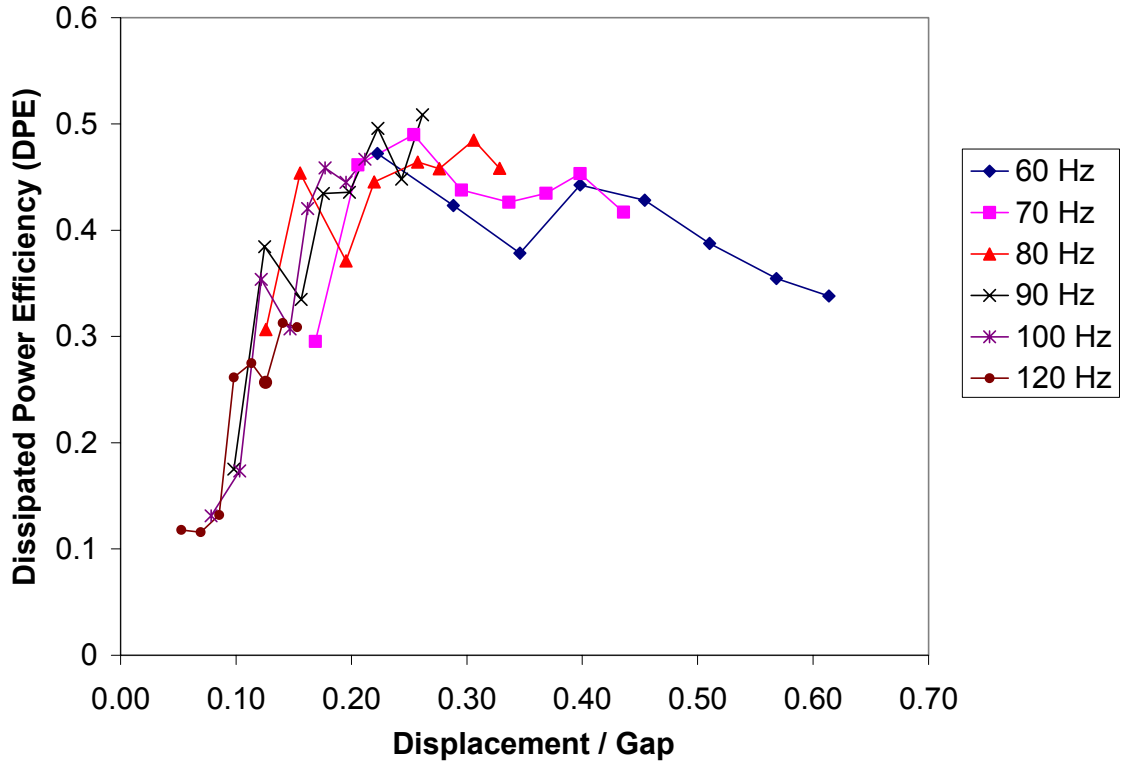


Figure 5.5: DPE collapse on frequency. 22 3/16 inch particles. Gap = 2.37 mm

5.1.2 Collapse of Power Dissipation Efficiency With Respect to Gap Size

Next, the collapse with respect to gap size was tested for all five particle sizes.

Figure 5.6 shows the dissipated power data for 1/8 inch particles at different gap sizes.

Re-plotting the data using *DPE* vs. *Displacement/Gap* gives Figures 5.7 - 5.11, which show how the data collapses with respect to gap size. For each of these plots, data for all frequencies is included since collapse with respect to frequency has already been shown.

Collapse on gap size is generally good, with small gap sizes being outliers for the majority (3/32, 5/32, 3/16 inch) of cases. For these cases, the small gap sizes do not

achieve the peak DPE of larger gap sizes. This is an important design consideration, since it illustrates the inability of the PID to achieve maximum dissipation *at any displacement* once the gap size becomes too small. This seems to occur when the ratio of gap size divided by particle size falls in the range of 0.15 – 0.30.

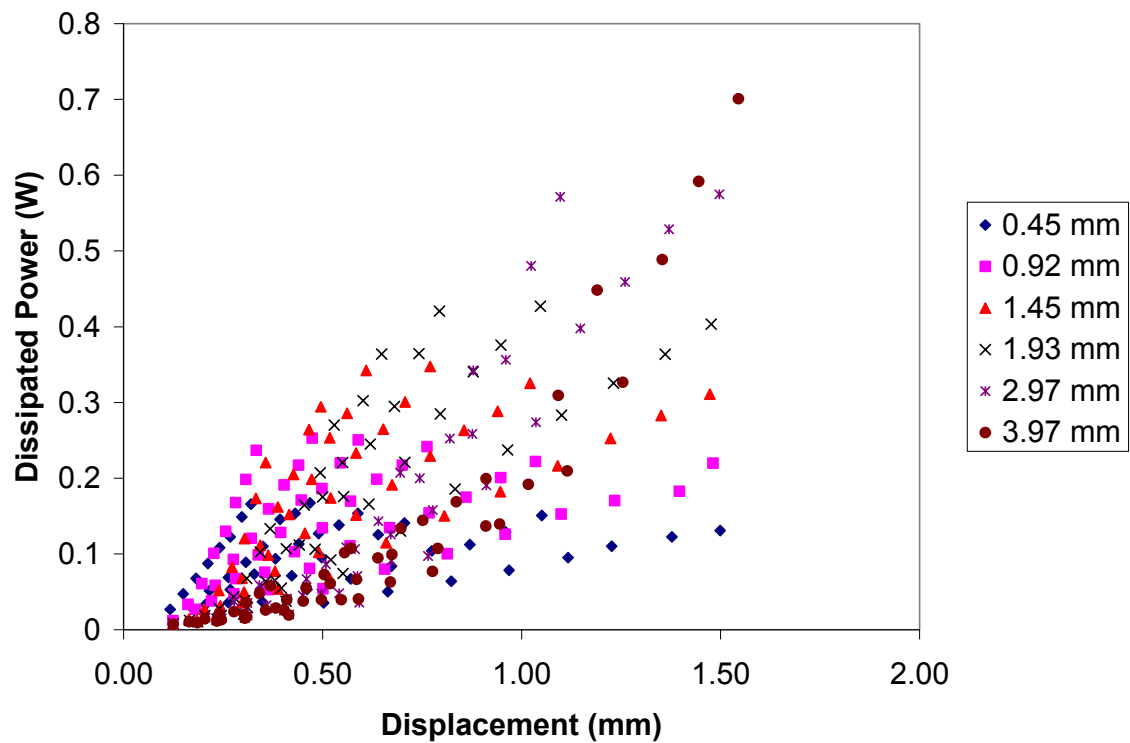


Figure 5.6: Uncollapsed dissipated power data. 1/8 inch particles.

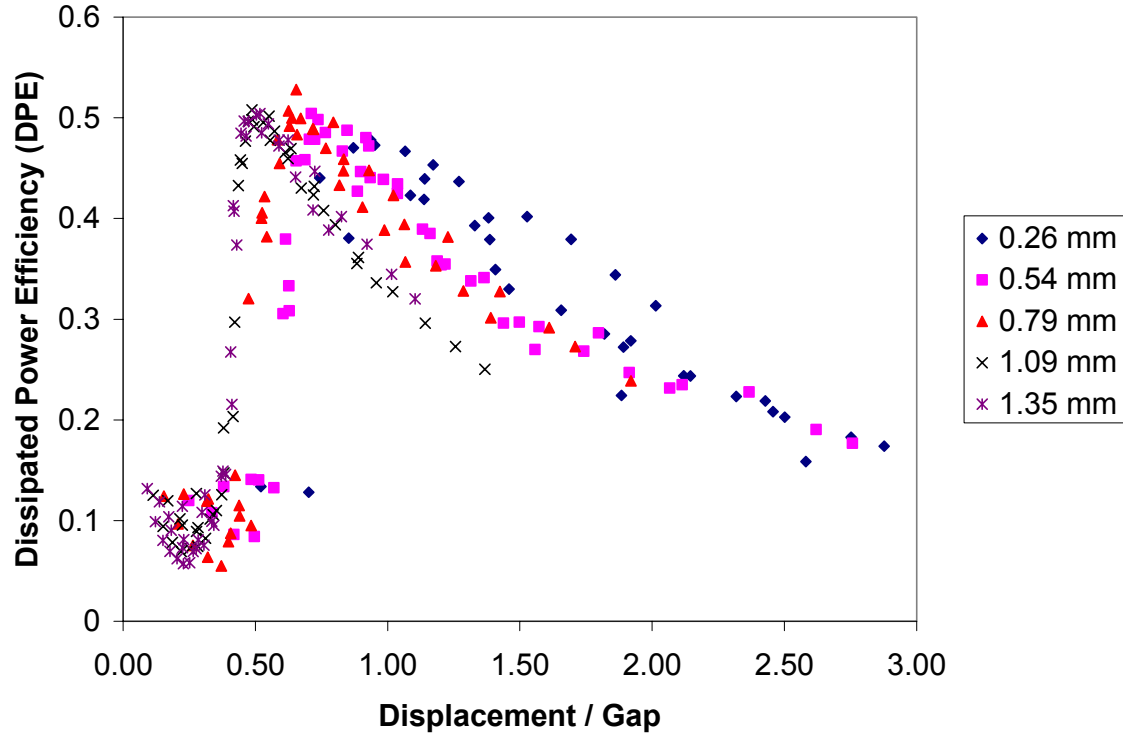


Figure 5.7: DPE collapse on gap size. 600 1/16 inch particles

The data for 1/16 inch particles does not collapse as well as the larger particles, but still captures the basic trend of the data very well. This will be explored in greater detail in a later section.

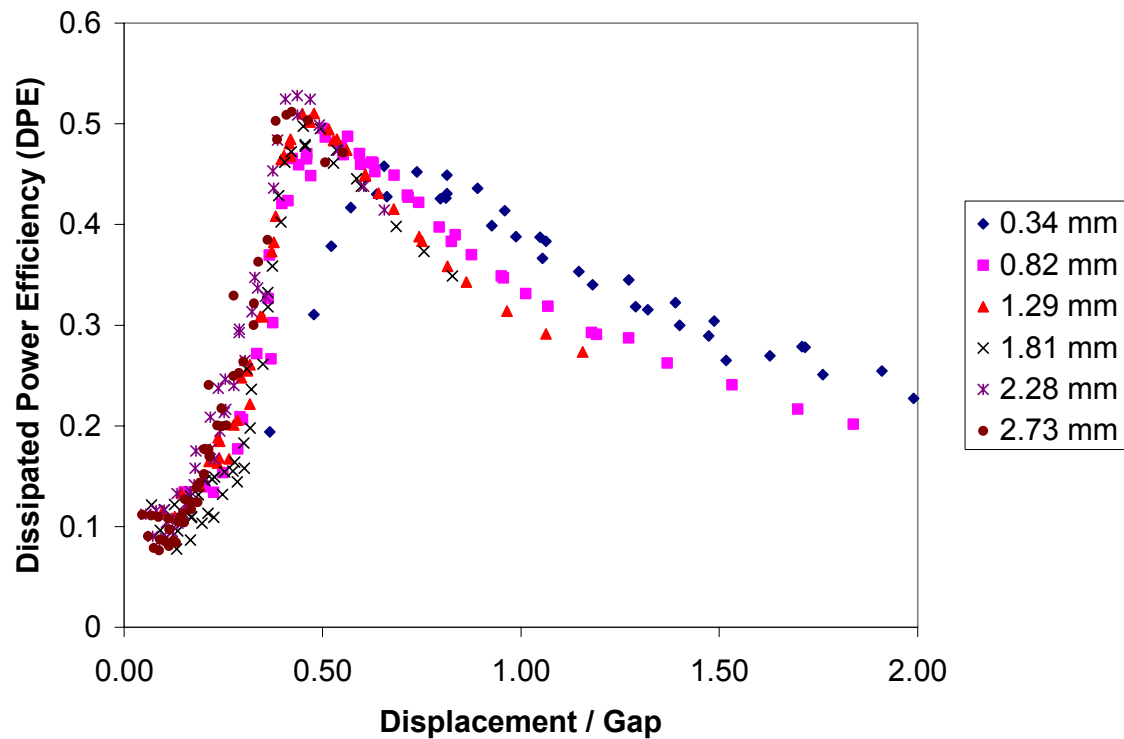


Figure 5.8: DPE collapse on gap size. 174 3/32 inch particles

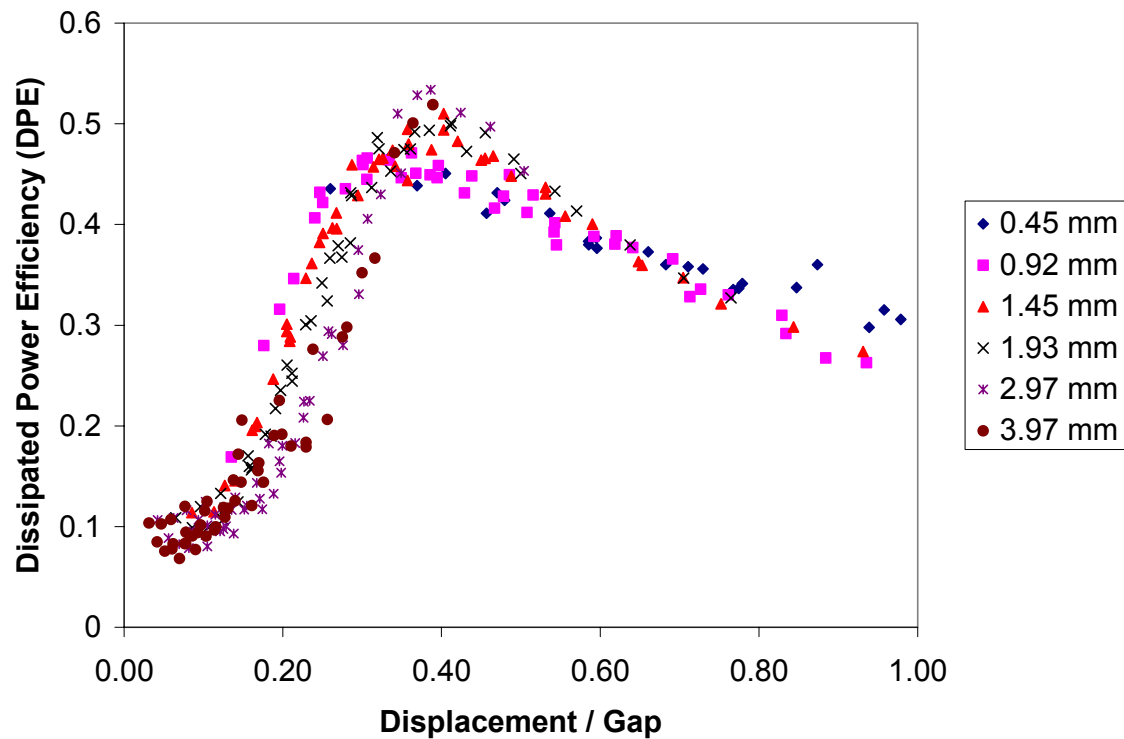


Figure 5.9: DPE collapse on gap size. 75 1/8 inch particles

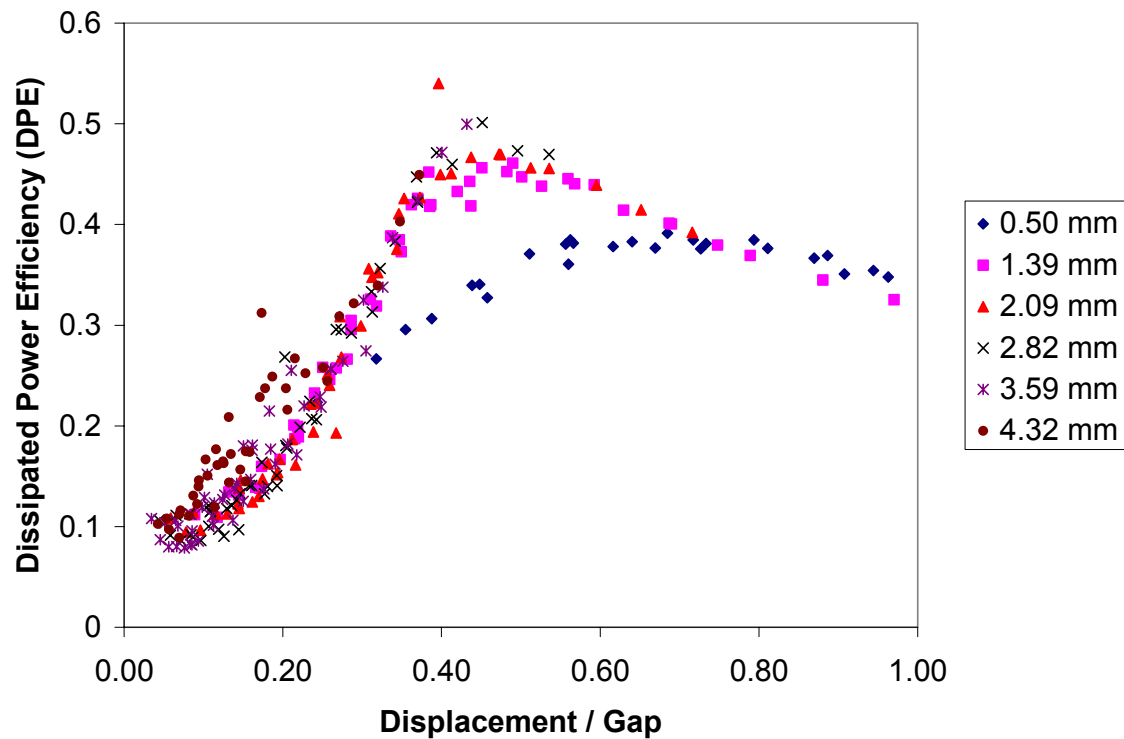


Figure 5.10: DPE collapse on gap size. 37 5/32 inch particles

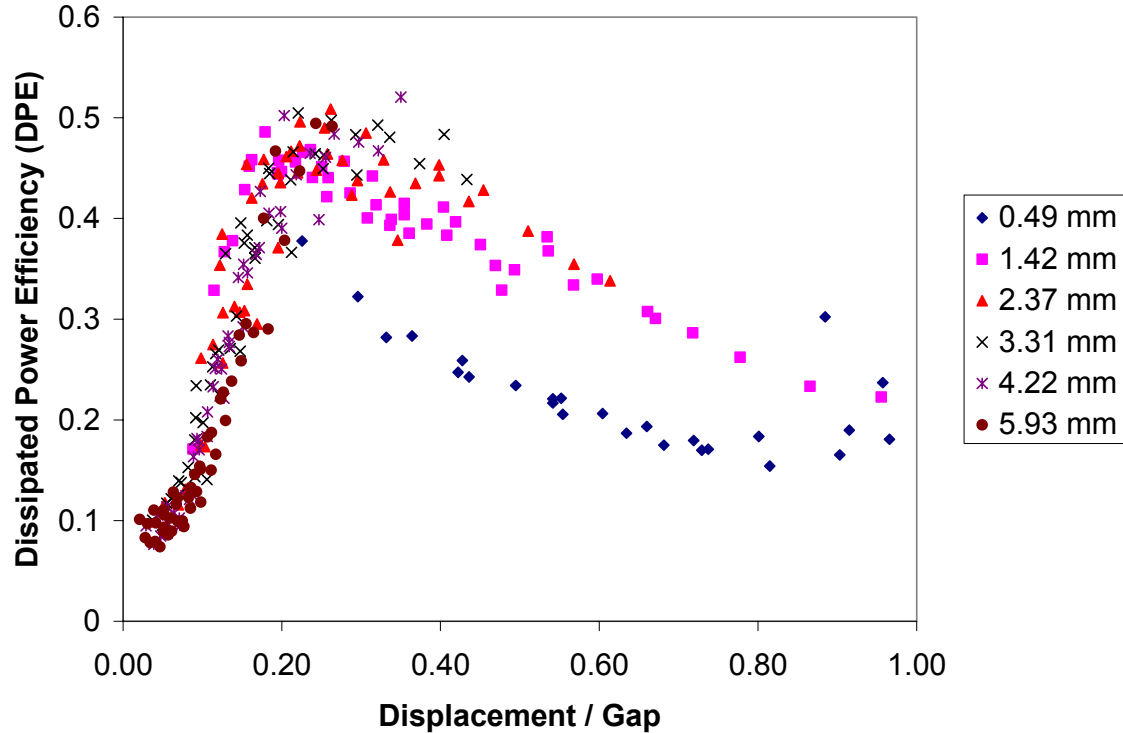


Figure 5.11: DPE collapse on gap size. 22 3/16 inch particles

5.1.3 Collapse of Dissipated Power Efficiency With Respect to Particle Size

The uncollapsed dissipated power data for all particle sizes is shown in Figure 5.12. It is clear that it would be extremely difficult for a designer to make use of the data when it is represented in this manner. The collapse of data with respect to particle size is shown in Figure 5.13. Initial inspection shows that the data does not collapse very well, but the removal of the smallest gap size for each particle size results in a better collapse (Figure 5.14). The collapse is still not complete, with peak values of

DPE for smaller gap sizes generally occurring at larger values of displacement/gap compared to larger gap sizes.

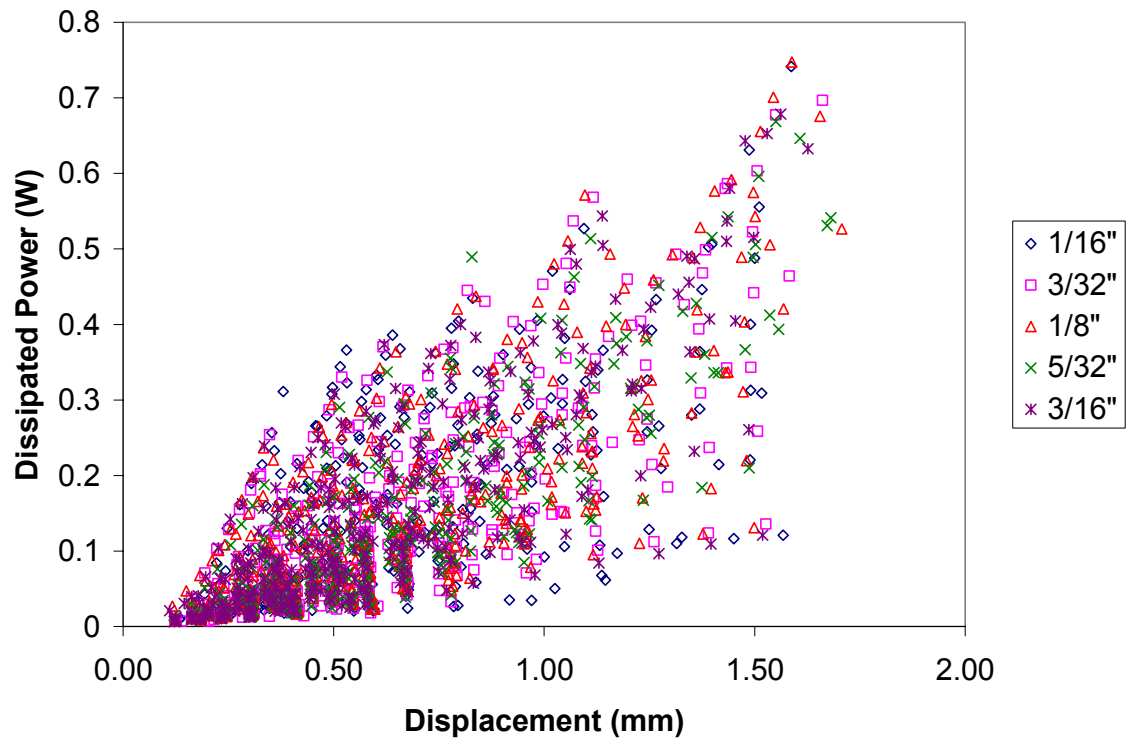


Figure 5.12: Uncollapsed dissipated power data for different particle sizes

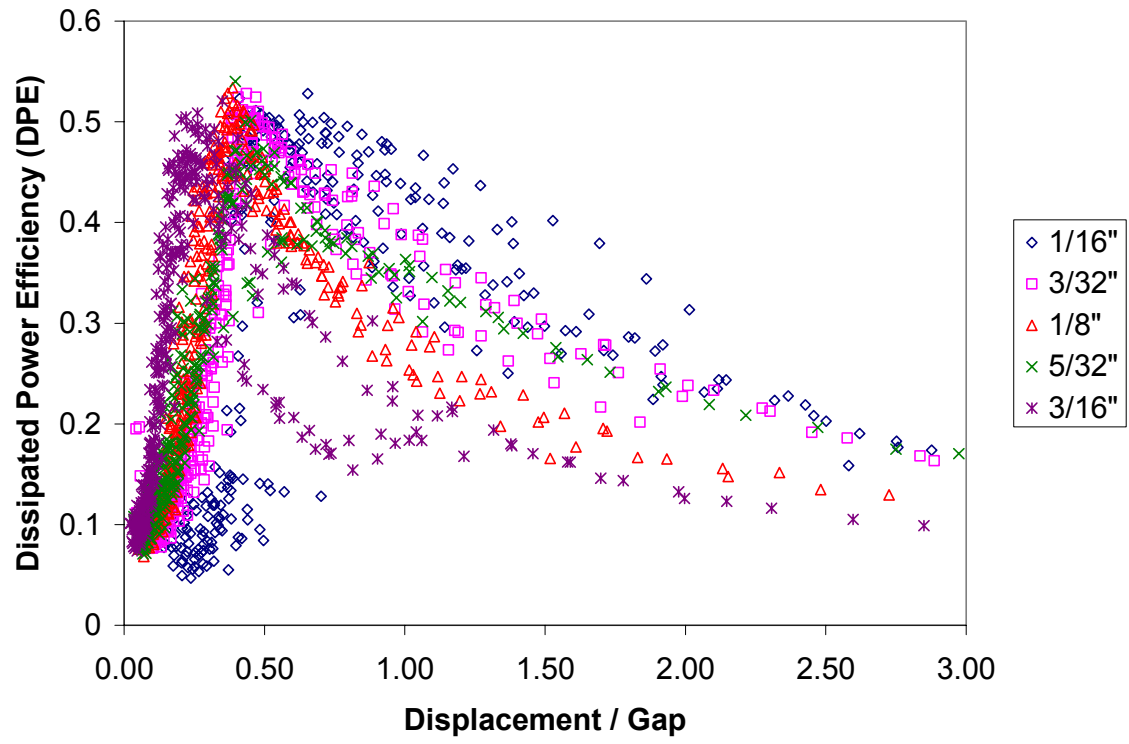


Figure 5.13: DPE collapse on particle size. 10.5 grams total particle mass

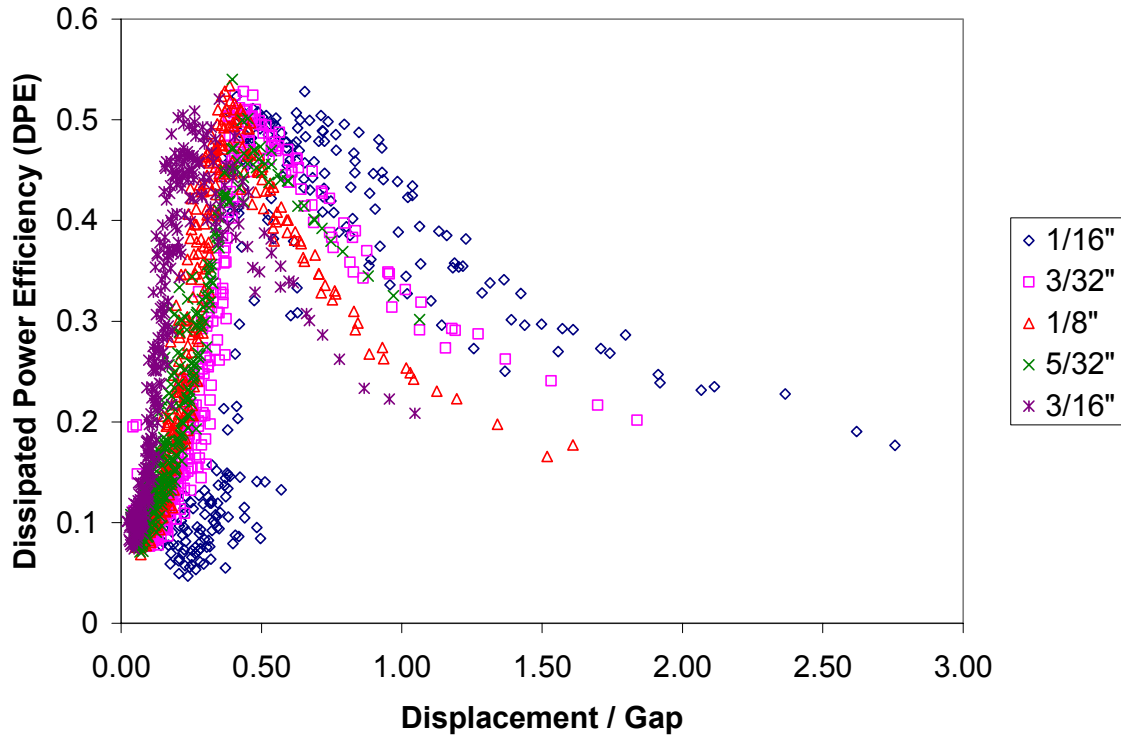


Figure 5.14: DPE collapse on particle size with smallest gap sizes removed. 10.5 grams total particle mass

In order to collapse the data fully, an additional variable needs to be introduced to the x-axis which takes the particle motion following impact of the particle bed with the enclosure into account. Observation of the slow motion videos in Chapter 4 showed that the larger particles had more expansion of the particle bed immediately after impact. This can result in a lower effective gap size. It can also be observed that as long as the total particle mass and container dimensions are kept constant, larger particles had a fewer number of particle layers. Based on these observations, an estimation of the number of layers for each particle size was performed (Table 5.2) and included in the denominator. The estimation was geometrically based, and was the total number of

particles divided by the approximate number of particles that would form a single layer when placed inside the enclosure.

Table 5.2: Number of layers for 10.5 gram particle bed

Particle size (inches)	Number of particles	Est. number of layers
1/16	600	7.0
3/32	232	5.4
1/8	75	4.5
5/32	37	4.0
3/16	22	3.1

The collapse with the number of layers included is presented in Figure 5.15. Once again, the smallest gap size for each particle size has been removed. The collapse can be considered quite good.

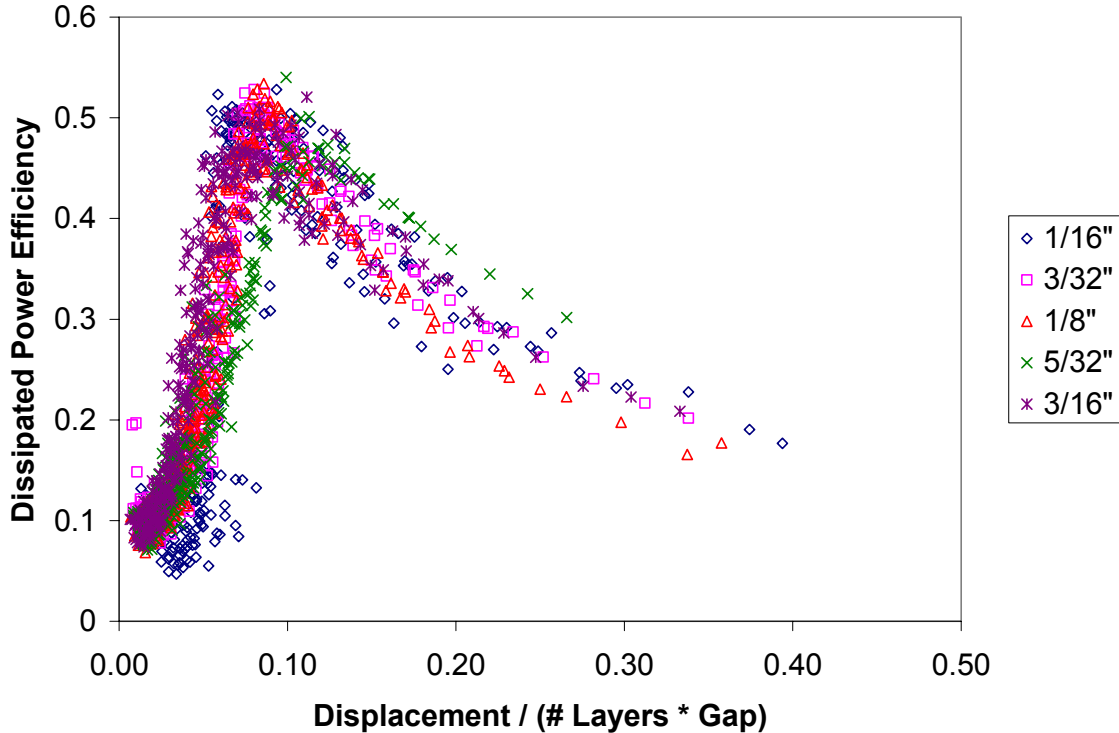


Figure 5.15: DPE collapse on particle size with smallest gap sizes removed and number of layers included. 10.5 grams total particle mass.

5.1.4 Collapse of Dissipated Power Efficiency With Respect to Particle Mass

A second, less complete set of data was taken for a more massive particle bed of approximately 14 grams, compared to the 10.5 grams used previously. A list of the particle sizes, quantity, and mass are given in Table 5.3. The number of layers was estimated in the same manner as before and the number of layers for the 14 gram particle bed is listed in Table 5.4.

Table 5.3: Particle sizes, quantity, and mass. 14 gram particle bed.

Diameter (in.)	Quantity	Mass per BB (grams)	Total Mass (grams)
1/16	800	0.0175	14.00
3/32	232	0.0605	14.04
1/8	100	0.1408	14.08

Table 5.4: Number of layers for 14 gram particle bed

Particle size (inches)	Number of particles	Est. number of layers
1/16	800	10.0
3/32	232	7.3
1/8	100	6.0

Plots containing both the 10.5 gram and 14 gram particle beds are shown in Figures 5.16 - 5.18. These plots include data taken over the entire range of frequencies and gap sizes for the 1/16, 3/32 and 1/8 inch particle sizes. All the plots show that the collapse with respect to total particle mass is successful. The location and magnitude of the peak DPE is the same for both particle bed masses, and the data points are generally in the same location. Figure 5.16 shows the fairly large spread of data for the 1/16 inch case. This occurs because of the difficulty to get this particular particle size to collapse with respect to gap size (Figure 5.7).

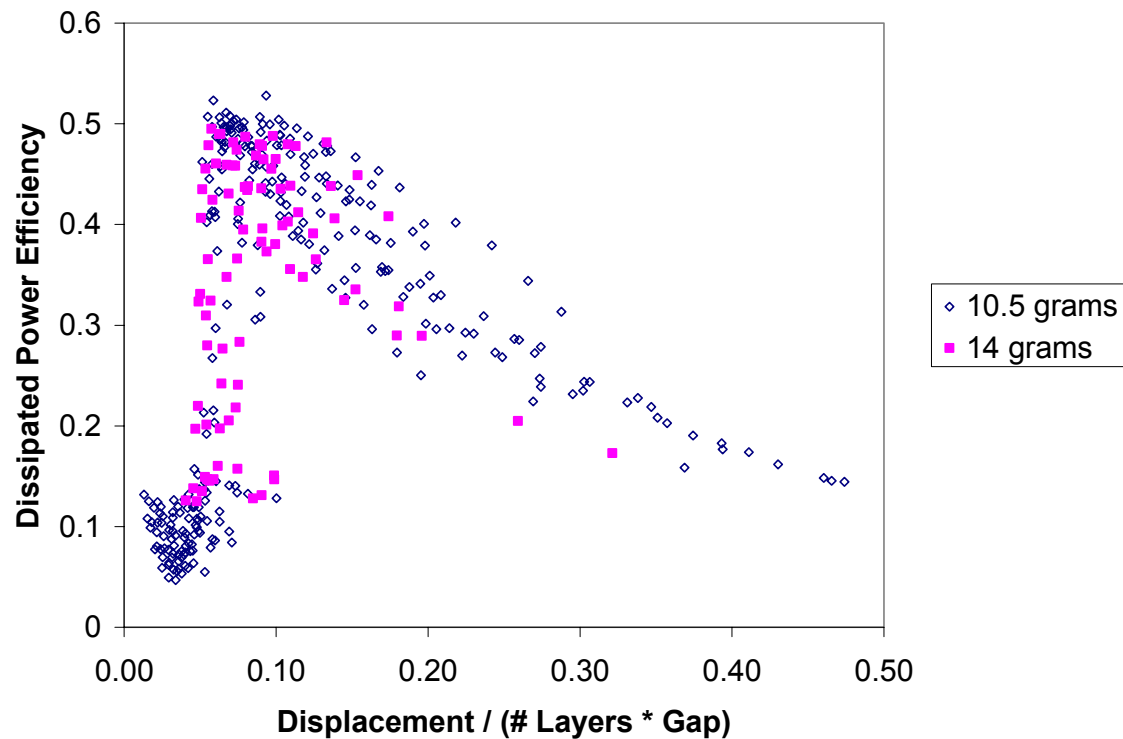


Figure 5.16: DPE collapse on total particle mass. 1/16 inch particles.

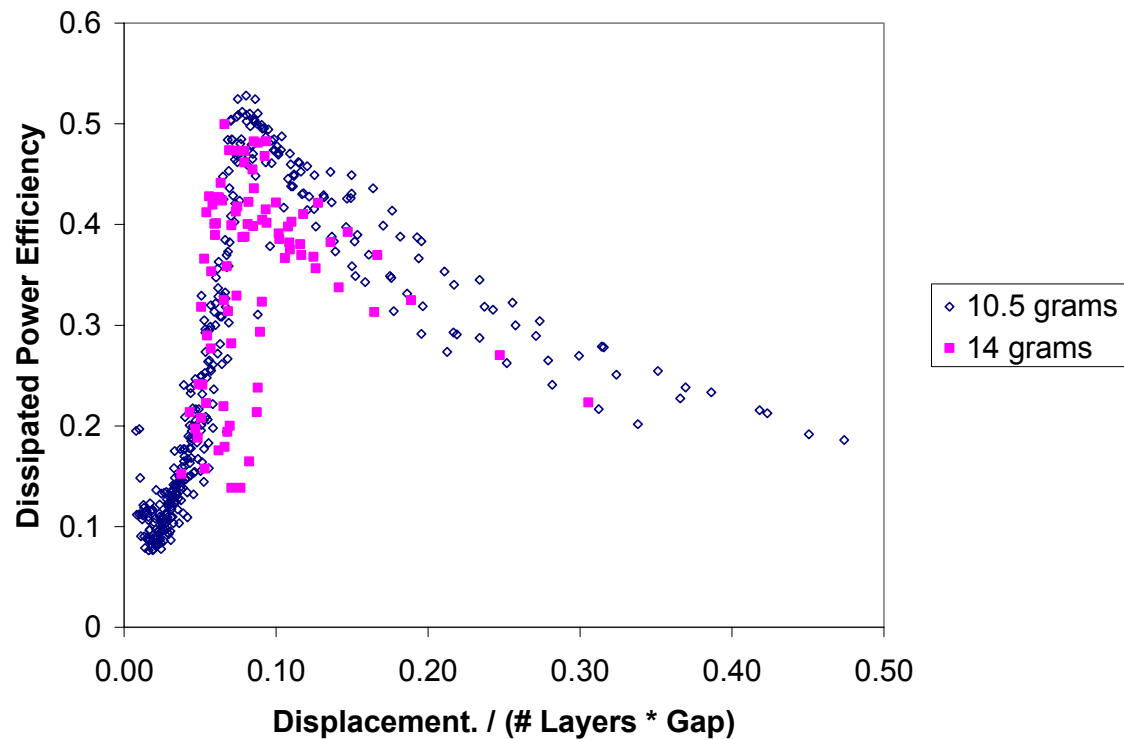


Figure 5.17: DPE collapse on total particle mass. 3/32 inch particles.

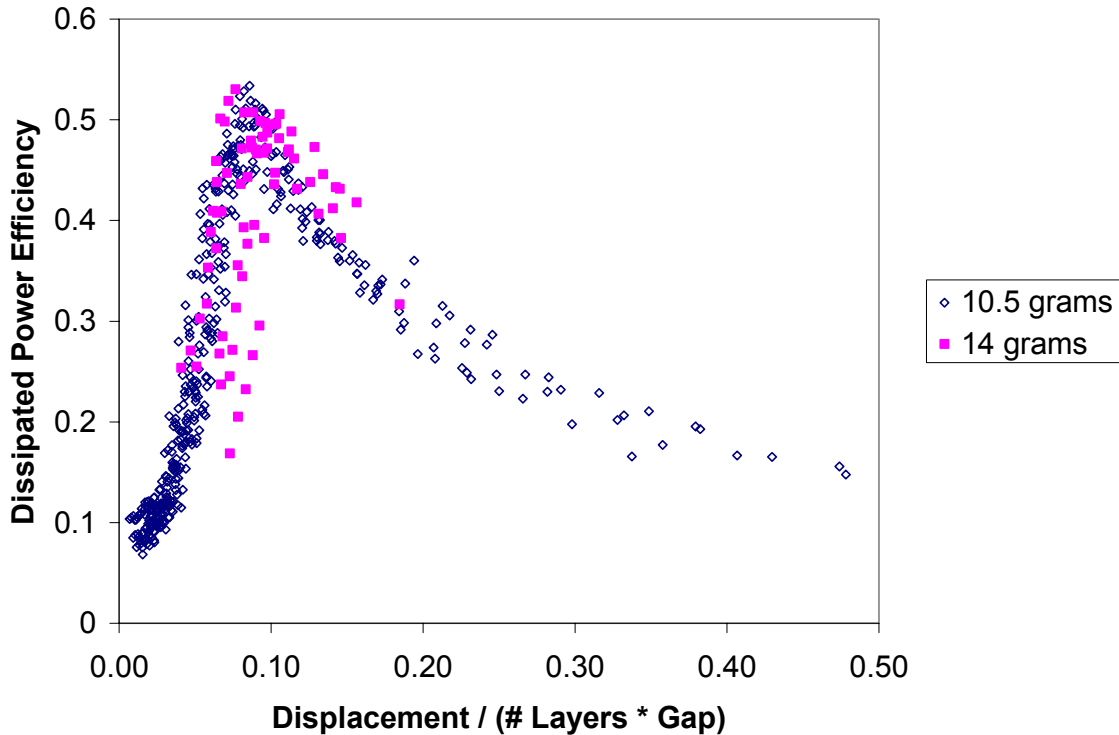


Figure 5.18: DPE collapse on total particle mass. 1/8 inch particles.

5.1.5 Curve Fit of Dissipated Power Efficiency Master Curve

Now that the master design curve for dissipated power has been collapsed with respect to all design parameters, trendlines are fitted to the data to provide designers with a mathematical relationship between the dissipated power efficiency of the PID and its design parameters. Several different types of equations were used for the curve fit, and the ones that qualitatively fit best were chosen. The curve fit emphasized the 1/16, 3/32, and 1/8 inch data sets because they had the fewest number of outliers. Figure 5.19 shows all of the dissipated power data and the curve fits that were applied.

There are two sets of data that do not fit the curve fit very well. The first outlier corresponds to 5/32 inch particles and has a DPE that is consistently higher than the trendline. This occurs because the 5/32 inch particle bed has a partial layer (see Figure 3.25) which results in an artificially low measurement of gap size. Correcting the gap size to its “true” higher value would shift the data set to the left, allowing it to better fit the trendline. The second outlier corresponds to 3/16 inch particles at very small gap size. For cases of large particles with small gap sizes, it is possible that not all of the particles in the particle bed move. This means that the mass term in the denominator of the DPE term is too high. Replacing the total mass of the particle bed with the *mass of the moving particles in the bed* will raise the DPE of the second outlier, allowing it to better fit the trendline.

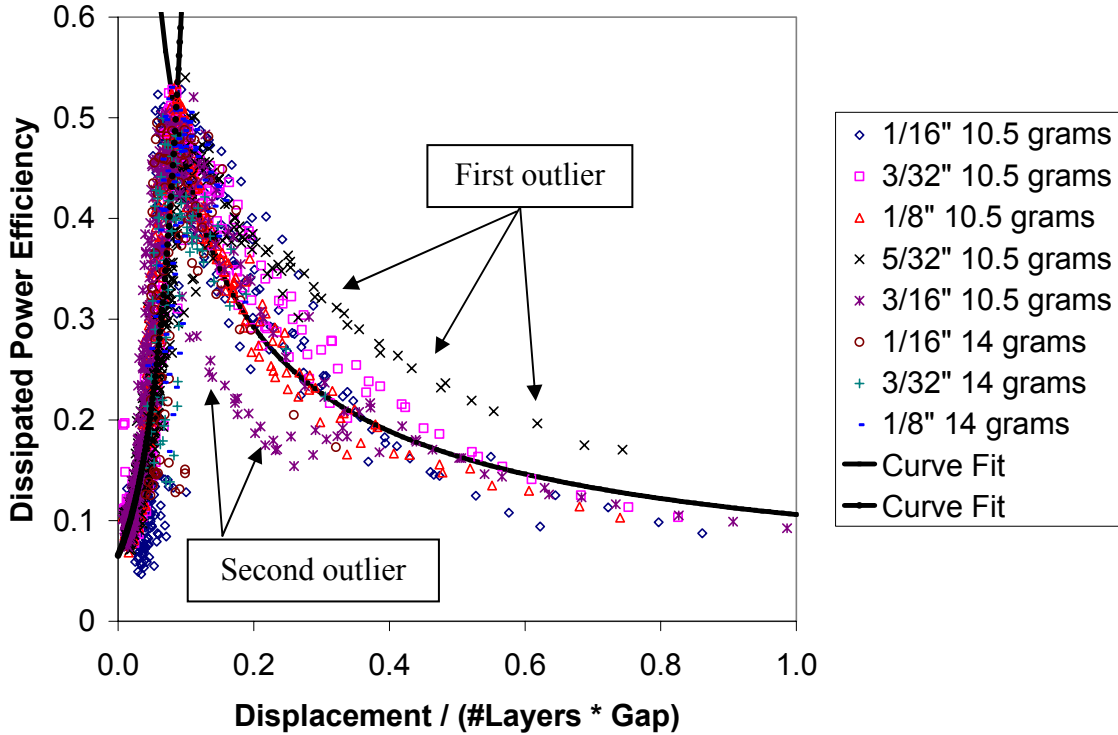


Figure 5.19: Curve fits for dissipated power master curve.

The trendline is piecewise, with separate equations describing the regions before and after the peak. Mathematically, it is presented as

$$DPE = \begin{cases} C_1 e^{C_2 \Delta} & \text{for } 0 < \Delta < \Gamma \\ C_3 \Delta^{-C_4} & \text{for } \Gamma < \Delta \end{cases}, \quad (5.2)$$

where $\Delta \equiv \text{Displacement} / (\# \text{Layers} \times \text{Gap})$, C_1 , C_2 , C_3 , and C_4 are constants, and Γ is the value of Δ that coincides with the peak dissipated power efficiency. For this data set, the constants have the following values:

$C_1 = 0.0653$ $C_2 = 23.911$ $C_3 = 0.106$. $C_4 = 0.63$ $\Gamma = 0.085$	(5.3)
---	--------------

5.2 Collapse of Data Curve for Mass

The same data in Section 5.1 was used to generate the master design curve for mass. Recall that the approximate effective mass of the PID, m , is computed as

$m \approx \frac{Imag\{P\}}{\omega V_{rms} V^*}$	(5.4)
--	--------------

where $Imag\{P\}$ is the reactive component of power, ω is the frequency, and V is the velocity.

Like the master design curve for dissipated power, there was a desire to collapse the entire data set into a single two-dimensional plot that would allow a designer to easily predict the effective mass of the PID under different conditions. To this end, the term *Mass Efficiency of the Particle Bed (MEPB)* is introduced. It is the ratio of the approximate particle mass measured by the reactive power divided by the statically measured particle mass. Like PDE, it is unitless and has a value that should lie between zero and one. Mathematically, it is defined as

$MEPB \equiv \frac{m - m_{encl}}{m_{pb,s}},$	(5.5)
--	--------------

where m_{encl} is the static mass of the enclosure and $m_{pb,s}$ is the static mass of the particle bed.

To keep the master design curves consistent, and knowing that the motion of the particle bed affects the effective mass as well as the dissipated power, the same term (*displacement/gap*) was used as the x-axis. Collapse of the mass data was done in the same systematic manner as the dissipated power data.

5.2.1 Collapse of Mass Efficiency With Respect to Frequency

Figure 5.20 shows how the effective mass varies with displacement. Figures 5.21, 5.22, and 5.23 show how the MEPB data collapses with respect to frequency for various particle and gap sizes. Unlike the DPE data, collapse with respect to frequency exists for both sets of axis. Like the DPE plots (see Figure 5.5), the data for large particles (3/16 inch) is noisier than the data for smaller particles. This is due to the higher impact forces involved with a fewer number of more massive particles.

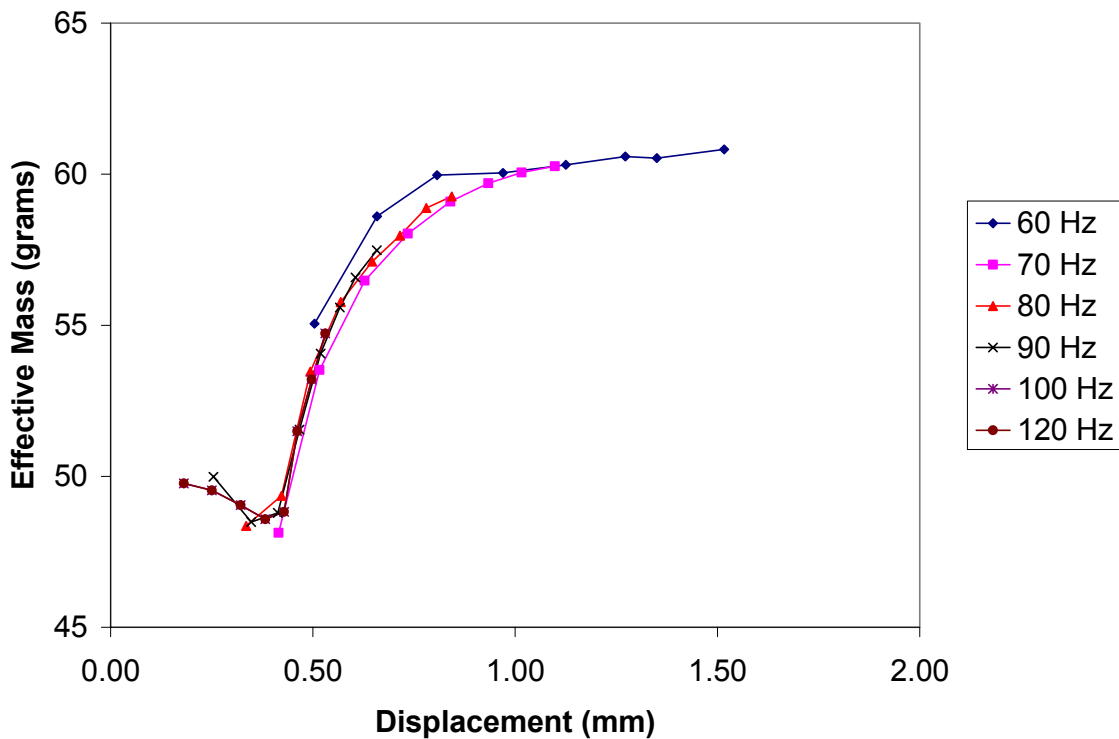


Figure 5.20: Effective mass vs. displacement, 600 1/16 inch particles, gap = 0.79 mm

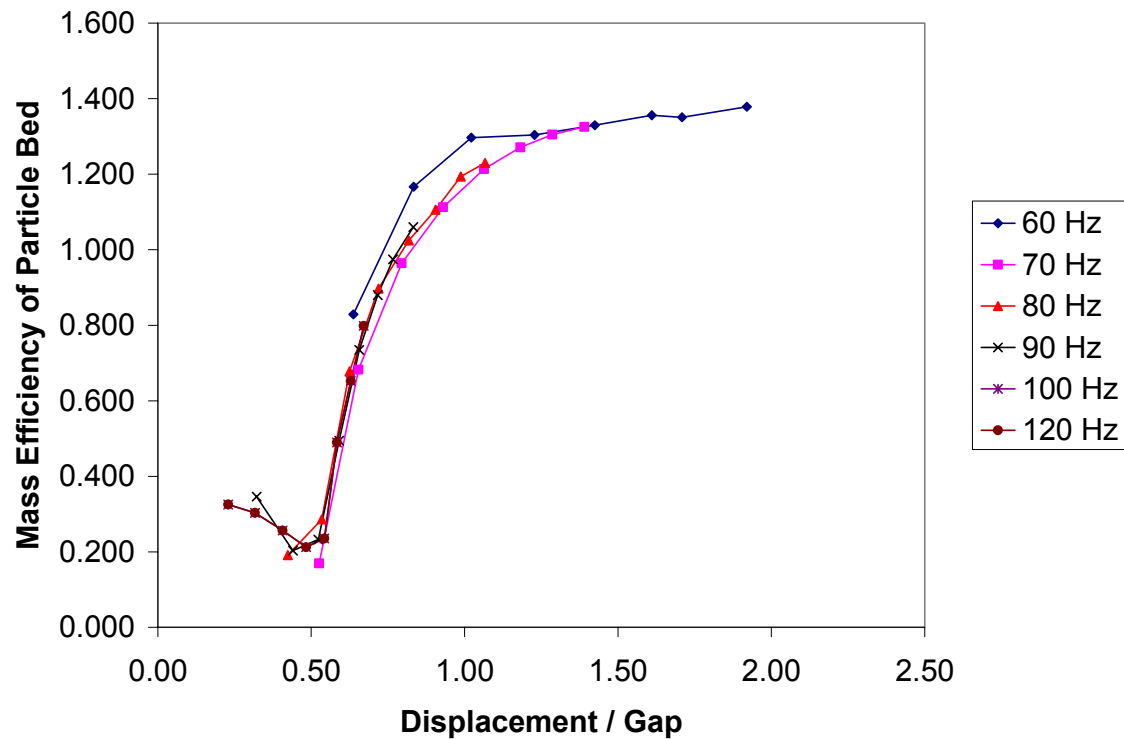


Figure 5.21: MEPB collapse on frequency, 600 1/16 inch particles, gap = 0.79 mm

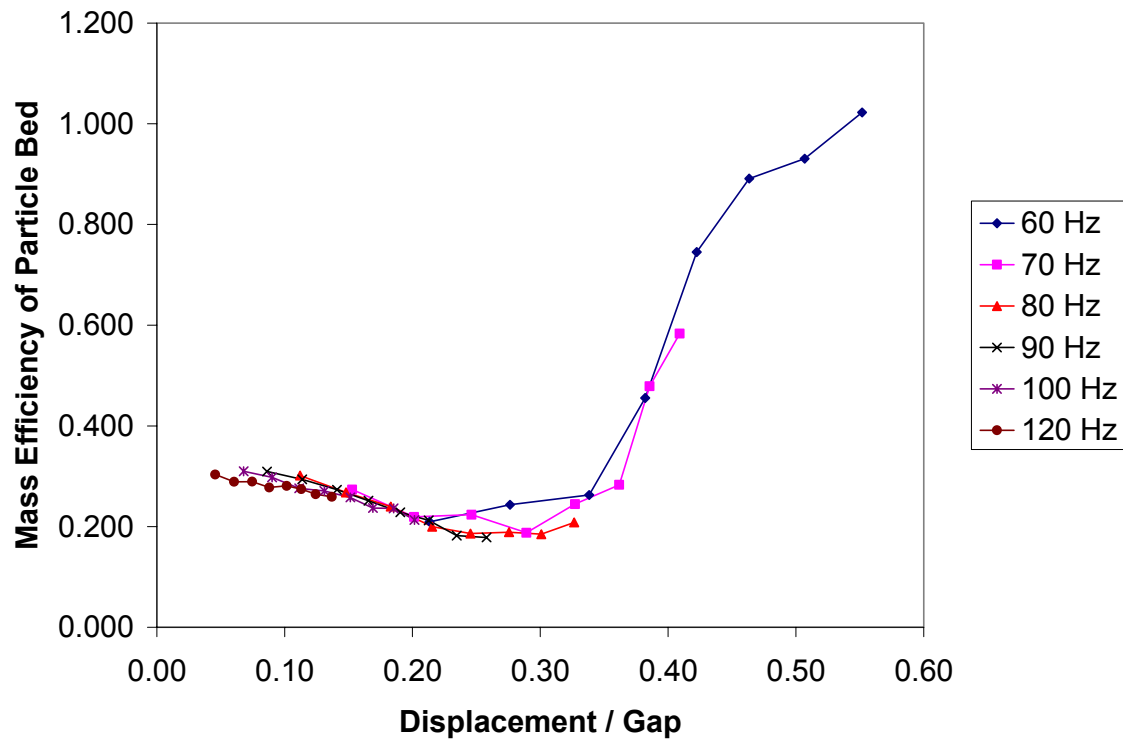


Figure 5.22: MEPB collapse on frequency, 174 3/32 inch particles, gap = 2.73 mm

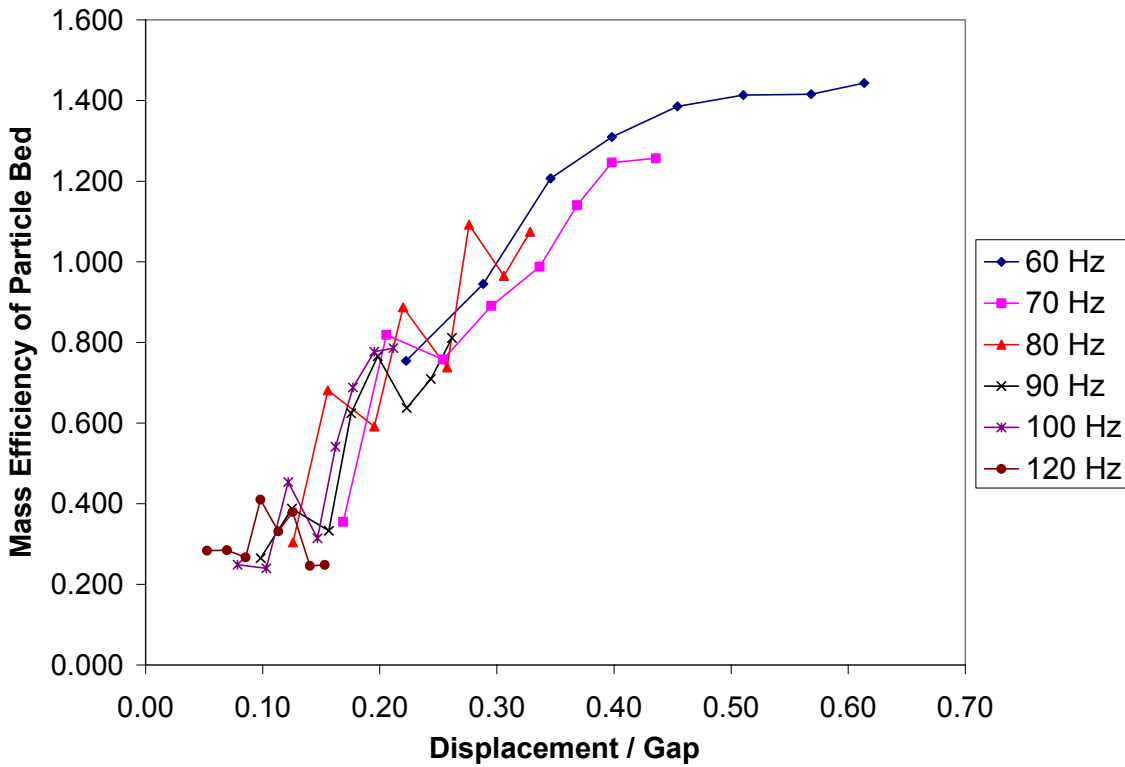


Figure 5.23: MEPB collapse on frequency 22 3/16 inch particles, gap = 2.37 mm

5.2.2 Collapse of Mass Efficiency With Respect to Gap Size

Figure 5.24 shows how the uncollapsed effective mass data for 3/32 inch particles. Figures 5.25 – 5.29 show how the data collapses on gap size. Collapse is generally good, with small gap sizes being outliers for the majority (3/32, 5/32, 3/16) of cases. The data for 1/16 inch particles did not collapse as well as the larger particle sizes. This will be addressed in a later section.

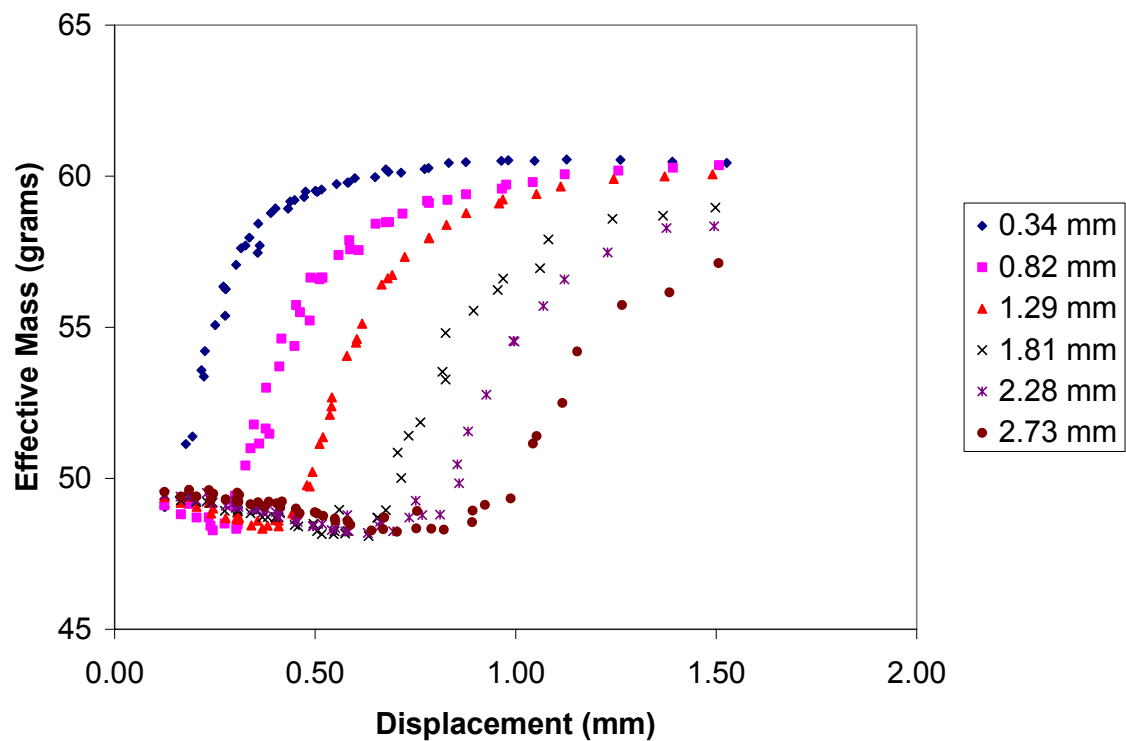


Figure 5.24: Effective mass vs. displacement for 174 3/32 inch particles

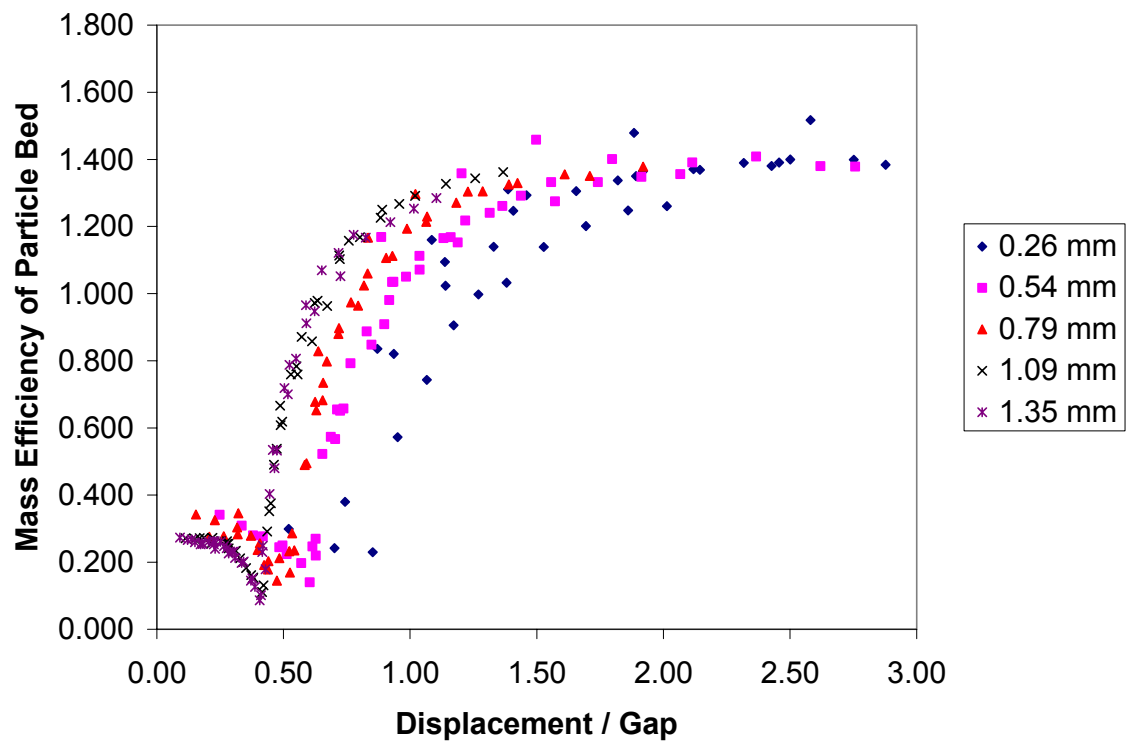


Figure 5.25: MEPB collapse on gap size, 600 1/16 inch particles

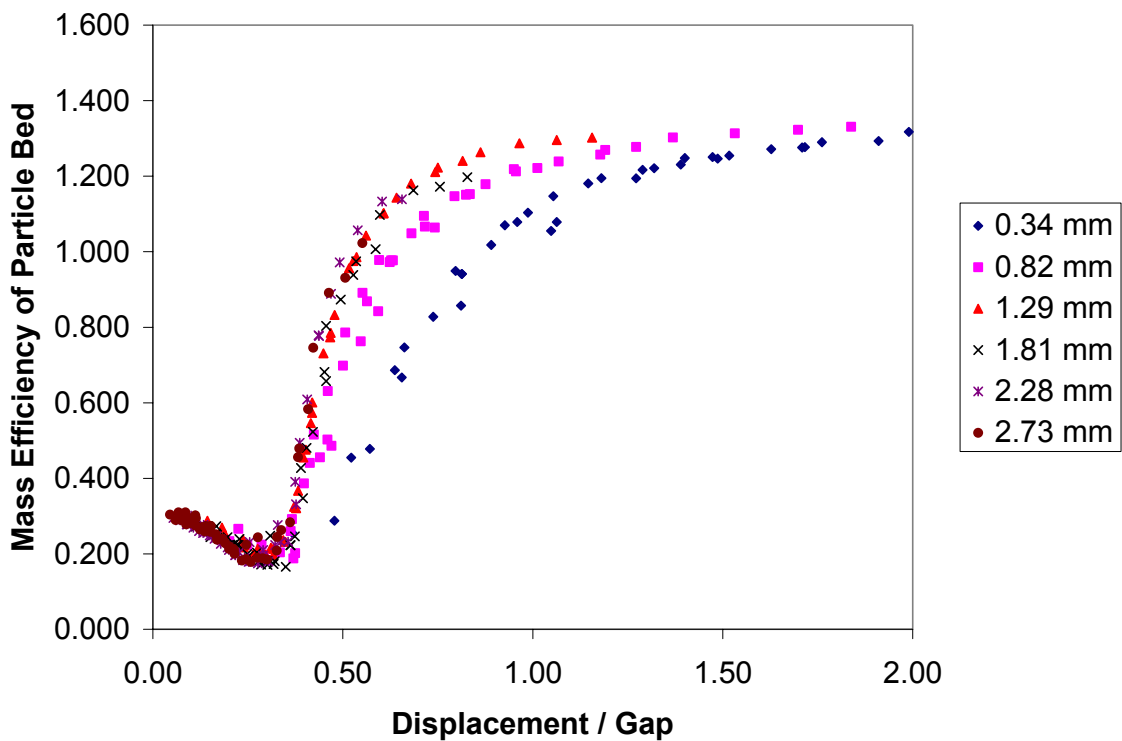


Figure 5.26: MEPB collapse on gap size, 174 3/32 inch particles

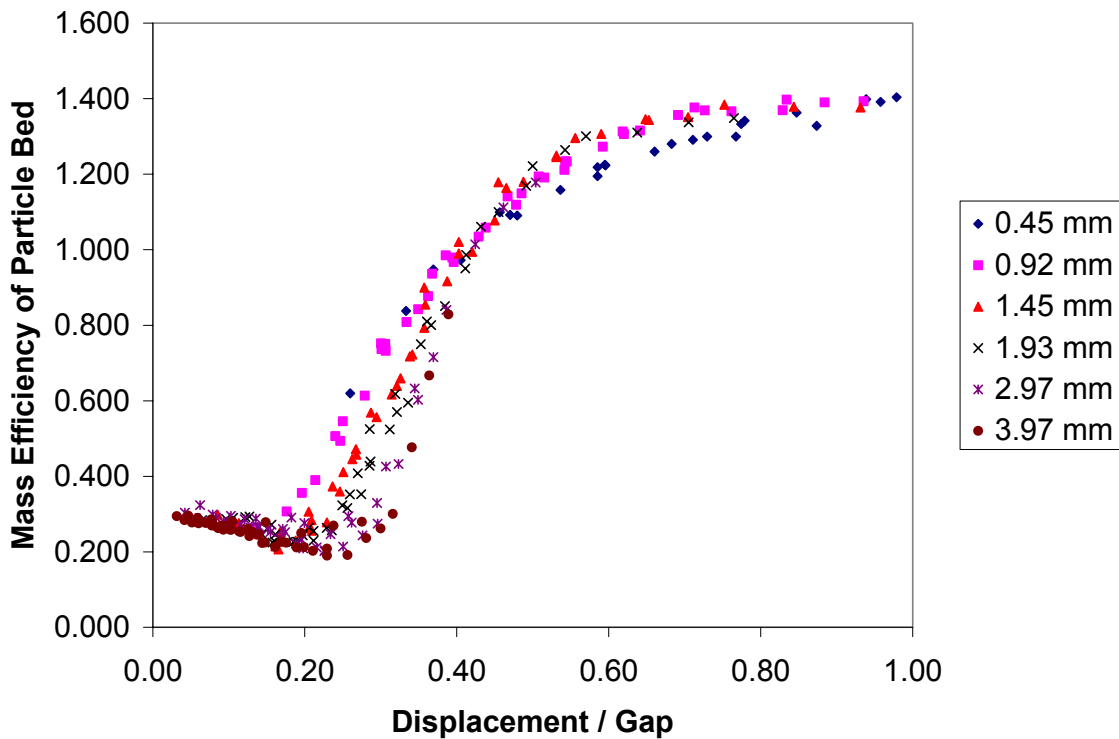


Figure 5.27: MEPB collapse on gap size, 75 1/8 inch particles

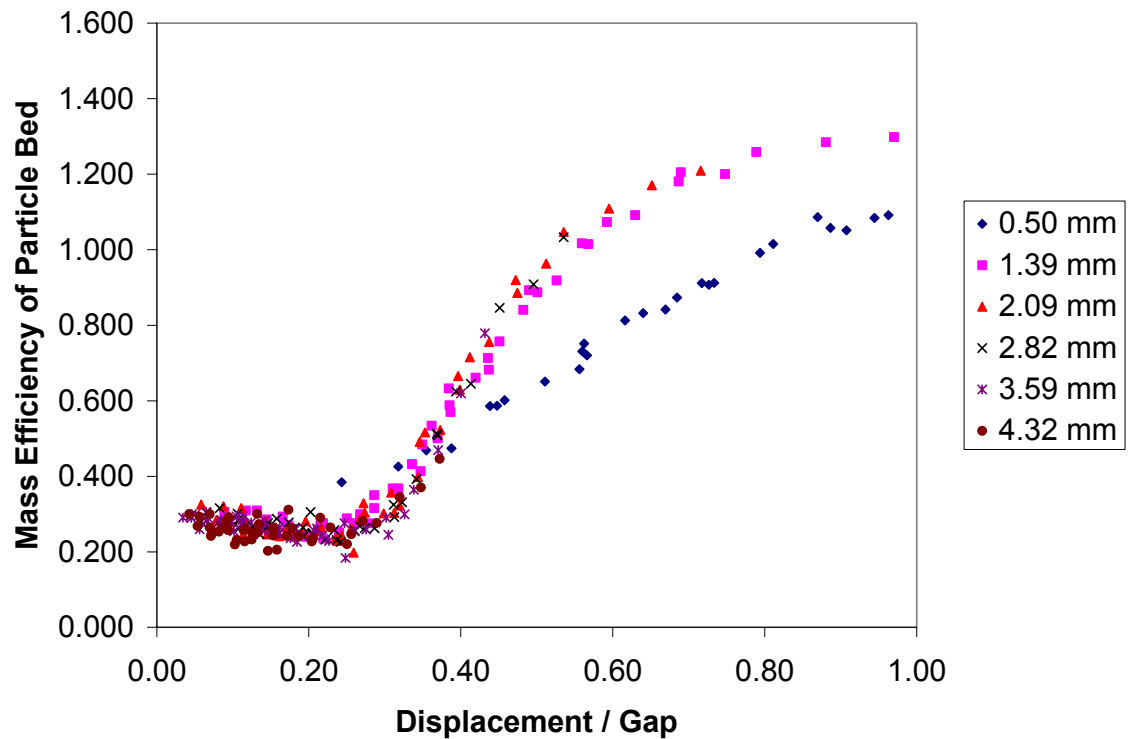


Figure 5.28: MEPB collapse on gap size, 37 5/32 inch particles

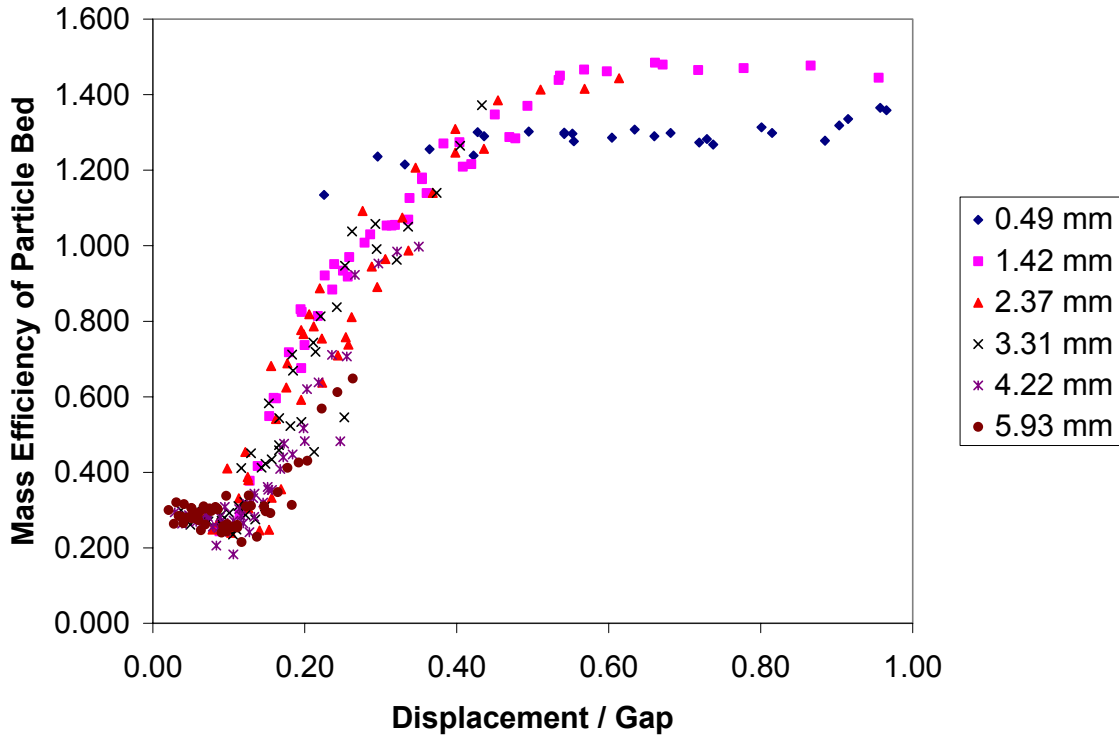


Figure 5.29: MEPB collapse on gap size, 22 3/16 inch particles

5.2.3 Collapse of Mass Efficiency With Respect to Particle Size

Figure 5.30 shows the uncollapsed effective mass data for all particle sizes. Dividing the displacement by gap and expressing the effective mass as MEPB gives Figure 5.31, which shows the failure of the MEPB data to collapse with respect to particle size. Recall that the DPE data also failed to collapse on particle size (see Figures 5.13 and 5.14), and that the collapse was enabled by the inclusion of the number of layers in the denominator of the x-axis. Figure 5.32 shows how including the number of layers also collapses the mass data with respect to particle size.

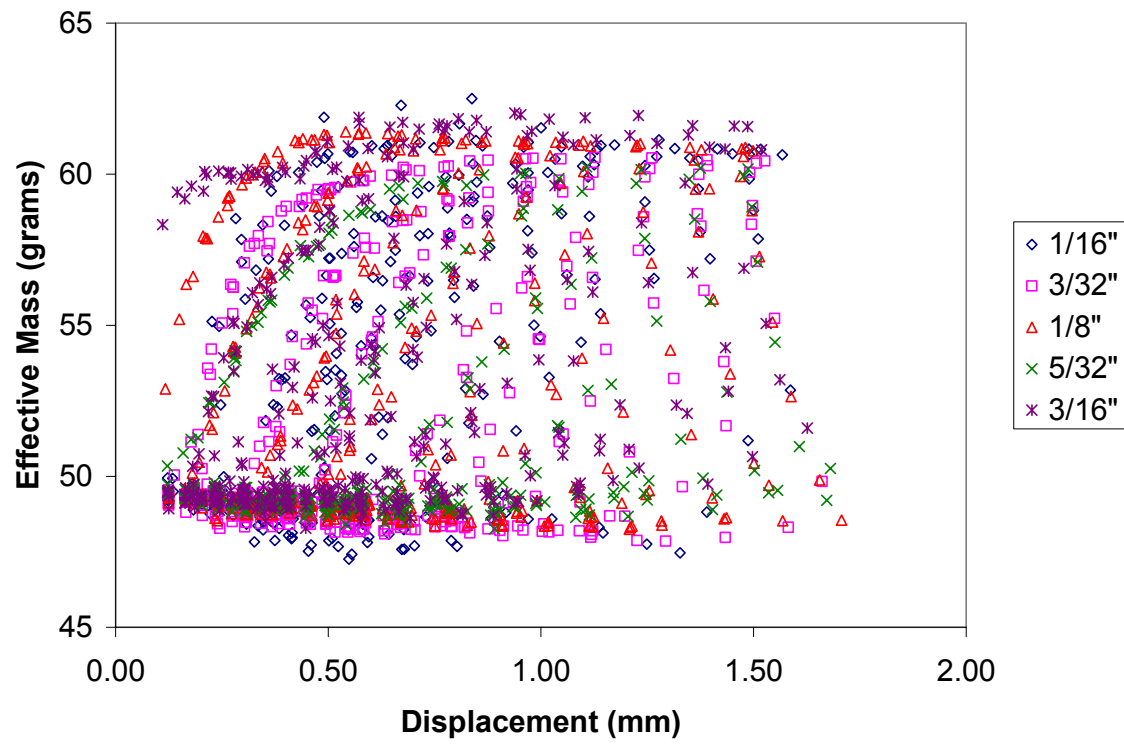


Figure 5.30: Effective mass vs. displacement for all particle sizes

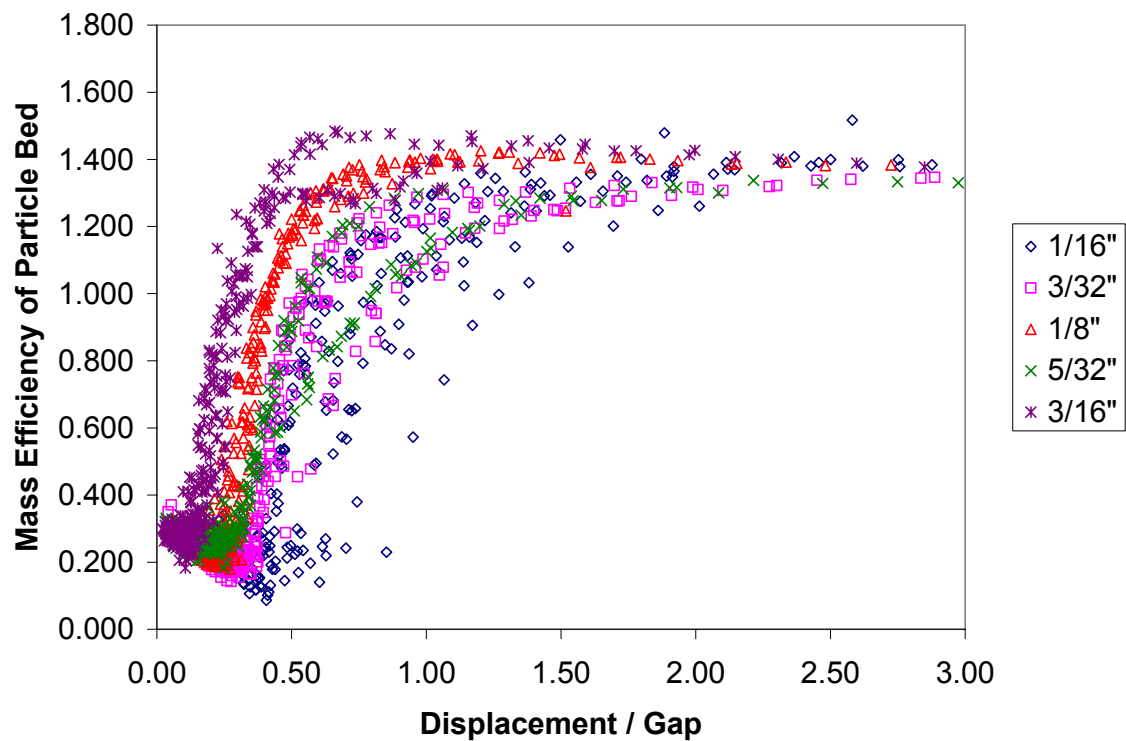


Figure 5.31: MEPB collapse on particle size, 10.5 grams total particle mass

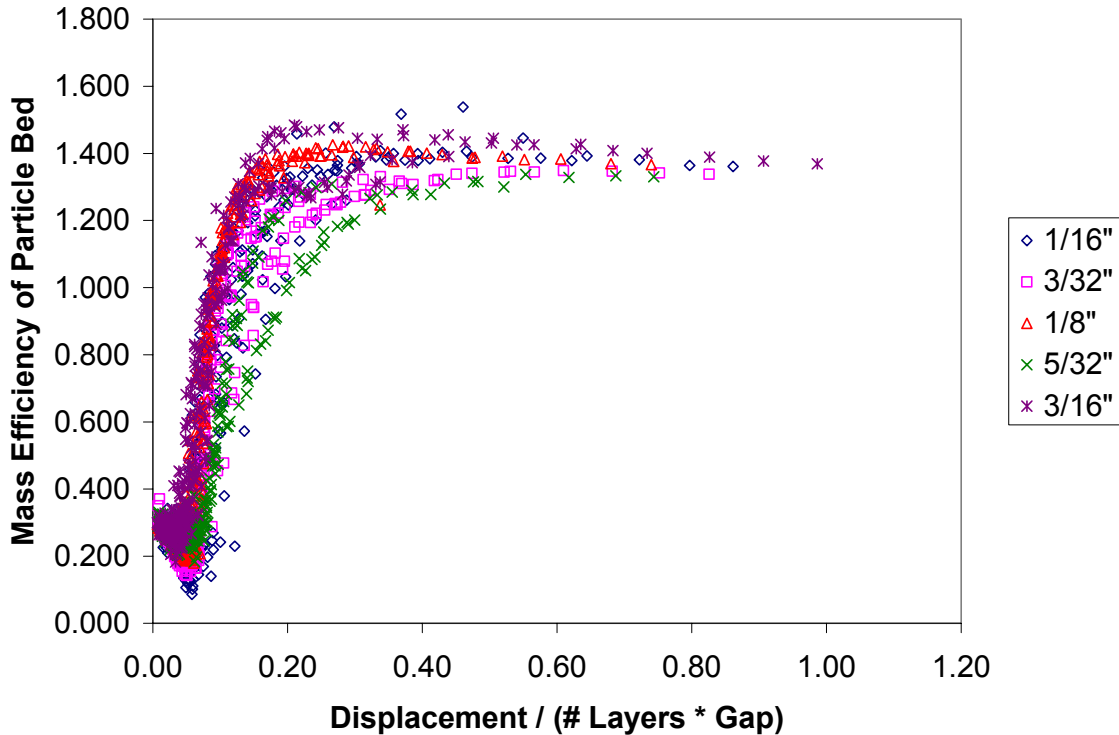


Figure 5.32: MEPB collapse on particle size with number of layers included, 10.5 gram total particle mass

5.2.4 Collapse of Mass Efficiency With Respect to Particle Mass

Finally, the collapse of the mass data with respect to total particle bed mass is examined. Figures 5.33 - 5.35 compare the mass data for particle beds of 10.5 and 14 grams. The collapse with respect to particle bed mass is not as good as the dissipated power data (Figures 5.16 - Figure 5.18). The trend of the data is the same for both particle bed masses, but the minimum MEPB for the 14 gram particle bed is consistently lower than the 10.5 gram particle bed. Therefore, it cannot be concluded that the MEPB data collapses on particle mass.

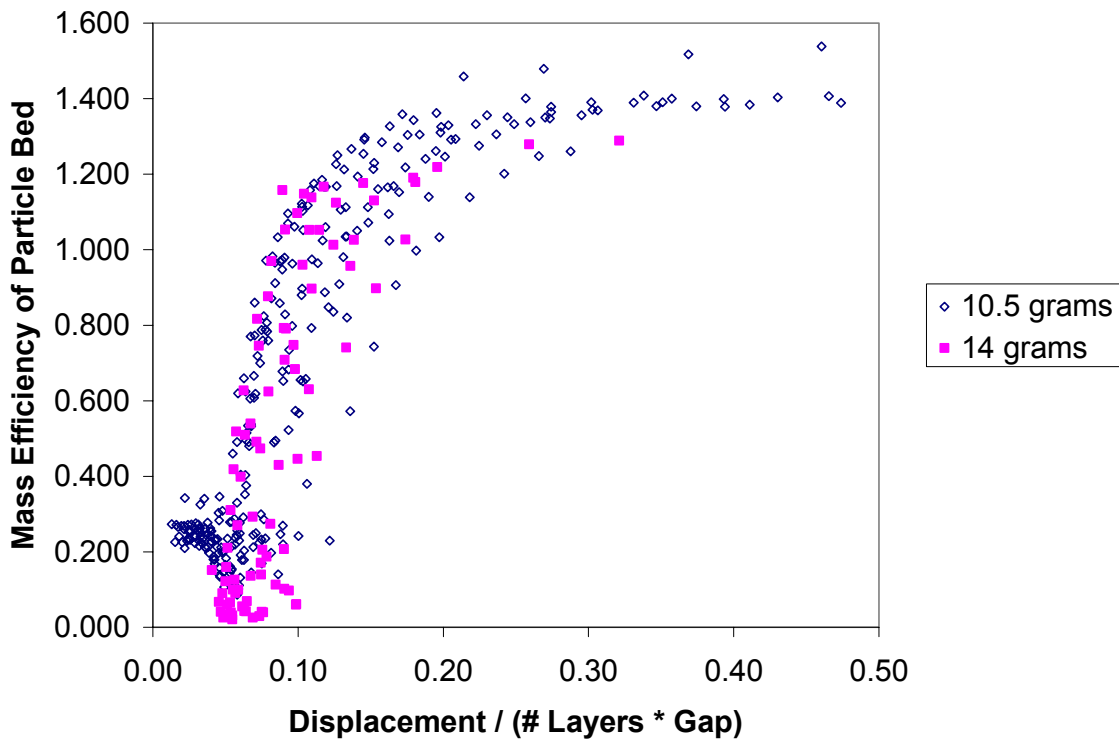


Figure 5.33: MEPB collapse on total particle mass, 1/16 inch particles

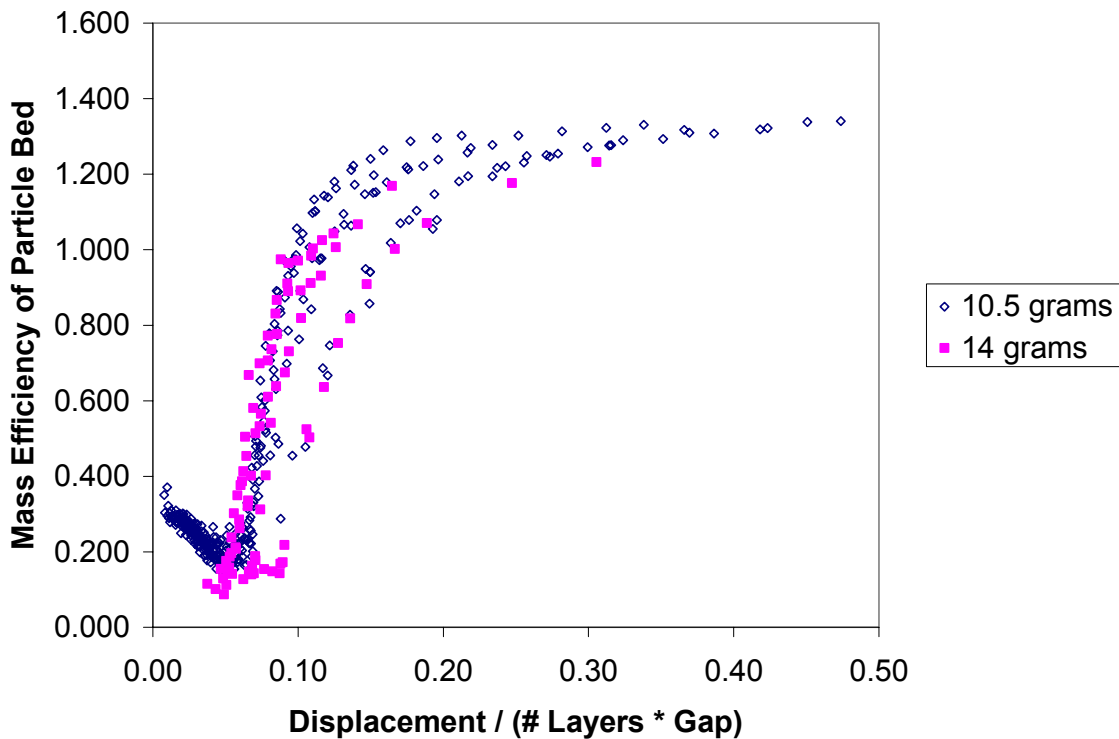


Figure 5.34: MEPB collapse on total particle mass, 3/32 inch particles

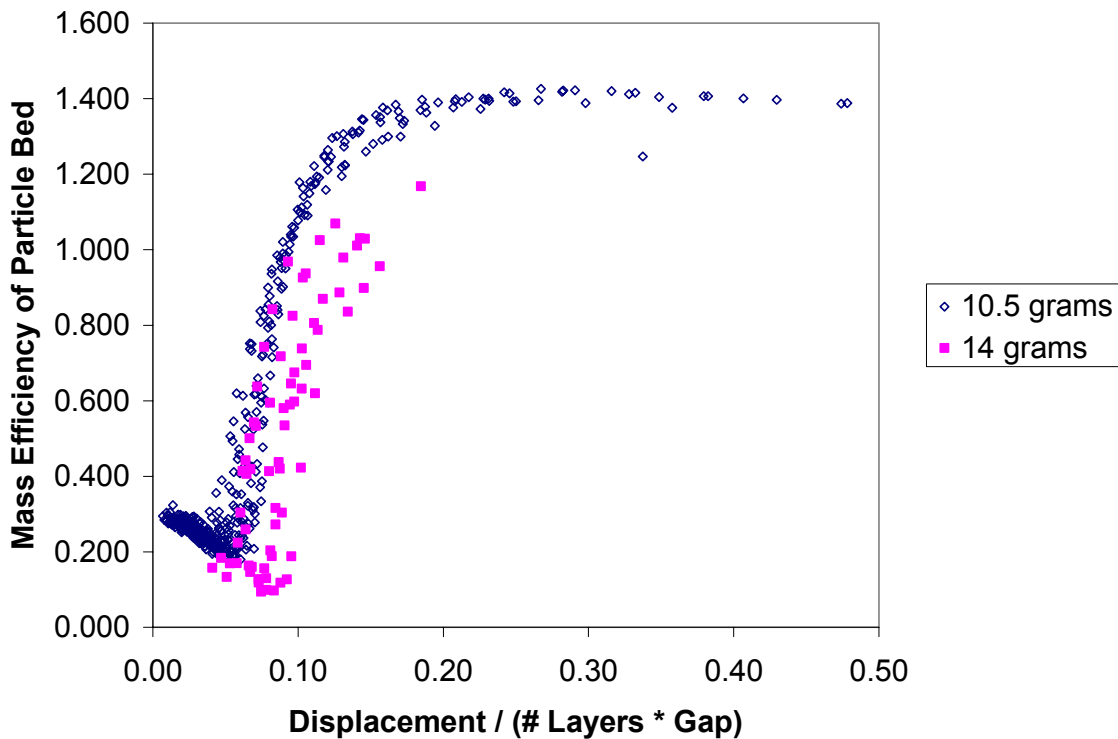


Figure 5.35: MEPB collapse on total particle mass, 1/8 inch particles

5.2.5 Curve Fit of Mass Efficiency Master Curve

Trendlines were fitted to the mass data in the same manner as the dissipated power data. Since collapse on particle bed mass could not be achieved, only the data for the 10.5 gram particle mass was fit. Figure 5.36 shows the mass data and the trendlines that were applied.

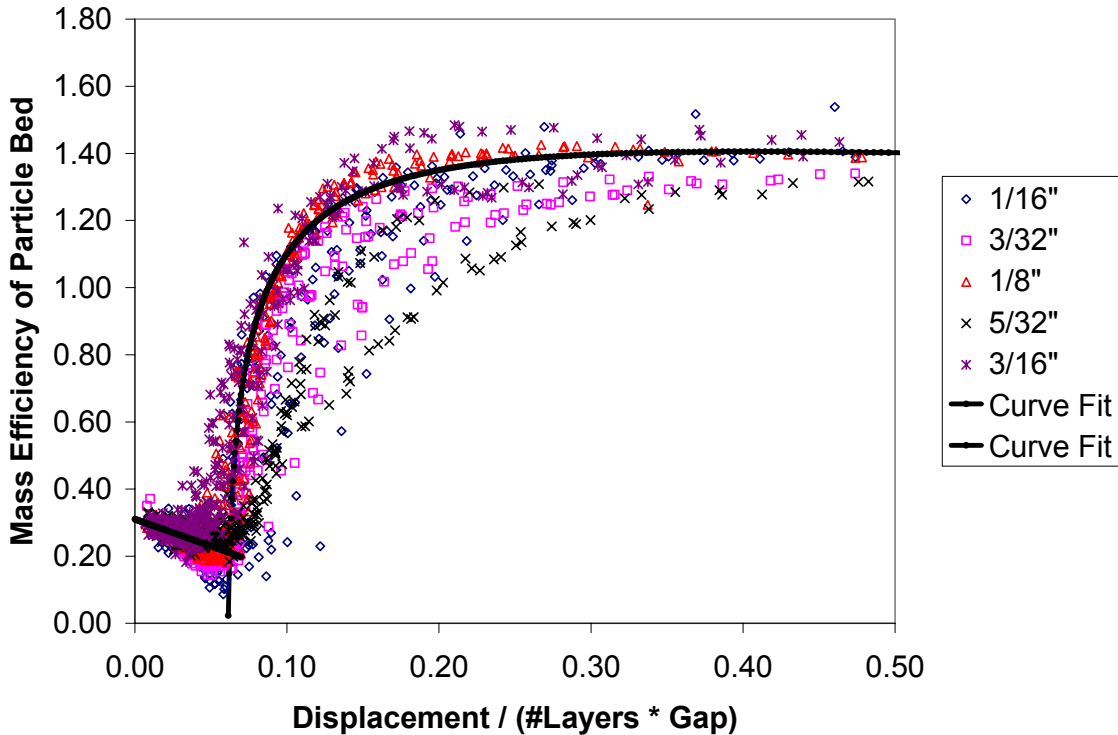


Figure 5.36: Curve fits for mass efficiency master curve

The trendline is piecewise, with separate equations describing the regions before and after the dip. The equations are

$$MEPB = \begin{cases} C_5\Delta + C_6 & \text{for } 0 < \Delta < \Sigma \\ (C_7 \ln(\Delta - C_8) + C_9) \times C_{10} (\Delta - C_{11})^{-C_{12}} & \text{for } \Delta > \Sigma \end{cases} \quad (5.6)$$

where C_5, C_6, \dots, C_{12} are constants, and Σ is the value of Δ that coincides with the minimum mass efficiency. For this data set, the constants have the following values:

$C_5 = -1.6$ $C_6 = 0.31$ $C_7 = 0.3$ $C_8 = 0.06$ $C_9 = 2.0$. $C_{10} = 0.7$ $C_{11} = -0.1$ $C_{12} = 0.26$ $\Sigma = 0.063$	(5.7)
--	-------

5.3 Comparison and Interpretation of Master Design Curves

A superposition of the master design curves for dissipated power and mass is shown in Figures 5.37 and 5.38. Both figures show only the data for the 10.5 gram particle bed. The dip in the MEPB curve consistently occurs at a smaller value of Δ than the peak in the DPE curve. To understand why this occurs, it is important to understand how the particle motion relates to the shape of the two design curves.

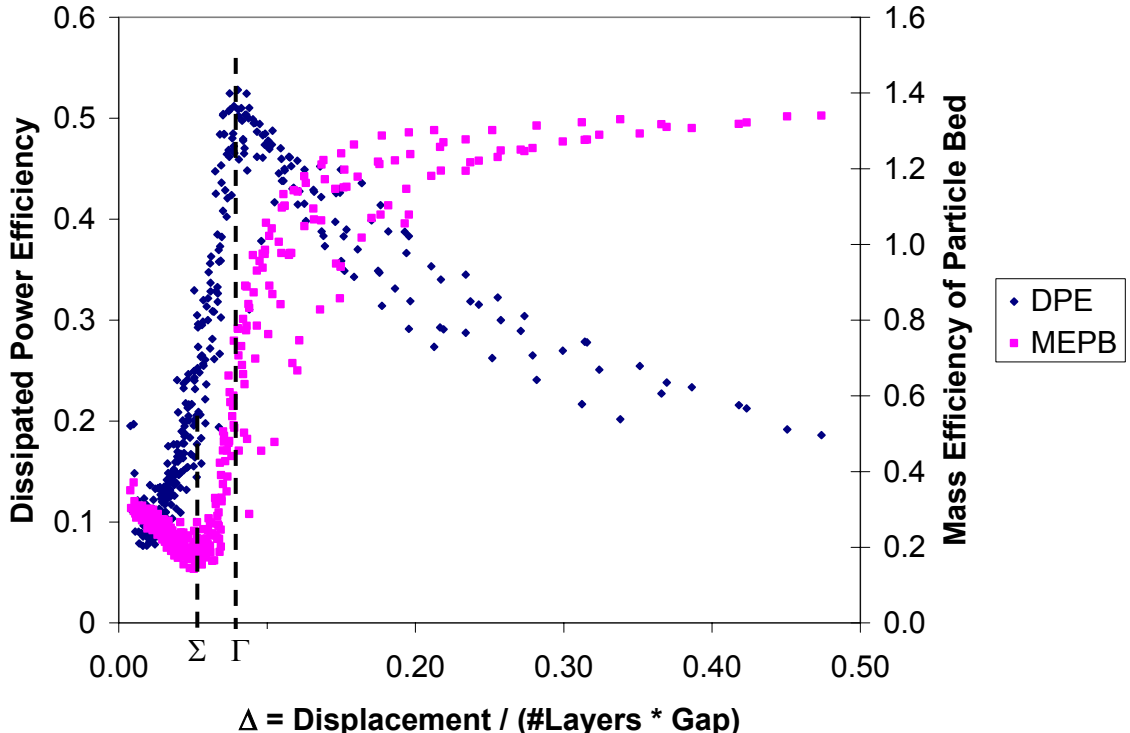


Figure 5.37: Superposition of master design curves, 3/32 inch particles, 10.5 gram particle bed

The mass efficiency of the particle bed is directly related to the fraction of time the particle bed remains in contact with the enclosure. The MEPB curve initially decreases at very low values of Δ because the particles do not come into contact with the ceiling. Therefore, as Δ increases the time between floor impacts increases, and the particles spend more time in the air. This causes a decrease in the mass efficiency. The dip of the MEPB curve corresponds to a condition where the particle bed begins to impact the ceiling of the enclosure. Friend and Kinra called this the “osculation” condition [23] and it is illustrated in Figure 5.39. The dark line depicts the motion of the particle bed and the other two lines show the motion of the floor and ceiling of the

enclosure. As Δ increases beyond the osculation condition, the particle bed continues to impact the ceiling and spend a decreasing amount of time traveling through the air. For high values of Δ , the mass efficiency of the particle bed exceeds its theoretical maximum of unity. This is a phenomenon that was previously discussed in Section 3.3.4. The possible presence out-of-phase impacts between the particle bed and enclosure masses are cited as a possible explanation.

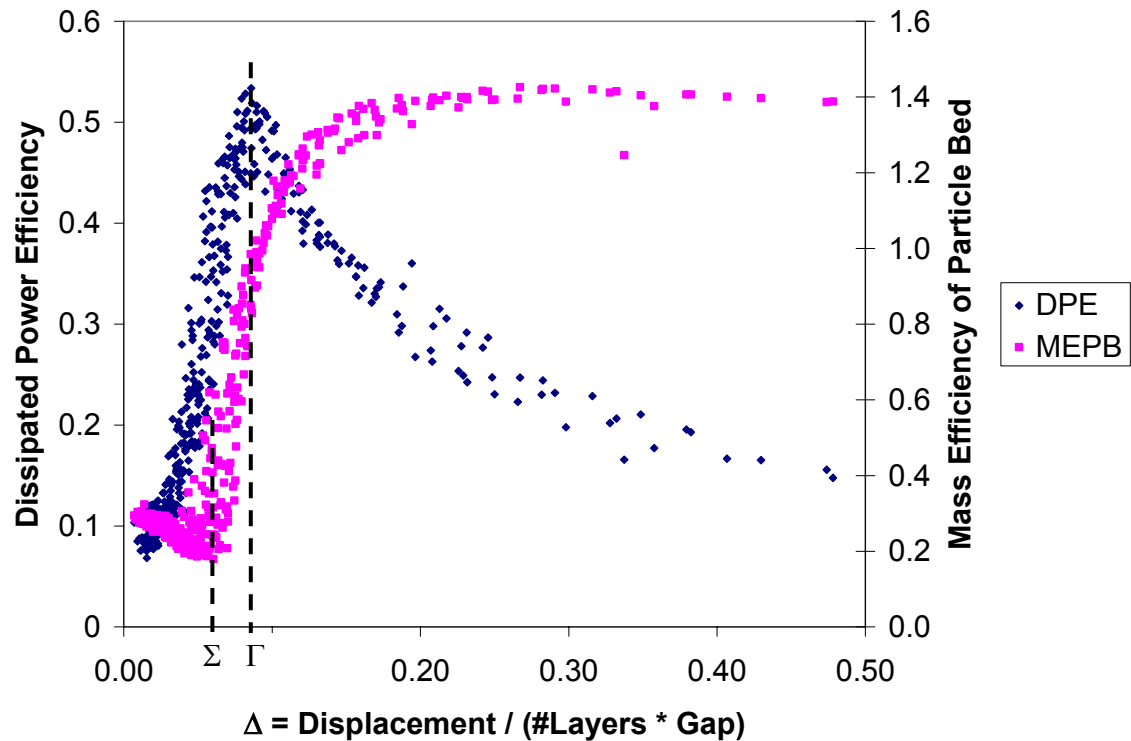


Figure 5.38: Superposition of master design curves, 1/8 inch particles, 10.5 gram particle bed

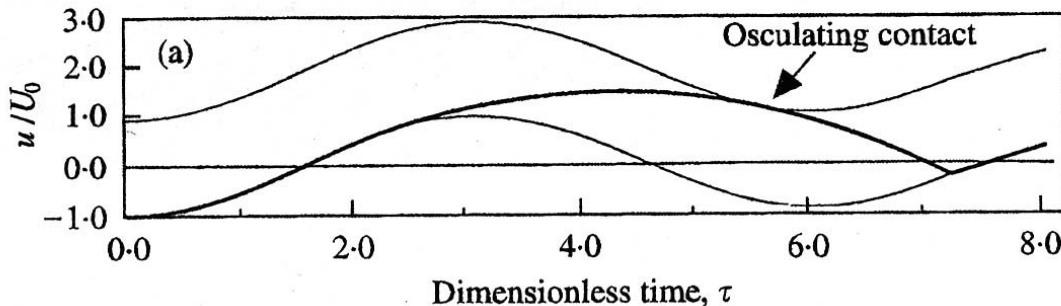


Figure 5.39: Osculation condition. Source: R.D. Friend and V.K. Kinra, *Journal of Sound and Vibration*, 233(1), pp. 93-118. Particle impact damping. 2000.

The slow motion videos in Chapter 4 showed that the amount of power dissipated is determined in part by the relative difference in the velocities of the particle bed and enclosure. This observation can be used to explain the shape of the DPE curve. The peak value of DPE occurs when $\Delta = \Gamma$ and corresponds to the case where the relative difference between the velocities of the particle bed and enclosure are maximized. This was illustrated in Figure 4.3 and is duplicated here as Figure 5.40.

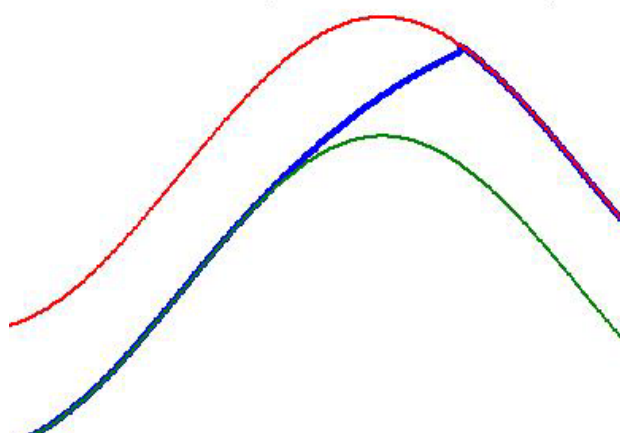


Figure 5.40: Impact between particle bed and enclosure for $\Delta = \Gamma$

For $\Delta < \Gamma$, the particle bed spends a greater time traveling through the air. This allows gravity to significantly reduce the velocity of the particle bed, and results in less dissipation. This was illustrated in Figure 4.5 and is duplicated here as Figure 5.41. Higher values of Δ lower the time the particle bed spends in the air, which reduces the influence of gravity, resulting in higher dissipation.

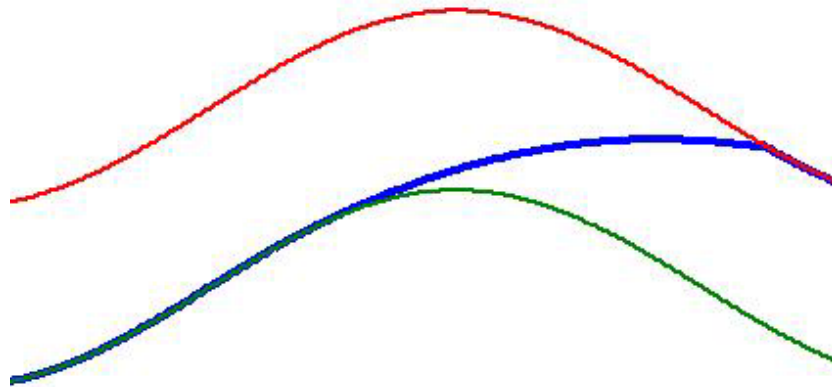


Figure 5.41: Impact between particle bed and enclosure for $\Delta < \Gamma$

For $\Delta > \Gamma$, the particle bed spends a relatively small amount of time in the air. This allows it to escape the influence of gravity, but results in an impact when the enclosure is moving towards the particle bed at relatively low velocity. For very high values of Δ , the enclosure can even be moving *away* from the particle bed at impact. These conditions result in lower power dissipation and were illustrated in Figure 4.4 (duplicated as Figure 5.42).

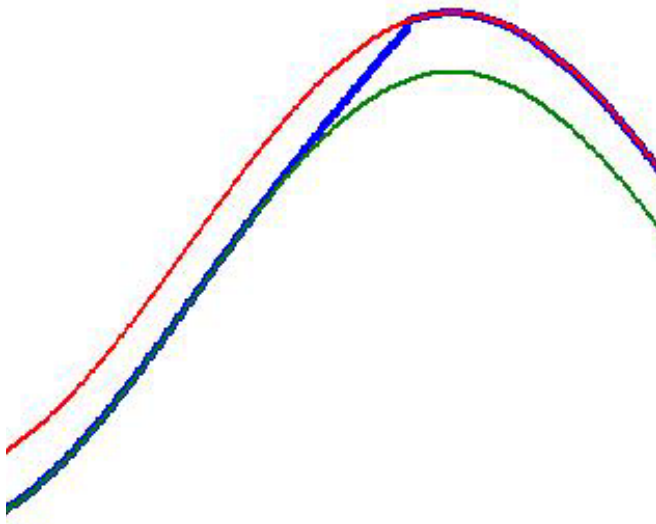


Figure 5.42: Impact between particle bed and enclosure for $\Delta > \Gamma$

5.4 Implementation of Video Correction

It was previously noted that the collapse of the master design curves on gap size was not as good for small particle sizes (see Figures 5.7 and 5.25). Careful observation of the slow motion videos revealed that the gap sizes in the videos appeared to be larger than those measured. Based on these observations, a series of comparisons between the gap sizes measured manually and estimated from the videos was done. The video gap size was estimated by analyzing a single frame showing the largest gap, which occurred immediately after impact. Digital calipers were used to measure the gap on the video screen, and the scaling was determined by measuring the diameter of a single particle. Since the diameter of the particles is known, the video gap size is found as

$$\text{Video Gap} = \frac{\delta_{gap}}{\delta_{dia}} \times D, \quad (5.8)$$

where δ_{gap} and δ_{dia} are the measurements of the gap and particle diameter with the digital calipers, respectively, and D is the known diameter of a single particle in millimeters. A sample measurement is shown in Figure 5.43. It is important to note that the particle beds in the videos are identical to the 10.5 gram particle beds used in the power measurements.

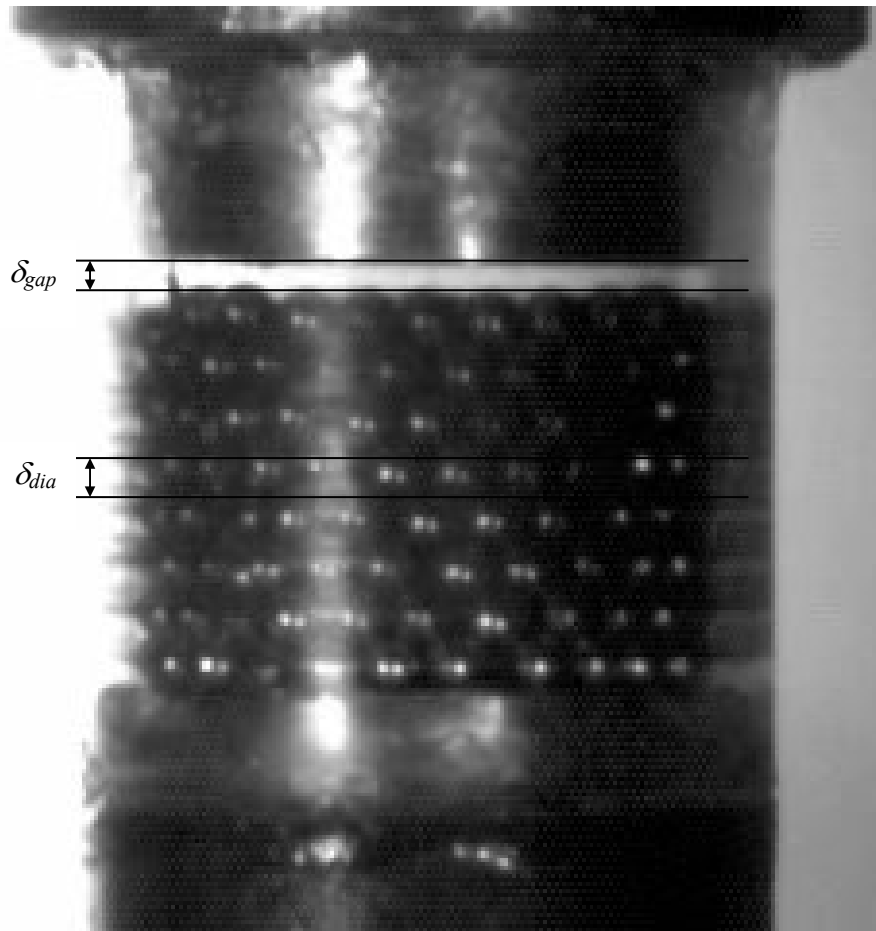


Figure 5.43: Sample measurement of video gap, 1/16 inch particles

Figure 5.44 shows the difference between the video and measured gaps for the 1/16 and 1/8 inch particle sizes. A comparison for the 3/32 inch particle size could not be done because the video data did not exist, but a plot was generated by interpolating the 1/16 and 1/8 inch data. The larger particles contained too much motion throughout the particle bed to make a measurement possible.

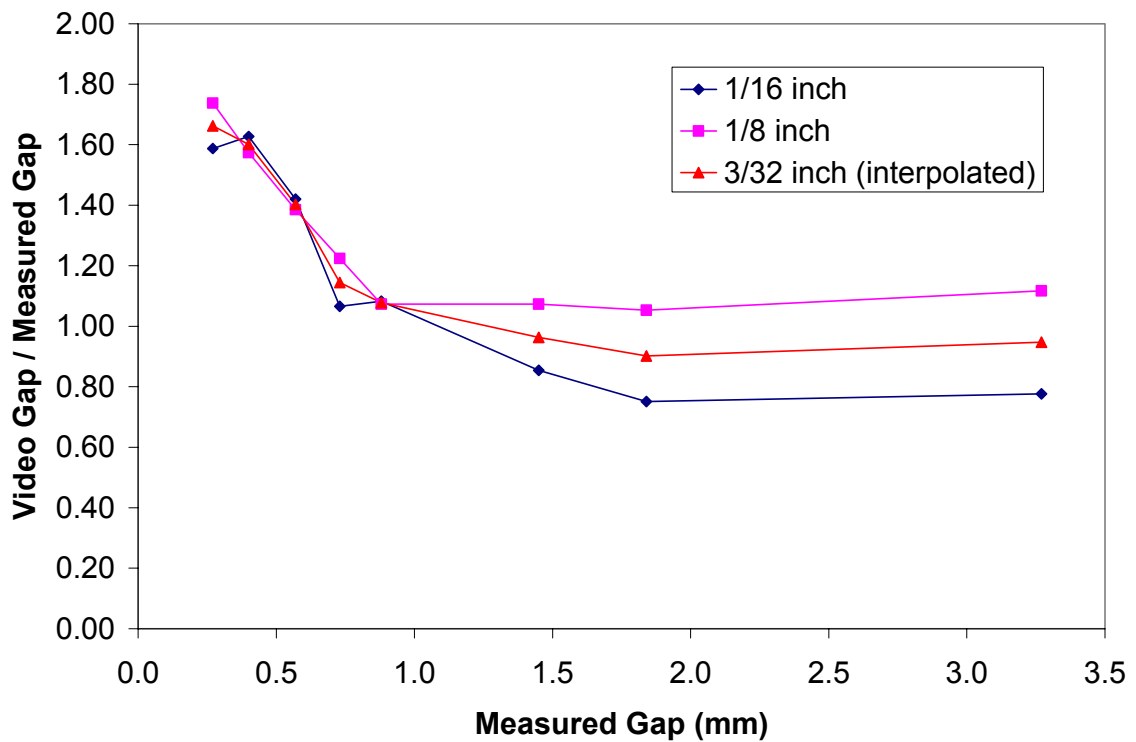


Figure 5.44: Comparison of video gap and measured gap

At small values of measured gap, the video gap is significantly larger. As the measured gap increases, the ratio between the video and measured gap steadily decreases until it reaches some constant value. This constant value is reached at a measured gap of around 1.9 millimeters for the 1/16 inch particles and 1.0 millimeters for the 1/8 inch particles. In most cases, the video gap is greater than the measured gap. This is due to

the compression of the particle bed upon impact. Static measurement of the gap does not take into account the increased gap size that would come from a compressed particle bed.

Since a constant ratio is reached at a smaller measured gap for the larger particle size, it implies that a particle bed consisting of a fewer number of larger particles is less compressible. One possibility the ratio decreases with increasing measured gap is because there is less bed compression at higher measured gaps. Another possibility is that the amount of compression in the particle bed does not change with increasing measured gap but as the measured gap becomes larger, the contribution to the video gap that the compressed bed provides becomes relatively smaller. This is expressed mathematically as

$$\frac{d_{\text{video}}}{d_{\text{meas}}} = \frac{d_{\text{meas}} + d_{\text{comp}}}{d_{\text{meas}}}, \quad (5.9)$$

where d_{video} is the video gap size, d_{meas} is the measured gap size, and d_{comp} is the gap size contribution from the compressed particle bed. For cases where $d_{\text{meas}} \gg d_{\text{comp}}$, the contribution from the compression essentially equals zero.

For the 1/16 inch particles, measured gaps greater than ~1.0 result in a video gap that is *smaller* than the measured gap. This may be due to errors in measuring both the video and the measured gap.

The data from Figure 5.44 was used to generate new master design curves for both mass and dissipated power. The plots for the 1/16, 3/32, and 1/8 inch particle sizes were “corrected”, while the 5/32 and 3/16 inch plots were left unaltered partially because no video gap data was available, and partially because the measured gap sizes were

assumed to be large enough so that the gap size contribution from the compression of the particle bed was negligible.

Figures 5.45 and 5.46 show the collapse of the dissipated power and mass data on video gap size. The collapse is significantly better than the case where no video correction was performed (Figures 5.7 and 5.25).

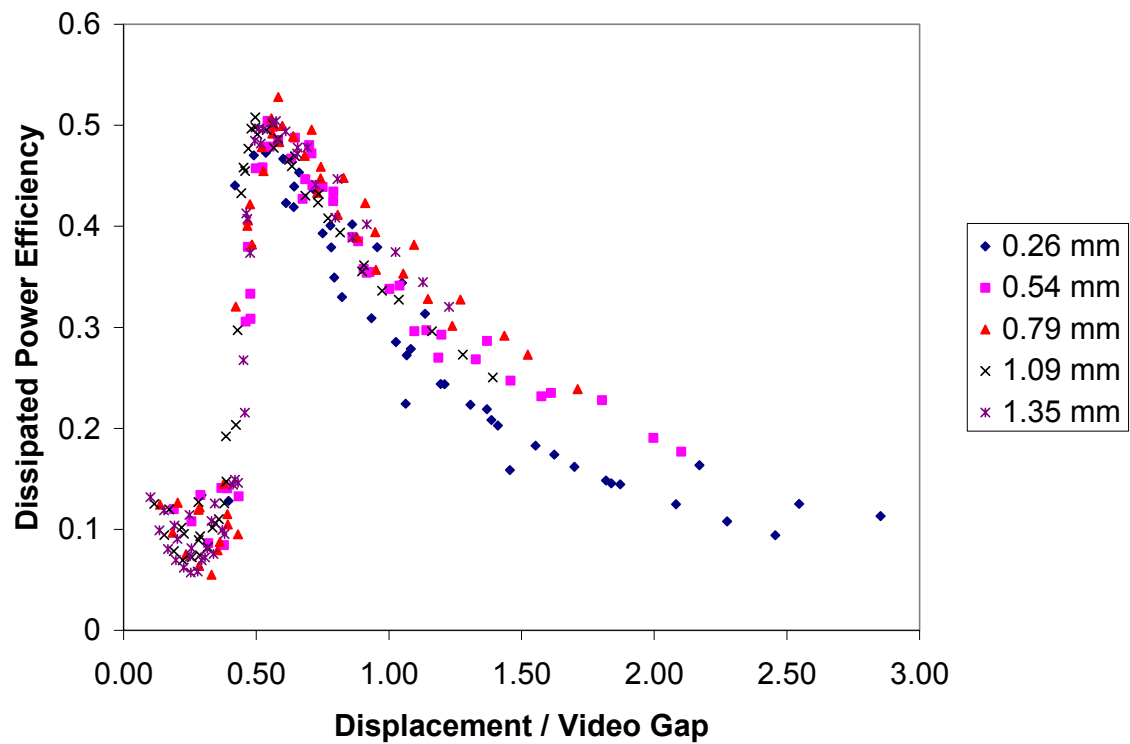


Figure 5.45: PDE collapse on gap size with video correction. 600 1/16 inch particles

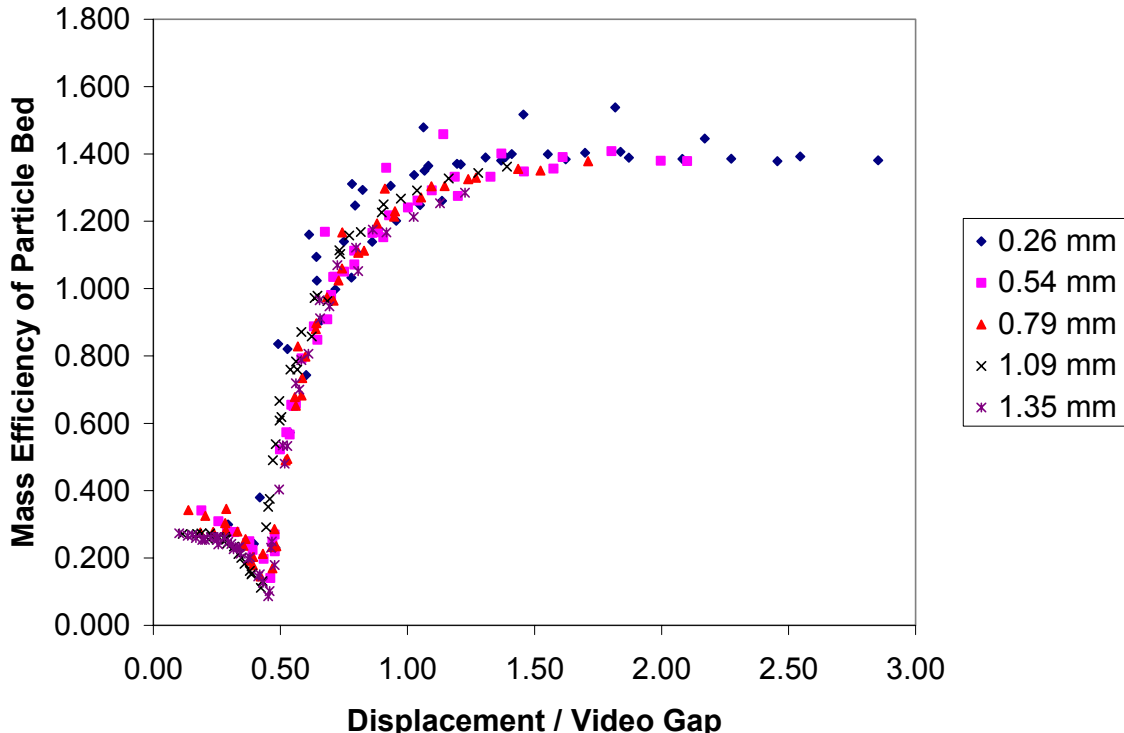


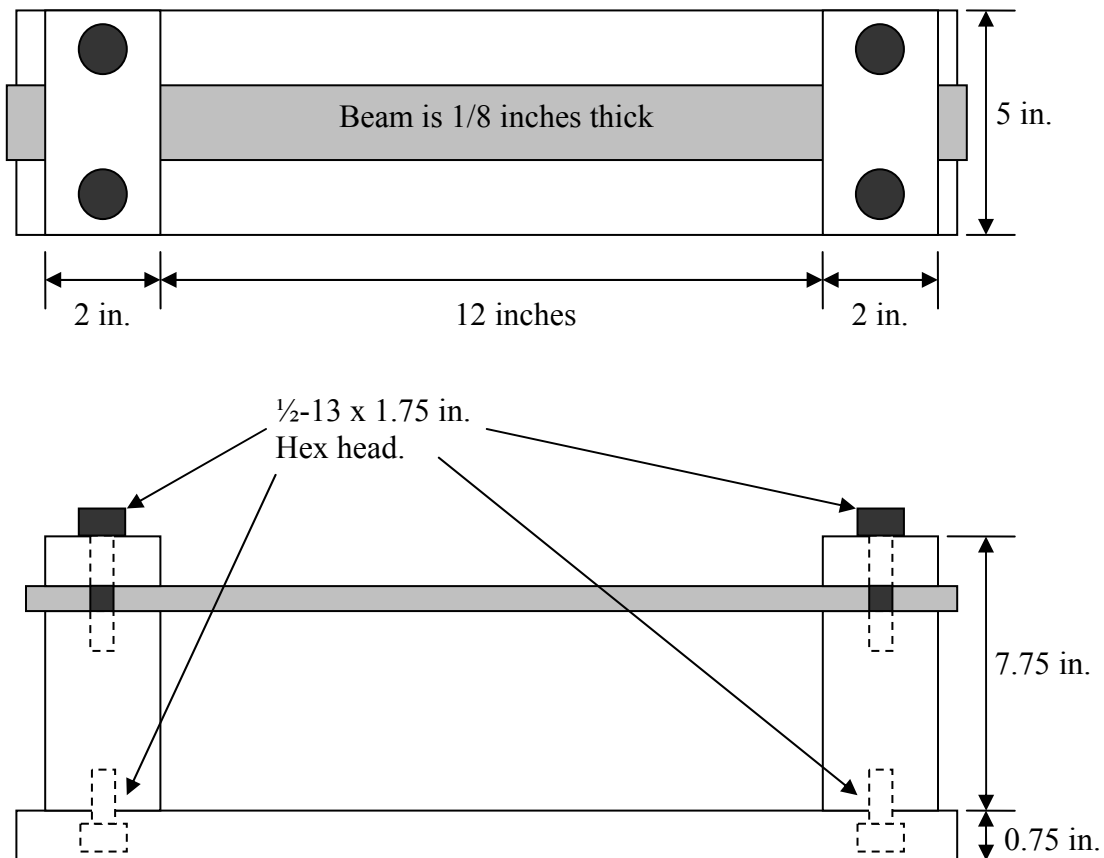
Figure 5.46: MEPD collapse on gap size with video correction. 600 1/16 inch particles

Although implementing a video correction greatly assists in the collapse of the master design curves around the design variables, it may not always be practical or possible to use a video correction. Video correction requires the use of high speed photography equipment and a transparent enclosure, both of which might not be available. With this in mind, this thesis will use the master design curves that were generated without any video correction (Figures 5.19 and 5.36). It is recommended that the designer consider the fact that when using a large amount of small particles in a PID with small gap sizes, the compression of the particle bed will cause the effective gap size to be larger than the measured.

5.5 Relating the Master Design Curves to a Structure

In order to demonstrate the relevance of the master design curves, a particle impact damper was placed on a structure which was then excited. Loss factor and natural frequency measurements were made and compared to the master design curves for dissipated power efficiency (DPE) and mass efficiency of the particle bed (MEPB), respectively.

The experimental setup is identical to the one used in Chapter 3, Section 2.3, although the description and illustrations have been repeated here for the sake of convenience. An aluminum 6061 T6 beam was clamped to a ground structure which was in turn clamped to a seismic table (Figure 5.47). The beam is excited at its center with an electromagnetic shaker, which is connected to the beam with stingers and hex nuts. A force sensor and laser vibrometer were used to measure the input force and velocity of the beam center, respectively. This setup is shown in Figure 5.48. The particle enclosure is constructed entirely of aluminum, features an aluminum screw top, and is pictured in Figure 5.49. 75 brass ball bearings measuring 1/8 inch in diameter were placed inside the enclosure, which was attached to the beam's center. A full list of the experimental equipment is given in Table 5.5, and a picture of the completed setup is given in Figure 5.50.



(Drawing not to scale)

Figure 5.47: Aluminum ground structure with clamped beam

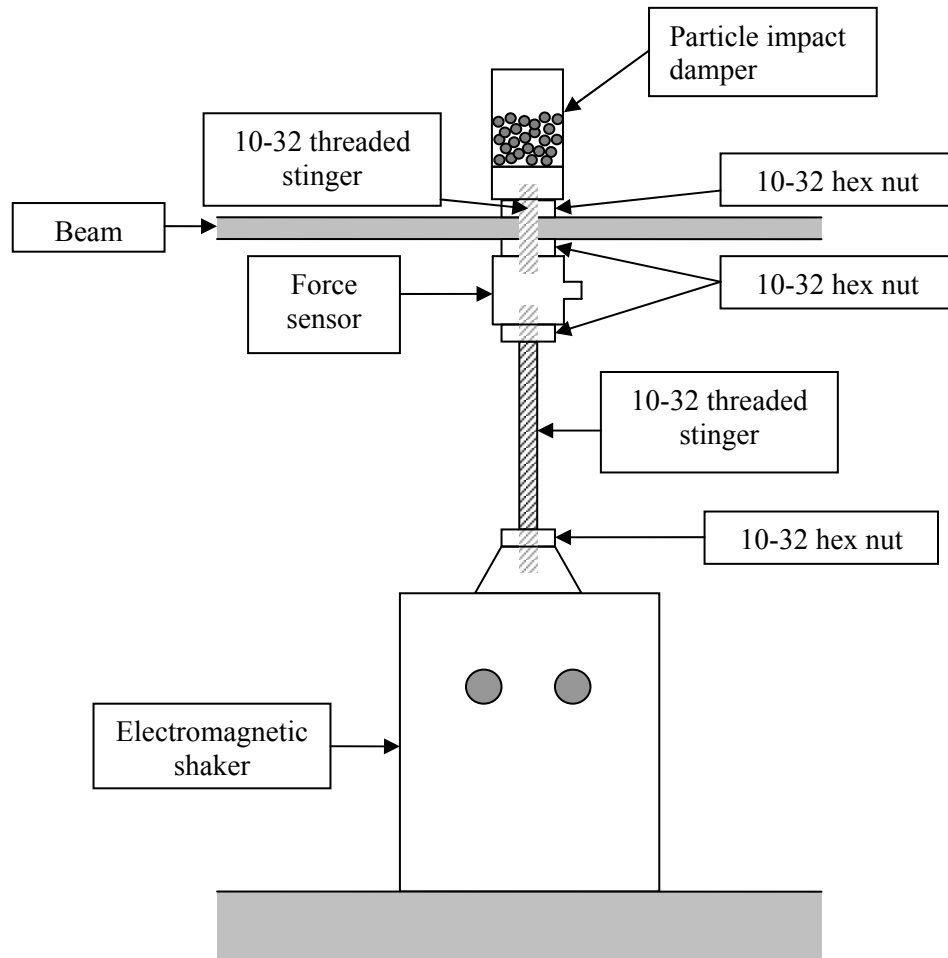


Figure 5.48: Attachment of shaker, force sensor, and PID to beam center



Figure 5.49: Aluminum enclosure with adjustable screw top

Table 5.5: List of experimental equipment

Quantity	Description
1	12 x 2 x 1/8 inch aluminum 6061 T6 beam
1	Particle enclosure
75	1/8 inch brass ball bearings
1	Beam clamping and grounding assembly
1	LDS V203 electromagnetic shaker SN 51884-19
1	PCB 208A02 force sensor SN 9801
1	Agilent 35670A dynamic signal analyzer
1	Polytec OFV 502 fiber interferometer with Polytec OFV 2600 vibrometer controller
2	10-32 threaded stinger
4	10-32 hex nut
4	Clamps
1	Roll of reflective tape

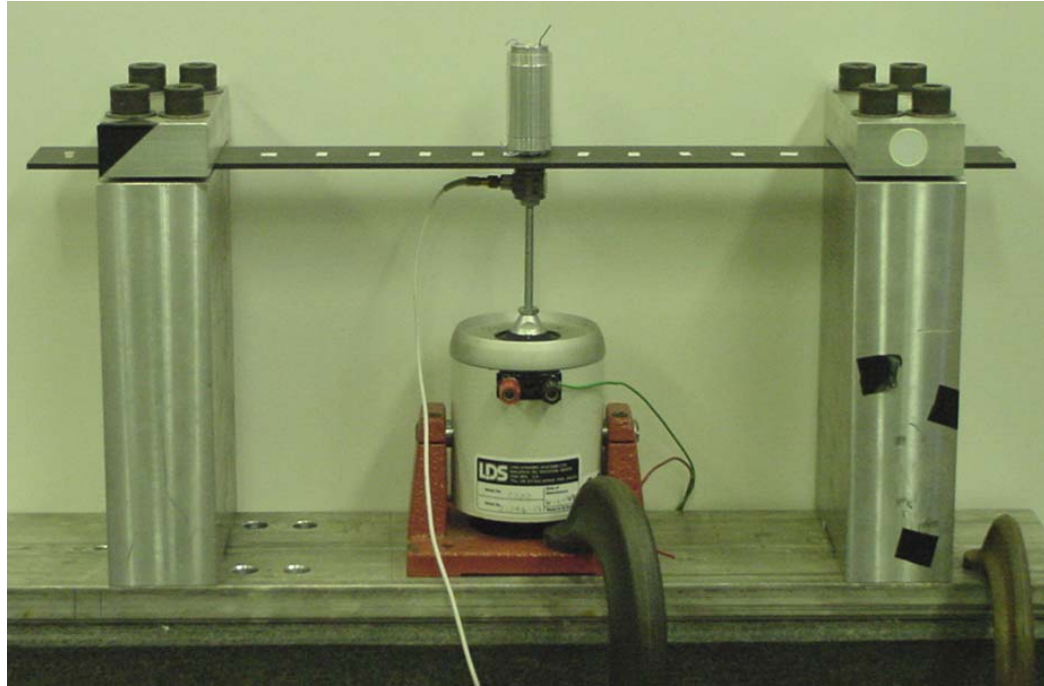


Figure 5.50: Completed beam setup

The beam was excited with a sine sweep input through its first natural frequency at different amplitudes, and with different gap sizes on the PID. The pole-zero curve fitting method (described in Appendix B, section 4) was used to compute the loss factor and natural frequency of the beam with the PID attached.

5.5.1 Prediction of Loss Factor from DPE Master Design Curve

Figure 5.51 shows a superposition of the loss factors measured during the experiment and the master design curve for power dissipation efficiency derived earlier. The gap size is indicated in the legend. The scaling between the two y-axes is arbitrary, but the agreement between the shapes of the loss factors and design curves are excellent.

The peak loss factor and both DPE occur at the same value of Δ , which is critical because it allows a designer to design a PID that provides maximum damping.

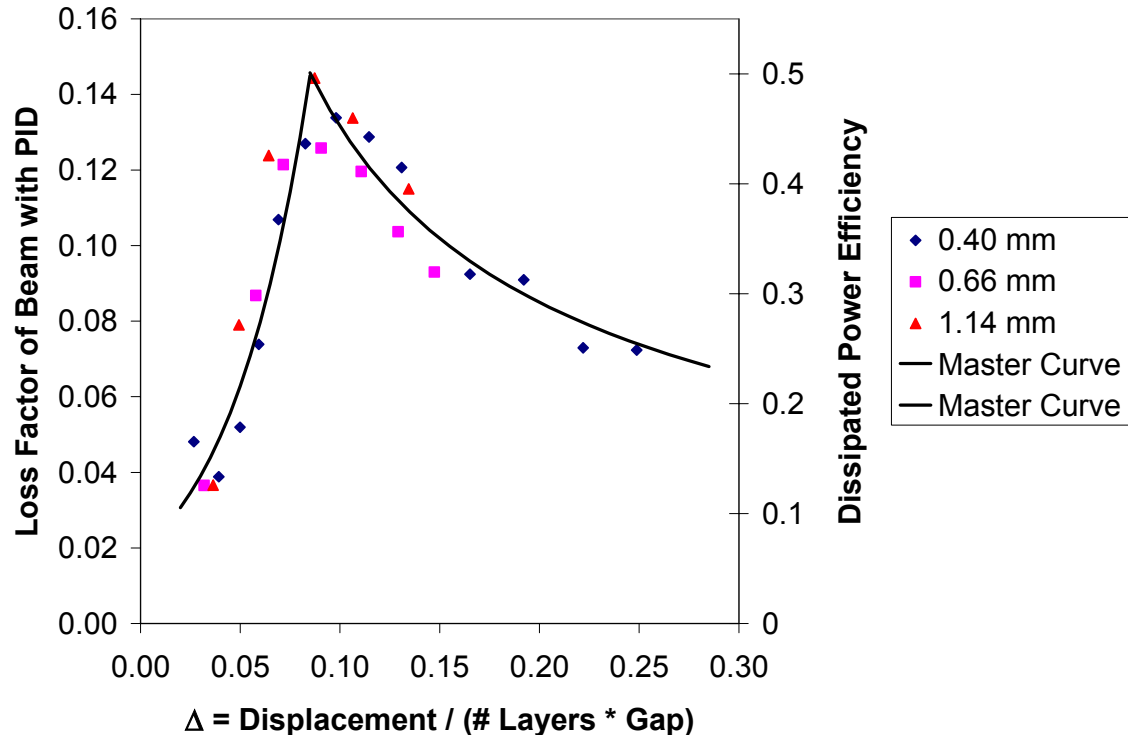


Figure 5.51: DPE master design curve and loss factor

The trends are nearly identical, but the loss factor and DPE curves are numerically different. This prevents the designer from predicting the actual value of the loss factor, which may be important in certain applications, such as active control. This can be overcome in one of two ways. The first method is take a measurement of the kinetic energy in the system, and the second method is to take one or two loss factor measurements and scale the curves.

Method One – Measurement of Kinetic Energy

Recall that the loss factor is the dissipated energy divided by the maximum energy in the system. This is expressed in terms of power as

$$\eta = \frac{\text{Real}\{P\} / \omega}{E_{\text{maximum}}} \quad (5.10)$$

where $\text{Real}\{P\}$ is the dissipated power, ω is the frequency in rad/sec, and E_{maximum} is the maximum amount of kinetic energy in the system at resonance. Equations 5.1 and 5.10 can be combined to give

$$\eta = DPE \times \frac{m_{\text{bed}} |V|^2}{E_{\text{maximum}}}. \quad (5.11)$$

The terms of Eq. 5.11 can be rearranged to express a ratio between DPE and loss factor:

$$\frac{DPE}{\eta} = \frac{E_{\text{maximum}}}{m_{\text{bed}} |V|^2}. \quad (5.12)$$

For the clamped beam that was used in this experiment, the maximum kinetic energy in the system at resonance can be calculated as the total kinetic energy in the beam plus the kinetic energy in any discrete attachments. The discrete attachments include the mass of the stingers and hex nuts, the moving mass of the shaker element, and the mass of the empty enclosure. This is expressed as

$$E_{\text{maximum}} = E_{\text{beam}} + \frac{1}{2} \sum_{i=1}^M m_j v_j^2 \quad (5.13)$$

where E_{beam} is the kinetic energy in the beam, m_j is the mass of any discrete attachments, and v_j is the velocity of those discrete attachments. The discrete attachments are all attached to the center of the beam, and therefore all have velocity equal to the beam's center.

Since it has been previously shown that the first mode shape of this beam very closely approximates the theoretical mode shape of a clamped-clamped beam (see Figure 3.12), the kinetic energy in the beam can be determined by integrating along the beam's length, L .

$$E_{beam} = \frac{1}{2} m_b \int_0^L [W_1(x)]^2 dx \quad (5.14)$$

$W_1(x)$ is the analytical expression for the mode shape of a clamped-clamped beam and is given [75] as

$$W_1(x) = A_1 [\sinh \beta_1 x - \sin \beta_1 x + \alpha_1 (\cosh \beta_1 x - \cos \beta_1 x)], \quad (5.15)$$

where

$$\alpha_1 = \frac{\sinh \beta_1 L - \sin \beta_1 L}{\cos \beta_1 L - \cosh \beta_1 L} \quad (5.16)$$

and $\beta_1 L = 4.730041$. A_1 is a constant whose value is determined by evaluating

$$W_1(x = L/2) = v_o, \quad (5.17)$$

where v_o is the velocity of the beam's center.

Using Equations 5.13 - 5.17, the kinetic energy in the system was calculated, and the ratio of DPE/ η was found to be 4.05. The scaling of the y-axes in Figure 5.51 has been updated to reflect this ratio. This is shown in Figure 5.52, which shows that using kinetic energy to scale the master curve results in a prediction of loss factor that is slightly low.

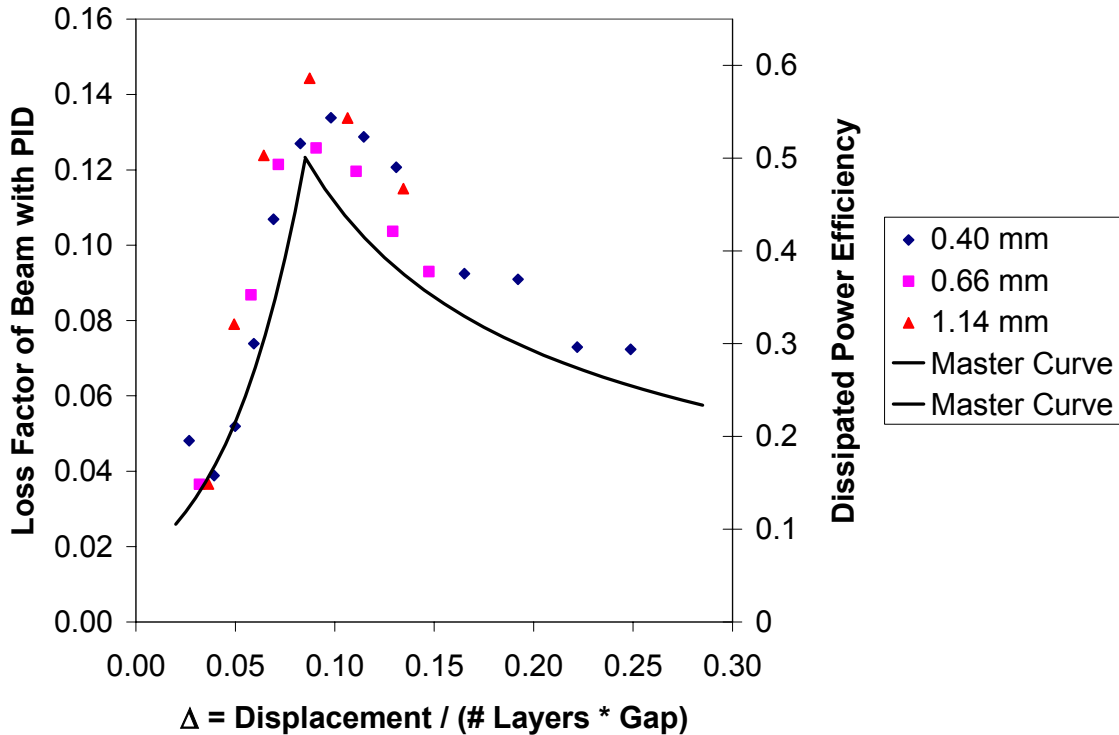


Figure 5.52: DPE master design curve and loss factor, y-axes scaled to 4.05

Method Two – Calibrate Scaling Between Loss Factor and DPE

The second way to find the loss factor is to calibrate the scaling between the loss factor and dissipated power efficiency. This is done by simply taking one or two loss factor measurements and comparing them to the values on the DPE master curve. For example, at the peak, the loss factor is 0.14 and the DPE is 0.5. Dividing 0.5 by 0.14 indicates that the DPE is 3.57 times greater than the loss factor at all points along the curve. This scaling is in good agreement with the scaling determined by the kinetic energy calculation in method one, which was 4.05. The scaling of the y-axes in Figure 5.51 has been updated to reflect the ratio of 3.57. This is shown in Figure 5.53,

which shows that calibrating the scaling gives excellent agreement between loss factor and the master curve.

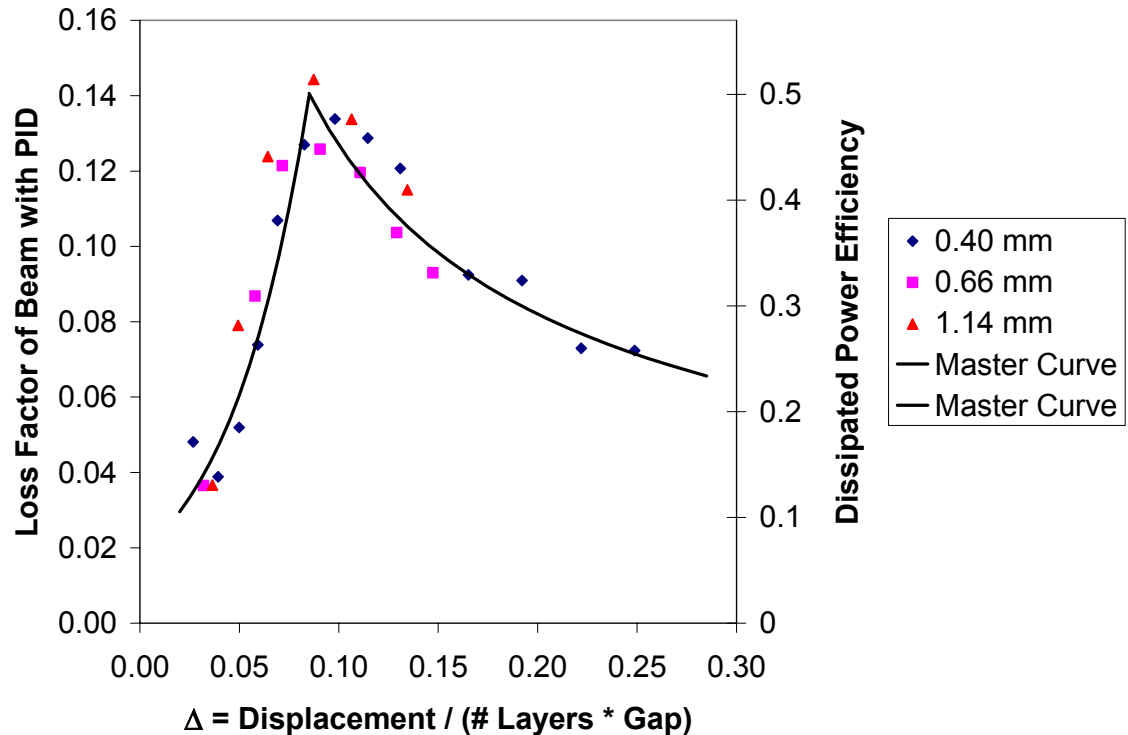


Figure 5.53: DPE master design curve and loss factor, y-axes scaled to 3.57

5.5.2 Prediction of Effective Mass from MEPP Master Design Curve

The effective mass of the PID was computed from the beam's first natural frequency. This was done by analytically solving for the first natural frequency of a beam with a mass in the center. The beam in the experiment has been referred to as having rigid boundary conditions, but the "true" boundary conditions of the experimental

beam are less than perfectly rigid. Therefore, a beam with pinned ends, rotary springs of stiffness K_I at each end, and a mass in the center M_I , is analyzed (Figure 5.54).

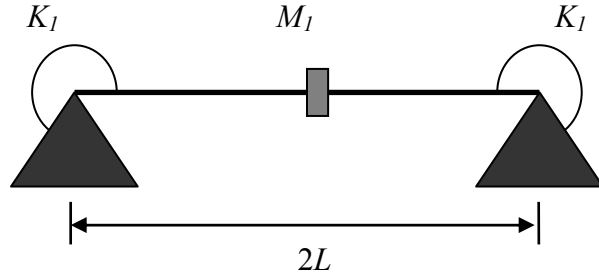


Figure 5.54: Pinned beam with rotary springs and center mass

Since the beam is symmetric about its center, it can be divided in half, giving the beam shown in Figure 5.55. The beam is half of its original length, and the right end has been replaced by a rotationally rigid boundary condition. It should be noted that using the beam's symmetry restricts the analysis to odd modes, i.e. modes whose eigenvectors are symmetric about the beam's center.

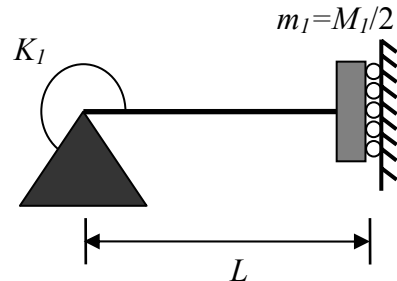


Figure 5.55: Half of symmetric beam

The equation of motion for the free vibration of a uniform beam is

$$c^2 \frac{\partial^4 w}{\partial x^4}(x, t) + \frac{\partial^2 w}{\partial t^2}(x, t) = 0, \quad (5.18)$$

where

$$c = \sqrt{\frac{EI}{\rho A}}. \quad (5.19)$$

E is the modulus of elasticity, I is the area moment of inertia, ρ is the density, A is the cross-sectional area, w is the lateral displacement of the beam, x is the coordinate along the length of the beam, and t is time.

The free vibration solution is found by using the method of separation of variables as

$$w(x, t) = W(x)T(t). \quad (5.20)$$

Substituting Eq. 5.20 into Eq. 5.18 leads to

$$\frac{c^2}{W(x)} \frac{d^4 W(x)}{dx^4} = -\frac{1}{T(t)} \frac{d^2 T(t)}{dt^2} = a \quad (5.21)$$

where $a=\omega^2$ is a positive constant. Eq. 5.21 can be written as two equations:

$$\frac{d^4 W(x)}{dx^4} - \beta^4 W(x) = 0 \quad (5.22)$$

and

$$\frac{d^2 T(t)}{dt^2} + \omega^2 T(t) = 0, \quad (5.23)$$

where

$$\beta^4 = \frac{\omega^2}{c^2} = \frac{\rho A \omega^2}{EI}. \quad (5.24)$$

The solution of Eq. 5.22 is

$$W(x) = C_1 \cos \beta x + C_2 \sin \beta x + C_3 \cosh \beta x + C_4 \sinh \beta x . \quad (5.25)$$

There are four boundary conditions for the beam, two at each end. They are

$$W(x = 0) = 0 , \quad (5.26)$$

$$EI \frac{\partial^2 w}{\partial x^2}(x = 0) = K_1 \frac{\partial w}{\partial x}(x = 0) , \quad (5.27)$$

$$EI \frac{\partial^3 w}{\partial x^3}(x = L) = \frac{M_1}{2} \frac{\partial^2 w}{\partial t^2}(x = L) = -\omega^2 \frac{M_1}{2} w(x = L) , \quad (5.28)$$

and

$$\frac{\partial w}{\partial x}(x = L) = 0 . \quad (5.29)$$

Substituting Equations 5.26 - 5.29 into Eq. 5.25 and writing in matrix form gives

$$\begin{bmatrix} 1 & 0 & 1 & 0 \\ -EI\beta & -K_1 & EI\beta & K_1 \\ Z_1 & Z_2 & Z_3 & Z_4 \\ -\sinh \beta L & \cos \beta L & \sinh \beta L & \cosh \beta L \end{bmatrix} \begin{bmatrix} C_1 \\ C_2 \\ C_3 \\ C_4 \end{bmatrix} = 0 \quad (5.30)$$

where

$$\begin{aligned} Z_1 &= \beta^3 EI \sin \beta L + \omega^2 m_1 \cos \beta L \\ Z_2 &= -\beta^3 EI \cos \beta L + \omega^2 m_1 \sin \beta L \\ Z_3 &= \beta^3 EI \sinh \beta L + \omega^2 m_1 \cosh \beta L \\ Z_4 &= \beta^3 EI \cosh \beta L + \omega^2 m_1 \sinh \beta L \end{aligned} \quad (5.31)$$

The natural frequencies are found by setting the determinant of the square matrix in Eq. 5.30 to zero and solving for β , which must be done numerically.

The total mass at the center of the beam is comprised of both the effective mass of the PID as well as the combined mass of the stingers and hex nuts. This is expressed as

$$M_1 = m_{ss} + m, \quad (5.32)$$

where m_{ss} is the combined mass of the stingers and hex nuts (13.35 grams), and m is the effective mass of the PID.

The value of the rotary spring, K_I , was found by measuring the first natural frequency of the beam without the PID attached. This value of K_I was then used to solve for the effective mass of the PID, m .

Figure 5.56 shows the effective mass of the PID as calculated by the beam's first natural frequency. The effective mass follows the same trend as the MEPB master design curve. Recall that the effective mass should theoretically have a lower bound equal to the static mass of the PID without any particles (46.35 grams), and an upper bound equal to the static mass of the PID with particles (56.85 grams). The figure clearly shows that the upper bound has been violated. This is in agreement with observations made previously in Chapter 3, section 3.4, and lends further credibility to the possibility that the PID can have an effective mass that exceeds its statically measured mass.

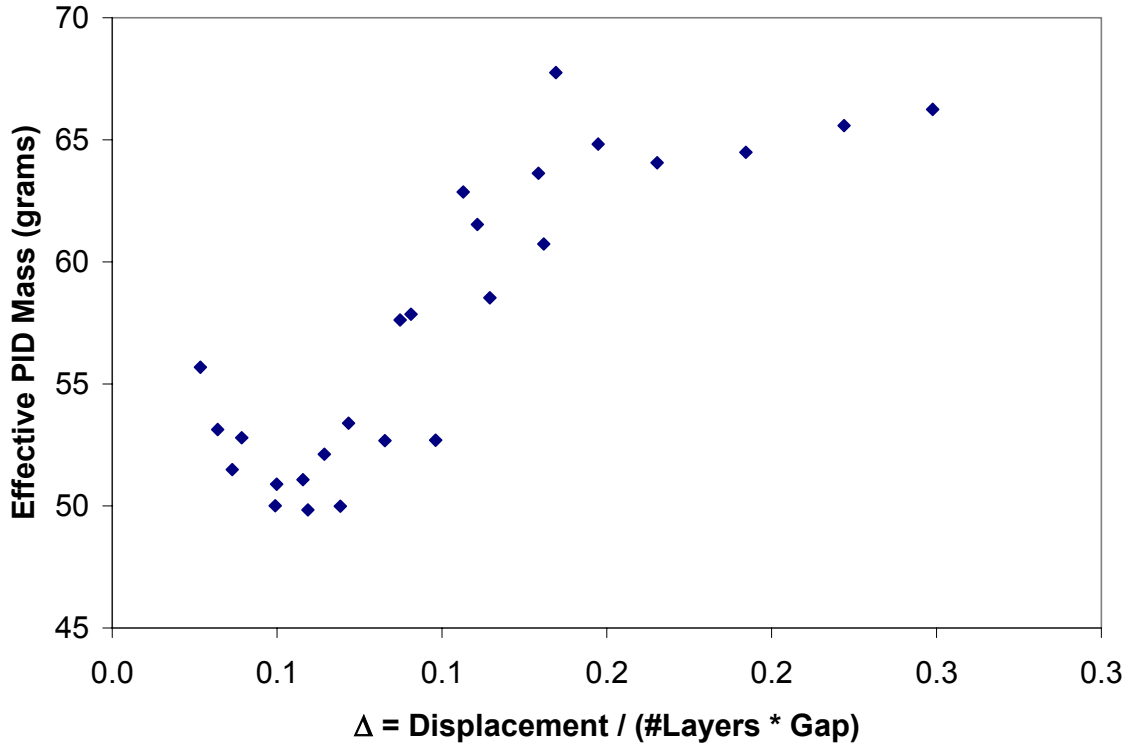


Figure 5.56: Effective mass of PID calculated from beam's first natural frequency

The mass efficiency of the particle bed (MEPB) was calculated from the effective mass using Eq. 5.5 and is superposed with the master design curve for mass in Figure 5.57. The basic trend of the two data sets is similar, and the dip (osculation point) occurs at the same value of Δ , but otherwise there is not much agreement.

There are several sources of error. One is that the equation used to calculate the effective mass of the PID is not completely correct because the experimental beam does not have perfectly rigid boundary conditions, as is assumed in the equation. Another possibility is that the imaginary, or reactive component of power contains elements that are not purely mass-like. Other errors exist in the pole-zero natural frequency computation and power measurements. The results are still deemed acceptable for the

purposes for this work because the primary objective is to design optimal PID treatments that give maximum damping. Predicting the mass contribution of the PID is a secondary concern.

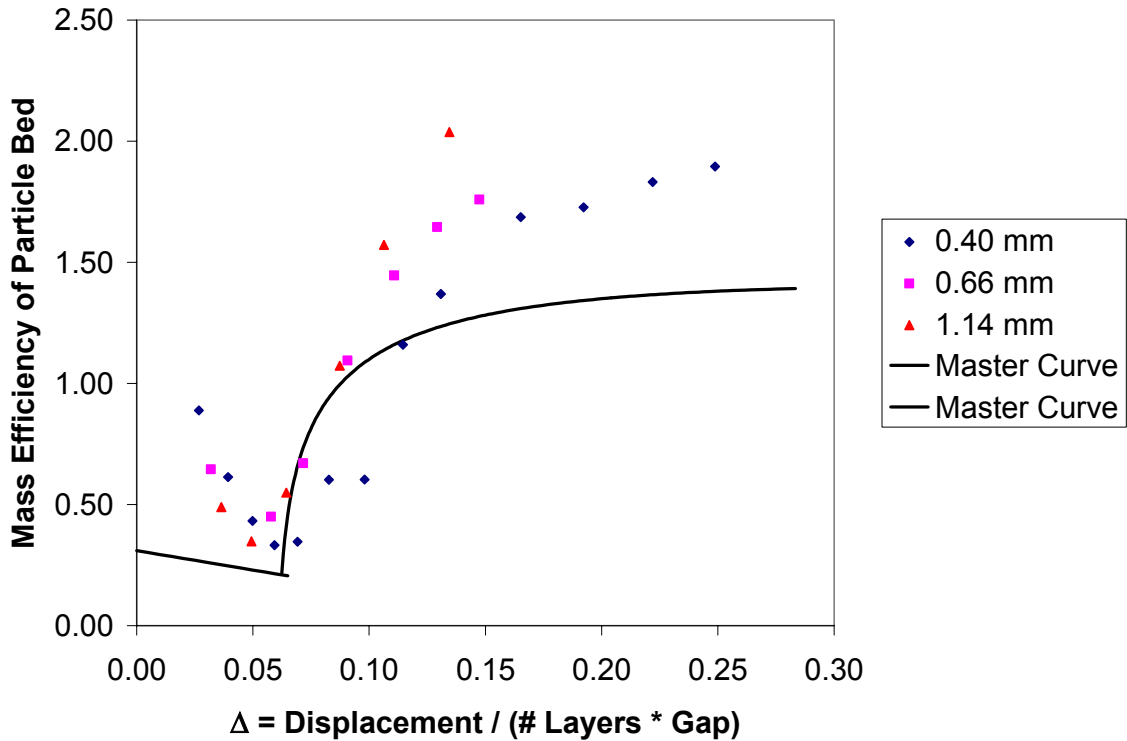


Figure 5.57: Mass efficiency of the particle bed based on natural frequency and master design curve

5.6 PID Design Recommendations

This section presents several recommendations for the design of particle impact damping treatments. Included are suggested strategies to build the master design curves,

limits of the design curves, some general recommendations for PID design, and other considerations a designer may wish to take into account.

5.6.1 Building the Master Design Curves

When designing a PID for a particular application, the first step is to build the master design curves by taking several power measurements. These measurements should ideally be conducted under conditions that approximate the range of conditions (displacement, frequency) of the application. The properties (gap size, particle size, particle bed mass) of the PID should likewise cover the full range of the design space as much as is practically possible. The trendline for the dissipated power efficiency master design curve is defined by two constants for each part of the curve. The trendline for mass efficiency of the particle bed is defined by two constants for the part of the curve pertaining to floor impacts only, and by six constants for the part of the curve pertaining to floor and ceiling impacts. Therefore, a minimum of twelve measurement points need to be taken, one for each constant. However, for greater accuracy, it is recommended that a significantly larger number of measurement points be taken. It is particularly important to accurately capture the peak of the DPE master design curve, since it corresponds to the highest amount of damping.

5.6.2 Limitations of the Master Design Curves

It is important to keep the limitations of the master design curves in mind. Using the master design curves to design PID's for conditions or with properties outside of those used to generate the design curves carries some risk, which is the possibility that the fundamental assumptions concerning the behavior of the particle bed will be violated. These assumptions are that the particle bed moves together (exhibits bulk motion), that it is under the influence of gravity, the impacts occur at regularly spaced intervals, and that the impacts between the particle bed and enclosure wall are inelastic. Examples of cases that could violate these assumptions include zero-gravity conditions, horizontal excitation of the enclosure, non-sinusoidal excitation, and the use of a single particle or layer of particles.

Since the master design curve for mass did not accurately match the mass contribution of the PID when placed on a structure, great care should be taken when attempting to predict the mass effect. This is especially true when the primary structure has a mass that is close to the effective mass of the PID. For many applications, however, the mass of the primary structure will be significantly larger than that of the PID. In these cases, the inaccuracies of the master design curve for mass may not prove significant.

5.6.3 Recommended Number of Layers

The behavior of the particles, and therefore the damping efficiency of the PID, is dependent upon the variable $\Delta = \text{Displacement} / (\# \text{Layers} \times \text{Gap})$. The displacement, or

amplitude of the vibration is typically not under the control of the designer, which means that the two critical design variables for a given PID are the number of particle layers and gap size. To maintain maximum damping, the number of layers and the gap size are inversely related, e.g. if the number of layers is doubled, the gap size must be halved. It has been shown that large gap sizes are advantageous because they result in a PID that is more robust: small changes or measurement errors in gap size can still result in optimal or near-optimal damping. Using a large gap size requires the number of layers to be small, which brings up two concerns. The first is that the assumptions that the particle bed moves together and impacts the enclosure inelastically will be violated. The second concern is that using a small number of layers can result in a damper that is very noisy. Conversely, it was shown that using a large number of layers results in greater bed compression, which makes the measurement of gap sizes more difficult. Therefore, based on the experiments done here, the recommended number of layers is between four and five.

Regardless of the number of layers chosen, it is important to ensure that the gap size is not so small as to prevent the peak dissipated power efficiency from being reached. This was observed when a very small gap size was used for a relatively large particle size.

5.6.4 Other Recommendations and Considerations

The amount of power dissipated is proportional to the amplitude of vibration. Therefore, particle impact dampers are ideally placed on structures in locations of high

motion. Using more massive particle beds also increases the total amount of power dissipated. However, increasing the effective mass of the PID too much can have detrimental effects, including undesired mass-loading effects on the primary structure, and a significant reduction in the amplitude of vibration at the location of the PID.

Noise is another concern, as the repeated impacts of the particles can be quite loud. Using smaller particles decreases the amount of noise emitted, but it tends to increase the number of layers, with the adverse effects previously discussed. Another solution is to use a viscoelastic material to coat the inside of the enclosure or the particles. The effect this might have on performance has not been thoroughly studied, however.

5.6.5 Recommended Design Procedure

Designing the PID for a vibrating structure will be an iterative process. The first step is to perform a dynamic analysis of the primary structure. The frequency of interest, the vibration amplitude of the attachment point, and the kinetic energy in the untreated structure should be determined. The second step is to determine the required mass of the particle bed. This is based on the target loss factor as well as the amount of kinetic energy in the untreated structure. If the required particle mass exceeds a design constraint, then the target loss factor may need to be lowered. The third step is to determine the response of the structure with the PID attached. Adding a PID results in a reduction of the vibration amplitude at the attachment point due to both the damping and mass effects. Since the damping and mass characteristics of the PID are nonlinear with

respect to vibration amplitude, the calculation of the response of the structure must be iterated until a steady solution is reached. In order for the target loss factor to be achieved, the design variables of the PID (gap size, number of layers, total particle mass) may need to be changed to compensate for the decreased amplitude.

5.7 Summary and Conclusions

In this chapter, the power measurements taken for a broad range of frequencies, displacements, particle sizes, gap sizes, and particle bed masses were collapsed on non-dimensional parameters into two master design curves. One curve is for dissipated power and the other is for the effective mass of the particle impact damper. These design curves explain the fundamental physics of PID behavior and can be used by designers to design treatments for vibrating structures.

An experiment was conducted on a beam structure in an attempt to validate the master design curves. It was discovered that the match between loss factor and the design curve for dissipated power efficiency was nearly exact. Unfortunately, the design curve for mass efficiency of the particle bed did not match the effective mass as computed from the natural frequency of the beam. This is a secondary concern, since the primary focus is to design PID's for maximum damping capacity. The beam experiment also gave greater credence to the possibility that the effective mass of the PID can exceed the statically measured mass under certain conditions.

Finally, a series of recommendations were made concerning the design of PID treatments. Construction and limitations of the master design curves were discussed, as well as the recommended number of particle layers, and other concerns such as noise.

Chapter 6

Conclusions and Future Work

This thesis focuses on the use of particle impact dampers (PIDs) to add damping to vibrating systems. It has three fundamental goals: 1) to develop better insight into the behavior of PIDs, 2) to identify and characterize key design variables, and 3) to develop a model of the damping and mass properties of the PID.

6.1 Early Experimental Work

Early experiments were designed to provide a preliminary insight into the behavior of particle impact dampers, aid in the identification of key design variables, and shape the experiments that were to follow.

It was revealed that the placement of a PID on a vibrating structure is important. Locations of higher motion allow the PID to dissipate more energy. Changing the gap size revealed that the amount of dissipation was maximized at an optimum value. The effective mass of the PID was also affected, generally decreasing with increasing gap size. The formation of a dark coating on the particles caused a reduction in the amount of damping provided by the PID. Certain materials such as copper and aluminum were found to form this dark coating at a faster rate than other materials such as brass. The decision was made to use brass particles in following experiments to avoid the formation of this dark coating and thereby increase the repeatability of the data.

6.2 Development and Verification of Power Measurement Technique

It was quickly realized that using the traditional method of determining the damping contribution of the particle impact damper by measuring loss factor would have significant drawbacks. Therefore, a method to measure the dissipative and reactive components of power flow into the particle impact damper was devised. Unlike loss factor measurements, these measurements can be made at any frequency and amplitude and can be applied to any structure. They are also considerably less time consuming than loss factor measurements. In order to relate the results of this thesis to the work in the literature, equations were developed to relate the dissipative and reactive power to loss factor added to a base structure and effective mass, respectively.

A series of experiments were conducted to validate the power measurement technique. Power measurements were made of several lumped masses to confirm the computation of effective mass from reactive power. Comparison of the computed masses with the statically measured masses agreed. Next, a series of experiments was conducted that demonstrated dissipated power measurements could be used to predict the loss factor added to a structure with a PID under the same operating conditions.

6.3 Measurement of Particle Impact Damper Properties Using Power

An extensive series of measurements was performed that characterized the damping and mass properties of PIDs with respect to key design variables, as well as any interdependence between variables. Based on past literature and the earlier experimental work, the key design variables were identified as amplitude, frequency, gap size, particle

size, and mass of the particle bed. All of these measurements were done with vertical excitation of the PID.

Increasing the amplitude (displacement) of the PID causes an increase in dissipated power, effective mass, and the optimum gap size required to obtain maximum power dissipation. A transition displacement was also found, which corresponds to the conditions that result in ceiling impacts by the particle bed. Exceeding the transition displacement generally results in higher amounts of dissipated power and effective mass.

The effect of particle size was determined by using different numbers of different sized particles, while keeping the total mass of the particle bed the same. It was found that the peak power dissipation obtained at the optimum gap size is the same for all particle sizes, which implied the dependence of the peak power on the mass of the particle bed. Increasing the size of the particles results in higher optimum gap sizes. Also, larger particles have a greater range of gap sizes that result in near-maximum dissipation. This is important from a design standpoint, because it means that using larger particles results in a more robust damper. Finally, larger particle sizes result in a higher effective mass.

A neural network was used to interpolate the available data and determine the effect of frequency. Increasing the frequency of excitation generally increases the dissipated power. The exception exists for small particles with small gap sizes. In this case, the dissipated power seems relatively independent of frequency.

6.4 Slow Motion Videos

High speed digital video cameras were used to observe the motion of the particles in slow motion. The goal was to gain insight into the behavior of the particle bed, explain some of the data trends previously observed, and to provide a foundation for modeling efforts.

The videos showed how changing the orientation of the enclosure from vertical excitation to horizontal excitation drastically changes the behavior of the particles. Vertical excitation is characterized by bulk motion of the particle bed, whereas horizontal motion causes the particles to move like a liquid “sloshing” from side to side. This observation led to the decision to limit modeling efforts and observation to the case of vertical excitation.

Impact of the particle bed with the enclosure wall appears to be nearly instantaneous and almost perfectly inelastic. A slight expansion and contraction of the particle bed also occurs. Using a single larger particle instead of a bed of particles results in extremely unpredictable behavior.

The optimum gap size occurs under conditions where the particle bed and enclosure are moving towards each other at maximum relative velocity. Gap sizes below optimum size cause the impact to occur when the enclosure has low relative velocity, and gap sizes above optimum result in the deceleration of the particle bed by the force of gravity. Particle beds consisting of larger particles exhibit greater expansion after impact, which decreases the spacing between the particle bed and the enclosure. The result is an

increase in the range of gap sizes that still result in ceiling impact as well as a higher optimum gap size.

Finally, higher amplitudes result in prolonged contact between the particle bed and the enclosure. This results in a higher effective mass.

6.5 Master Design Curves

The available power data was condensed into two master design curves, one for dissipated power, and one for effective mass. These design curves explain the fundamental physics of PID behavior and can be easily used by designers to design PID treatments. The data is systematically collapsed around unitless parameters that are comprised of the following design variables: frequency, gap size, displacement, particle size (or number of layers), and total mass.

The x-axis reflects the motion of the particles relative to the enclosure. For that reason, *displacement/(# layers * gap size)* was chosen. The y-axis reflects the damping and mass properties of the PID. Therefore, the y-axis of both design curves was expressed as an efficiency. The damping properties are expressed as the dissipated power efficiency (DPE), which is the ratio of the dissipated power divided by the total power in the particle bed. The mass properties are expressed in terms of the mass efficiency of the particle bed (MEPB), which is a ratio of the effective mass of the particle bed divided by its static mass.

The DPE master design curve is characterized by a peak, which corresponds to the maximum possible power dissipation. The MEPB master design curve is

characterized by a dip, which is the “osculation” condition. This is where the particle bed begins to impact the enclosure ceiling.

To verify the master design curves, a PID was placed on a beam with clamped boundary conditions. The loss factor measurements are in excellent agreement with those estimated using the DPE master design curve. The effective mass measurements do not agree as extensively with the MEPD design curve. They do however, have the same basic trends and predicted the osculation point in the same place.

6.6 Design Recommendations

The damping and mass properties of a PID are a function of displacement, gap size, and the number of layers in the particle bed. Since the displacement of the PID is not typically under the control of a designer, gap size and number of layers are the primary design considerations. Based on the work presented in this thesis, it is recommended that between four and five particle layers be used, and the gap size adjusted accordingly.

PID's should also be placed in locations of high motion, where they will be able to dissipate more power. Increasing the mass of the particle bed will increase the power dissipated, but it will also increase the effective mass, which can cause a reduction in the amplitude of vibration, and negate the added power dissipation from the added mass. Finally, the amount of acoustic noise emitted by the PID may need to be taken into consideration. Generally, a fewer number of larger particles emits more noise than a greater number of smaller particles.

6.7 Summary of Major Contributions

The major contributions from this thesis are presented below.

- Development of a power measurement technique, which allows for the rapid measurement of the dynamic properties of the particle impact damper. The primary advantage of this technique over traditional techniques is the ability to take measurements at any amplitude and frequency, and to apply the results to any structure.
- Exploration of the mass effect of the particle impact damper, which had not been extensively explored by other researchers. This includes insights on how the effective mass of the PID can change with varying amplitude, gap size, particle size, and particle mass.
- Direct observation of particle motion under varying conditions, which is an important contribution to the insight necessary to explain data trends and predict behavior.
- Identification of the key design variables, which are amplitude, frequency, gap size, particle size, and particle mass.
- The development of master design curves that predict the damping and mass properties of a PID and provide insight into particle behavior. This includes the “osculation” condition, which corresponds to minimum effective mass, and the

peak dissipated power efficiency, which corresponds to the maximum difference in relative velocity between the particle bed and enclosure.

- A set of recommendations which should prove helpful to designers. This includes proper selection of the number of layers in the particle bed, and adjusting the gap size accordingly. It also includes recommendations on PID placement and mass of the particle bed, as well as acoustic noise considerations.

6.8 Future Work

This thesis has established a set of techniques that allow for the development of master PID design curves. However, additional research is needed to address discrepancies in this work and different scenarios. These include:

- Excitation in orientations other than the vertical. This includes horizontal excitation, as well as orientations in between the vertical and horizontal.
- Response of the particle impact damper to non-sinusoidal motion.
- Excitation at high frequencies (greater than 1000 Hz).
- The use of non-spherical particles or non-metallic particles.
- The use of conglomerate particle beds comprised of different particle sizes and shapes.
- Use of viscoelastic or other “soft” materials to coat the enclosure and/or particles to reduce emitted noise and increase dissipated power.
- Shaped impact plates to increase power dissipation, e.g. concave impact plates that could increase particle-particle interaction upon impact.

- Active control of the gap size to allow for changing operating conditions.
- The development of optimization algorithms that could recommend non-intuitive solutions.
- Clarification of the reactive component of power, which predicts effective masses that can exceed the static mass of the particle impact damper.

Bibliography

1. L.L. Beranek, *Noise and Vibration Control*. McGraw-Hill, New York. 1971.
2. L.H. Bell and D.H. Bell, *Industrial Noise Control: Fundamentals and Applications*. Marcel Dekker, Inc., 1994.
3. P. Lieber and D.P. Jensen, *Transactions of the ASME*. pp. 523-530. An acceleration damper: Development, design, and some applications. 1945.
4. C. Grubin, *Trans. ASME, Journal of Applied Mechanics*. **23**(3), pp. 373-378. On the theory of the acceleration damper. 1956.
5. G.B. Warburton, *Trans. ASME, Journal of Applied Mechanics*. **24**, pp.322-324. Discussion of On the theory of the acceleration damper. 1957.
6. M.A. Valuswami and F.R.E. Crossley, *Trans. ASME, Journal of Engineering for Industry*. pp. 820-827. Multiple impacts of a ball between two plates. Part 1: some experimental observations. August 1975.
7. M.M. Sadek, B. Mills, *Journal of Mechanical Engineering Science*, **12**(4), pp. 268-277. Effect of gravity on the performance of an impact damper: part 1. Steady-state motion. 1970.
8. M.M. Sadek, C.J.H. Williams, *Journal of Mechanical Engineering Science*, **12**(4), pp. 278-287. Effect of gravity on the performance of an impact damper: Part 2. Stability of vibrational modes. 1970.
9. C.N. Bapat and S. Sankar, *Journal of Sound and Vibration*, **99**(1), pp. 85-94. Single unit impact damper in free and forced vibration. 1985.
10. S. Ema and E. Marui, *International Journal of Machine Tools and Manufacture*, **34**(3), pp. 407-421. A fundamental study on impact dampers. 1994.
11. C. Cempel and G. Lotz, *Journal of Structural Engineering*, **119**(9), pp. 2642-2652. Efficiency of vibrational energy dissipation by moving shot. September 1993.
12. A. Papalou and S.F. Masri, *Journal of Vibration and Control*, **4**, pp. 361-379. An experimental investigation of particle dampers under harmonic excitation. 1998.
13. J.J. Hollkamp and R.W. Gordon, *Proceedings of SPIE – The International Society for Optical Engineering. Smart Structures and Materials. Passive Damping and*

- Isolation: Mar 2-3, 1998. San Diego, CA, 3327*, pp. 2-12. Experiments with Particle Damping. 1998.
14. A. Papalou and S.F. Masri, *Earthquake Engineering and Structural Dynamics*, **25**, pp. 253-267. Response of impact dampers with granular materials under random excitation. 1996.
 15. H.V. Panossian and D.L. Bice, *Rocketdyne Corporation Document*. Low frequency applications of non-obstructive particle damping (NOPD).
 16. S.F. Masri, *The Journal of the Acoustical Society of America*, **47**(1), pp. 229-237. General motion of impact dampers. 1970.
 17. N. Popplewell and M. Liao, *Journal of Sound and Vibration*, **146**(3), pp. 519-526. A simple design procedure for optimum impact dampers. 1991.
 18. W.M. Mansour and D.R. Teixeira Filho, *Journal of Sound and Vibration*, **33**(3), pp. 247-265. Impact dampers with Coulomb friction. 1974.
 19. S.F. Masri and A.M. Ibrahim, *Earthquake Engineering and Structural Dynamics*, **1**, pp. 337-346. Stochastic excitation of a simple system with impact damper. 1973.
 20. C.N. Bapat, N. Popplewell, K. McLachlan, *Journal of Sound and Vibration*, **87**(1), pp. 19-40. Stable periodic motions of an impact pair. 1983.
 21. N. Popplewell, C.N. Bapat, K. McLachlan, *Journal of Sound and Vibration*, **87**(1), pp. 41-59. Stable periodic vibroimpacts of an oscillator. 1983.
 22. Blazejcyk-Okolewska and Peterka, *Chaos, Solitons & Fractals*, **9**(8), pp. 1321-1338. An investigation of the dynamic system with impacts. 1998.
 23. R.D. Friend and V.K. Kinra, *Journal of Sound and Vibration*, **233**(1), pp. 93-118. Particle impact damping. 2000.
 24. S.F. Masri and A.M. Ibrahim, *Journal of the Acoustical Society of America*, **53**(1), pp. 200-211. Response of the impact damper to stationary random excitation. 1973.
 25. M.A. Veluswami, F.R.E. Crossley, G. Horvay, *Journal of Engineering for Industry, Transactions of the ASME*, pp. 838-835. Multiple impacts of a ball between two plates. Part 2: Mathematical modeling. August 1975.
 26. S. Chatterjee, A.K. Mallik, A. Ghosh, *Journal of Sound and Vibration*, **193**(5), pp. 1003-1014. Impact dampers for controlling self-excited oscillation. 1996.

- 27 Y. Araki, I. Yokomichi, J. Inoue, *Bulletin of JSME*, **28**(241), pp. 1466-1472. Impact damper with granular materials (2nd report, both sides impact in a vertical oscillating system). July 1985.
- 28 Y. Araki, Y. Jinnouchi, J. Inoue, *ASME PVP Division*, **133**, pp. 87-93. Impact damper with granular materials. 1988.
- 29 Y. Araki, Y. Jinnouchi, J. Inoue, I. Yokomichi, *Seismic Engineering*, **182**, pp. 73-79. Indicial response of impact damper with granular material. July 23-27, 1989.
- 30 I. Yokomichi, Y. Araki, Y. Jinnouchi, J. Inoue, *Journal of Pressure Vessel Technology*, **118**, pp. 95-103. Impact damper with granular materials for multibody system. February 1996.
- 31 S. Maley, *Particulate Enhanced Damping of Sandwich Structures, Ph.D. Dissertation, Purdue University*. August 2001.
- 32 B.L. Fowler, E.M. Flint, S.E. Olson, *Proceedings of SPIE – The International Society for Optical Engineering. Smart Structures and Materials. Damping and Isolation*. **3989**, pp. 356-367. Effectiveness and predictability of particle damping. 2000.
- 33 B.L. Fowler, E.M. Flint, S.E. Olson, *Proceedings of SPIE – The International Society for Optical Engineering. Smart Structures and Materials*. Paper #4331-20. Design methodology for particle damping. March 4-8, 2001.
- 34 C. Saluena, S.E. Esipov, T. Poschel, S. Simonian, *Proceedings of SPIE – The International Society for Optical Engineering. Smart Structures and Material: Passive Damping and Isolation. Mar 2-3, 1998. San Diego, CA*. **3327**, pp. 23-29. Dissipative properties of granular ensembles. 1998.
- 35 C. Saluena, S.E. Esipov, D. Rosenkranz, H. Panossian, *Proceedings of SPIE – The International Society for Optical Engineering. Smart Structures and Material: Passive Damping and Isolation. Mar 1-2, 1999. Newport Beach, CA*. **3672**, pp. 32-42. On modeling of arrays of passive granular dampers. 1999.
- 36 C. Saluena, T. Poschel, S.E. Esipov, *Physical Review E*, **59**(4), pp. 4422-4425. Dissipative properties of vibrated granular materials. April 1999.
- 37 C. Tianning, M. Kuanmin, H. Xieqing, M.Y. Wang, *Proceedings of SPIE – The International Society for Optical Engineering. Smart Structures and Material: Damping and Isolation. Mar 5-7, 2001. Newport Beach, CA*. **4331**, pp. 294-301. Dissipation mechanisms of non-obstructive particle damping using discrete element method. 2001.

38. B. Wang and M. Yang, *Journal of Materials Processing Technology*, **105**, pp. 67-72. Damping of honeycomb sandwich beams. 2000.
39. S. Maley and C.T. Sun, *Advances in Aerospace Materials and Structures, ASME, AD-58*, pp. 53-64. Particulate enhanced damping in sandwich structures. 1999.
40. H.V. Panossian, *1990 JANNAF Propulsion Meeting, 2-4 October, Anaheim, CA*. Structural damping/acoustic attenuation optimization via NOPD. 1990.
41. H.V. Panossian, *Proceedings of Damping '89*, p. KBC 1-9. Nonobstructive impact damping applications for cryogenic environments. 1989.
42. K.P. Duffy, R.L. Bagley, O. Mehmed, *NASA Tech Briefs, LEW-16833*. A self-tuning impact damper for rotating blades.
43. S. Ema and E. Marui, *International Journal of Machine Tools & Manufacture*, **36**(3), pp. 293-306. Damping characteristics of an impact damper and its application. 1996.
44. E. Skipor and L.J. Bain, *Trans. ASME, Journal of Mechanical Design*, **102**, pp. 338-343. Application of impact damping to rotary printing equipment. April 1980.
45. T. Sato, K. Tanaka, S. Aida, Y. Mouri, *JSME International Journal, Series C*, **38**(3), pp. 434-440. Vibration isolation in a system using granular medium. 1995.
46. Z. Ying and S.E. Semercigil, *Journal of Sound and Vibration*, **150**(3), pp. 520-530. Response of a new tuned vibration absorber to an earthquake-like random excitation. 1991.
47. S.E. Semercigil, D. Lammers, Z. Ying, *Journal of Sound and Vibration*, **156**(3), pp. 445-459. A new tuned absorber for wide-band excitations. 1992.
48. F. Collette, D. Huynh, S.E. Semercigil, *Proc. Of the International Modal Analysis Conference, IMAC*, **1**, pp. 404-410. Further results with tuned absorber – impact damper combination. 2000.
49. S. Ma and S.E. Semercigil, *Journal of Sound and Vibration*, **208**(3), pp. 349-366. A modified passive tuned absorber for secondary systems under random excitation. 1997.
50. S.S. Simonian, *Proceedings of SPIE – The International Society for Optical Engineering. Smart Structures and Material: Passive Damping. Mar 1-2, 1995. San Diego, CA*, **2445**, pp. 149-160. Particle beam damper. 1995.

51. H.R. Hamilton III, G.S. Riggs, J.A. Pickett, *Journal of Structural Engineering*, **126**(4), pp. 530-537. Increased damping in cantilevered traffic signal structures. 2000.
52. A.A. Oledzki, I. Siwicki, J. Wisniewski, *Mechanism and Machine Theory*, **34**, pp. 243-253. Impact dampers in application for tube, rod and rope structures. 1999.
53. S. Ema, E. Marui, *International Journal of Machine Tools & Manufacture*, **40**, pp. 1141-1156. Suppression of chatter vibration of boring tools using impact dampers. 2000.
54. M.D. Thomas, W.A. Knight, M.M. Sadek, *Journal of Engineering for Industry*, pp. 859-866. The impact damper as a method of improving cantilever boring bars. August 1975.
55. B.D. Nordwall, *Aviation Week and Space Technology*, pg. 50. New material could lessen blast risk to aircraft. January 7, 2002.
56. C. Cempel, *Journal of Sound and Vibration*, **40**(2), pp. 249-266. Receptance model of the multi-unit vibration impact neutralizer – “MUVIN”. 1975.
57. C.N. Bapat and S. Sankar, *Journal of Sound and Vibration*, **103**(4), pp. 457-469. Multiunit impact damper – re-examined. 1985.
58. L.C. Sutherland, *Sonic and Vibration Environments for Ground Facilities... a Design Manual*. National Aeronautics and Space Administration. George C. Marshall Space Flight Center, Huntsville, Alabama. NAS8-11217. 1968. pp. 3-123.
59. S.S. Rao, *Mechanical Vibrations*, Third Edition. Addison-Wesley Publishing Company. 1995. pp. 204-205.
60. G.T. Murray. *Introduction to Engineering Materials: Behavior, Properties, and Selection*. Marcel Dekker, Inc. 1993. p. 123.
61. D.L. Cronin and N.K. Van, *Trans. ASME, Journal of Engineering for Industry*, pg. 1295-1300. November 1975.
62. N. Popplewell and S.E. Semercigil, *Journal of Sound and Vibration*, **133**(2), pp. 193-223. Performance of the bean bag impact damper for a sinusoidal external force. 1989.
63. G.F. Franklin, J.D. Powell, A. Emami-Naeini. *Feedback Control of Dynamic Systems*. Third Edition. Addison-Wesley Publishing Company, Inc. 1994.
64. www.airpot.com. Specifications for Stock Dashpot Model 2KS160.

65. H. Demuth and M. Beale. *Neural Network Toolbox: For Use with MATLAB[®]*. Version 4. The Mathworks, Inc. 2002. pp. 1-5 to 1-7.
66. L. Fausett. *Fundamentals of Neural Networks: Architectures, Algorithms, and Applications*. Prentice-Hall, Inc. Upper Saddle River, New Jersey. 1994. p. 289.
67. H. Demuth and M. Beale. *Neural Network Toolbox: For Use with MATLAB[®]*. Version 4. The Mathworks, Inc. 2002. pp. 5-2.
68. M.T. Hagan, H.B. Demuth, and M. Beale. *Neural Network Design*. PWS Publishing Company, 1996. pp. 11-8 to 11-4.
69. H. Demuth and M. Beale. *Neural Network Toolbox: For Use with MATLAB[®]*. Version 4. The Mathworks, Inc. 2002. pp. 5-28 to 5-29.
70. M.T. Hagan and M.B. Menhaj. “Training Feedforward Networks with the Marquardt Algorithm.” *IEEE Transactions on Neural Networks*. Vol. 5, No. 6. November 1994.
71. M.T. Hagan, M.B. Demuth, and M. Beale. *Neural Network Design*. PWS Publishing Company. 1996. pp. 12-19 to 12-27.
72. J.S. Arora. *Introduction to Optimum Design*. Mc-Graw Hill, Inc. 1989. p. 319.
73. J.S. Arora. *Introduction to Optimum Design*. Mc-Graw Hill, Inc. 1989. p. 326.
74. S. Ema and E. Marui. “Damping Characteristics of an Impact Damper and its Application.” *International Journal of Machine Tools & Manufacture*. Vol. 36, No. 3. 1996. pp. 293-306.
75. S.S. Rao, *Mechanical Vibrations*, Third Edition. Addison-Wesley Publishing Company. 1995. p. 527.

Appendix A

Description of Enclosures

This Appendix provides detailed descriptions and machine drawings of the enclosures used in the experiments. Assembly instructions are also included in the event duplicate enclosures are desired.

There are two enclosures that were primarily used in the particle impact damper experiments. The first enclosure is constructed primarily of aluminum with transparent, acrylic walls. The second enclosure is constructed entirely of aluminum. Both enclosures have an adjustable screw top and securing ring which allows the gap size to be easily and securely adjusted.

A.1 Acrylic-Aluminum Enclosure

This enclosure is constructly mostly of aluminum and features an acrylic wall, which allows for direct observation of particle motion. This is the enclosure used for the high speed digital videos in Chapter 4. A picture of the enclosure with particles is shown in Figure A.1.



Figure A.1: Acrylic-aluminum enclosure

The enclosure consists of five parts which are displayed in an exploded assembly view in Figure A.2. Epoxy is used to connect the cap, enclosure wall, and bottom. The securing ring, screw top, and cap connect with threads.

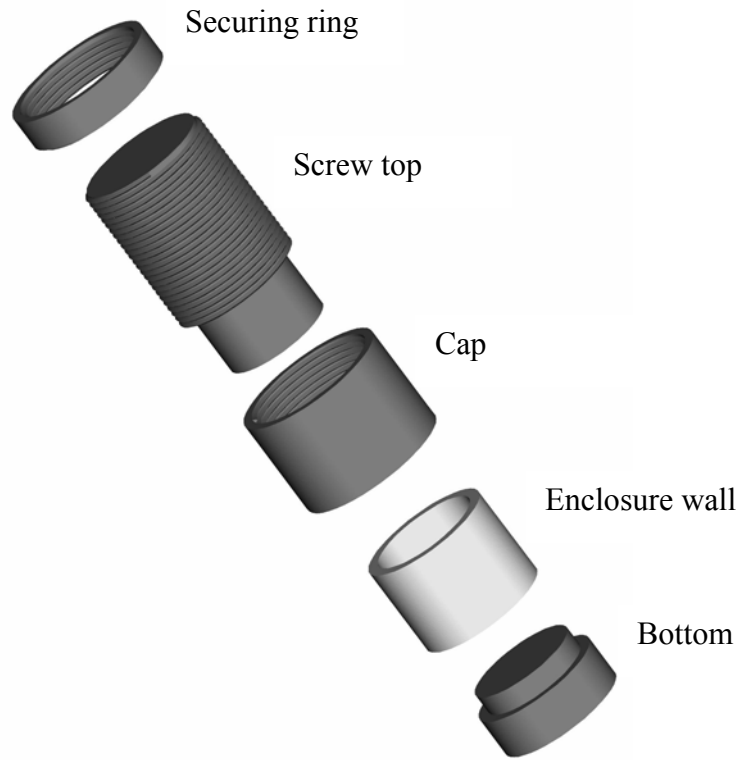


Figure A.2: Exploded view of acrylic-aluminum enclosure

Machine drawings of each part are shown in Figures A.3 - A.7.

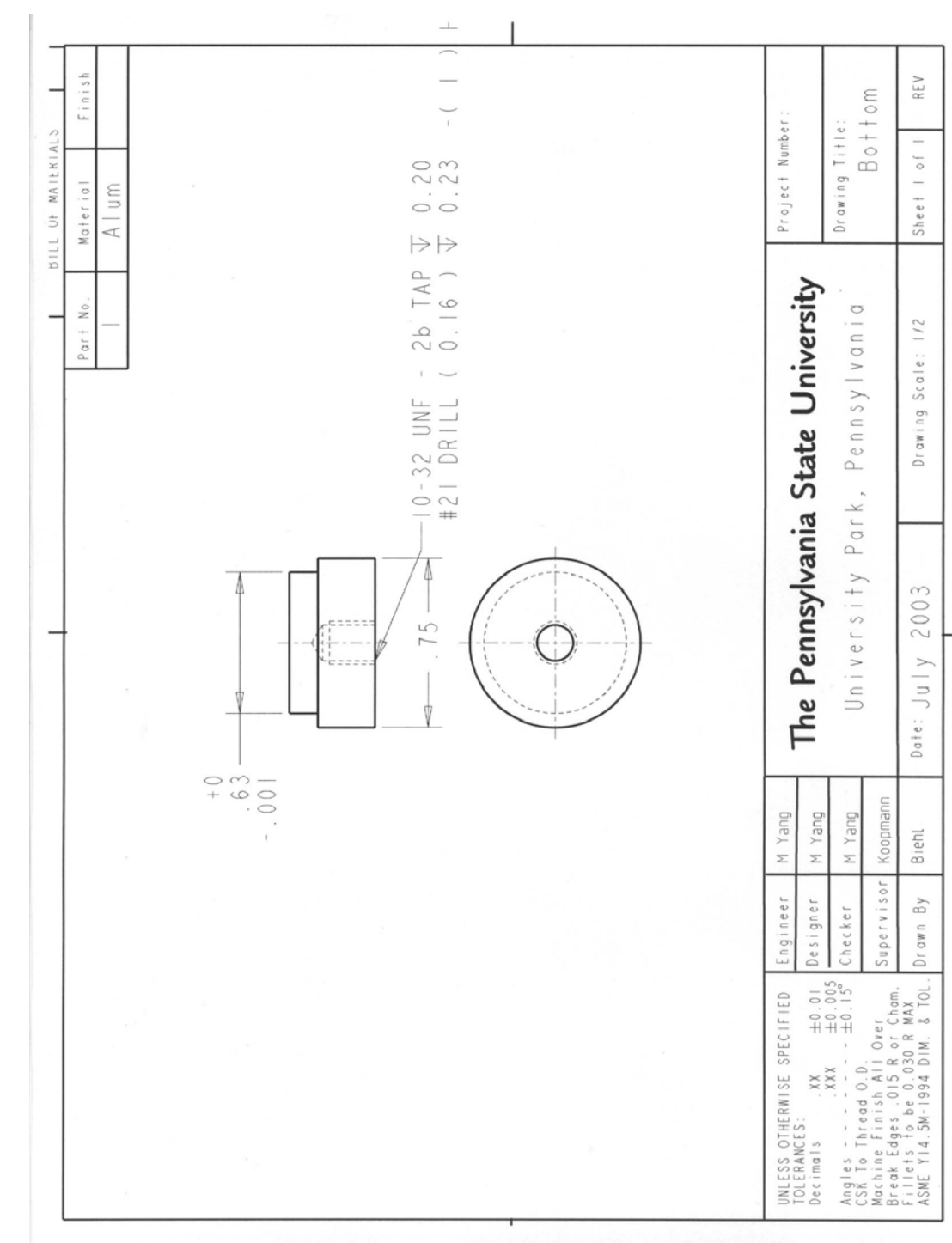


Figure A.3: Acrylic-aluminum enclosure – bottom machine drawing

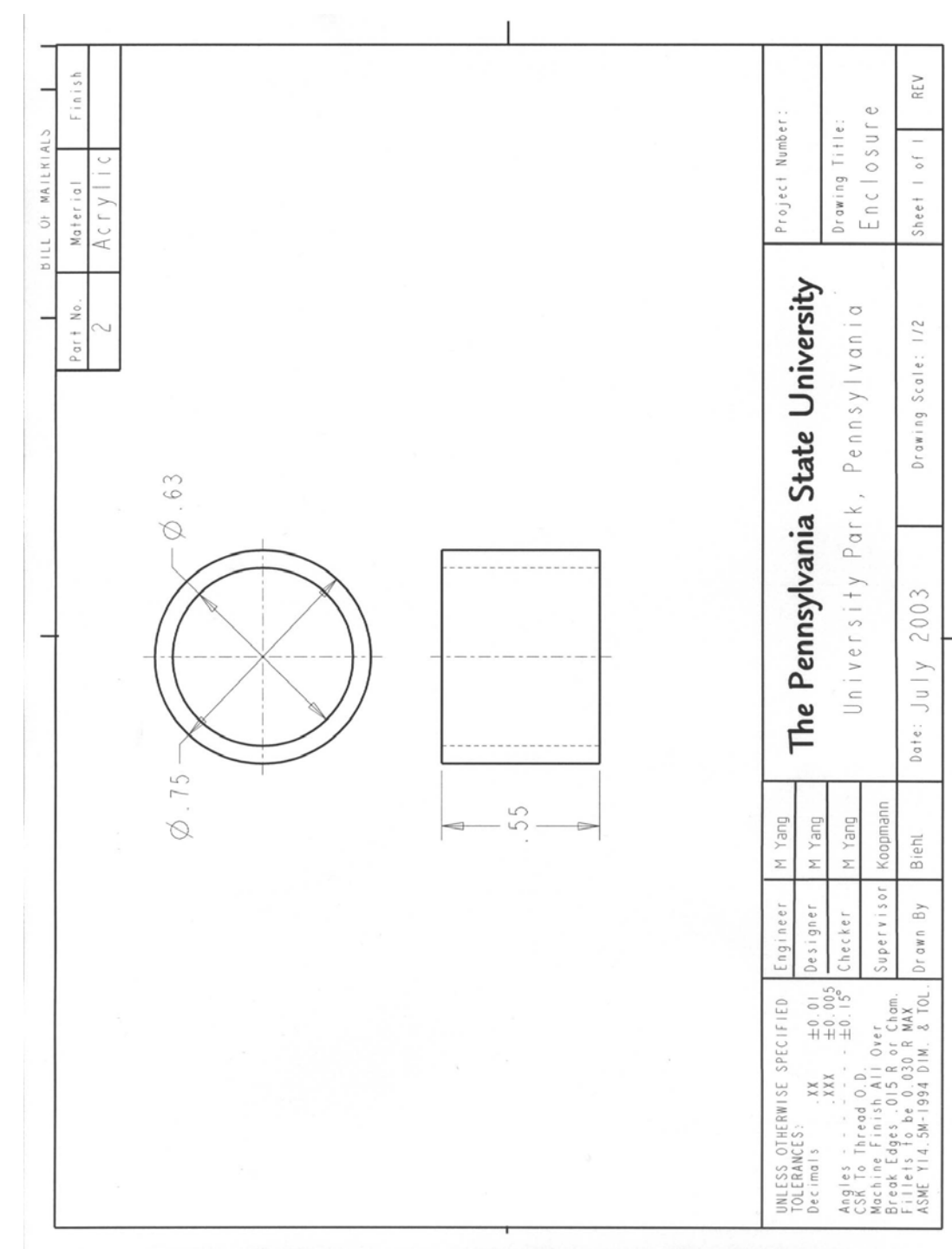


Figure A.4: Acrylic-aluminum enclosure – enclosure wall machine drawing

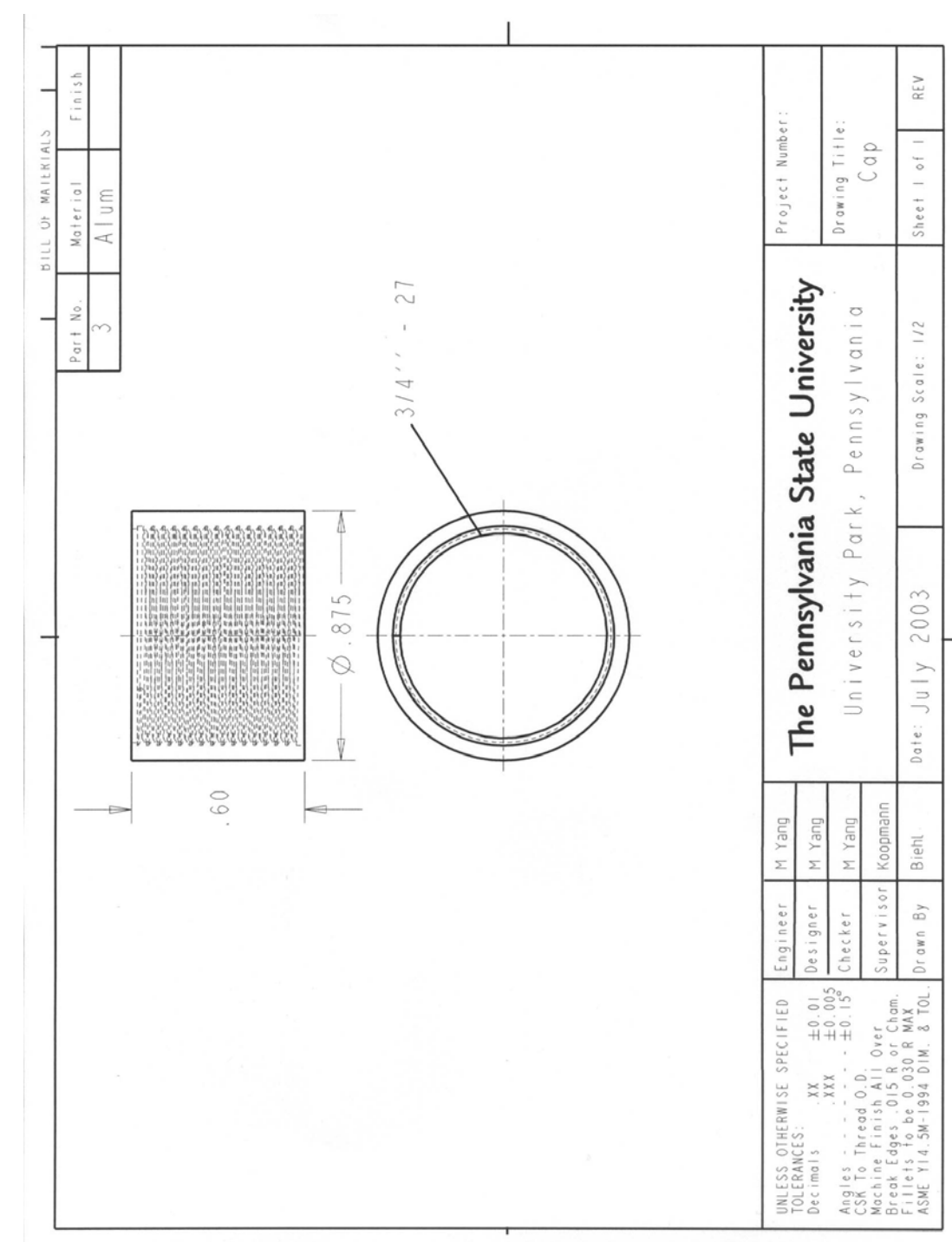


Figure A.5: Acrylic-aluminum enclosure – cap machine drawing

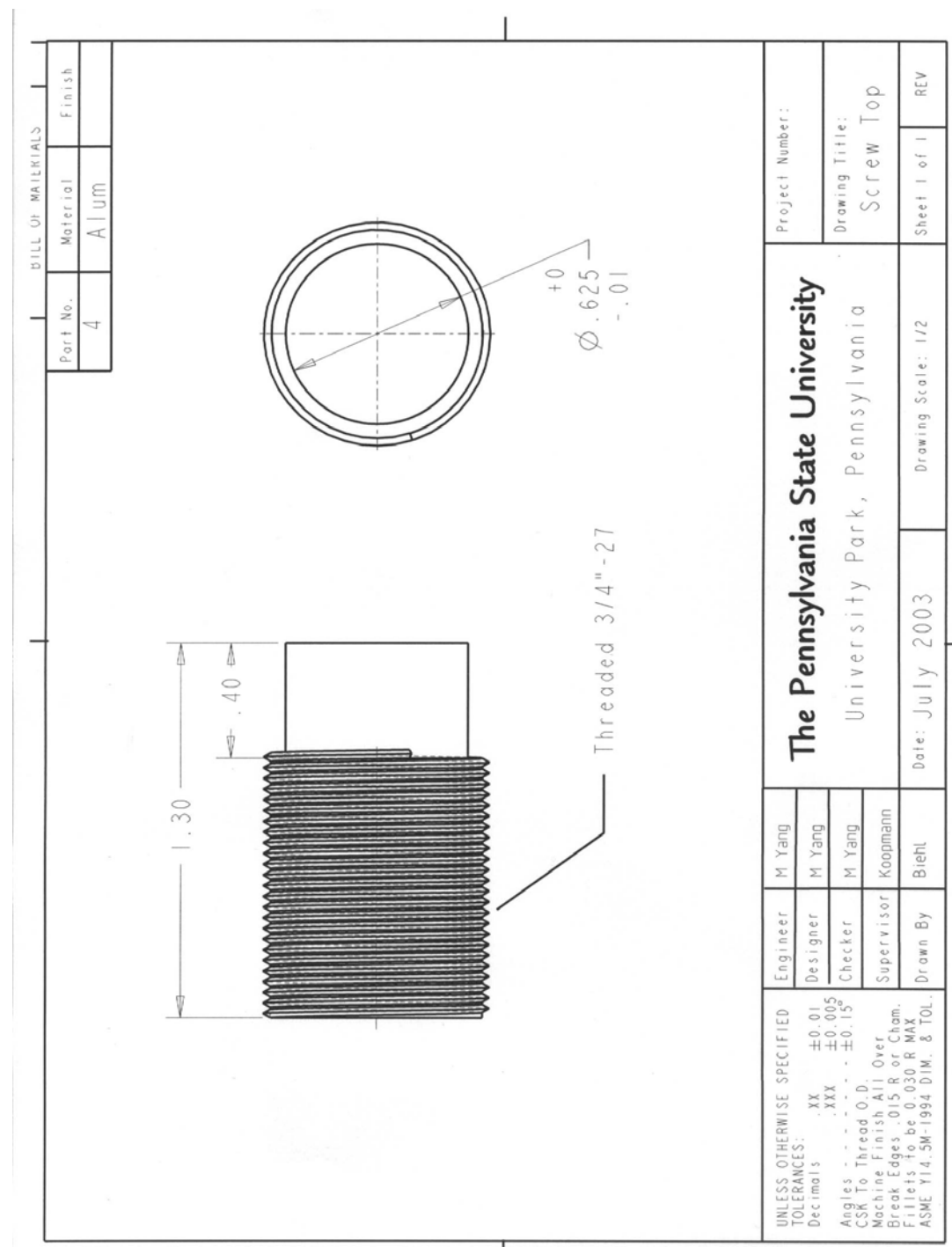


Figure A.6: Acrylic-aluminum enclosure – screw top machine drawing

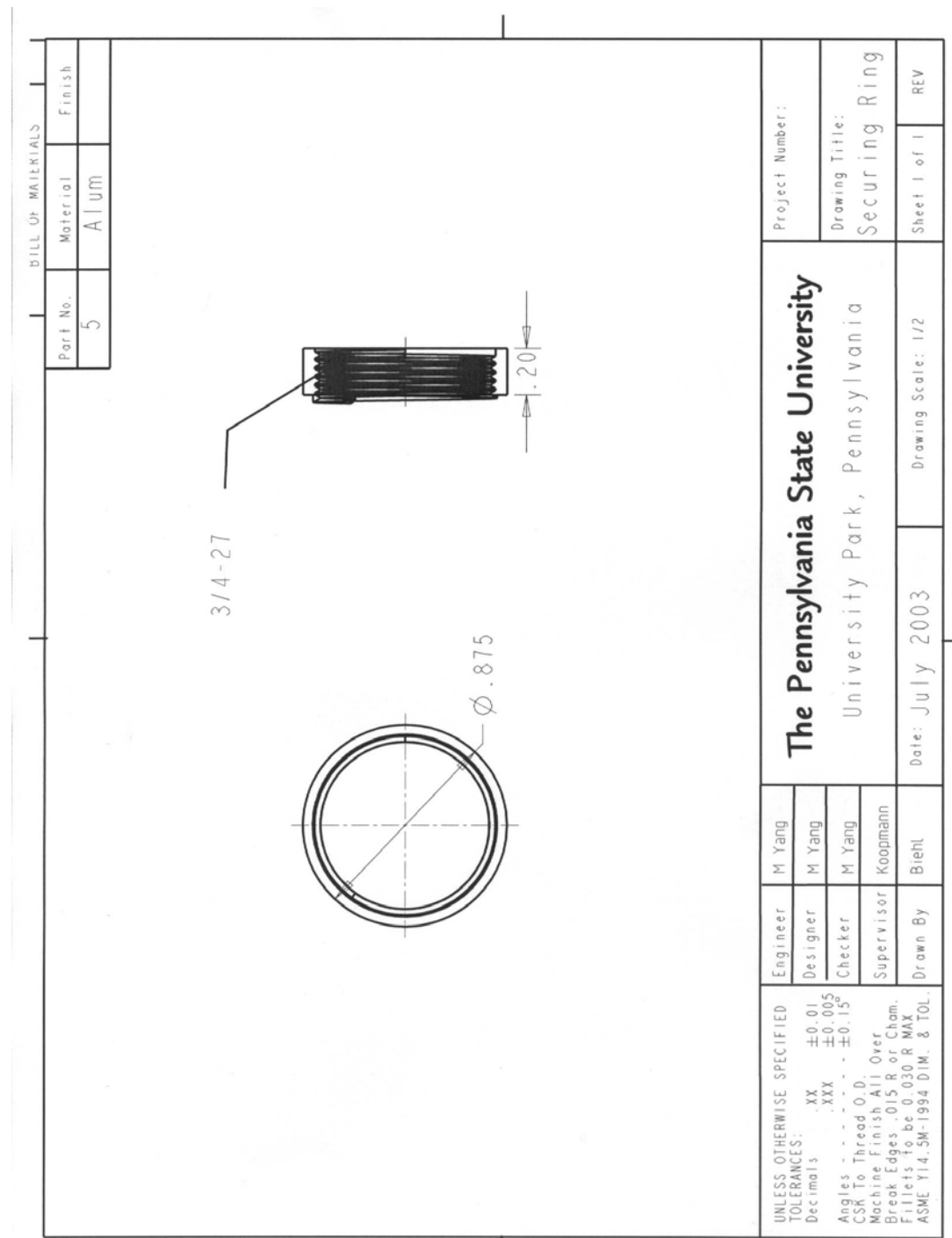


Figure A.7: Acrylic-aluminum enclosure – securing ring machine drawing

A.2 Aluminum Enclosure

This enclosure is constructed entirely out of aluminum. A picture of the enclosure is shown in Figure A.8.

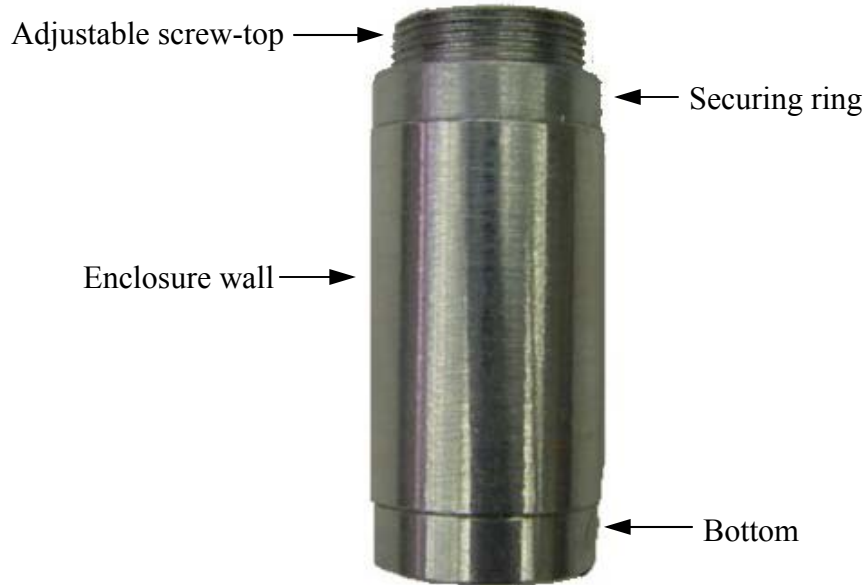


Figure A.8: Aluminum enclosure

The enclosure consists of four parts which are displayed in an exploded assembly view in Figure A.9. All parts connect through mating threads. Machine drawings of each part are shown in Figures A.10 - A.13.

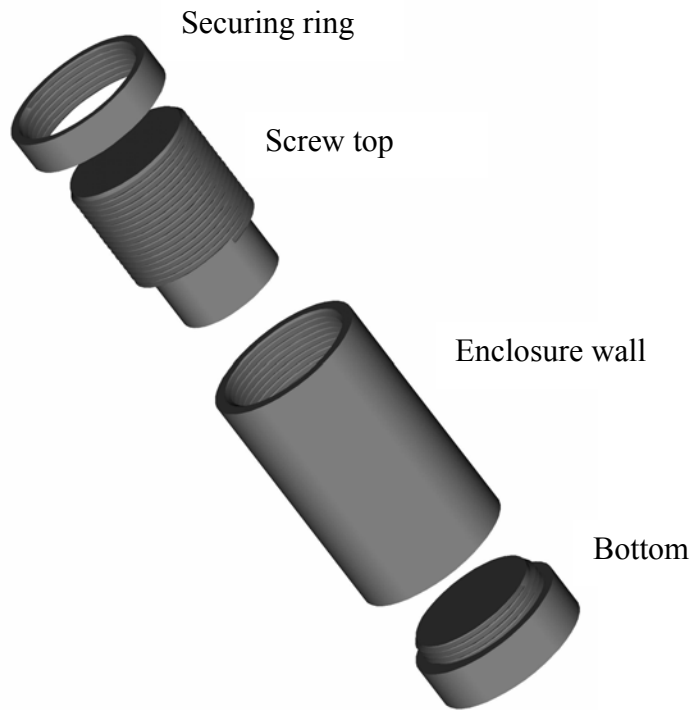


Figure A.9: Exploded view of aluminum enclosure

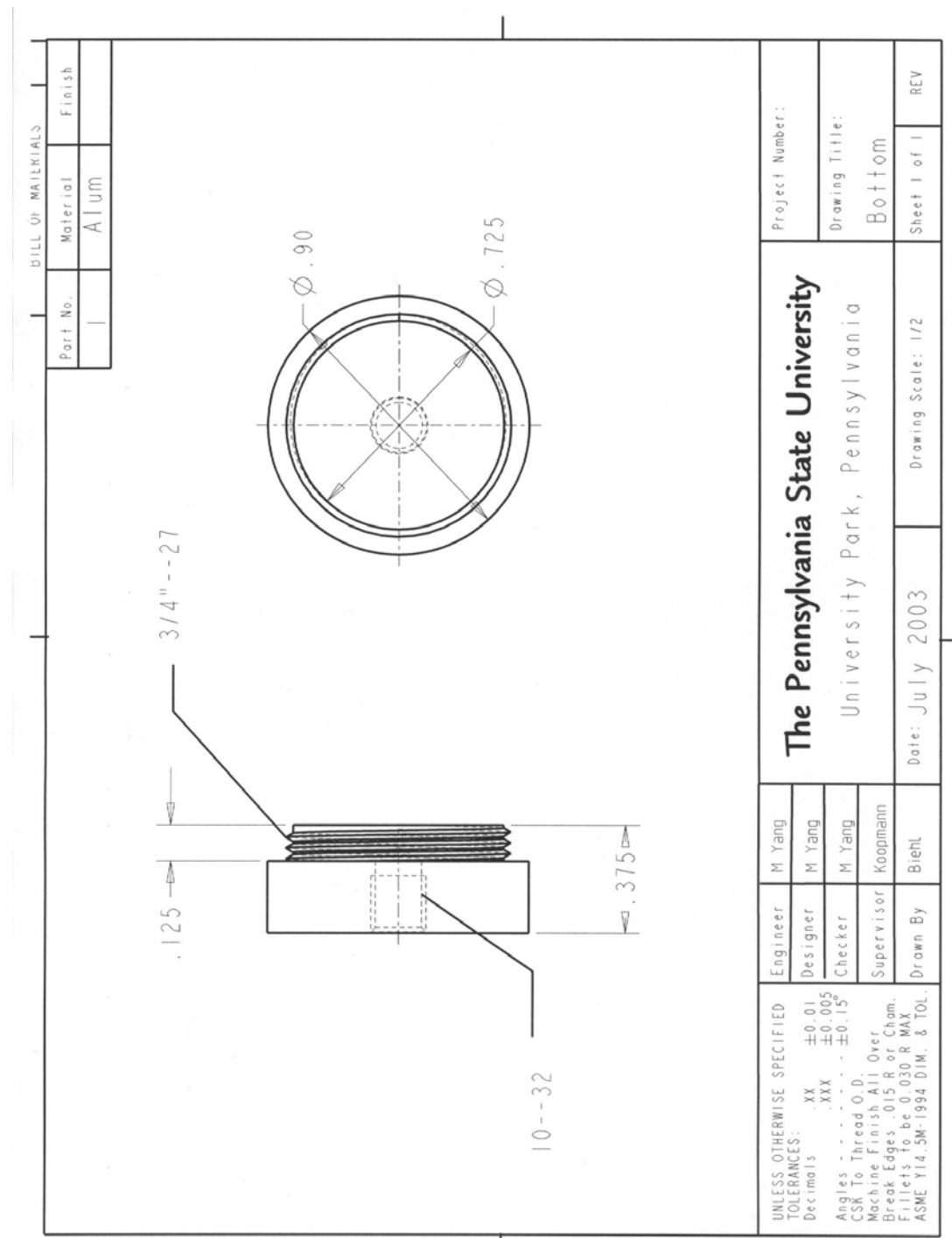


Figure A.10: Aluminum enclosure – bottom machine drawing

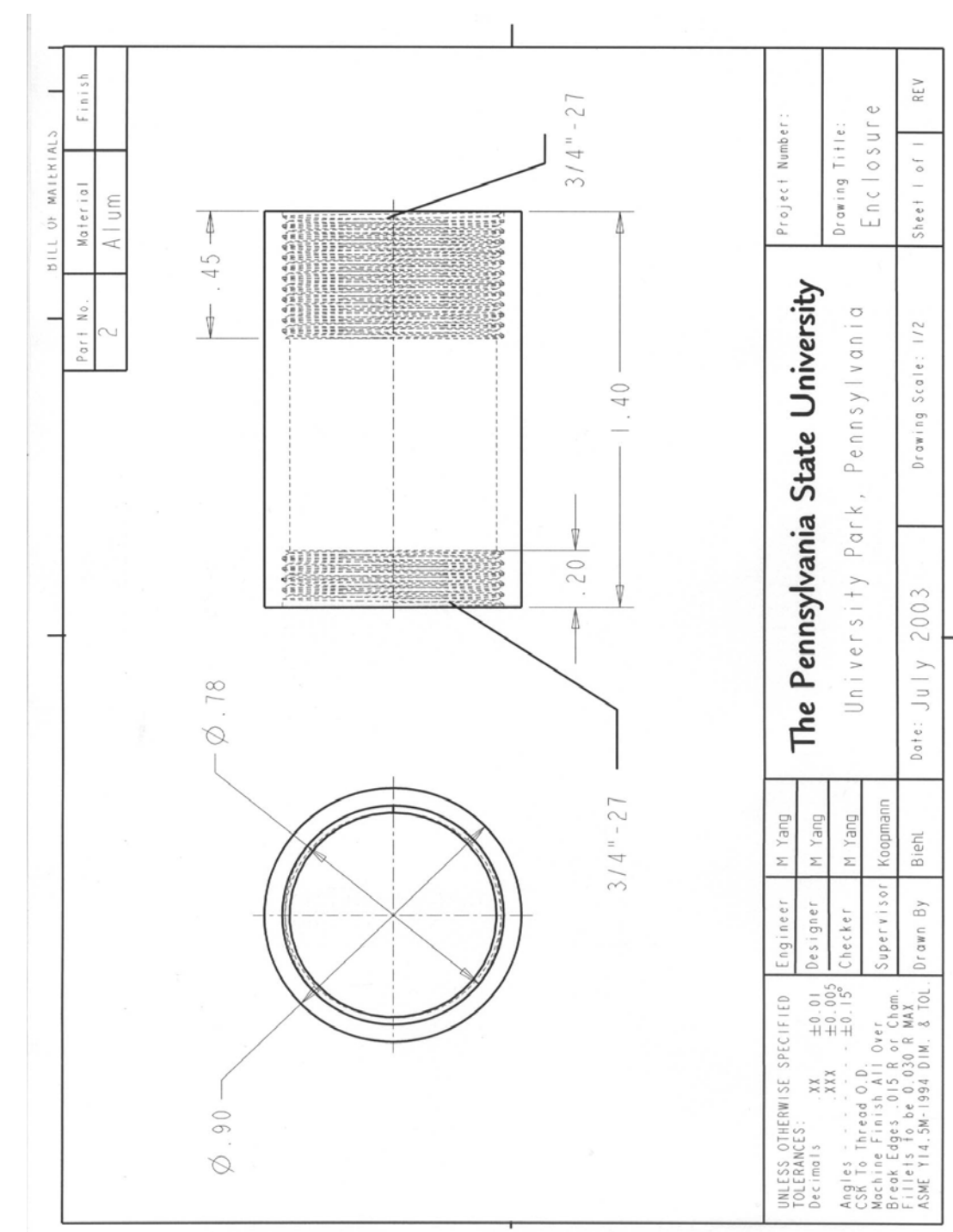


Figure A.11: Aluminum enclosure – enclosure wall machine drawing

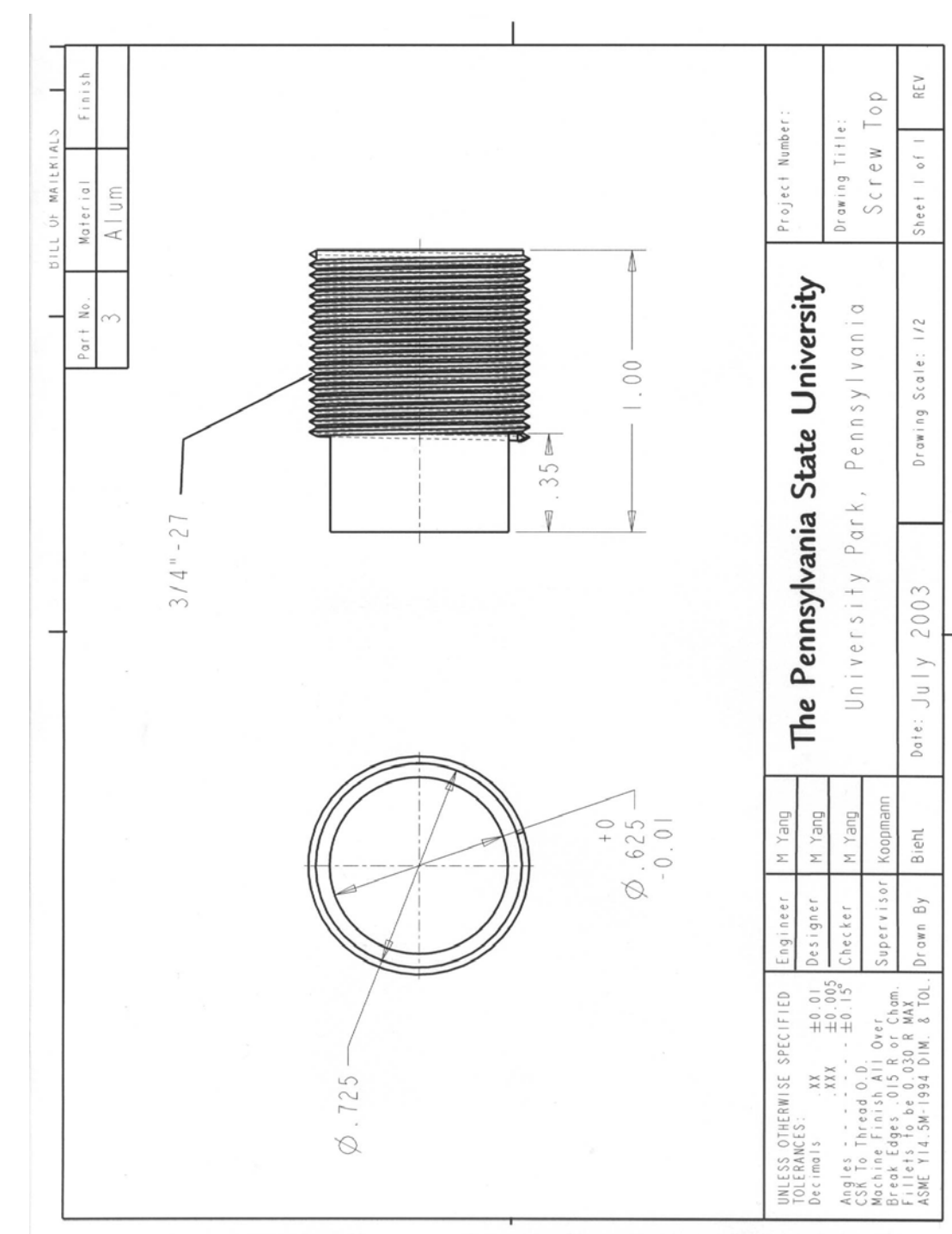


Figure A.12: Aluminum enclosure – screw top machine drawing

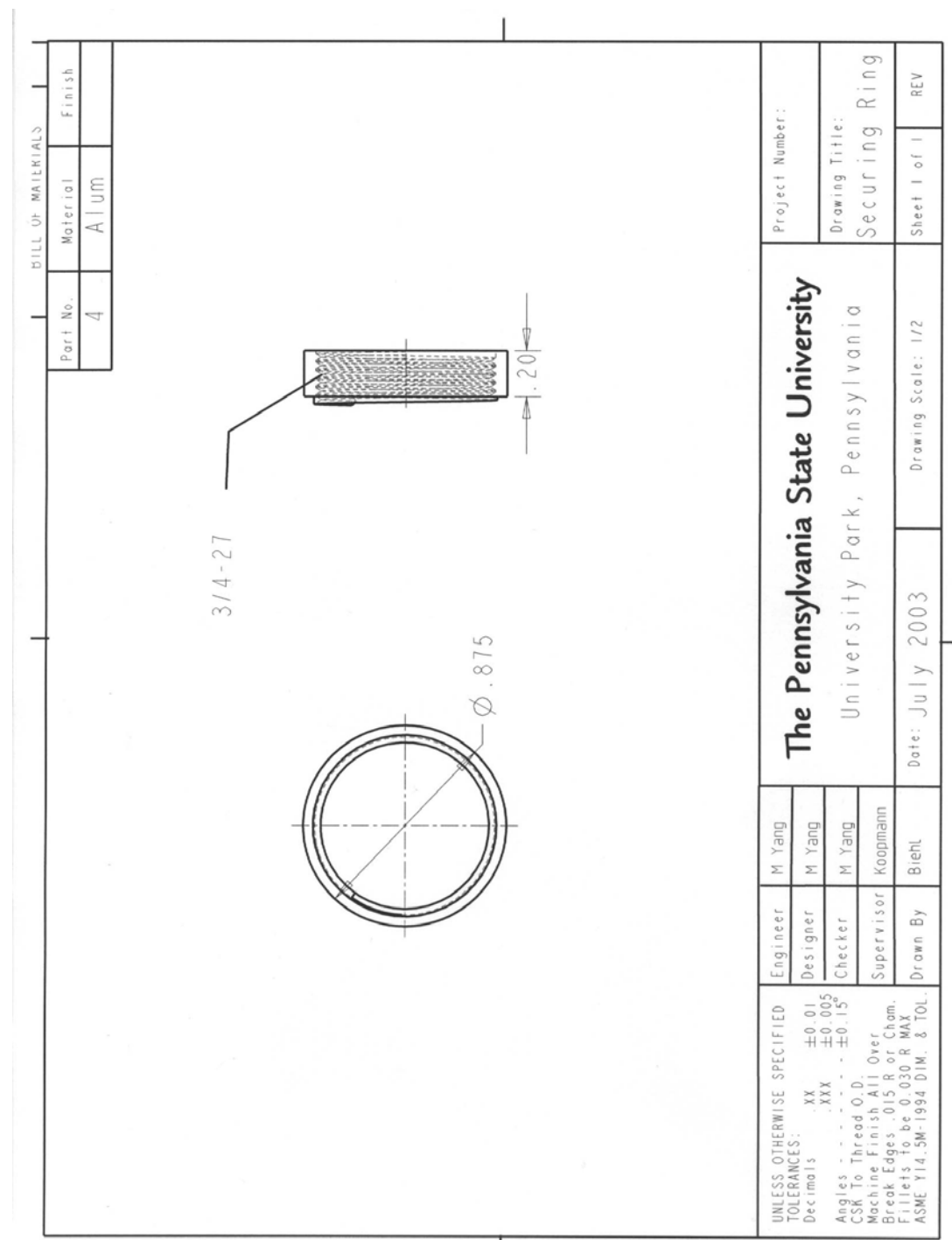


Figure A.13: Aluminum enclosure – securing ring machine drawing

Appendix B

Supplementary Power Measurement Verifications

This appendix describes other experiments conducted to verify the measurement of power, and the subsequent predictions of added loss factor and effective mass. This includes the analysis and correction of transducer phase error, the verification that power dissipation only occurs at the frequency of excitation, details about how the loss factor is calculated using the pole-zero method, and verification of the calculation of loss factor from dissipated power using an Airpot pneumatic damper.

B.1 Analysis of Transducer Phase Error

A force sensor and laser velocimeter are used to measure the force and velocity signals required for the power and conductance measurements. These measurements can be very sensitive to any phase error between the transducers, especially if the phase angle between the force and velocity signals is small.

The active component of power (which in this case is also the power dissipated by the PID) can be written as

$$\text{Real}\{P\} = |F_{rms}| |V_{rms}| \cos(\phi_F - \phi_V) \quad (\text{B.1})$$

where $(\phi_F - \phi_V)$ is the phase difference between the force and velocity signals in radians.

If a phase error, ϕ_e , is introduced, Eq. B.1 becomes

$$\text{Real}\{P_{\text{error}}\} = |F_{\text{rms}}| |V_{\text{rms}}| \cos(\phi_F - \phi_V + \phi_e) \quad (\text{B.2})$$

The percent error can be written as

$$\%Error|_{\text{Real}\{P\}} = \frac{\text{Real}\{P_{\text{error}}\} - \text{Real}\{P\}}{\text{Real}\{P\}} \times 100\% \quad (\text{B.3})$$

The expression for percent error for conductance is equivalent to Eq. B.3 because conductance is simply the dissipated power divided by the square of the magnitude of the force.

The sensitivity of the dissipated power and conductance measurements is shown in Figures B.1 and B.2. It is apparent that the dissipated power and conductance measurements are very sensitive to even small transducer phase errors. Measurements that have a larger phase difference between the force and velocity signals are less sensitive to transducer phase error.

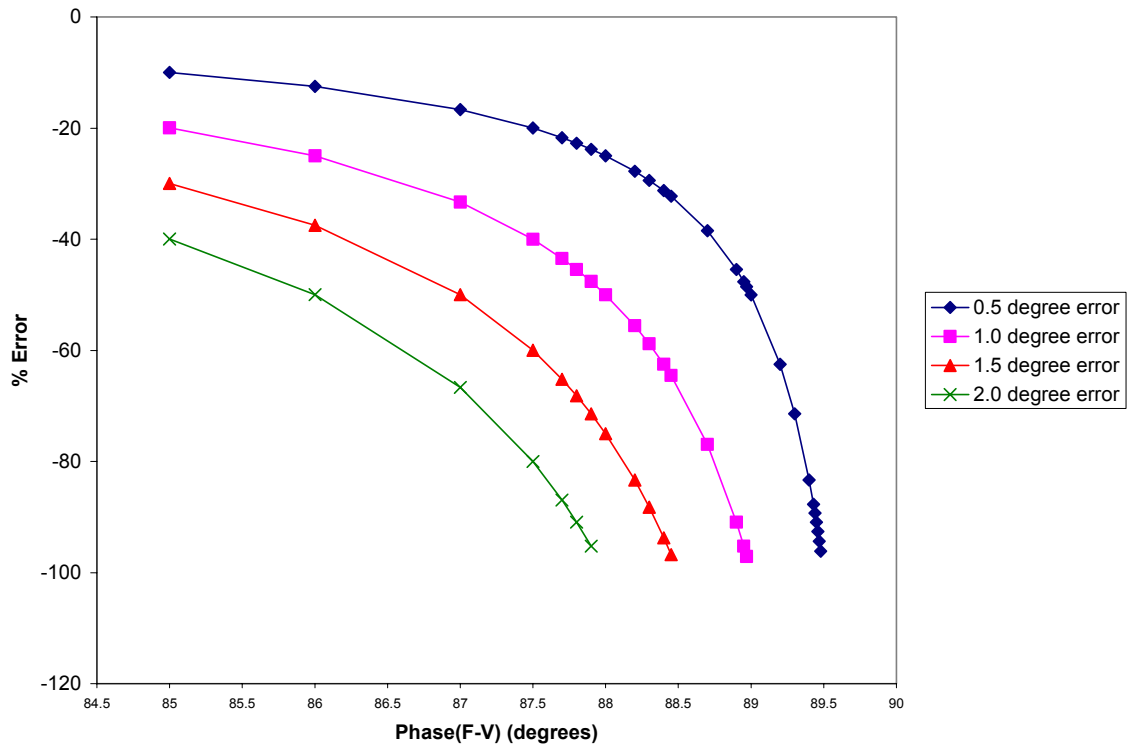


Figure B.1: Transducer phase error for dissipated power. Percent error vs. $(\phi_F - \phi_V)$.

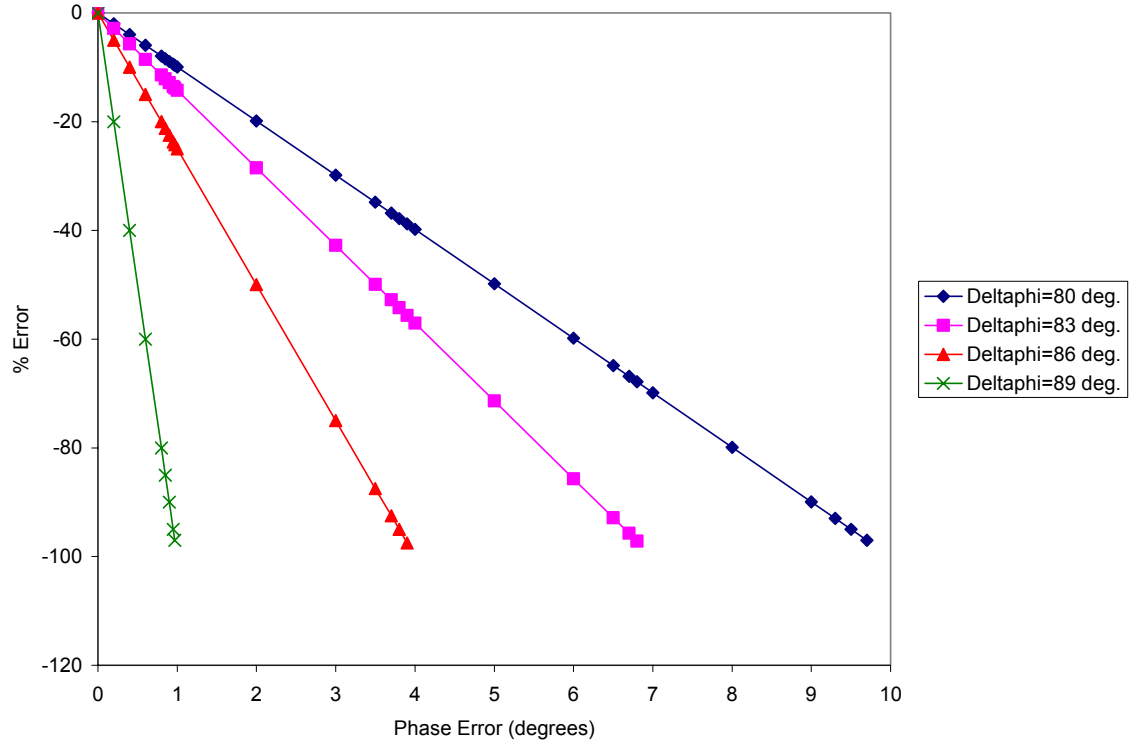


Figure B.2: Transducer phase error for dissipated power. Percent error vs. phase error.

Adapting the procedure above, the imaginary part of the power without and with a phase error can be written as

$$\text{Imag}\{P\} = |F_{rms}|V_{rms}|\sin(\phi_F - \phi_V)| \quad (\text{B.4})$$

and

$$\text{Imag}\{P_{error}\} = |F_{rms}|V_{rms}|\sin(\phi_F - \phi_V + \phi_e)|. \quad (\text{B.5})$$

The percent error is written

$$\%Error|_{\text{Imag}\{P\}} = \frac{\text{Imag}\{P_{error}\} - \text{Imag}\{P\}}{\text{Imag}\{P\}} \times 100\%. \quad (\text{B.6})$$

The sensitivity of the trapped power to transducer phase error is shown in Figures B.3 and Figure B.4. It is apparent that trapped power, although affected by transducer phase error, is significantly less sensitive than active power. Phase errors as high as 10% only cause a 1.5% error.

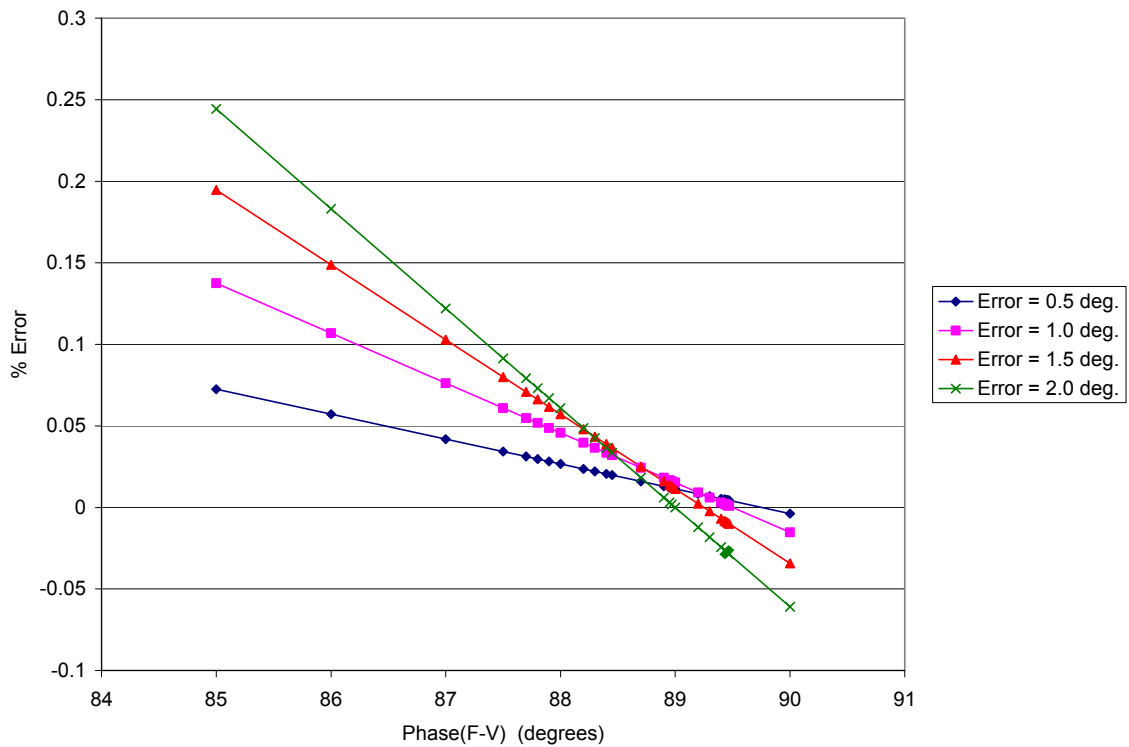


Figure B.3: Transducer phase error for trapped power. Percent error vs. $(\phi_F - \phi_V)$.

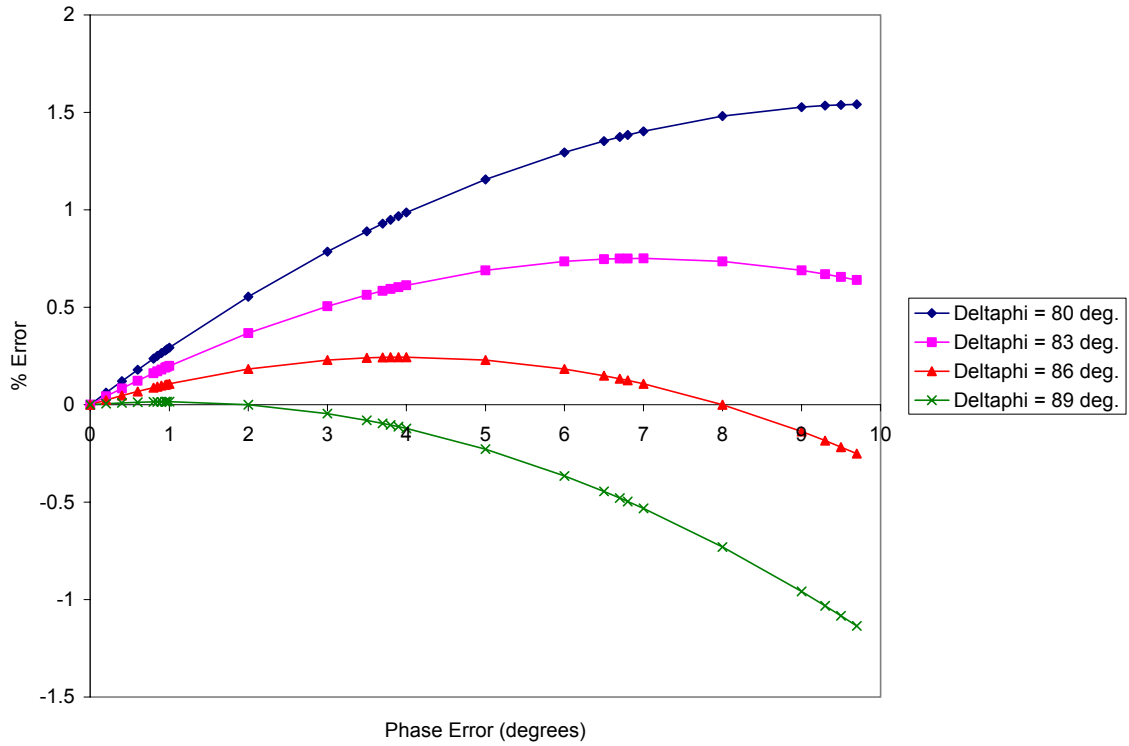


Figure B.4: Transducer phase error for trapped power. Percent error vs. phase error.

B.1.1 Correction of Transducer Phase Error

The transducer phase error can be corrected by calibrating the power measurements with a lumped mass. A schematic of the experimental setup is shown in Figure B.5 and a picture of the setup is shown in Figure B.6. Table B.1 provides a specific list of the equipment used. The shaker is clamped to a massive granite table to reduce the likelihood of any interaction between the shaker and ground. A force sensor placed between the shaker and lumped mass provides the force data, and a laser vibrometer is used to measure the velocity data.

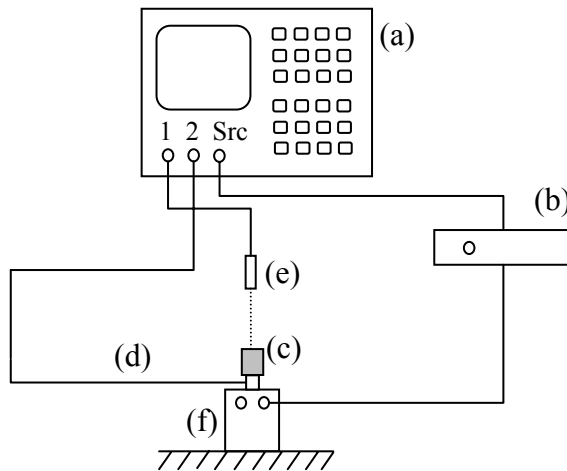


Figure B.5: Schematic of transducer phase error calibration setup.

Table B.1: Description of individual components for transducer phase error calibration

(a)	Agilent 35670A dynamic signal analyzer
(b)	SPA 400 stereo amplifier
(c)	Lumped mass
(d)	PCB 208M51 force sensor SN 10996
(e)	Polytec OFV 502 fiber interferometer with Polytec OFV 2600 vibrometer controller
(f)	Electromagnetic shaker – Clamped to massive granite table

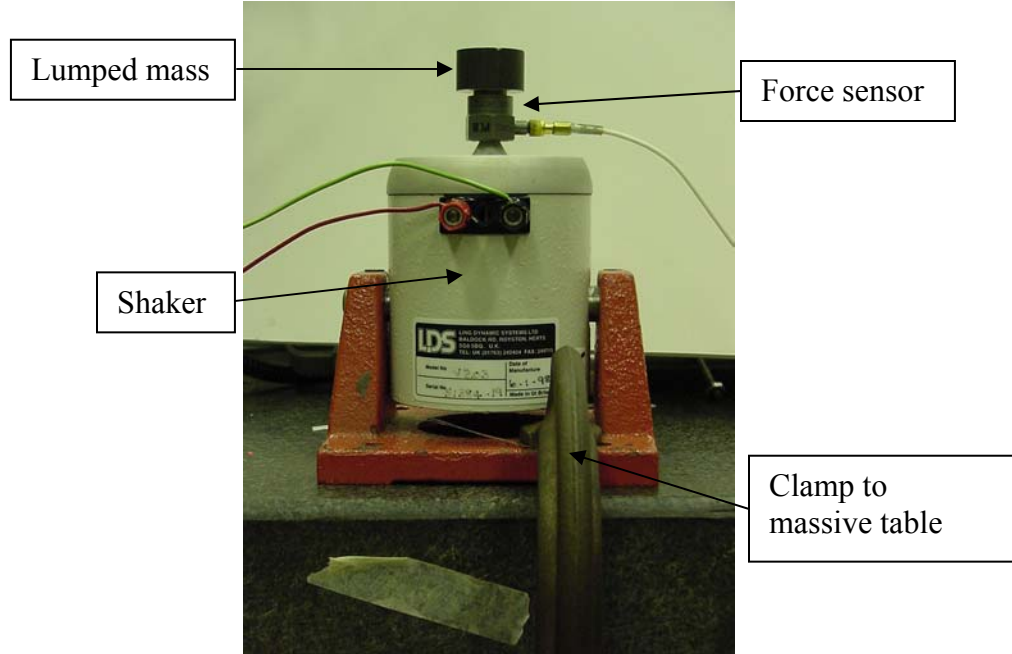


Figure B.6: Picture of transducer phase error calibration setup.

To calibrate the transducer phase error, the impedance (Force/Velocity) of the lumped mass is measured. Theoretically, the phase of the impedance should be $\pi/2$ radians. The phase error is therefore

$$\phi_e = \angle\left(\frac{F}{V}\right) - \frac{\pi}{2} \text{ radians.} \quad (\text{B.7})$$

The phase-corrected force, F_c , is

$$F_c = |F| \angle(\phi_F - \phi_e) = |F| \cos(\phi_F - \phi_e) + i |F| \sin(\phi_F - \phi_e). \quad (\text{B.8})$$

B.2 Verification of Power at Discrete Frequency

It was initially unclear whether the dissipated and trapped power occurred only at the frequency of excitation or over a broad spectrum. An impact typically excites the structure over a broad frequency range. If the PID dissipates and traps power at many frequencies, it would be necessary to sum up the power over the entire frequency range.

Particles of varying sizes were placed inside an aluminum enclosure (see Appendix A) with an adjustable screw top. The enclosure was then attached to a force sensor which was in turn placed upon an electromagnetic shaker. A laser vibrometer was used to measure the velocity, and an Agilent dynamic signal analyzer was used to collect and process the data from 0-12800 Hz in 16 Hz increments. A schematic is illustrated in Figure B.7 and a picture is shown in Figure B.8. Table B.2 provides a detailed listing of the equipment used.

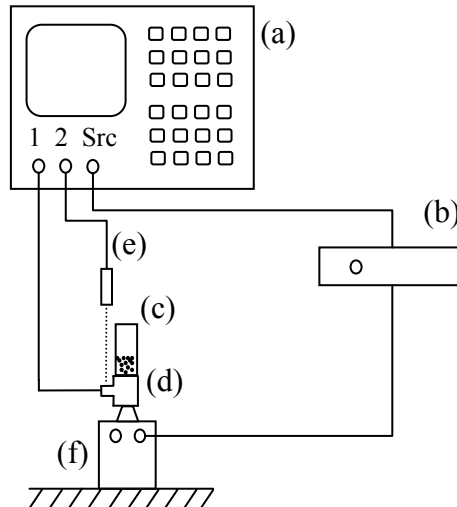


Figure B.7: Schematic of power measurement setup

Table **B.2**: Description of individual components for power measurement

(a)	Agilent 35670A dynamic signal analyzer
(b)	SPA 400 stereo amplifier
(c)	Particle Impact Damper
(d)	PCB 208M51 force sensor SN 10996
(e)	Polytec OFV 502 Fiber Interferometer with Polytec OFV 2600 Vibrometer Controller
(f)	Electromagnetic shaker – Clamped to massive granite table

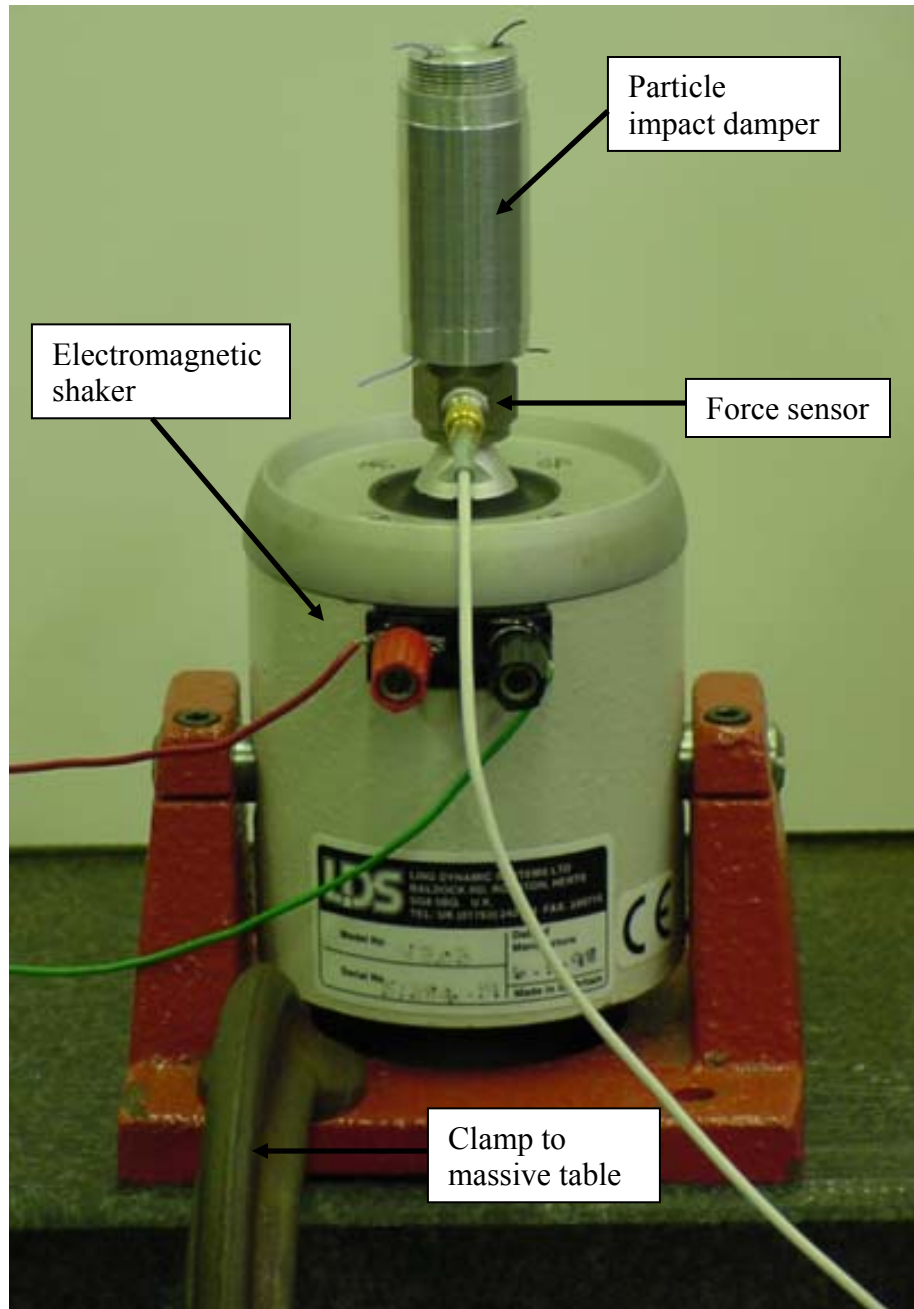


Figure B.8: Picture of power measurement setup (laser vibrometer not shown)

Spherical brass ball bearings with diameters of 1/16, 1/8, and 3/32 inches were used as the particles. The total mass of all three particle beds was kept equal, and

therefore there are a greater number of smaller particles. The enclosure was excited with a sinusoidal input at 80 Hz at two different velocities. The gap size was selected to be a value that provided near-optimum power dissipation. A summary of the experimental parameters is given in Table **B.3** and the results for the three particles sizes at two different velocities are given in Figures **B.9 - B.14**.

Table B.3: Summary of experimental parameters

Particle diameter (in.)	1/16	1/8	3/32
Number of particles used	600	75	22
Total mass of particle bed (grams)	10.50	10.56	10.56
Frequency of excitation (Hz)	80	80	80
First velocity (m/s pk)	0.238	0.235	0.225
Second velocity (m/s pk)	0.368	0.352	0.361
Gap size (mm)	0.94	1.53	1.88

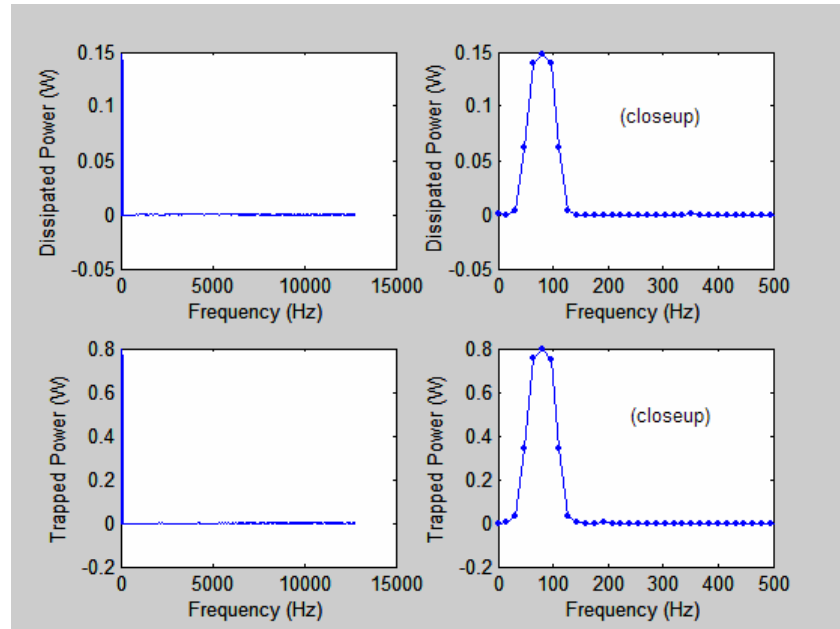


Figure B.9: Verification of discrete power dissipation – 1/16" particles, 0.238 m/s pk

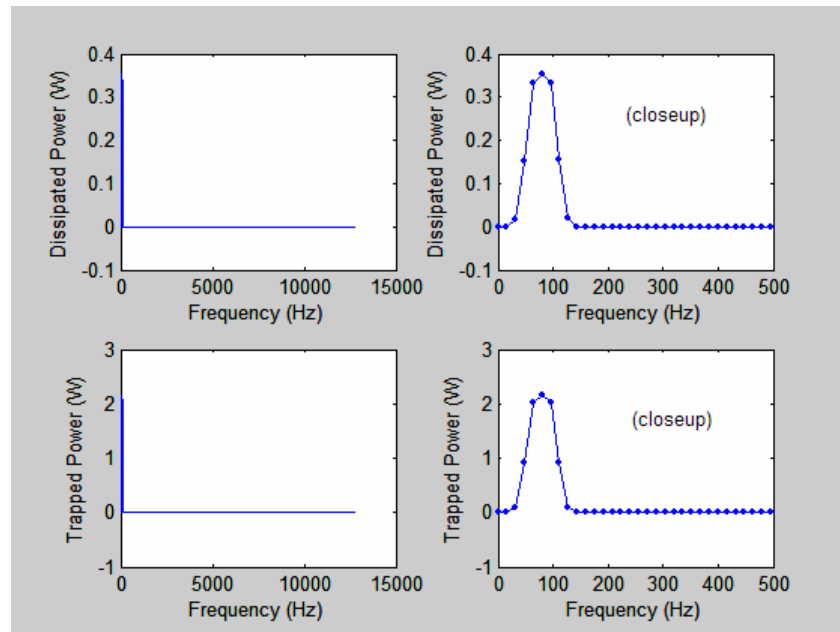


Figure B.10: Verification of discrete power dissipation – 1/16” particles, 0.368 m/s pk

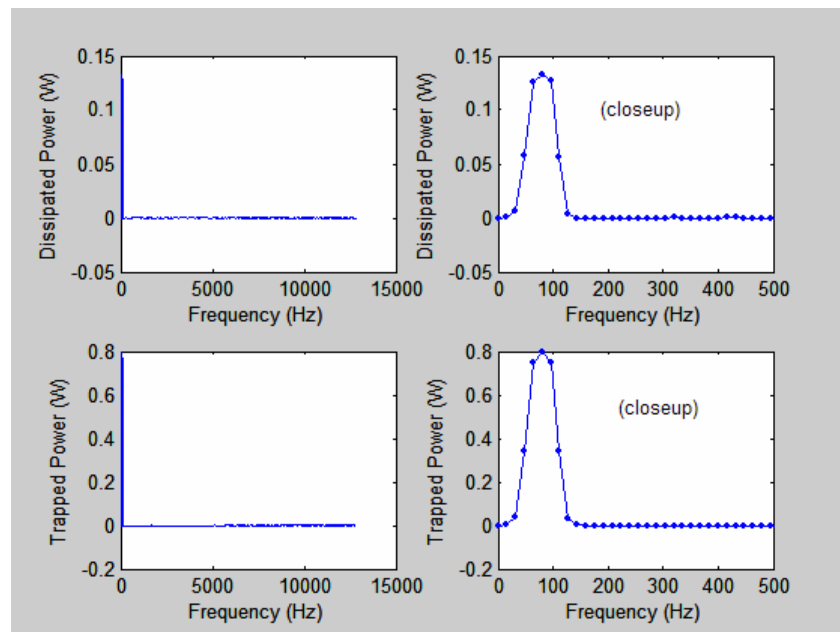


Figure B.11: Verification of discrete power dissipation – 1/8” particles, 0.235 m/s pk

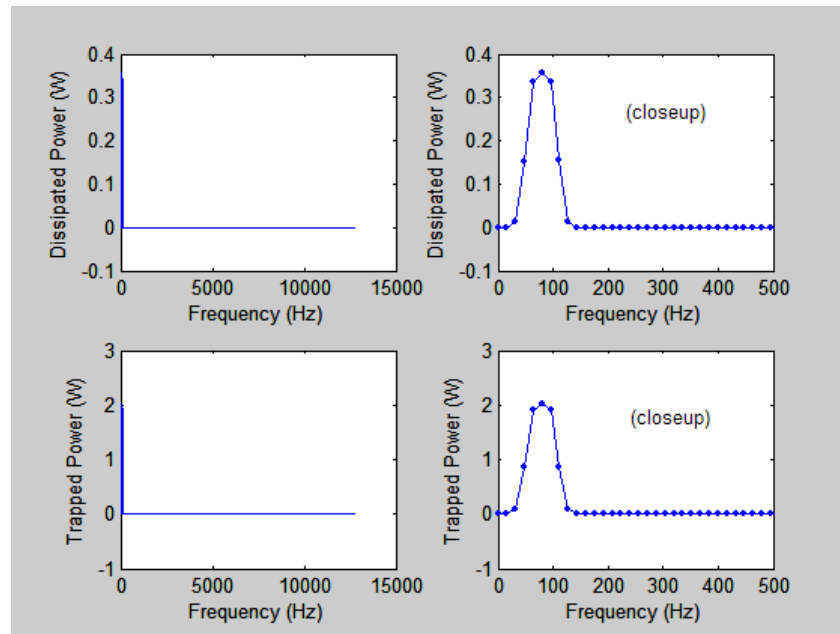


Figure B.12: Verification of discrete power dissipation – 1/8” particles, 0.352 m/s pk

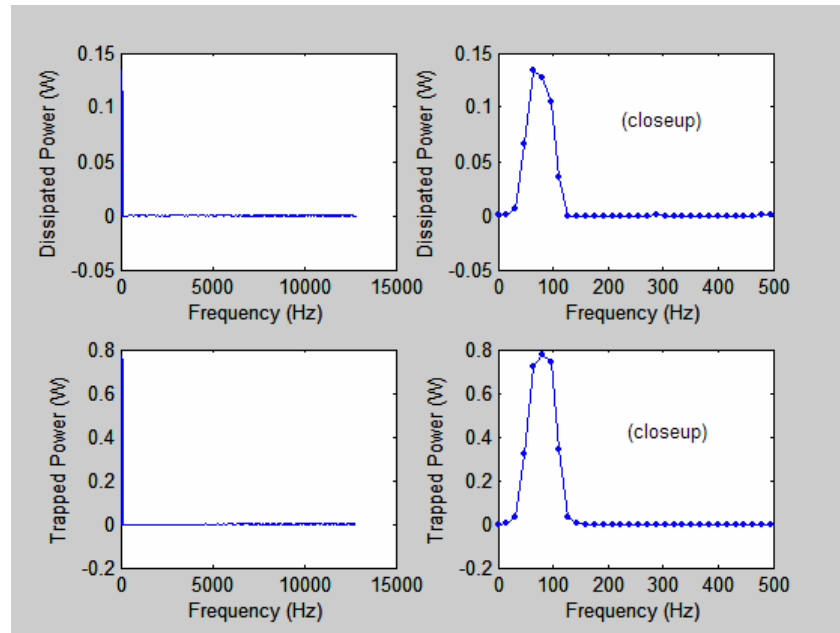


Figure B.13: Verification of discrete power dissipation – 3/32” particles, 0.225 m/s pk

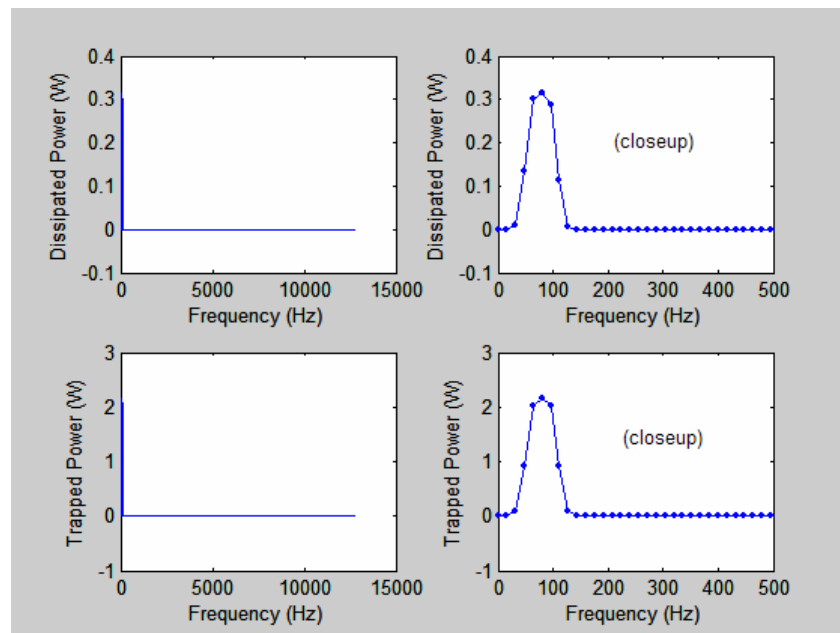


Figure B.14: Verification of discrete power dissipation – 3/32” particles, 0.361 m/s pk

Figures **B.9 - B.14** show that there is a peak for both the trapped and dissipated power at the frequency of excitation, which was 80 Hz for all cases. The peak does not approximate a perfect delta function. This width is likely due to the use of the Flat Top window, which emphasizes the accuracy of the signal magnitude over the accuracy of the signal frequency.

Overall, it is shown that for different sized particles at different velocities, the dissipated and trapped power only occurs at the frequency of excitation. This means that the total power will not need to be summed over the frequency spectrum.

B.3 Measurement of Loss Factor Using Pole-Zero Curve Fitting Method

The remainder of this appendix deals with predicting the loss factor and resonance shift on structures by using measured power data. The loss factor is usually calculated by taking half-power measurements at the resonance frequency. This method has the drawback of requiring interpolation between data points, which can lead to error.

The Agilent 35670A dynamic signal analyzer has a built-in function that performs a curve fit of the existing transfer function and calculates a pole-zero fit. The eigenvectors that describe a system are orthogonal, which means they are linearly independent. This leads to the expansion theorem, which states that the response of a structure can be described by a linear combination of its eigenvectors. By expressing the system in *modal space*, the system can be decoupled into a set of second-order

differential equations, with each equation corresponding to a single eigenvector and eigenvalue.

The transfer function for an oscillator in Laplacian form is

$$H(s) = \frac{b(s)}{a(s)} = \frac{\omega_n^2}{s^2 + 2\xi\omega_n s + \omega_n^2} \quad (\text{B.9})$$

where ω_n is the natural frequency, ξ is the damping coefficient, and s are the complex poles defined by

$$s = -\sigma \pm i\omega_d.$$

The poles are found by equating the denominator to zero and solving for s [63]. Since complex poles always occur in complex conjugate pairs, the denominator will look like

$$a(s) = (s + \sigma - i\omega_d)(s + \sigma + i\omega_d) = (s + \sigma)^2 + \omega_d^2 \quad (\text{B.10})$$

Comparing Eq. B.10 with the denominator in Eq. B.9 results in

$$\sigma = \xi\omega_n \quad (\text{B.11})$$

and

$$\omega_d = \omega_n \sqrt{1 - \xi^2} \quad (\text{B.12})$$

The damping coefficient can be solved by combining Equations B.11 and B.12. This gives

$$\xi = \frac{\sigma}{\omega_d} \sqrt{\left(1 + \frac{\sigma^2}{\omega_d^2}\right)^{-1}} \quad (\text{B.13})$$

The loss factor η is related to the damping coefficient through

$$\eta = 2\xi \quad (\text{B.14})$$

Equations **B.12**, **B.13**, and **B.14** can then be used to solve for the loss factor and natural frequency. The location of the complex poles is illustrated in Figure **B.15**.

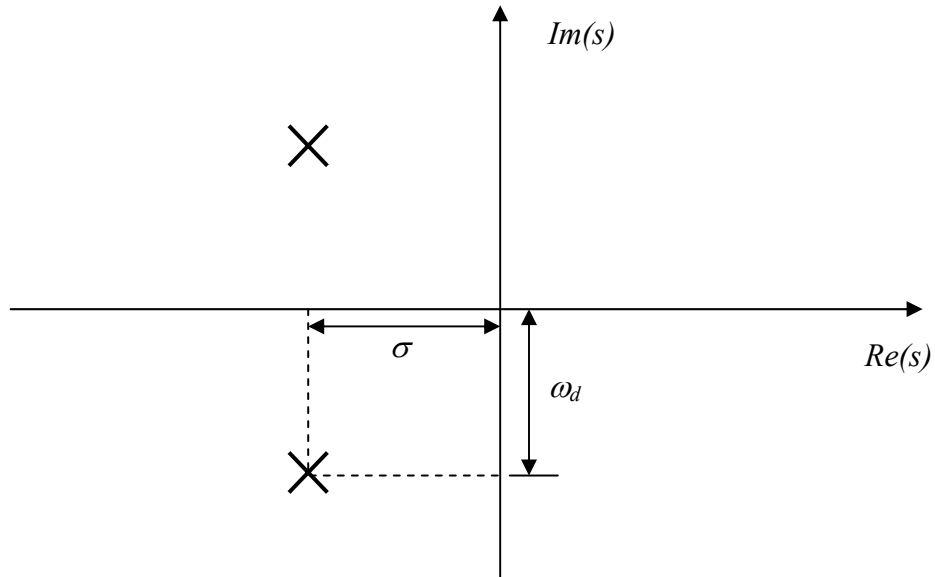


Figure **B.15**: s -plane plot for a pair of complex poles

B.4 Verification of Power Measurement Using Airport Pneumatic Viscous Damper

To verify the computation of loss factor using dissipated power, an Airport pneumatic viscous damper was attached to an aluminum beam clamped at both ends.

The Airpot damper is model number 2KS160A2.0F and has an adjustable damping coefficient between 0-1.75 N/(mm/s). A full schematic is shown in Figure **B.16**.

The beam measures 30" x 2" x 1/8" and is made of 6160 T6 aluminum. Each end is clamped into an aluminum ground structure (Figure **B.17**), and the ground structure is attached to a massive granite table with multiple clamps.

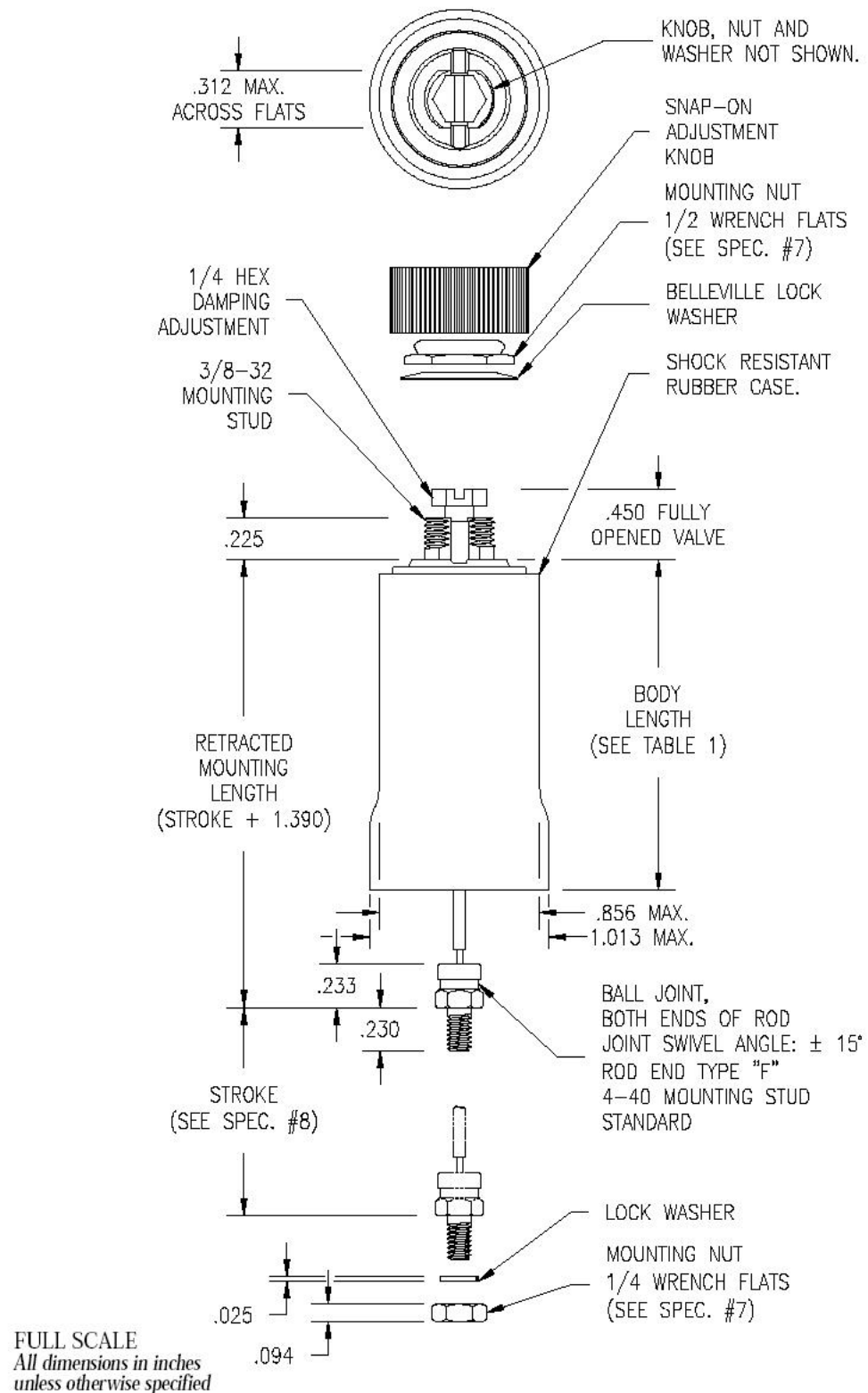
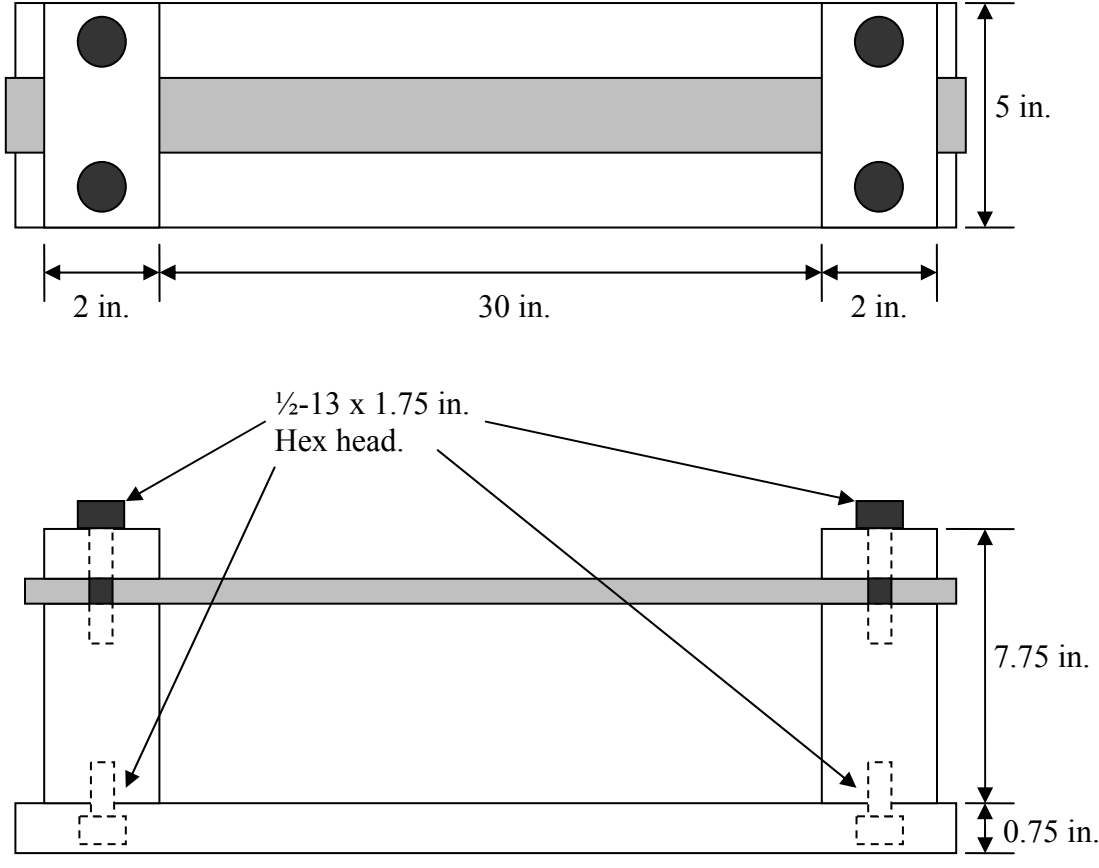


Figure B.16: Airpot model 2KS160A2.0F dashpot. Source: <http://www.airpot.com>. Specifications for Stock Dashpot Model 2KS160.



(Drawing not to scale)

Figure B.17: Aluminum ground structure with clamped beam

A small hole was drilled in the center of the beam, and an electromagnetic shaker was connected to the center of the beam by placing a threaded stinger through the hole. One hex nut was used on either side of the beam to “sandwich” the beam and connect it to the stinger. A force sensor was placed below the beam to measure the input force, and

an impedance head was placed on top of the beam to measure the acceleration of the center of the beam and the force between the beam and the dashpot (Figure B.1). An impedance head was used to measure acceleration instead of the laser velocimeter because the Airpot ground structure (see Figure B.18) obscured direct measurement of the beam motion. Acceleration can be converted to velocity with the well known equation

$$V = \frac{A}{i\omega} \quad (\text{B.15})$$

where A is the complex acceleration.

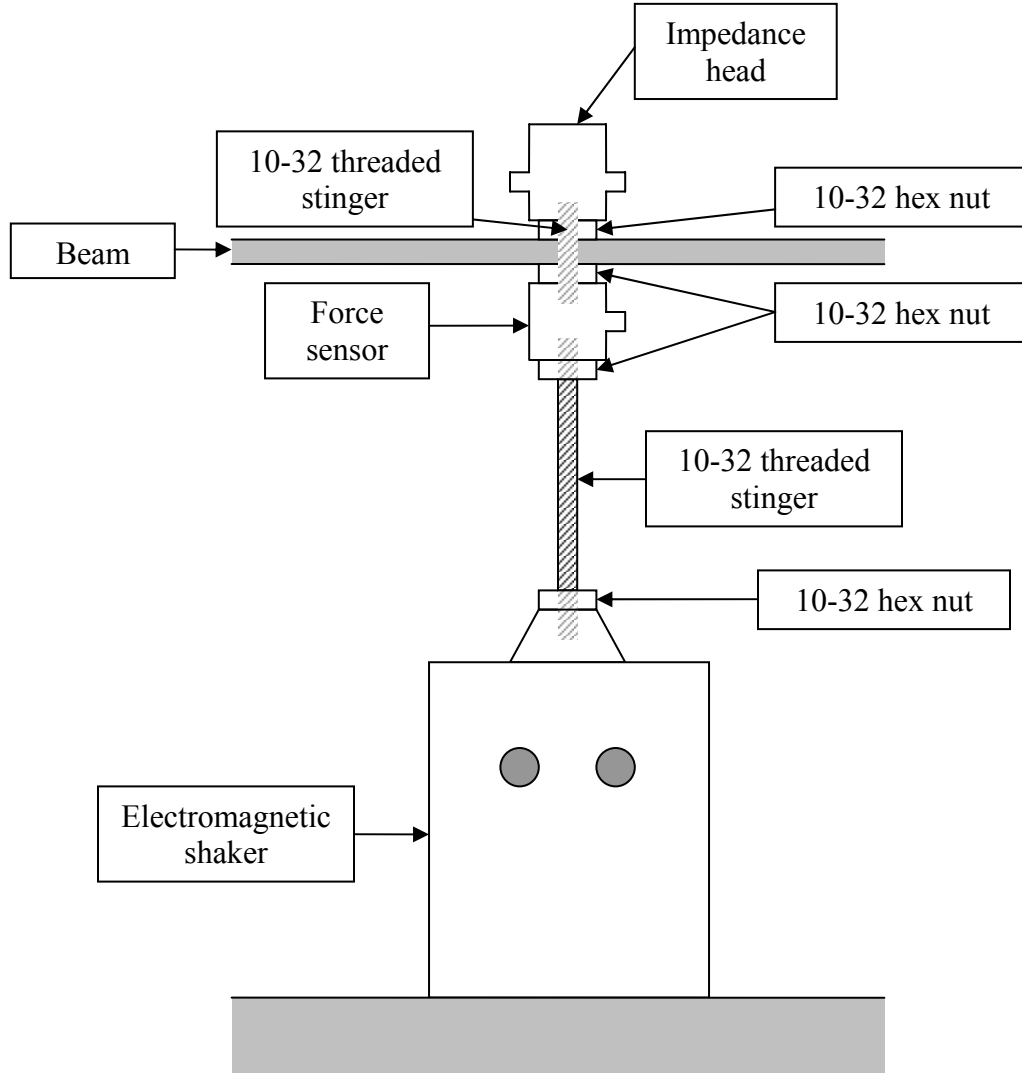


Figure B.18: Attachment of shaker, force sensor, and impedance head to beam center

The mounting stud of the Airpot damper was threaded into the impedance head using a nut with two different thread types. The top part of the damper was connected to a sheet metal framework, constructed of 16 gauge steel sheet metal. The framework was held together with L-brackets. A large steel mass was clamped to the framework to keep it connected to ground. A picture of the completed setup is shown in Figure B.19.

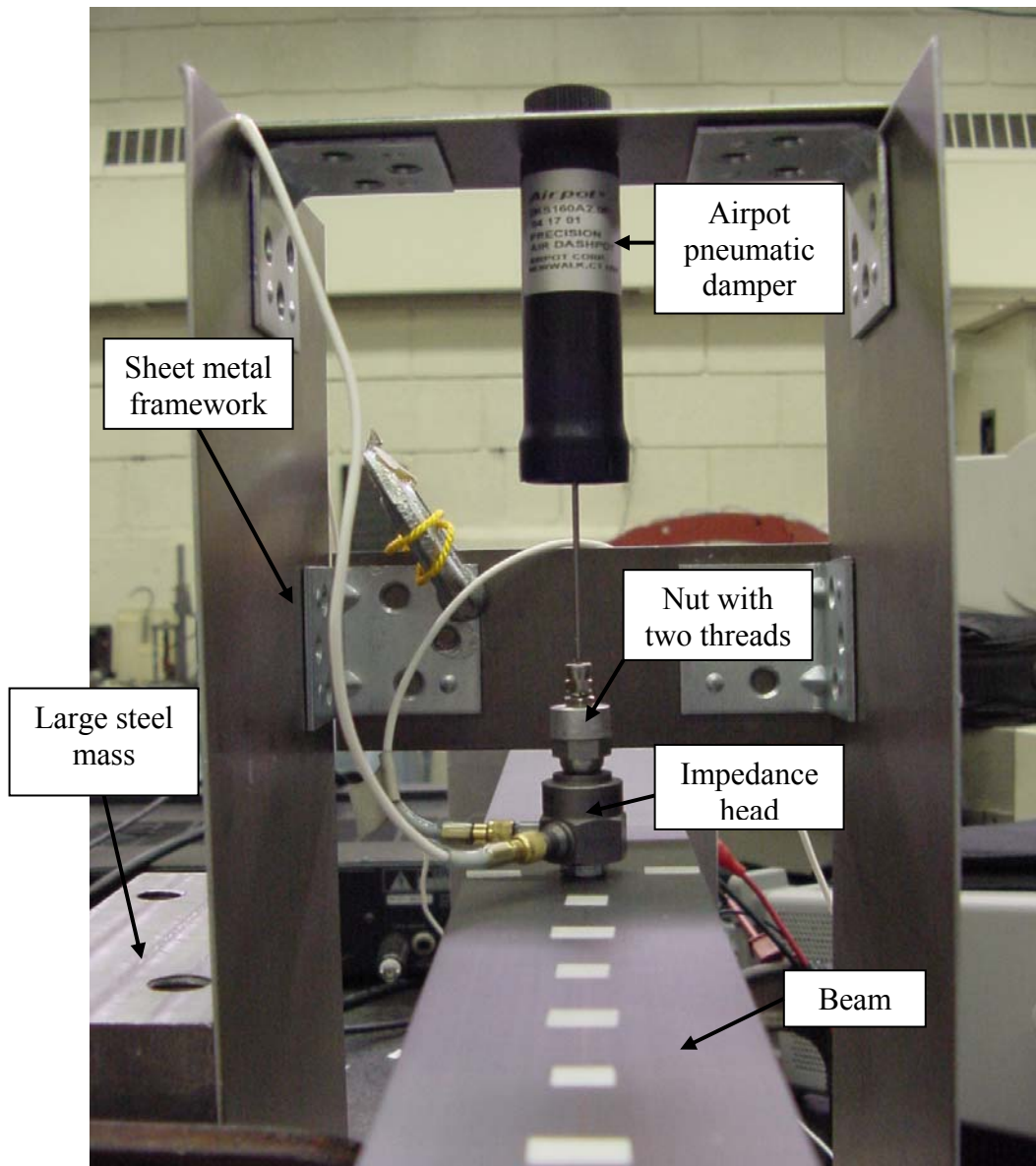


Figure B.19: Beam with Airpot dashpot attached

The velocity profile of the beam was measured by moving the Polytec laser vibrometer along the length of the beam and measuring the vertical motion of the beam in one-inch increments along the centerline. The force sensor was used as a phase reference. This measurement was used to calculate the kinetic energy of the beam, which

is required for the loss factor prediction. A picture of the entire setup is illustrated in Figure **B.20** and a list of all experimental equipment is in Table **B.4**.

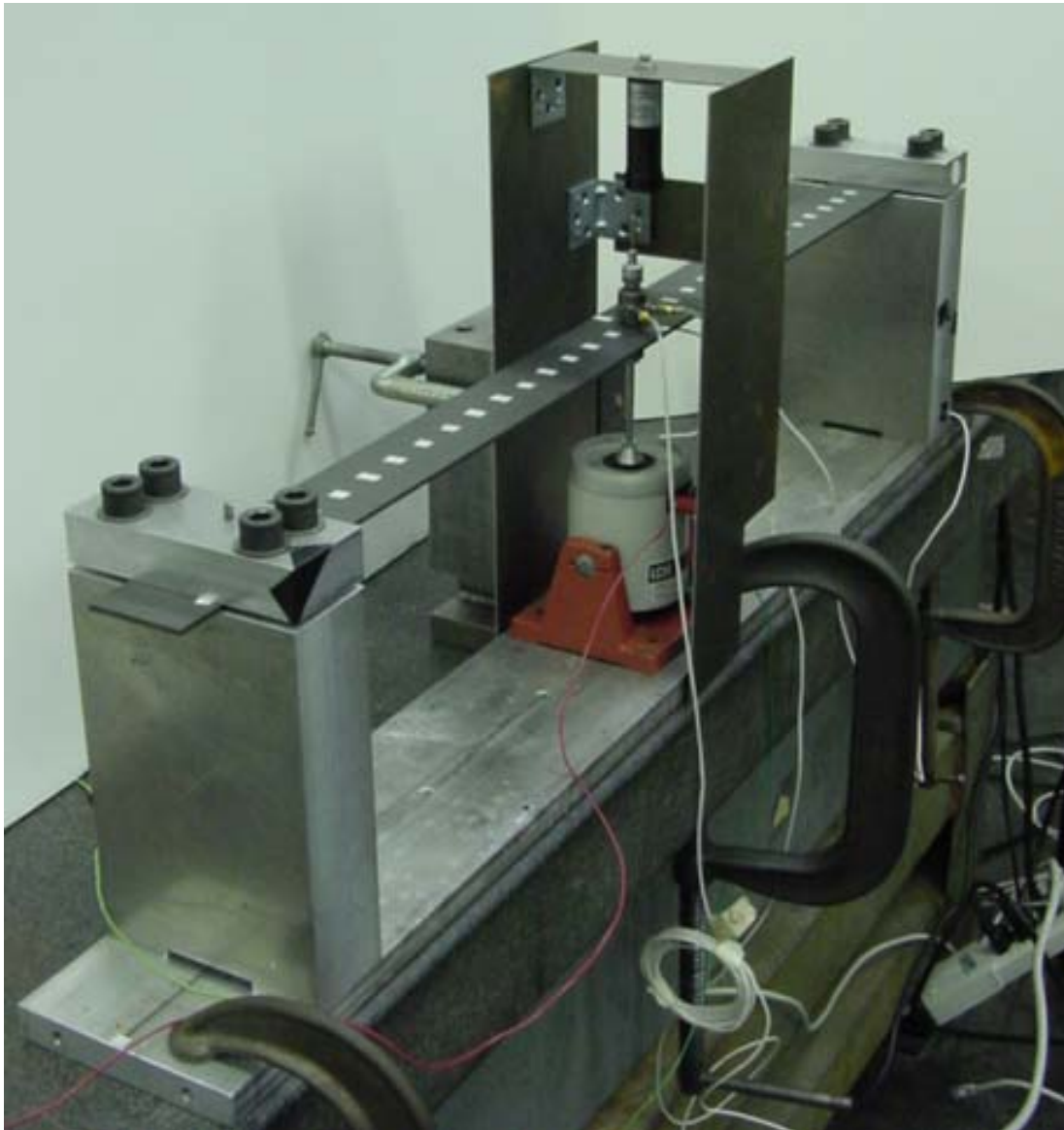


Figure **B.20**: Entire beam with Airpot attached

Table **B.4**: List of experimental equipment for Airpot verification experiment

Quantity	Description
1	30" x 2" x 1/8" aluminum 6160 T6 beam
1	Beam clamping and grounding assembly
1	Airpot model 2KS160A2.0F pneumatic damper
1	Grounding framework for Airpot damper
1	Large steel mass for grounding framework
1	LDS V203 electromagnetic shaker SN 51884-19
1	PCB U288C01 impedance head SN 764
1	PCB 208A02 force sensor SN 9801
1	Agilent 35670A dynamic signal analyzer
1	Polytec OFV 502 fiber interferometer with Polytec OFV 2600 vibrometer controller
2	10-32 threaded stinger
4	10-32 hex nut
4	Clamps
1	Roll of reflective tape

The velocity profile along the length of the beam with the Airpot damper attached was measured. This was done at the beam's first natural frequency (25 Hz) and at different amplitudes (Figure **B.21**). Note the velocity profile at the center of the beam was not measured because the grounding framework blocked the laser. It is apparent that the velocity profile matches the theoretical first eigenvector for a clamped-clamped beam. Also, the addition of the Airpot damper does not cause any significant change in the velocity profile. Finally, the velocity profile is insensitive to the amplitude of vibration for the range shown. This indicates that the velocity profile, and therefore the kinetic energy along the entire beam can be calculated from a velocity measurement at a single location. The equation for the kinetic energy in the beam is found by discretizing the beam into N segments and summing the energy in each segment.

$$E_{maximum} = \frac{1}{2} \sum_{i=1}^N m_i v_i^2 + \frac{1}{2} \sum_{j=1}^M m_j v_j^2 \quad (\text{B.16})$$

where m_i is the mass of the i th segment, v_i is the transverse velocity of the center of the i th segment, m_j is the mass of any discrete attachments, and v_j is the velocity of those discrete attachments. Discrete attachments include stingers, hex nuts, impedance heads, and other moving elements that add to the kinetic energy of the entire system.

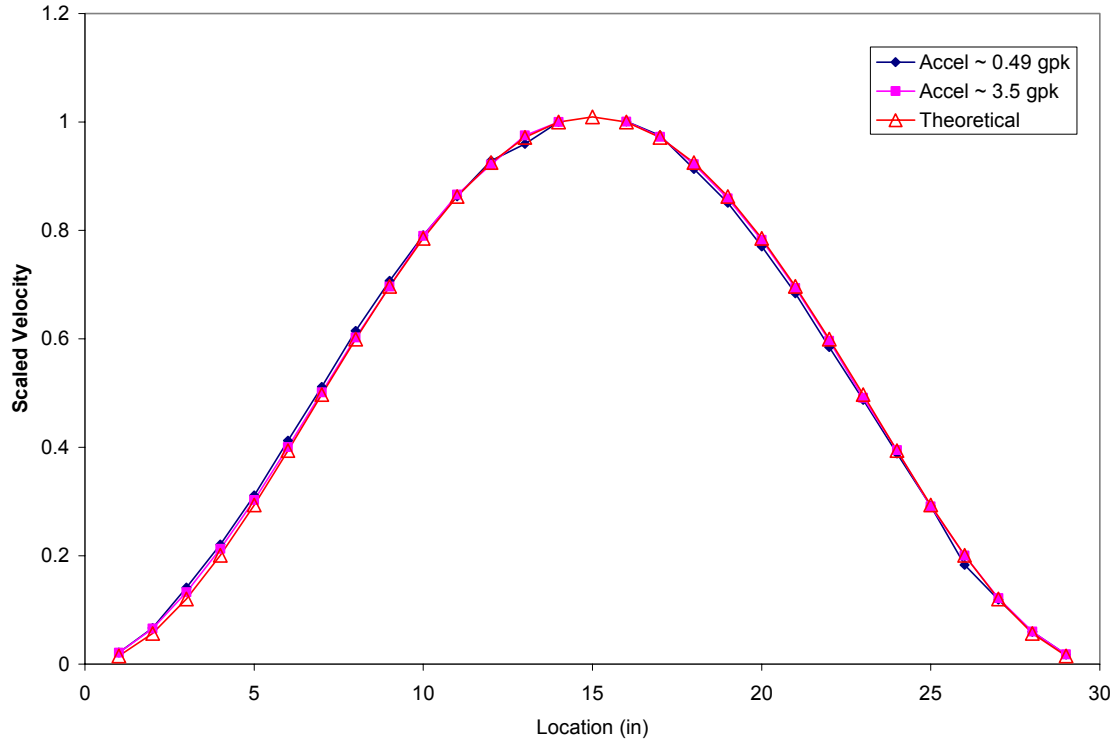


Figure B.21: Velocity profile of beam with Airpot damper

A small tungsten mass was used to calibrate the transducer phase error over a range of amplitudes. Then, the mass was removed and replaced by the Airpot damper. The beam was excited by a slow sine-sweep through its first resonance frequency at different amplitudes. The pole-zero method was used to calculate the loss factors. The

loss factor of the beam without any attachments was also calculated, and found to be 0.0031.

The dissipated power was calculated by using the complex force and velocity at the resonance peak from the slow sine-sweep measurement. It was decided that an *in situ* measurement of power would provide a good indicator of the accuracy of the method under the “best possible” circumstances. Other tests will use power measurements taken with the damping structure mounted to a shaker, and independent of any structure.

The measured and predicted loss factors are shown in Figure B.22. Measured loss factors refer to those calculated from the pole-zero fit, while predicted loss factors are those calculated from the dissipated power and kinetic energy measurements. Also note that the loss factor for the bare beam has been subtracted from the measured loss factors. Therefore, Figure B.22 only shows the loss factor contribution of the Airpot damper.

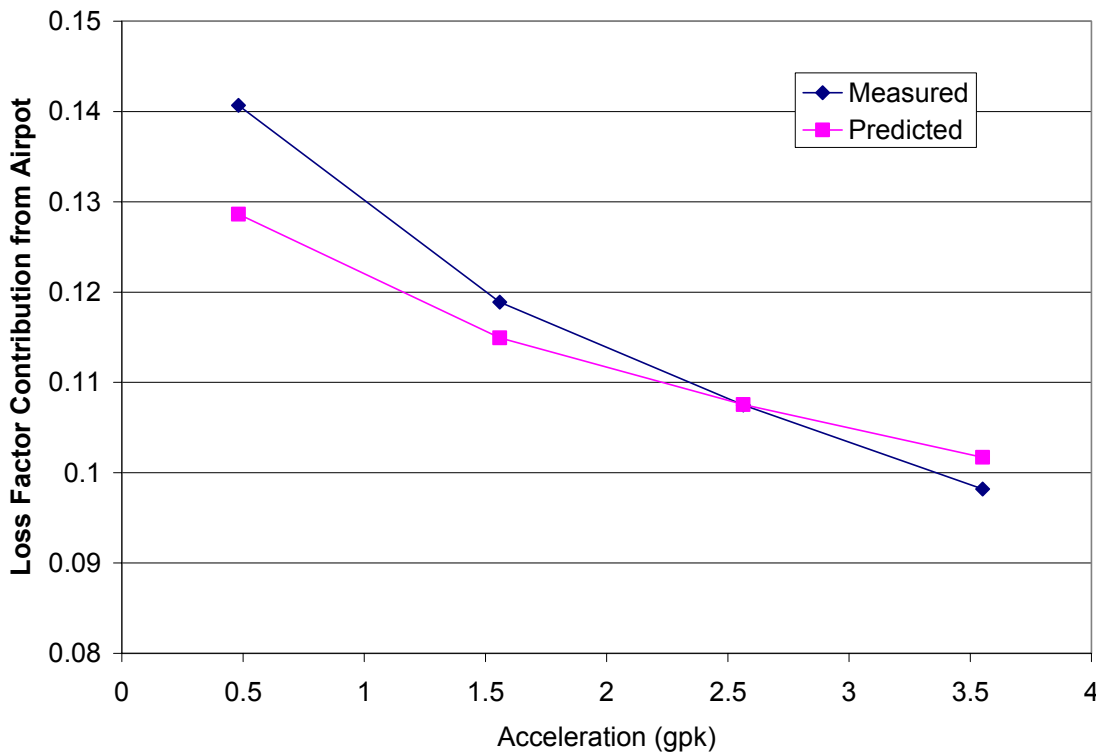


Figure B.22: Measured and predicted loss factors for Airpot damper

The loss factors predicted from the *in situ* power measurements match the measured loss factors within an acceptable error. The largest error is 0.012 and occurs at the lowest acceleration (0.48 gpk).

Appendix C

Interpolation with Neural Networks

Neural networks are named for and inspired by biological nervous systems. Therefore, they consist of simple elements, called *neurons*, operating in parallel. Neural networks have found use in a wide range of areas, including signal processing, pattern recognition, speech recognition, artificial intelligence, and finance [65]. In this thesis, neural networks will be used to interpolate results within a “cloud of data” for multiple inputs and a single output.

C.1 Fundamentals of Neural Networks

Most neurons consist of a single scalar input with a bias, as seen in Figure C.1.

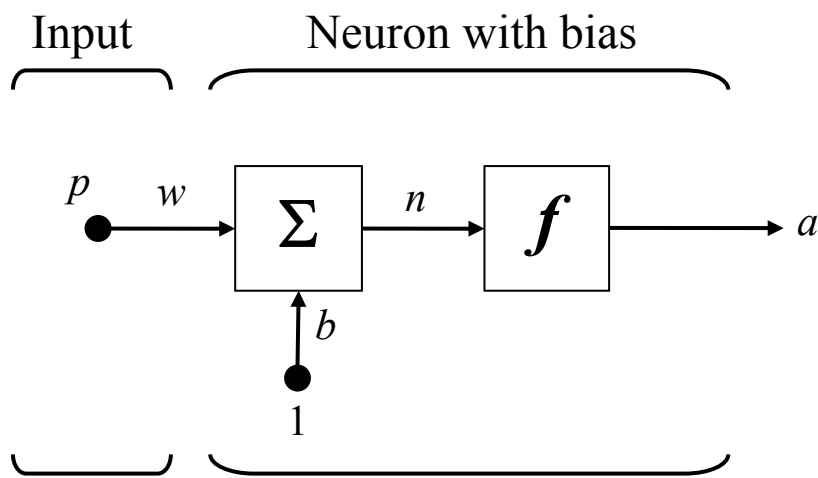


Figure C.1: Simple neuron with bias

The scalar input p is multiplied by the weight w and summed with the bias b to get n , another scalar. This is then passed through an “activation function” f , to compute the output a . Typically, the output a is compared to a target t . Assuming that there is some error, the weights and biases are trained so that the output achieves a certain value.

There are several different types of activation functions. One of the most simple is the hard-limit function shown in Figure C.2. The hard-limit activation function limits the output of the neuron to zero if the input argument n is less than zero, or sets it to one if n is greater than zero.

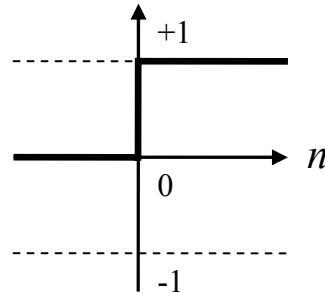


Figure C.2: Hard-limit activation function

Prior to training, the network inputs and targets are often scaled to fall within a specified range. This makes the training algorithms more efficient, particularly if the inputs or targets vary greatly in value. The algorithm that was used in this thesis is

$$p_{scaled} = \frac{2(p - p_{min})}{p_{max} - p_{min}} - 1. \quad (\text{C.1})$$

Naturally, any outputs need to be post-processed to reverse the scaling. This is done with the following equation.

$$p = \frac{1}{2}(p_{scaled} + 1)(p_{max} - p_{min}) + p_{min}. \quad (\text{C.2})$$

Note that the target t can be substituted for the input p in either of the above equations.

C.2 Backpropagation Networks

Backpropagation networks consist of one or more layers of hidden neurons that lie between the input and output neurons. They are named after the training method, known as the *backpropagation of errors* [66]. This is simply a gradient-based optimization problem designed to minimize the total squared error of the output computed by the net. They are popular for data interpolation and prediction because once properly trained, they tend to give reasonable results for inputs they have never seen [67].

The training method consists of three stages: feedforward of input training pattern, the calculation and backpropagation of the associated error, and the adjustment of the weights and biases.

C.2.1 Training Algorithm for Backpropagation Networks

The multilayer network shown in Figure C.3 can be solved using the Gauss-Newton method. There are R inputs, S_1 neurons in the first layer, S_2 neurons in the second layer, and S_3 neurons in the third layer. The same network is presented in abbreviated notation in Figure C.4.

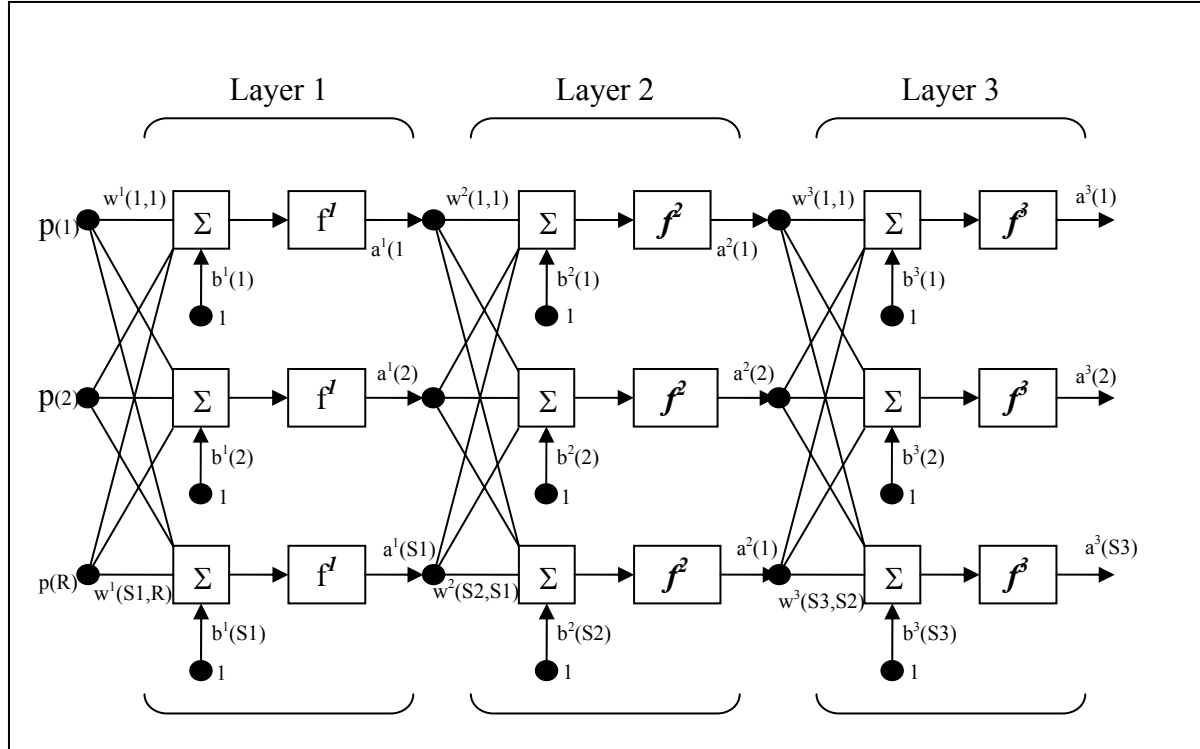


Figure C.3: Three-layer network

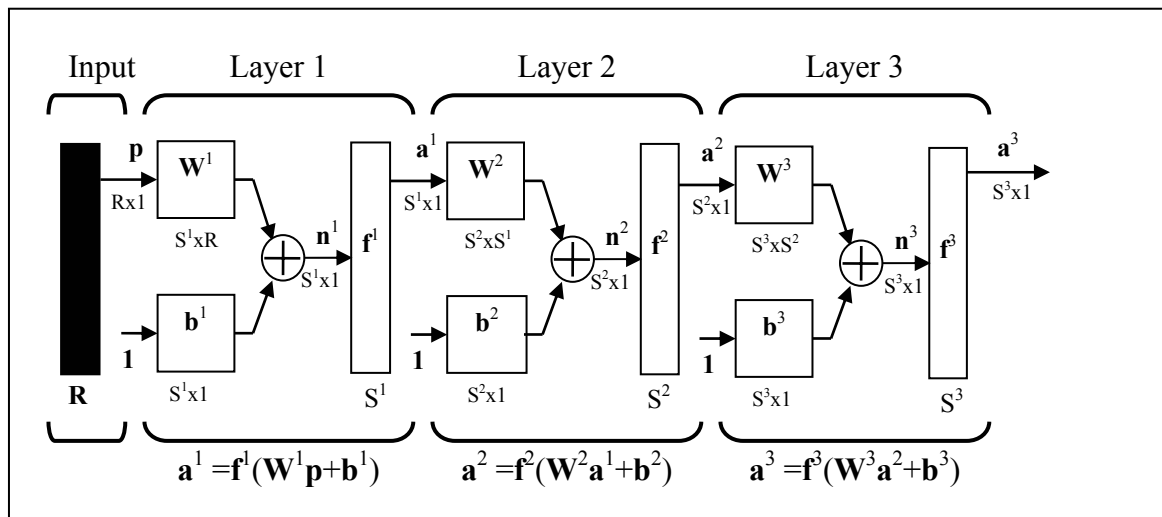


Figure C.4: Three-layer network, abbreviated notation

The following derivation was adapted from Hagan, Demuth, and Beale [68]. The total input to the i th unit in layer $m+1$ is

$$n_i^{m+1} = \sum_{j=1}^{S^m} w_{i,j}^{m+1} a_j^m + b_i^{m+1}. \quad (\text{C.3})$$

The output of unit i is

$$a_i^{m+1} = f^{m+1}(n_i^{m+1}). \quad (\text{C.4})$$

For a network with M layers, we rewrite Eq. C.4 in vector form as

$$\mathbf{a}^{m+1} = \mathbf{f}^{m+1}(\mathbf{W}^{m+1} \mathbf{a}^m + \mathbf{b}^{m+1}), \quad m = 0, 1, \dots, M-1 \quad (\text{C.5})$$

Where

$$\mathbf{W}^{m+1} = \begin{bmatrix} w_{1,1}^{m+1} & w_{1,2}^{m+1} & \cdots & w_{1,S^m}^{m+1} \\ w_{2,1}^{m+1} & w_{2,2}^{m+1} & \cdots & w_{2,S^m}^{m+1} \\ \vdots & \vdots & & \vdots \\ w_{S^{m+1},1}^{m+1} & w_{S^{m+1},2}^{m+1} & \cdots & w_{S^{m+1},S^m}^{m+1} \end{bmatrix} \quad (\text{C.6})$$

We can rename the input p as a^0 and express it in vector form as

$$\mathbf{a}^0 = \mathbf{p}. \quad (\text{C.7})$$

Similarly, we can express the outputs in the last layer as

$$\mathbf{a} = \mathbf{a}^M \quad (\text{C.8})$$

In the backpropagation algorithm, a set of input and output pairs are provided:

$$\{\mathbf{p}_1, \mathbf{t}_1\}, \{\mathbf{p}_2, \mathbf{t}_2\}, \dots, \{\mathbf{p}_Q, \mathbf{t}_Q\}, \quad (\text{C.9})$$

where \mathbf{p}_q is a network input, and the output for the same network is \mathbf{t}_q .

The error, or performance index is the mean square error. For a multi-layer network, the error at the k th iteration is

$$\hat{F}(\mathbf{x}) = (\mathbf{t}(k) - \mathbf{a}(k))^T (\mathbf{t}(k) - \mathbf{a}(k)) = \mathbf{e}^T(k) \mathbf{e}(k). \quad (\text{C.10})$$

The algorithm will attempt to minimize this error by adjusting the magnitude of the weights and biases.

The steepest descent method updates the new weights and biases with the following equations.

$$w_{i,j}^m(k+1) = w_{i,j}^m(k) - \alpha \frac{\partial \hat{F}}{\partial w_{i,j}^m} \quad (\text{C.11})$$

$$b_{i,j}^m(k+1) = b_{i,j}^m(k) - \alpha \frac{\partial \hat{F}}{\partial b_i^m} \quad (\text{C.12})$$

The derivative terms can be found by using the chain rule:

$$\frac{\partial \hat{F}}{\partial w_{i,j}^m} = \frac{\partial \hat{F}}{\partial n_i^m} \frac{\partial n_i^m}{\partial w_{i,j}^m} \quad (\text{C.13})$$

$$\frac{\partial \hat{F}}{\partial b_i^m} = \frac{\partial \hat{F}}{\partial n_i^m} \frac{\partial n_i^m}{\partial b_i^m} \quad (\text{C.14})$$

We define the sensitivity of \hat{F} to the i th element of the net input at the m th layer as

$$s_i^m \equiv \frac{\partial \hat{F}}{\partial n_i^m} \quad (\text{C.15})$$

Substituting equations C.3, C.13, C.14, and C.15 into C.11 and C.12 allows the steepest descent algorithm to be expressed as

$$w_{i,j}^m(k+1) = w_{i,j}^m(k) - \alpha s_i^m a_j^{m-1}$$
(C.16)

$$b_i^m(k+1) = b_i^m(k) - \alpha s_i^m.$$
(C.17)

This can be expressed in matrix form as

$$\mathbf{W}^m(k+1) = \mathbf{W}^m(k) - \alpha \mathbf{s}^m (\mathbf{a}^{m-1})^T$$
(C.18)

$$\mathbf{b}^m(k+1) = \mathbf{b}^m(k) - \alpha \mathbf{s}^m$$
(C.19)

where

$$\mathbf{s}^m \equiv \frac{\partial \hat{F}}{\partial \mathbf{n}^m} = \begin{bmatrix} \frac{\partial \hat{F}}{\partial n_1^m} \\ \frac{\partial \hat{F}}{\partial n_2^m} \\ \vdots \\ \frac{\partial \hat{F}}{\partial n_{S^m}^m} \end{bmatrix}$$
(C.20)

The sensitivities \mathbf{s}^m are computed by *backpropagating* the sensitivities from the $m+1$ th layer. The following Jacobian matrix will be used to derive the recurrence relationship for the sensitivities.

$$\frac{\partial \mathbf{n}^{m+1}}{\partial \mathbf{n}^m} \equiv \begin{bmatrix} \frac{\partial n_1^{m+1}}{\partial n_1^m} & \frac{\partial n_1^{m+1}}{\partial n_2^m} & \dots & \frac{\partial n_1^{m+1}}{\partial n_{S^m}^m} \\ \frac{\partial n_2^{m+1}}{\partial n_1^m} & \frac{\partial n_2^{m+1}}{\partial n_2^m} & \dots & \frac{\partial n_2^{m+1}}{\partial n_{S^m}^m} \\ \vdots & \vdots & & \vdots \\ \frac{\partial n_{S^m}^{m+1}}{\partial n_1^m} & \frac{\partial n_{S^m}^{m+1}}{\partial n_2^m} & \dots & \frac{\partial n_{S^m}^{m+1}}{\partial n_{S^m}^m} \end{bmatrix}$$
(C.21)

We consider the i,j element of the matrix by substituting equation C.3 into C.21:

$$\begin{aligned} \frac{\partial n_i^{m+1}}{\partial n_j^m} &= \frac{\partial \left(\sum_{l=1}^{S^m} w_{i,l}^{m+1} a_l^m + b_i^{m+1} \right)}{\partial n_j^m} = w_{i,j}^{m+1} \frac{\partial a_j^m}{\partial n_j^m} \\ &= w_{i,j}^{m+1} \dot{f}^m(n_j^m) \end{aligned} \quad (\text{C.22})$$

where

$$\dot{f}^m(n_j^m) = \frac{\partial f^m(n_j^m)}{\partial n_j^m} \quad (\text{C.23})$$

The Jacobian matrix can now be rewritten as

$$\frac{\partial \mathbf{n}^{m+1}}{\partial \mathbf{n}^m} = \mathbf{W}^{m+1} \dot{\mathbf{F}}^m(\mathbf{n}^m), \quad (\text{C.24})$$

where

$$\dot{\mathbf{F}}^m(\mathbf{n}^m) = \begin{bmatrix} \dot{f}^m(n_1^m) & 0 & \dots & 0 \\ 0 & \dot{f}^m(n_2^m) & \dots & 0 \\ \vdots & \vdots & \ddots & \vdots \\ 0 & 0 & \dots & \dot{f}^m(n_{S^m}^m) \end{bmatrix}. \quad (\text{C.25})$$

The recurrence relation for the sensitivity (Eq. C.20), can now be rewritten by invoking the chain rule and substituting

$$\mathbf{s}^m = \dot{\mathbf{F}}^m(\mathbf{n}^m) (\mathbf{W}^{m+1})^T \mathbf{s}^{m+1} \quad (\text{C.26})$$

It is now apparent how the backpropagation network gets its name. The sensitivities are propagated backwards from the last to the first layer.

To find the starting point, \mathbf{s}^M , we substitute Eqs. C.8 and C.10 into C.15 to get

$$s_i^M = \frac{\partial \hat{F}}{\partial n_i^M} = \frac{\partial (\mathbf{t} - \mathbf{a})^T (\mathbf{t} - \mathbf{a})}{\partial n_i^M} = \frac{\partial \sum_{j=1}^{S^M} (t_j - a_j)^2}{\partial n_i^M} = -2(t_i - a_i) \frac{\partial a_i^M}{\partial n_i^M}. \quad (\text{C.27})$$

The derivative in the final term can be rewritten through the use of Equation C.4.

$$\frac{\partial a_i^M}{\partial n_i^M} = \frac{\partial(\dot{f}^M(n_i^M))}{\partial n_i^M} = \dot{f}^M(n_i^M) \quad (\text{C.28})$$

Now Equation C.27 can be written as

$$s_i^M = -2(t_i - a_i)\dot{f}^M(n_i^M). \quad (\text{C.29})$$

This can be expressed in matrix form as

$$\mathbf{s}^M = -2\dot{\mathbf{F}}^M(\mathbf{n}^M)(\mathbf{t} - \mathbf{a}). \quad (\text{C.30})$$

In many backpropagation networks, a hyperbolic tangent is chosen as the activation function. The equation for the hyperbolic tangent is

$$f_{\tanh}(x) = \frac{2}{1+e^{-2x}} - 1 \quad (\text{C.31})$$

and its derivative is

$$\dot{f}_{\tanh}(x) = \frac{4e^{-2x}}{(1+e^{-2x})^2}. \quad (\text{C.32})$$

Figures C.5 and C.6 show what the hyperbolic tangent and its derivative look like.

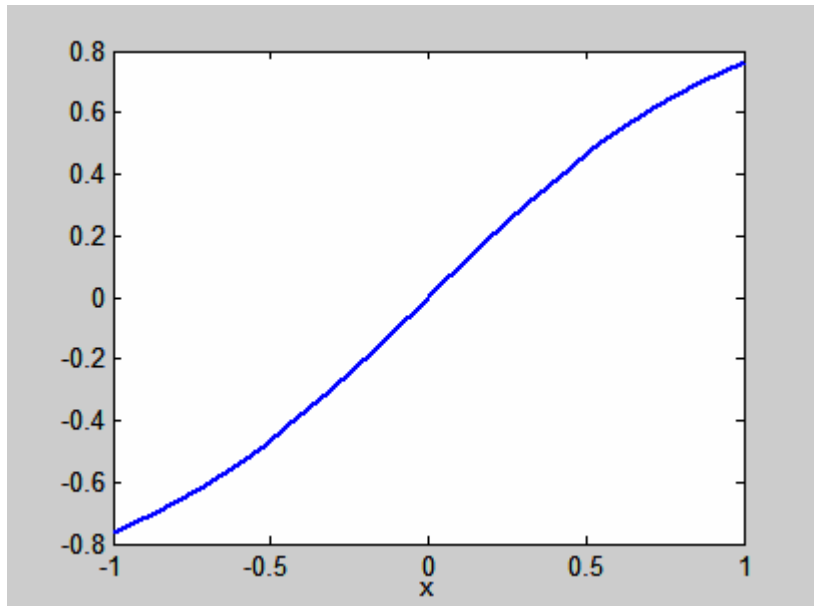


Figure C.5: Hyperbolic tangent

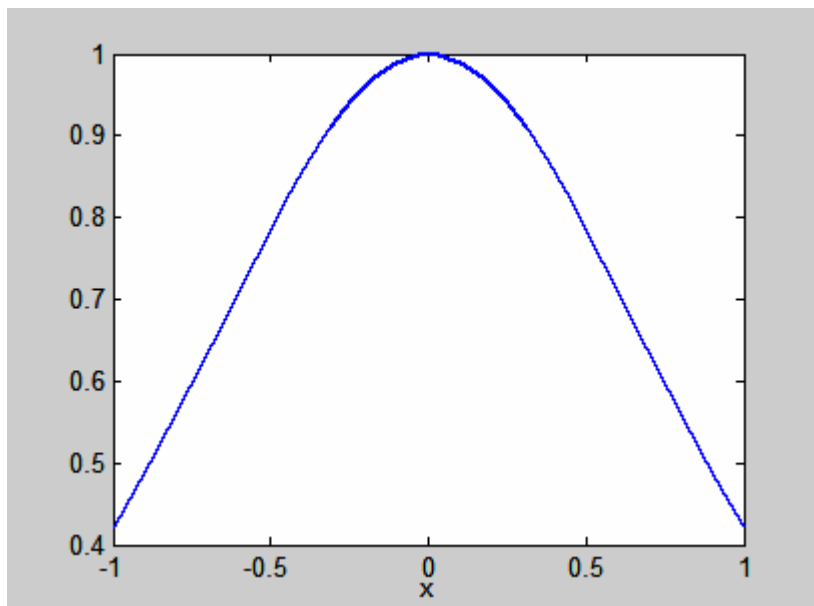


Figure C.6: First derivative of hyperbolic tangent

C.2.2 Summary of Training Algorithm for Backpropagation Networks

After the initial weights and biases are chosen (often randomly), they are propagated forward through the network using Equations C.5, C.7, and C.8. Once the error is calculated, the sensitivities are propagated backwards through the network layer-by-layer with Equations C.26 and C.30. The weights and biases are updated using Equations C.18 and C.19. These steps are repeated until the stopping condition is met.

Stopping conditions are defined by the user, and are usually met when the error is below a certain level, the program has run for a specified number of iterations, or when the magnitude of the gradient has dropped below a specified level.

C.2.3 The Levenberg-Marquardt Algorithm

The Levenberg-Marquardt algorithm is a variation of Newton's method and is the fastest method for training backpropagation networks of medium-size. It is particularly well suited for implementation with Matlab[®], since the solution of the matrix equations is a built-in function [69]. The following derivation begins with a derivation of the Newton and Gauss-Newton methods, and leads into the Levenberg-Marquardt algorithm [70, 71].

In the steepest descent method described previously, first-order derivatives were used to determine the direction of travel. This causes the algorithm to converge at a relatively slow rate. The aim of Newton's method is to use a second-order Taylor's series expansion of the objective function about the current design point [72]. A Hessian matrix is used which allows for a much faster quadratic rate of convergence.

The second-order Taylor series expansion of the function $f(\mathbf{x})$ is

$$f(\mathbf{x})|_{\mathbf{x}=\mathbf{x}_{k+1}} = f(\mathbf{x})|_{\mathbf{x}=\mathbf{x}_k} + \mathbf{g}_k^T \Delta \mathbf{x} + 0.5 \Delta \mathbf{x}^T \mathbf{A}_k \Delta \mathbf{x} \quad (\text{C.33})$$

where $\mathbf{g}_k \equiv \nabla F(\mathbf{x})|_{\mathbf{x}=\mathbf{x}_k}$, $\Delta \mathbf{x} = \mathbf{x}_{k+1} - \mathbf{x}_k$ denotes a small change in the input and

$\mathbf{A}_k = \nabla^2 f(\mathbf{x})|_{\mathbf{x}=\mathbf{x}_k}$ is the Hessian of f at the point \mathbf{x} .

If \mathbf{A}_k is positive semidefinite, there is a $\Delta \mathbf{x}$ that gives a global minimum for f . Furthermore, if the Hessian is positive definite, the global minimum is unique. For optimum conditions ($\partial f / \partial (\Delta \mathbf{x}) = \mathbf{0}$), Equation C.33 becomes

$$\mathbf{g}_k + \mathbf{A}_k \Delta \mathbf{x} = \mathbf{0}. \quad (\text{C.34})$$

Assuming \mathbf{A}_k is nonsingular, we solve for $\Delta \mathbf{x}$:

$$\Delta \mathbf{x} = -\mathbf{A}_k^{-1} \mathbf{g}_k \quad (\text{C.35})$$

and we can write

$$\mathbf{x}_{k+1} = \mathbf{x}_k - \mathbf{A}_k^{-1} \mathbf{g}_k. \quad (\text{C.36})$$

For a backpropagation network, $F(\mathbf{x})$ is a sum of squares function:

$$F(\mathbf{x}) = \sum_{i=1}^N v_i^2(\mathbf{x}) = \mathbf{v}^T(\mathbf{x}) \mathbf{v}(\mathbf{x}), \quad (\text{C.37})$$

and the j th element of the gradient is

$$[\nabla F(\mathbf{x})]_j = \frac{\partial F(\mathbf{x})}{\partial x_j} = 2 \sum_{i=1}^N v_i(\mathbf{x}) \frac{\partial v_i(\mathbf{x})}{\partial x_j}. \quad (\text{C.38})$$

The gradient can be written in matrix form as

$$\nabla F(\mathbf{x}) = 2 \mathbf{J}^T(\mathbf{x}) \mathbf{v}(\mathbf{x}) \quad (\text{C.39})$$

where the Jacobian matrix \mathbf{J} is

$$\boxed{\mathbf{J}(\mathbf{x}) = \begin{bmatrix} \frac{\partial v_1(\mathbf{x})}{\partial x_1} & \frac{\partial v_1(\mathbf{x})}{\partial x_2} & \dots & \frac{\partial v_1(\mathbf{x})}{\partial x_n} \\ \frac{\partial v_2(\mathbf{x})}{\partial x_1} & \frac{\partial v_2(\mathbf{x})}{\partial x_2} & \dots & \frac{\partial v_2(\mathbf{x})}{\partial x_n} \\ \vdots & \vdots & & \vdots \\ \frac{\partial v_N(\mathbf{x})}{\partial x_1} & \frac{\partial v_N(\mathbf{x})}{\partial x_2} & \dots & \frac{\partial v_N(\mathbf{x})}{\partial x_n} \end{bmatrix}} \quad (\mathbf{C.40})$$

The k,j element of the Hessian matrix is

$$\boxed{[\nabla^2 F(\mathbf{x})]_{k,j} = \frac{\partial^2 F(\mathbf{x})}{\partial x_k \partial x_j} = 2 \sum_{i=1}^N \left\{ \frac{\partial v_i(\mathbf{x})}{\partial x_k} \frac{\partial v_i(\mathbf{x})}{\partial x_j} + v_i(\mathbf{x}) \frac{\partial^2 v_i(\mathbf{x})}{\partial x_k \partial x_j} \right\}}, \quad (\mathbf{C.41})$$

and can be expressed in matrix form as

$$\boxed{\nabla^2 F(\mathbf{x}) = 2\mathbf{J}^T(\mathbf{x})\mathbf{J}(\mathbf{x}) + 2\mathbf{S}(\mathbf{x})} \quad (\mathbf{C.42})$$

where

$$\boxed{\mathbf{S}(\mathbf{x}) = \sum_{i=1}^N v_i(\mathbf{x}) \nabla^2 v_i(\mathbf{x})}. \quad (\mathbf{C.43})$$

By assuming $\mathbf{S}(\mathbf{x})$ to be small, the Hessian matrix is approximated as

$$\boxed{\nabla^2 F(\mathbf{x}) \approx 2\mathbf{J}^T(\mathbf{x})\mathbf{J}(\mathbf{x})}. \quad (\mathbf{C.44})$$

The *Gauss-Newton* method is obtained by substituting Equation C.44 into C.36:

$$\boxed{\mathbf{x}_{k+1} = \mathbf{x}_k - [\mathbf{J}^T(\mathbf{x}_k)\mathbf{J}(\mathbf{x}_k)]^{-1}\mathbf{J}^T(\mathbf{x}_k)v(\mathbf{x}_k)}, \quad (\mathbf{C.45})$$

The advantage of the Gauss-Newton method over the Newton method is that the second-order derivatives do not need to be calculated. However, one of the problems with the Gauss-Newton method is that the matrix $\mathbf{H} = \mathbf{J}^T\mathbf{J}$ may not be invertible. To overcome this, an addition is made to the approximate Hessian matrix:

$$\boxed{\mathbf{G} = \mathbf{H} + \mu\mathbf{I}} \quad (\mathbf{C.46})$$

The value of μ can be increased until \mathbf{G} is positive definite, and therefore the matrix will be invertible.

The *Levenberg-Marquardt* algorithm is created by substituting the approximate Hessian matrix, Equation C.46, into Equation C.45.

$$\mathbf{x}_{k+1} = \mathbf{x}_k - [\mathbf{J}^T(\mathbf{x}_k)\mathbf{J}(\mathbf{x}_k) + \mu_k \mathbf{I}]^{-1} \mathbf{J}^T(\mathbf{x}_k) \mathbf{v}(\mathbf{x}_k) \quad (\text{C.47})$$

or

$$\Delta \mathbf{x}_k = -[\mathbf{J}^T(\mathbf{x}_k)\mathbf{J}(\mathbf{x}_k) + \mu_k \mathbf{I}]^{-1} \mathbf{J}^T(\mathbf{x}_k) \mathbf{v}(\mathbf{x}_k). \quad (\text{C.48})$$

As μ_k is increased, the algorithm behaves like the steepest descent algorithm, which works well far away from the solution point. For smaller μ_k the algorithm becomes Gauss-Newton, which is more effective near the solution point [73].

The algorithm begins with μ_k set to some small value. If a step that yields a smaller value for the performance index cannot be found, the step is repeated for a larger μ_k . Conversely, μ_k is decreased when a step is taken that yields a smaller value for the performance index. This increase or decrease is typically done by multiplying or dividing μ_k by a scalar.

In the standard backpropagation procedure described earlier, the derivatives of the squared errors were computed. The computation for the Jacobian requires the computation of the derivatives of the errors, not the squared errors.

In Equation C.40, the vectors are

$$\mathbf{v}^T = [v_1 \quad v_2 \quad \cdots \quad v_N] = [e_{1,1} \quad e_{2,1} \quad \cdots \quad e_{S^M,1} \quad e_{1,2} \quad \cdots \quad e_{S^M,Q}] \quad (\text{C.49})$$

and

$$\mathbf{x}^T = [x_1 \quad x_2 \quad \cdots \quad x_n] = [w_{1,1}^1 \quad w_{1,2}^1 \quad \cdots \quad w_{S^1,R}^1 \quad b_1^1 \quad \cdots \quad b_{S^1}^1 \quad w_{1,1}^2 \quad \cdots \quad b_{S^M}^M] \quad (\text{C.50})$$

where $N=QxS^M$ and $n=S^I(R+I)+S^2(S^I+I)+\dots+S^M(S^{M-1}+I)$.

Substitution of these vectors into Eq. C.40 gives

$$\mathbf{J}(\mathbf{x}) = \begin{bmatrix} \frac{\partial e_{1,1}}{\partial w_{1,1}^1} & \frac{\partial e_{1,1}}{\partial w_{1,2}^1} & \cdots & \frac{\partial e_{1,1}}{\partial w_{S^1,R}^1} & \frac{\partial e_{1,1}}{\partial b_1^1} & \cdots \\ \frac{\partial e_{2,1}}{\partial w_{1,1}^1} & \frac{\partial e_{2,1}}{\partial w_{1,2}^1} & \cdots & \frac{\partial e_{2,1}}{\partial w_{S^1,R}^1} & \frac{\partial e_{2,1}}{\partial b_1^1} & \cdots \\ \vdots & \vdots & & \vdots & \vdots & \vdots \\ \frac{\partial e_{S^M,1}}{\partial w_{1,1}^1} & \frac{\partial e_{S^M,1}}{\partial w_{1,2}^1} & \cdots & \frac{\partial e_{S^M,1}}{\partial w_{S^1,R}^1} & \frac{\partial e_{S^M,1}}{\partial b_1^1} & \cdots \\ \frac{\partial e_{1,2}}{\partial w_{1,1}^1} & \frac{\partial e_{1,2}}{\partial w_{1,2}^1} & \cdots & \frac{\partial e_{1,2}}{\partial w_{S^1,R}^1} & \frac{\partial e_{1,2}}{\partial b_1^1} & \cdots \\ \vdots & \vdots & & \vdots & \vdots & \vdots \end{bmatrix} \quad (\text{C.51})$$

The Marquardt sensitivity is defined as

$$\tilde{s}_{i,h}^m \equiv \frac{\partial v_h}{\partial n_{i,q}^m} = \frac{\partial e_{k,q}}{\partial n_{i,q}^m} \quad (\text{C.52})$$

where $h=(q-I)S^M+k$.

The elements of the Jacobian matrix are now

$$[\mathbf{J}]_{h,l} = \frac{\partial e_{k,q}}{\partial w_{i,j}^m} = \tilde{s}_{i,h}^m a_{j,q}^{m-1} \quad (\text{C.53})$$

and

$$[\mathbf{J}]_{h,l} = \frac{\partial e_{k,q}}{\partial b_i^m} = \tilde{s}_{i,h}^m. \quad (\text{C.54})$$

The Marquardt sensitivities at the final layer are calculated as

$$\begin{aligned}\tilde{s}_{i,h}^M &= \frac{\partial e_{k,q}}{\partial n_{i,q}^M} = \frac{\partial(t_{k,q} - a_{k,q}^M)}{\partial n_{i,q}^M} = \frac{\partial a_{k,q}^M}{\partial n_{i,q}^M} \\ &= \begin{cases} -\dot{f}^M(n_{i,q}^M) & \text{for } i = k \\ 0 & \text{for } i \neq k \end{cases}\end{aligned}\quad (\text{C.55})$$

In matrix form, this is

$$\tilde{\mathbf{S}}_q^M = -\dot{\mathbf{F}}^M(\mathbf{n}_q^M) \quad (\text{C.56})$$

here $\dot{\mathbf{F}}^M(\mathbf{n}_q^M)$ is defined in Equation C.25.

The Marquardt sensitivities can now be backpropagated through the layers using

$$\tilde{\mathbf{S}}^m = [\tilde{\mathbf{S}}_1^m | \tilde{\mathbf{S}}_2^m | \dots | \tilde{\mathbf{S}}_\mathcal{Q}^m] \quad (\text{C.57})$$

where

$$\tilde{\mathbf{S}}_q^m = \dot{\mathbf{F}}(\mathbf{n}_q^m)(\mathbf{W}^{m+1})^T \tilde{\mathbf{S}}_q^{m+1}. \quad (\text{C.58})$$

C.2.4 Summary of Levenberg-Marquardt Training Algorithm for Backpropagation Networks

Once the initial weights and biases are chosen, and the outputs calculated, compute the sum of squared errors over all inputs using Equation C.37. Compute the sensitivities (Equations C.56-C.58) and the elements of the Jacobian matrix (Equations C.53 and C.54). The biases and weights are updated using Equation C.48 and the sum of squared errors is recomputed. If the sum of squared errors becomes smaller, decrease the

value of μ and repeat all the steps. If the sum of squared errors becomes larger, increase the value of μ and re-update the biases and weights.

VITA

Michael Y. Yang

Education

The Pennsylvania State University, University Park, Pennsylvania

Doctor of Philosophy in Mechanical Engineering
Master of Science in Mechanical Engineering - Conferred May 2001

Purdue University, West Lafayette, Indiana

Bachelor of Science in Mechanical Engineering - Conferred May 1997

Publications

Yang, M.Y. and Koopmann, G.H. "An Inverse Method to Compute Equivalent Forces on a Structure Based on Sound Power Measurements." *Journal of Sound and Vibration* (2002) **252**(1), 65-82.

Yang, M.Y., Koopmann, G.H., Lesieurte, G.A., Hambric, S.A. "Attenuation of High Amplitude Vibrations with Particle Dampers." *Proceedings of 2002 ASME International Mechanical Engineering Congress and Exposition*. November 17-22, 2002, New Orleans, Louisiana. NCA-32689.

Yang, M.Y. "Passive Techniques in Environmental Noise Control." *Innovations and Materials for Green Engineering*. Volume 2. December 1998.

Honors

National Science Foundation (NSF) Graduate Research Trainee
Dean's Fellowship – Pennsylvania State University
Honorable Mention – NSF Graduate Research Fellowship
Dean's List